STRESS CORROSION CRACKING OF ZIRCALOY

IN THE PRESENCE OF IODINE

by

DAVID BRUCE KNORR

B.S. Lehigh University
(1974)

S.M. Massachusetts Institute of Technology
(1977)

SUBMITTED TO THE DEPARTMENT OF
MATERIALS SCIENCE AND ENGINEERING IN PARTIAL
FULFILLMENT OF THE
REQUIREMENTS FOR THE
DEGREE OF

DOCTOR OF SCIENCE

at the

MASSACHUSETTS INSTITUTE OF TECHNOLOGY

September 1981

ⓒ   Massachusetts Institute of Technology

Signature of Author_____
Department of Materials Science and Engineering
August 7, 1981

Certified by_____
Regis M. Pelloux
Thesis Supervisor

Accepted by_____
Regis M. Pelloux
Chairman, Departmental Committee on Graduate Students

STRESS CORROSION CRACKING OF ZIRCALOY

IN THE PRESENCE OF IODINE

by

DAVID BRUCE KNORR

Submitted to the Department of Materials Science and Engineering on August 7, 1981, in partial fulfillment of the requirements for the degree of Doctor of Science.

ABSTRACT

A two part experimental research program is conducted to investigate the effect of several materials variables on the initiation and propagation of stress corrosion cracks (SCC) in Zircaloy in an iodine environment. Fracture mec' \ics crack propagation specimens (double cantilever beam) are machined from several directions in textured Zircaloy plate, pre-notched or fatigue precracked, and loaded to constant initial displacement. Stress corrosion cracks propagate to crack arrest in a flowing Ar + 4 Pa I_2 gas stream at 300°C. Stress intensity at crack arrest, K_{ISCC}, is calculated, and fracture surfaces are examined. The variables studied are microstructure as determined by heat treatment and crystallographic texture.

Internal gas pressurization tests on reactor grade cladding tubes from two separate suppliers are done in an environment of Ar and a small quantity of iodine at 320°C with several tests conducted at 390°C. Hoop stress versus time to failure is measured, and fracture features are analyzed. The materials variables considered are crystallographic texture, ID surface condition, and hoop residual stress.

The tests on fracture mechanics specimens show that crystallographic texture has a strong influence on K_{ISCC}. K_{ISCC} is lowest when a large volume fraction of basal poles are oriented in the crack opening direction and increases as the basal poles become progressively misoriented. For equivalent textures recrystallized material has a larger K_{ISCC} than stress-relieved material. The principal mode of crack propagation is transgranular cleavage near the basal plane. Several ductile modes of separation such as tearing between facets and fluting complement cleavage. The increase in K_{ISCC} with basal pole misorientation is due to the ductile modes of separation which are more prevalent as K_{ISCC} increases. Cleavage of misoriented basal planes is a secondary contribution to the higher K_{ISCC} values. In recrystallized material regions of intergranular propagation are observed with a transition to completely intergranular failure near K_{ISCC}.

In the tube pressurization tests of cladding from two different suppliers, the substantial difference in hoop stress versus time to failure behavior is due to texture. A more tangential tube texture results in shorter times to failure at a particular stress and a lower threshold stress. ID surface finish and heat treatment have a smaller, second order effect on SCC susceptibility. Residual hoop stress at the levels found in these two lots has no effect on SCC behavior.

Both crack initiation and crack propagation are strongly influenced by texture. Lifetime is limited by crack initiation at 320°C, but initiation occurs more readily at 390°C. Strain accumulation and localization are important to the crack initiation process. Fracture features associated with crack propagation are qualitatively similar in both fracture mechanics and tube pressurization specimens. High stress/high K favors small cleavage facets and more ductile features while low stress/low K favors larger cleavage facets with less tearing between facets.

Thesis supervisor: R. M. Pelloux

Title: Professor of Materials Engineering

To my parents

TABLE OF CONTENTS

LIST OF FIGURES

LIST OF FIGURES (continued)

LIST OF FIGURES (continued)

LIST OF FIGURES (continued)

LIST OF TABLES

LIST OF TABLES (continued)

ACKNOWLEDGEMENTS

I would like to sincerely thank Prof. Regis Pelloux for his help and guidance during the progress of this research program. I would also like to express my gratitude to Dr. Leo Van Swam of Exxon Nuclear Company, Inc. who acted more as an advisor than a contract monitor by providing both materials and critical technical feedback during the term of this research. I wish to thank Prof. Ron Latanision and Prof. John Meyer for serving on my thesis committee and for their constructive comments on this manuscript.

The sponsorship of this research by Exxon Nuclear Company, Inc. is gratefully acknowledged. Their continued support during the entire term of the program was critical to the successful completion of this thesis.

Finally, I would like to thank both present and past members of the research group for their critical comments and moral support. In particular, I am grateful to Jim Shewbridge for his large effort in helping build the tube pressurization facility and for discussions on the technical aspects of my work.

1. INTRODUCTION

Operating experience with light water reactor (LWR) fuels has shown that the Zircaloy cladding is susceptible to failure soon after a sudden local power increase which follows appreciable irradiation. The first indication of these pellet-clad interaction (PCI) failures was reported in 1964 [1]. By the early 1970's most reactor vendors found that failure by PCI was a performance limiting effect [2-4]. Fission product iodine was implicated as the corrosive specie in the failure process by iodine and tellurium deposits near the fuel failure locations [1] and from the discovery by Rosenbaum [5,6] that iodine could embrittle the Zircaloy fuel cladding in out-of-reactor tests.

Stress corrosion cracking (SCC) is strongly implicated as the failure mechanism based on the observations that:

- a time delay between power increase and failure signal is present indicating a time dependent process [3];

- irradiated cladding loaded with fresh fuel, i.e. no fission product inventory, did not fail in high power tests that would fail with irradiated fuel [4,7];

- cracks initiated at the cladding inside surface where fission product deposits are found;

- the fracture surfaces of incipient cracks strongly resemble the fracture features in iodine embrittled laboratory tests which are both different from the fracture surfaces formed with no environmental effect [3,4,8,9].

17

Several reviews of the failure processes for Zircaloy fuel rods are available [10,11].

In general, the PCI failure phenomenon should be referred to as environmentally assisted fracture of Zircaloy. Laboratory tests in gaseous iodine should be termed iodine assisted fracture of Zircaloy. The mechanism of environmental failure in Zircaloy is not unambiguously known although several have been proposed [12]. The above terminology implies no specific mechanism as does the term stress corrosion cracking. Tests in liquid metal environments clearly fall under the category of liquid metal embrittlement (LME). Historically, however, iodine failures are referred to as stress corrosion cracks [5,6,12] so this label is retained throughout this thesis.

Three elements are essential for SCC to occur: an aggressive environment, a tensile stress, and a susceptible material. The pellet-clad interaction exerts a local tensile stress while release of volatile fission products to the cladding inside surface provides the environment resulting in failure of the susceptible Zircaloy. Fig. 1.1 presents an overview of the SCC process which will be used to organize subsequent discussion. Each of these factors in the PCI failure phenomenology has a counterpart in the laboratory experiments. The knowledge gained from the study of both PCI fuel failure phenomena and laboratory studies is applied toward understanding the processes leading to PCI failure, modeling them, and designing PCI failure resistant fuel.

The background and literature survey, Section 2, considers each of the three broad categories indicated in Fig. 1.1: PCI failure pheno-menology, laboratory experiments, and analysis and solutions. Emphasis is placed on the laboratory experiments since this section is most

relevant to the experimental portion of this thesis. Section 3 describes the plate and tubing materials used in the experimental program. Three types of tests are conducted: crack arrest tests with fracture mechanics specimens, tube pressurization tests on reactor grade cladding, and split ring tests. The plan of work, results, and discussion are presented in Sections 4, 5 and 6, respectively, with a sub-section devoted to each type of test. An additional sub-section of the discussion is devoted to consideration of several critical issues regarding iodine SCC phenomenology such as crack initiation, crack propagation, the role of stress and strain, and relevance of this work to irradiated materials. Section 8 gives the summary and conclusions while Section 9 details additional research that could be done to supplement the work presented in this thesis.

FIGURE 1.1   OVERVIEW OF STRESS CORROSION CRACKING FAILURES IN ZIRCALOY

ENVIRONMENT   SUSCEPTIBLE MATERIAL   STRESS

PCI FAILURE
PHENOMENOLOGY

- FUEL ROD CHEMISTRY
- FAILED FUEL ROD CLADDING
- PCI MECHANICS

LABORATORY
EXPERIMENTS

ENVIRONMENTAL VARIABLES
- iodine conc.
- metal iodides
- hydrogen
- oxygen (air)
- water vapor
- liquid metals

MATERIALS VARIABLES
- heat treatment
- ID surface condition
- texture
- residual stress
- irradiation

MECHANICAL TEST CONDITIONS
- constant displacement
- constant stress
- constant extension rate
- crack growth

ANALYSIS AND
SOLUTIONS

SCC PHENOMENOLOGY

CRACK INITIATION
- oxide penetration
- initiation sites

CRACK PROPAGATION
- intergranular
- transgranular

MECHANICAL THRESHOLDS
- stress
- stress intensity
- strain
- strain rate

FRACTOGRAPHY

REMEDIES
- coatings
- barriers
- fuel redesign

MODELS
- mechanistic
- deterministic

2. BACKGROUND AND LITERATURE SURVEY

2.1   Description of PCI Failure Phenomenology

The three factors required for SCC are stress, environment, and material susceptibility. The PCI mechanics which lead to a tensile stress on the cladding are described. The environment at the clad inside surface is controlled by both the fuel/fission product chemistry and the release of fission products to the clad. Both factors are considered. The details of the material response to stress and aggressive fission products is deferred until Section 2.2.3.

2.1.1   PCI Mechanics

The basis for the mechanical interaction between pellet and cladding is the difference in the thermal expansion properties of the UO_2 fuel and the Zircaloy cladding. When a fuel rod is brought to power, several responses by the fuel and cladding are noted [13]. The clearance between the pellet and cladding decreases due to the larger thermal expansion of the fuel. The large parabolic temperature gradient in the fuel pellet causes a "barreling" phenomenon to occur. The hotter pellet center expands more than the cooler pellet surface causing the pellet to assume a non cylindrical shape with a convex top and concave sides. The corners of the hourglass-shaped pellet contact the clad first. The cladding deforms to fit the contours of the pellet stack either by further power increases which force hard contact between pellet and cladding or by creepdown of the cladding onto the pellet stack if close mechanical contact has not occurred previously.

Once mechanical contact is made, an increase in rod power level generates local stresses on the cladding. The outer region of the fuel cracks in response to the change in pellet temperature gradient. Stress and strain are concentrated at the ridges and at fuel cracks which are observed to be failure locations. A simplified model of the PCI process in Fig. 2.1 demonstrates the elements essential for fuel failure. The tensile stress in the cladding is relaxed by fuel and cladding creep and fission products are released to the cladding. PCI cracking occurs if the tensile stress remains above a critical stress with "corrosive" fission products present for a sufficient period of time. Fuel design and fuel operating conditions are utilized to minimize this possibility.

Several design changes are incorporated into current fuel designs to minimize mechanical interaction. Ridging is reduced by lowering pellet height to diameter ratio, dished ends, and chamfering [14]. Rod pre-pressurization with helium increases gap heat conductance and reduces cladding creepdown [15].

Five operating parameters are related to PCI [11]:

a) Burnup at low power prior to the ramp;

b) Maximum power during the ramp;

c) Difference between initial power level and final power level;

d) Average ramp rate;

e) Time at high power.

Failure occurs when fuel at a low power level receives a rapid power increase, e.g. by a control rod movement. Consequently, rates of power increase and maximum rod power rating are specified by the fuel vendor to minimize both local stress and fission product release.

Fuel failures in operating rods usually have low uniform strains at failure and little or no ridging. Ridge heights of less than 10 μm are often observed [9,16]. Low values of macroscopic strain are reported [4,9,17] with a measured diametral strain less than 0.07% given in one case [17]. Local strains occur at both ridges and fuel cracks. The strain concentration depends on the details of this interaction such as ridge height, ridge sharpness, coefficient of friction between cladding and fuel, fuel cladding bonding, and number of fuel cracks. Values of two to five times the macroscopic strain are predicted by deformation models [14,18].

2.1.2   Fuel Chemistry

The chemistry inside an operating fuel pin is very complex. Thermodynamic data obtained from out-of-pile experiments are used to model in-pile behavior. The results of post-irradiation tests are then used to verify these models. The large in-pile radiation fields can produce results that are different from predictions based on out-of-pile thermodynamic calculations. The variety of fission product species, numerous chemical states of the fission products, and interactions between fuel, clad, and fission products further complicate this analysis. In many cases thermodynamic relationships are not known.

The goal of this section is to define the chemical state of a light water reactor fuel pin to better understand the environment that is relevant to PCI failure. Oxygen potential and oxygen redistribution are discussed first. Fission product release to the cladding inside surface is then considered, including observations on the chemical form

and morphology of fission product deposits. Finally, the chemical form
and release of potential embrittling elements is discussed. Additional
references on fuel chemistry are available [19,20].

2.1.2.1 Oxygen Potential

Urania fuel undergoes a continuous change in oxygen distribution
and stoichiometry during burnup in LWR's. Oxygen is redistributed in the
temperature gradient of the fuel pin during the initial stages of burnup
where the slightly hyperstoichiometric fuel becomes richer in oxygen at
the fuel centerline and nearly stoichiometric at the cooler pellet OD
[21]. The oxygen gradient is attributed to $CO-CO_2$ transport of oxygen in
the temperature gradient [22,24]. At higher burnup cesium might also
participate in the transport process [21].

Burnup affects the oxygen balance in the fuel. Several competing
effects are present, some releasing oxygen and some consuming oxygen. The
increase in oxygen content of the fuel is attributed to the following
factors:

1. The fuel is slightly hyperstoichiometric at the beginning
    of life;

2. Fission of the fuel replaces uranium (valence +4) with a
    variety of fission product elements (rare earths,
    alkaline earths) having a net valence less than +4;

3. Plutonium is bred from U^{238}; since Pu can exist in valence
    states less than +4, the net effect is increased oxygen
    availability.

A decrease in the oxygen content of the fuel is due to:

1. Reaction of fission product cesium with urania to form cesium uranates; several cesium-urania compounds are reported to be stable [25] and these compounds are observed in post-irradiation examinations as cesium uranates or cesium-zirconium-urania compounds [4,9].

2. Oxidation of Zircaloy clad ID.

There is evidence that the processes that consume oxygen dominate those that release oxygen. Adamson et al. [21] measure the oxygen potential as a function of fuel element radius with an oxygen probe for fuel burnups of approximately 11,000 and 19,000 MWD/T. They find that the surfaces are slightly hypostoichiometric and the center of the fuel pins is more hypostoichiometric. Kleykamp [26] examines a fuel element with 41,000 MWD/T burnup with an electron microprobe and estimates the fuel stoichiometry from the composition of fission product precipitates. He reports that the initially hyperstoichiometric fuel (O/U = 2.003) is reduced to near or slightly below stoichiometric composition across most of the pellet radius. These results cannot be applied directly to LWR fuel elements due to differences in burnup, rod power, and amount of plutonium breeding. However, a clear trend of oxygen decrease in the urania fuel with burnup emerges. A substantial amount of oxygen is consumed by the oxidation of the clad ID. Oxide films are observed at the ID surface of fuel rods irradiated to moderate and high burnup [4,9,26-28]. Cubicciotti and Jones [19,40] attempt a semiquantitative oxygen balance for an LWR fuel rod.

The thermodynamic properties of urania fuel are modified by the accumulation of aliovalent fission products and plutonium bred from U^{238}. The yttrium, rare earth, and plutonium are in solid solution in the UO_2 matrix. Catlow [29] presents a general model that shows how the oxygen chemical potential of the fuel changes by doping with aliovalent cations. For metal to oxygen ratios, M/O, less than two, doping with either lower valent cation such as Mg^{+2} or La^{+3} or an electron donor such as Ce or Pu decreases the oxygen potential. This is demonstrated experimentally by Ce [30], Pu [31,32], Nb [31], and Pr [33] additions to give $(U,M)O_{2-x}$ and by Ce or a simulated fission product mixture of Pr, Ce, Zr, Nd and Y added to $(U_{0.75}, Pu_{0.25}) O_{2-x}$ [34].

Blackburn [35] proposes a model to calculate oxygen potential over UO_{2+x} which is expanded by Olander [36] to consider $(U,Pu)O_{2\pm x}$. Both experimental [30-33] and model [35,36] results are applied to breeder reactor, mixed oxide fuel since relatively large concentrations (10-20%) of Pu additions are considered. Concentrations of 3% or less are appropriate for the burnups and plutonium breeding characteristics of LWR fuel. The Blackburn/Olander model is modified to consider $(U_{1-q}, Pu_q)O_{2\pm x}$ where $q \leqslant .01$ are considered. Model development, equations, results, and applications are discussed in Appendix A. Fig. 2.2 shows some results of the calculations. The oxygen potential at slightly hypostoichiometric O/M ratios is significantly increased by Pu addition of only several tenths of a percent. A similar trend is expected for the rare earth fission products.

Given the complexity of the fuel chemistry, it is only possible to estimate the oxygen potential based on several assumptions. For

normal operation the pellet OD temperature is typically 723°C. If equilibrium exists across the pellet-clad gap and the Mo/MoO couple buffers the fuel with respect to oxygen [19], the oxygen partial pressure is calculated to be $\sim 3 \times 10^{-22}$ atm. If the fuel OD is slightly hypostoichiometric (O/M 1.999) [21,26], the oxygen partial pressure is calculated [21] to be $\sim 10^{-25}$ atm. However significant Pu is bred in these experiments, so the oxygen potential could be somewhat lower.

The situation becomes much more complicated if fission products migrate to the gap and fuel clad bonding occurs. Pellet-clad contact lowers the pellet OD temperature to approximately 500°C. The oxygen potential is modified by the presence of Cs-U-O, Cs-Zr-U-O, and/or Cs-O compounds whose thermodynamic properties including oxygen potential, are not known. An additional observation is that enhanced oxidation of the Zircaloy cladding is observed at cracks, pellet-pellet interfaces, and regions where the fuel contacts the clad [9,21]. This phenomenon might result from two different processes: 1) fission products and fuel causing a transition to breakaway oxidation kinetics because the film is no longer continuous and adherent; 2) greater availability of oxygen because a higher partial pressure of oxygen is established by exposing hotter fuel toward the center of the pellet at a pellet crack or pellet-pellet interface, rather than the pellet surface. If the later explanation is valid, the oxygen potential at the fuel cladding is higher than previous estimated.

An important observation of the effect of oxygen potential on PCI failure is made by Davies et al. [4]. They perform in-reactor SCC tests where irradiated and unirradiated cladding are loaded with annular

pellets of fresh fuel and irradiated fuel is placed in the annular regions. Oxygen potential in the hyperstoichiometric fresh fuel had to be reduced by niobium additions to cause failure of the Zircaloy cladding in ramp tests.

2.1.2.2   Fission Product Behavior

A review of fission product behavior in LWR's is published by Cubicciotti [25]. The major conclusions and observations of volatile fission products are restated here with some additional support from more recent studies.

Fission product release correlates directly with two fuel operating parameters: linear rod power and fission gas release. Bazin et al. [28] find a threshold curve where the linear power necessary for fission product release decreases with burnup. This release corresponds with the radial redistribution of fission products. Axial migration is observed only at very high power levels where significant restructuring of the fuel occurs. Fission product release is noted when fuel temperature exceeds the grain growth temperature of the UO_2 [20]. Although some contradictory evidence exists, fission products are released in approximately the same proportion that fission gases reach the free volume of the fuel rod [38,39]. A high level of fission gas release is usually associated with PCI failure.

A variety of fission products deposit on the fuel cladding. The elements most commonly observed are: Cs, Te, and I [1,9,28,40]. Careful examination reveals these and other minor elements: Cd, Ba, Pd, Ag, and Sn [4,26,41]. These elements have high and moderate vapor pressures in the fuel [40]. Much of the chemistry in the fuel-clad gap is determined by cesium which is the most abundant fission product to

reach the cladding. A Cs-U-O ceramic phase is often observed. The exact composition is not known since many phases are found in this system [25,42] and the composition might change depending on the chemical conditions. Other variants are Cs-Zr-U-O phases [28] and Zr-Cs-Sn-O phases [26]. The important point is that gaseous cesium is released from the fuel in either elemental form or as Cs_2O and reaches the cladding where it reacts to form a compound bonding the cladding and fuel together at points of contact. Other compounds detected in post-irradiation analysis are Cs_2Te [9,40] and CsI [1,9,40]. The minor elements are present in concentrations too low to determine their chemical form.

From the previous list of fission products only a few can cause cracking of the Zircaloy cladding. Screening programs [19,43] have identified the following environments:

a) Iodine, including zirconium iodide, but not cesium iodide;

b) Cadmium and cadmium dissolved in liquid cesium;

c) Liquid cesium, but only at temperature below 250°C [44];

d) Liquid cesium with iron contamination [45].

Liquid cesium is not observed in LWR fuel elements. The only scenario that could place liquid cesium at the fuel cladding would be release of gaseous elemental cesium from the fuel interior through fuel cracks followed by condensation. It should be pointed out the Cs_2O might be the gaseous specie. Thus cesium is not likely (although not excluded) to play a direct role in the PCI failures. Cadmium is present in much lower concentrations as a fission product than iodine accounting for the few observations of Cd at the clad surface. The low concentration and difficulties in transport to a crack site make cadmium an unlikely corrodent.

Iodine is expected to be combined as CsI from thermodynamic considerations. However, Peehs et al. [39] report that migration of Cs and I in a temperature gradient takes place without reaction, and release of these fission products is proportional to the fission gas release. Two mechanisms for the release of chemically combined iodine are possible. The reaction of CsI to form Cs-U-O compounds liberates iodine [39] and is predicted thermodynamically [65,66]. Radiolytic decomposition of CsI salts is also known to occur [46]. The iodine partial pressure in the fuel rod following a power ramp is low ($<10^{-5}$ Pa) [47]. This does not consider that the iodine released from the fuel might react quickly with the cladding without appreciable pressure buildup or that higher iodine concentrations might exist locally at fuel cracks or other locations of fission product release.

2.2   Laboratory Experiments

2.2.1   Chemical Factors

2.2.1.1   Zirconium-Iodine Chemistry

2.2.1.1.1 Compositions and Properties

Recent work has increased the understanding of the physical chemistry in the Zr-I system. The formation of lower iodides with nominal compositions of ZrI_3, ZrI_2, and ZrI is observed. Each of these iodides is known to exist over a range of stoichiometries rather than being a stoichiometric compound, although a stoichiometric ZrI_2 cluster compound is identified [48]. The extent of non-stoichiometry [48-52] is shown in Fig. 2.3. Disagreement exists as to the exact composition boundaries for the triiodide and diiodide. Some data in Fig. 2.3 are updated from earlier work by the same groups, specifically the Bhatti et al. [32] study from the earlier work by Sale and Shelton [57] and the Cubicciotti et al. [53-56] work from a Cubicciotti et al. [58] report. Daake and Corbett [50] attribute the reported variability in composition boundaries to analysis of lower iodides that had not reached equilibrium.

Several types of reactions are possible in condensed metal halide systems [59]. The reaction relevant to the zirconium-iodine system is the disproportionation reaction which, stated in the general form, is:

$$2MX_a(s) = MX_{a-1}(s) + MX_b(v) \tag{2.1}$$
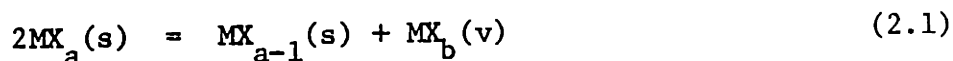
In all cases the evolved gas is ZrI_4. Fig. 2.4 plots $\log P_{ZrI_4}$ versus 1/T showing the fields of stability for the various iodides based on thermodynamic data [49-56]. The important point presented by Fig. 2.4 is

that lower iodides are formed under the appropriate conditions of iodine pressure and temperature although the kinetics may be sluggish. Subsequent discussion considers the methods of preparation, structure, and stability of each iodide.

Zirconium Tetraiodide. The material is generally prepared by reaction of iodide crystals with a slight excess of zirconium followed by sublimation of the product [53,60]. The final material varies in color from red-brown to mahogany. ZrI_4 tends to be very hygroscopic and reacts with moist air to yield HI and ZrO_2 so handling is normally done under dry, inert gas.

Zirconium Triiodide. Several methods are used to prepare zirconium triiodide. The most common involves the reduction of ZrI_4 vapor [61] or liquid [57,62] by Zr metal above 500°C. To circumvent problems of unreacted metal and uncertain intermediate, phases Daake and Corbett [56] reduce the ZrI_4 with $ZrI_{1.8}$. Dahl et al. [63] report the crystal structure to be distorted HCP anion lattice with Zr atoms in one-third of the octahedral sites. They also present x-ray diffraction data. The compound is reported to be blue-black, green-black, or brown-black in color [50,62,64], depending on the physical form and is pyrophoric.

Zirconium diiodide. Preparation of this compound is usually accomplished by heating zirconium triiodide to 360°-390°C causing disproportionation. The product is reported to be blue-black or black in color and is stable in air. Sale and Shelton [12] analyze the product by x-ray diffraction and find a structure similar to the triiodide. However, Daake and Corbett [50] report that the x-ray pattern from the lower limit

of triiodide stoichiometry is virtually identical with the diiodide reported by Sale and Shelton [62]. Although no. data are given, they state that the powder pattern from $ZrI_{1.8}$ is very different. It can be concluded that structural analysis of the diiodide is incomplete at this time.

Zirconium Moniodide. Only one study reports this material [54]. $ZrI_{2.4}$ is heated at 425°C and ZrI_4 condensed at the cool end of a tube. The product is black in color and granular in form. X-ray diffraction analysis is reported, but the structure is not analyzed.

2.2.1.1.2 Reaction Kinetics

Several aspects of the reaction kinetics in the Zr-I system are addressed. The reaction of iodine with zirconium and Zircaloy between 215° and 400°C at relatively high iodine pressures (≥ 6 Pa) is reported by several investigators [67-69]. Several reaction steps are observed. Chemisorption of iodine is followed by reaction to form ZrI_4 at relatively high iodine pressures [67]. The volatile ZrI_4 remains in the gas phase until either the pressure is sufficient to cause solid ZrI_4 condensation [68] or further reaction forms lower iodides from the excess zirconium in the system [68,69]. As thermodynamic equilibrium is approached, much of the iodine exists as condensed lower iodides; heating releases ZrI_4 by the disproportionation reaction, Eqn. (2.1). Both first [67] and second [68] order reaction kinetics are reported. The later study occurs at much higher iodine partial pressure than the former so a difference in rate controlling process might be responsible for the disparity in order of reaction kinetics.

At very low iodine partial pressures (10^{-4}-10^{-6} Pa) and 723°-1023°C, only the adsorption step is observed [70]. Chemisorption of monotonic iodine is described kinetically and compared to $ZrI_{1.05}$ formation in thermodynamic terms. A small amount of ZrI_4, 0.1% of total iodine pressure, is observed only at the lowest temperature, 723°C, and the highest iodine pressure, 10^{-4} Pa. Significant oxygen and carbon adsorption occurs below 687°C. It should be emphasized that significant extrapolation is required to apply this data to behavior at reactor operating temperatures of 300°-400°C.

Lower iodides form on zirconium and Zircaloy in a ZrI_4 environment between 300° and 500°C [71,72]. Sale [71] notes a coating of tri- or diiodide depending on temperature. Cubicciotti and Scott [72] found ZrI formation with higher iodides forming over the monoiodide. They also conclude that lower iodides form even when the system does not have sufficient time to reach equilibrium.

2.2.1.1.3 Iodine Concentration for SCC

A controversy in iodine SCC of Zircaloy is whether the iodine concentration should be expressed on an areal or a volumetric basis. The critical point concerns the mechanism of crack initiation. If gaseous iodine or iodide causes initiation, iodine concentration should be expressed on a volumetric basis. Conversely, if condensed iodides cause initiation, an areal basis is appropriate. Two factors indicate that the areal basis for iodine concentration should be used. The kinetic studies in the previous section indicate that lower (condensed) zirconium iodides form in the presence of excess zirconium. Peehs et al.

[81] report that, in tests with minute quantities of iodine, islands of microcracks form which probably correspond to local regions of condensed iodide. A small quantity of iodine released near a flaw causes failure while no failure occurs if iodine is released far from the flaw.

The threshold iodine condition for studies utilizing low iodine concentrations is given in Table 2.1. Several important trends are observed from the data. The concentration threshold is independent of stress level and deformation rate [81]. A trend of increasing threshold concentration with decreasing temperature is observed [81,82]. Most studies indicate no effect of iodine concentration on SCC susceptibility [18,109,116], however, Peehs et al. [81] find that threshold stress decreases with increasing iodine concentration above the concentration threshold [81].

The iodine environment in an SCC test depends on the type of test, static or flowing. In a static test purple iodine vapors are observed to clear from the test capsule in the first several minutes by reaction with Zircaloy [82]. Lower iodides form according to the kinetic factors discussed in the previous section. Thermodynamic equilibrium is never reached due to kinetic limitations. In a flowing system iodine is continuously introduced while ZrI_4 and probably some I_2 are removed. A dynamic equilibrium, but not thermodynamic equilibrium, is eventually established fixing the iodine potential in the gas. Reactions are then possible to form condensed lower iodide.

2.2.1.2   Corrosion of Metals by Iodine

The general corrosion behavior of Zircaloy and other materials used in the testing apparatus must be known since it relates directly

both to interpretation of the results of individual investigators and to the understanding of the chemical effects on iodine SCC. The metals of interest are Zr, Fe, Al, Cd, Cs, Cu, W, and Mo. The goal is to better understand the chemistry of various iodine SCC experiments. Observations by investigators during their iodine SCC tests are an important source of information on metal-iodine reactions.

Daniel and Rapp [73] review the corrosion behavior of metals in halide environments, including iodine. They show that all the metals listed above form stable iodides when exposed to iodine. Fig. 2.5 shows the standard free energy of formation, ΔG_f^o, versus temperature for several metal iodides of interest. The partial pressure of iodine in equilibrium with a metal iodide can be calculated from ΔG_f^o. Fig. 2.6 plots the equilibrium partial pressure of metal iodides versus temperature for several metal iodides.

2.2.1.2.1 Zircaloy Corrosion

The thermodynamics and kinetics in the Zr-I system are described in a previous section. The reaction of Zircaloy with iodine in laboratory test environments is introduced in the following discussion.

Tests are performed with either a constant I_2 partial pressure or a known initial iodine inventory. A constant P_{I_2} test consists either of a gas stream carrying a known partial pressure of iodine [18,74-79] or of an external supply of iodine crystals at constant temperature [67,80, 81]. ZrI_4 reaction product volatilizes and condenses on cool surfaces outside the test chamber. If the initial iodine partial pressure is sufficiently high, pitting of the zirconium or Zircaloy surface is observed [75,79].

Most investigators use a known iodine inventory for tests in a closed or stagnant system. The quantity of iodine is expressed as an initial weight, a weight per unit volume, or a weight per unit area. The partial pressure of iodine is initially high, then decays by reaction with the zirconium [68] or Zircaloy. Wood [82] reports that dense purple fumes of gaseous I_2 form in the test capsule with a calculated $P_{I_2} \sim 0.8$ atm. The fumes dissipate within several minutes leaving a red-brown deposit and a faint yellow gas. Continued exposure yields a yellow-brown deposit. Heavy pitting is observed under the deposit.

2.2.1.2.2 Corrosion of Other Metals

Metallic components are often in contact with iodine during SCC tests. Iron and various steels are most often present. They are added intentionally as "catalysts" [44,82-84], used as structural material in test apparatus construction [19,80,81,84-86], or employed in specimen loading in differential thermal expansion mandrel tests [6,80,85,87-89], fuel swelling simulation tests [85], or fracture mechanics specimens [82]. Other mandrel materials are aluminum and aluminum alloys [44,80,85,88,90], copper [80], and zirconium [18,76]. Copper and brass [88] proved to be unacceptable because of heavy attack by iodine so they are not discussed further. Molybdenum and molybdenum alloys are also used as materials of construction [18,74,76,77,79,92] because of the very low corrosion rates that are observed [73,93]. Subsequent discussion considers the iodine corrosion behavior of iron and steel, and of aluminum and its alloys in greater detail. Both intrinsic corrosion behavior and corrosion properties that are observed in iodine SCC tests are discussed.

Daniel and Rapp [73] report that both iron and stainless steel are attacked by iodine, but that iron is much less resistant. Stainless steel can handle iodine in the 250°–300°C range but is subject to pitting. Shapiro [93] gives corrosion data for stainless steel in 400 mm I_2 vapor at 450°C. The penetration rates are significant for several austenitic stainless steels and are about 50 to 1000 times the rates for some noble and refractory metals. Garlick and Wolfenden [80] report that iodine at an initial pressure of <0.2 torr is depleted by reaction with a stainless steel test chamber. Cubicciotti and Jones [19] detect iron on the heavily pitted internal specimen surfaces and fracture surfaces of internal pressurization samples and assume that the iron is transported from stainless steel end fittings where they find some attack. When iron is present as a "catalyst", corrosion of the iron occurs preferentially and the Zircaloy samples remain bright rather than heavily attacked and pitted [82,84]. Garlick [85] shows a fuel swelling simulation test specimen with a steel mandrel where significant pitting of the mandrel is evident but very little attack is observed on the specimen.

The number of observations of aluminum corrosion by iodine is more restricted. Daniel and Rapp [73] conclude that aluminum is not a practical material for handling iodine above 190°C, the melting point of AlI_3. Comments on aluminum corrosion during Zircaloy SCC tests are also limited. Une [88] reports that some iodine reacts with an aluminum alloy mandrel. Garlick and Wolfenden [80] speculate that variable results from testing with various iodine partial pressures might be caused by reaction between iodine and aluminum mandrels. Gangloff and Coffin [18] observe a large quantity of yellow deposit, presumed to be aluminum iodide, in fuel swelling simulation tests with an aluminum core.

2.2.1.2.3 Metal Iodides and Embrittlement of Zircaloy

From thermodynamic data and experimental observations, it is apparent that iodine reacts with any metallic material present during an SCC test, including specimen, "catalyst", and structural components. In some cases corrosion of materials other than the Zircaloy occurs preferentially depending on the reaction kinetics, e.g. the tests with the iron catalyst or steel mandrel. The proximity of the material to the test specimen is also relevant. Although Cubicciotti and Jones [19] observe iron on the surfaces of their internal pressurization specimen, the heavy pitting corrosion indicates that the transport of iron as iron iodide occurs subsequent to iodine attack of the Zircaloy. Thus, the iron iodide is less likely to have played a role in the cracking process. Corrosion of structural components results in depletion of the iodine available to the Zircaloy and establishes a certain partial pressure of metal iodide in contact with the specimen which is different from the case without the extraneous metal. Partial pressures of several metal iodides at 300°C, a typical test temperature, are given in Table 2.2.

Tests with iodides of Al and Fe are substantially more embrittling than I_2 or ZrI_4 environments [78,86]. The reduction in ductility with an aluminum mandrel in fuel swelling simulation tests [18] indicates that the test by Une [90,91] with an Al mandrel are not representative of iodine SCC condition of other tests. The increased embrittling effect of iron is consistent with the need for an iron "catalyst" to crack split ring specimens [82].

2.2.1.3   Oxygen Containing Environments

The effect of oxygen in an iodine SCC test is to promote the growth of an oxide film on the Zircaloy. The sources of oxygen are intentional O_2 gas additions [79,88,91,92,96], air [82,86], water vapor [83,86,87,91], and residual oxygen in an inert gas stream [38]. The oxide film prevents attack of the metal by the iodine. Several studies [82,83,88] note that purple I_2 vapors do not clear for several hours from test capsules containing air or oxygen and no zirconium iodide is formed. The amount of oxygen that must be present to prevent cracking depends on the quantity of iodine and form (iodine vapor or metal iodide). An example of a threshold oxygen pressure is given by Une [88] who reports that oxygen partial pressure above 3.7 kPa and 1.2 kPa at 300° and 350°C, respectively, prevented cracking. No correlation with oxide thickness (0.61 and 0.20 μm, respectively) is evident. The iodine chemistry is complicated by the use of aluminum mandrels, and the oxygen pressures represent initial values since a static system is used.

2.2.1.4   Liquid Metal Environments

Certain liquid and solid metals are known to embrittle Zircaloy. Cesium alone does not cause brittle failure in a variety of tests: slotted ring [44], differential thermal expansion mandrel [89], internal pressurization [87,89], uniaxial tension [43], fuel swelling simulation [44,45], and double cantilever beam [44]. Only dynamically loaded DCB specimens [44] failed by liquid metal embrittlement and only at temperatures below 250°C. Above 250°C cesium embrittles only when it dissolves other metals. At 300°C the cesium must be scavenged of oxygen

and contaminated with iron [45]. Contamination of cesium with Sr, Zn, Ca, or Y results in mild embrittlement [43]. By far the most aggressive liquid metal environments contain cadmium as solid cadmium, liquid cadmium, or cadmium dissolved in cesium [18,43,74,76,97-99].

A point of disagreement is the relative level of embrittlement between iodine and cadmium environments. Wood et al. [99] find that fuel swelling simulation specimens achieve much higher strain in cadmium than in iodine (3.5-4% versus 0.05%) although fracture features are similar. This conclusion disagrees with earlier studies where comparable low strain levels are observed in both environments [18,76].

2.2.2 Stress

Many types of specimen geometries and loading schemes have been used to study SCC in Zircaloy. Any test falls into one of four categories: 1) constant initial displacement; 2) constant stress; 3) constant extension rate; 4) crack growth. Table 2.3 lists all the specimen designs under these four categories, the laboratories or investigators that use them, the type of data typically obtained from each test, and the advantages and disadvantages of each specimen design. Fig. 2.7 shows schematic strain versus time and stress versus time relationships for each loading mode. The important characteristics of each test type are summarized below:

Constant displacement. This type of test gives a fixed total strain that is usually all elastic initially. As the test proceeds the elastic strain is converted into plastic strain and the stress decreases due to stress relaxation. An advantage of this type of loading

is its simplicity so screening of environmental and materials variables is easily accomplished. Difficulty arises when attempting to analyze the time dependent stress relaxation in the stress gradient induced by bending in the split ring specimens [101].

Constant stress. During the test, total strain increases due to creep of the Zircaloy. Some investigators [81,109,116] calculate an average strain rate by dividing the uniform strain at failure by the time to failure. This approach is a simplification since the primary and secondary creep characteristics of the material are not separated. The total surface area of stressed material depends on the specimen design. For instance, a much larger surface area of stressed material is exposed to iodine in the tube pressurization test than in the clad segment of a "localized ductility" test [74,96], or in the locally strained region in the indentor test [75,84,114].

Constant extension rate. This test is generally regarded to be more severe than the previous two because plastic strain is continuously being applied to the point of failure. The critical criteria then become the ductility of the fracture region and fracture appearance. The time to run a test is relatively short, one to three days at 10^{-6}/sec compared to potentially longer times in constant stress or crack growth tests, making the test attractive for screening materials and environmental variables. A strain rate is easily calculated; however, local instabilities such as necks or cracks raise the local strain rate. One difficulty is the separation of time dependent chemical effects. Various aspects of the constant extension rate test are described by Payer et al. [122].

Crack growth. Specimens are pre-cracked, generally by fatigue, to produce a sharp crack and are exposed to the environment of interest.

The procedure eliminates the crack initiation stage so that crack propagation alone is studied. Three types of loading, shown in Fig. 2.7, are analogous to the smooth specimen loading: 1) constant initial displacement, δ_i, 2) constant stress intensity, K, and 3) rising load K_{ISCC} tests [123]. Data are obtained as crack velocity da/dt versus K and/or K_{ISCC} in crack arrest tests. In tests on Zircaloy, specimens are usually produced from plate so microstructural differences between plate and tubing must be considered. Specimen designs and test procedures are discussed by Rolfe and Barsom [124]. Videm and Lunde [118] attempt crack growth measurements in pre-cracked tubing. Pre-machined flaws are also used to generate fracture mechanics data [19,74]. However, the flaws are relatively blunt so crack initiation must still occur.

Several elements of the tube testing techniques closely resemble the PCI conditions in-reactor. The loading conditions in Fig. 2.1 most resemble the constant displacement type of test in Fig. 2.7 where the stress relaxes by creep following a stress ramp of the cladding. The local stress on the cladding is best simulated by the fuel swelling simulation test. A soft metal plug is compressed from the ends which expands against annular ceramic segments; these in turn load the cladding with stress and strain concentrations at the gaps between segments which simulate fuel cracks. The difficulty in using these representative loading schemes is analyzing the local stress and strain distribution as a function of time and correlating the mechanical conditions with environmentally dependent crack initiation and propagation. Thus, the impetus to use constant stress and constant extension rate tests lies in the relative simplicity of analyzing the loading aspects of the test.

The stress state is an important consideration in determining the susceptibility of Zircaloy to iodine SCC. Rajan et al. [125] predict that axial to hoop stress rations (σ_a/σ_h) vary from 0 to 1 at pellet-clad ridges. Several contradictions exist regarding stress ratio effects on SCC. Attempts to fail Zircaloy by SCC under constant stress uniaxial loading prove unsuccessful [6,80,84]. The more severe constant extension rate test is necessary to cause uniaxial failure [43,91]. Syrett et al. [112] test internally pressurized cladding tubes under σ_a/σ_h from 0 to ∞ emphasizing values from 0 to 1. Maximum susceptibility is observed in uniaxial hoop tension, i.e. $\sigma_a/\sigma_h \approx 0$, when hoop stress is plotted against time to failure. This result contradicts the conclusions derived from uniaxial tests.

When SCC failure strain is plotted against stress ratio, the minimum occurs at $\sigma_a/\sigma_h = 0.5 - 0.7$ [91,112] which is close to the stress ratio for plane strain loading. This leads to the conclusion that plain strain is the most severe loading condition. A ductility minimum occurs under plane strain loading in air at room temperature [126-128]. Although Zircaloy is more isotropic at reactor operating temperatures [127,129], a ductility minimum is still observed. Thus, this behavior is probably a consequence of the mechanical response to the multiaxial loading rather than the aggressive environment.

2.2.3   Materials Variables

Environment and stress have been discussed in relation to Zircaloy SCC. The remaining requirement, material susceptibility, is considered in terms of the materials variables listed in Fig. 1.1 and

Table 2.4. This section introduces each materials characteristic by defining the range of each parameter and the characteristic effects on SCC behavior. Their relation to the phenomenological aspects of crack initiation and crack propagation is deferred until the discussion section.

2.2.3.1   Heat Treatment

In the production of Zircaloy cladding tubes, the final tube reduction step is a cold-working operation. The cladding then receives either a stress-relief anneal to reduce residual stresses or a recrystallization treatment depending on the specifications of the particular fuel vendor. The recrystallization temperature is a complex function of cold-work, temperature, and time at temperature. Stress-relief temperatures are generally in the range 480-520°C, and recrystallization anneals are done between 560° and 580°C.

The mechanical properties are affected dramatically by the condition of the cladding as determined by the cold work/annealing steps. Burst and creep properties are often measured at room temperature and in the 300°-400°C range typical of operating conditions. The following summarizes the effects of annealing temperature [86,130,131]:

> o burst strength and ultimate tensile strength decrease continuously with annealing temperature; the steepest drop is found in the temperature range where recrystallization occurs and flattens when recrystallization is complete.
>
> o the yield strength shows the same trend as the burst and ultimate but the strength loss is greater.

○ higher levels of cold work shift the above transition in
  strength behavior to lower temperature.

○ ductility values increase corresponding to the loss in
  strength.

○ the above trends apply to tests at room temperature and
  elevated temperatures between 300° and 400°C.

○ creep behavior is a more complicated function of cold work,
  annealing temperature, test temperature, and stress; cold
  work has a larger effect than annealing temperature.

○ 300°C creep tests show trends in creep strength and
  ductility that are similar to the short term behavior
  while 400°C tests do not [131].

Table 2.4 reveals that heat treatment is one of the most widely
studied materials variables. Most studies compare two heat treatments,
a stress-relief and a recrystallized, however, Videm and Lunde [86]
investigate a series of heat treatments. Several trends in SCC behavior
emerge which can be correlated with mechanical properties:

○ higher annealing temperature lowers both the SCC threshold
  stress and the σ versus t_f failure curve; this behavior is
  best observed when a lot of material with stress-relief
  and recrystallization anneals are compared directly
  [86,109,116].

○ although the failure curve is lower for recrystallized
  material, it is a higher fraction of the short term stress
  and creep rupture curve than stress-relieved material.

o strain at failure is higher for recrystallized material;
this applies to both tube pressurization tests [86,109]
and constant extension rate tests [74,91].

2.2.3.2   Crystallographic Texture

Crystallographic texture is a term used to denote a non-random distribution of grains orientations in a solid. It will be discussed in greater detail and quantified by texture numbers defined in Section 4. Briefly, the c-axes, or basal poles, align preferentially in the radial-tangential (R-T) plane in Zircaloy cladding with no poles toward the axial direction. For the present discussion the R-T plane distribution can be defined as follows:

o radial - most basal poles in the radial direction with very few toward the tangential direction (also called a 0° texture);

o tube - maximum intensity of basal poles at 30°-40° from the radial direction in the R-T plane with fewer poles in the tangential direction (30° texture);

o tangential - most basal poles toward the tangential direction in the R-T plane with few near the radial direction (60° texture).

The texture is developed during the tube forming operation [130]. Most studies consider textures from 30° to the 50°-60° range. Some are able to cover a broader range of texture by choice of experimental technique [81,103].

Reports of texture effects on SCC susceptibility present mixed results. No effect is noted in some studies [103,114] while a large effect is observed in many studies [81,84,121,113]. Other investigators find some texture effect [82,83,111] but do not consider it to dominate iodine SCC behavior. One recurring problem is separating texture effect from the effect of other materials variables such as residual stress [111], surface condition [111,121], and strength as determined by heat treatment [82]. The type of test could play a role in determining texture effect [121] since many techniques are used as seen in Table 2.4.

As a first approximation, texture might be suspected to play a major role in iodine SCC of Zircaloy since the mechanical properties, particularly creep [131] are strongly affected by texture and the mode of crack propagation is crystallographic, i.e. transgranular cleavage, following a near basal plane path. This would make a tangential texture more susceptible which is observed by all investigators who observe a texture effect.

2.2.3.3 Residual Stress

Following the final heat treatment, it is normal practice for tubing vendors to straighten the tubing which reintroduces some residual stress. As in the case of texture, the opinions regarding residual stress effects on SCC are mixed. A particular study concludes no effect [85] while another finds a contributing but not overriding effect [117]. Several investigators report a large influence at high residual stress levels but little or no effect at low levels [82,83,90]. The largest effect is seen in split ring tests [82,83] where the stress gradient

across the specimen is know to affect the stress relaxation behavior of the specimen [101,121] and thus complicates an evaluation of residual stress effects [85].

2.2.3.4   Dissolved Hydrogen and Hydrides

Few studies of the effect of hydrogen on SCC performance are reported. Wood [83] shows that iodine exposure substantially enhances hydrogen pick up. This is due to iodine attack of the Zircaloy surface which leaves a clean surface for hydrogen absorption. However, he did not perform tests designed to isolate the effect of hydrogen on SCC performance. Polan and Tucker [87] conduct tube pressurization tests at 316°C and 360°C on specimens with 20, 60, and 190 ppm hydrogen. Little or no effect on time to failure is noted at these hydrogen concentrations. Hydrogen solubility in Zircaloy at 316° and 360°C is 86 and 140 ppm, respectively, [132] so these tests are run with both hydrogen in solution and hydride precipitate.

Cox [102] finds crack initiation at radial hydride platelets which probably results from hydride cracking when the specimen is loaded prior to testing since the low hydrogen concentration is in solution at the test temperature. In tubing normally resistant to cracking without dissolved hydrogen, the introduction of radial hydrides or hydride surface layers does not change susceptibility and in many cases reduces susceptibility [83,101,102].

2.2.3.5   ID Surface Condition

Since crack intiation occurs at the inside surface of the fuel cladding, surface finish is expected to play an important role in

iodine SCC susceptibility. Surface condition is a variable that is relevant to all laboratory tests, covers a variety of conditions, and is often not well characterized, particularly in relation to its effect on the crack initiation process. Surface condition variables fall broadly into three categories depending on how the surface features are formed:

1. Coatings and barriers - these fall under the category of PCI remedies since they are intended to eliminate SCC susceptibility.

2. Chemical surface treatments - Oxidation coatings and pickling are considered since chemical reactions determine the character of the surface.

3. Mechanical surface treatments - mechanical working of the surface by machining, honing, sand blasting, grit blasting, or shot peening creates features characteristic of worked metal; pre-machined defects such as flaws and scratches also fall under this category.

Production run Zircaloy tubing is usually pickled as one of the final steps so its surface condition falls in the chemical surface condition category. If no pickling is done, the as-formed surface (tubing) or as-rolled (plate) surface is considered under the mechanical surface treatment category. It is important to note that each investigator uses his own procedure to create a particular pickled surface finish, e.g. composition, temperature, time, degree of agitation or flow, amount of metal removed, etc. Thus, surfaces nominally given the same type of treatment in separate studies may not be comparable and could affect SCC behavior differently.

2.2.3.5.1 Coatings and Barriers

One approach to solving the PCI problem is to place a coating on the ID surface to protect the Zircaloy cladding. Two basic types are under development. AECL is testing graphite and siloxane coatings which are applied as a thin layer [12,83]. A second approach is under development at General Electric Company involving metal barrier coatings of either copper or pure zirconium [76]. The electrolytically deposited copper is not susceptible to iodine SCC. The pure zirconium liner is formed by a co-extrusion process and exhibits substantially reduced SCC susceptibility (but not immunity) compared to Zircaloy.

2.2.3.5.2 Chemical Surface Treatments

Oxide is formed on the Zircaloy either by a pre-filming treatment prior to testing or by oxidation during the test in the presence of both iodine and oxygen, water vapor, or air. A critical event relative to SCC is penetration of the oxide to allow iodine to access the underlying metal. These oxide films (≤ 0.2 μm) are penetrated without the application stress [12,7]. Residual traces of air in a test system do not appear to affect results [89,120] if a passivating oxide layer does not form. Reaction between iodine and Zircaloy with a thick (>1 μm) film occurs much more slowly [6,72]. Generally, the presence of an oxide film reduces susceptibility to SCC compared with unoxidized specimens [86, 89,120]. The environment is important because of the competing effects of repassivation at a crack in the oxide and reaction of the metal with iodine [79]. The presence of oxygen raises the failure threshold compared to a less oxidizing environment [38,90,91,120].

The effect of pickling is to increase the resistance of Zircaloy to iodine SCC [82,114,120]. Several mechanisms are postulated to explain this observation: removal of the oxide film which is replaced by a more impervious film, promotion of general iodine attack rather than local attack, and elimination of surface defects that promote crack initiation. A mechanistic assessment of the effect of pickling is not possible without a detailed comparison of the surface prior to pickling.

2.2.3.5.3 Mechanical Surface Treatments

The surface treatments in this category are mechanical polishing, honing, grit or sand blasting, and shot peening. The common element among them is the introduction of a mechanically worked layer on the cladding ID. The depth of the damaged layer and the possible introduction of surface flaws or microcracks are usually not evaluated. The treatments are described as follows:

- mechanical polish - the surface is ground circumferentially with successively finer metallographic papers ending with 3 μm diamond polishing compound [111]; the surface is very smooth with only a thin damage layer.
- honing - circumferential scratches should result from this treatment where a honing tool of bonded grit is used to remove metal [81].
- grit or sand blasting - a fine grit such as alumina or silicon carbide is sprayed from a nozzle at a glancing angle toward the axial direction; long axial scratches normally result [81,86,113,114,121].

o shot peening - a shot, often glass, sprayed from a nozzle

strikes the surface to introduce compressive residual

stresses in the surface [83]; a scratched surface with

some gouges can result [113,114].

In laboratory tests crack initiation is influenced by the

surface damage. Only Wood [83] notes a beneficial effect due to residual

surface compressive stresses. Most investigators report no effect [81,

86,114] or an increase in SCC susceptibility [113,121] compared to

untreated material.

Mechanically induced scratches or pre-flaws are introduced in

some studies to simulate defects. They are categorized with the

preceeding surface treatments because a machining operation is used to

form them. The defects are usually shallow, 100 μm or less in depth.

Cracks grow from the defects but the susceptibility is not always

decreased [104].

2.2.3.6   Irradiation

The effects of irradiation on iodine SCC must be considered

in terms of the changes in mechanical properties after saturation of

irradiation hardening. Recrystallized material hardens due to

irradiation. Both yield and ultimate tensile strengths increase substan-

tially [77,78,117,133]. A strength increase is also observed in

stress-relieved material, but the increase is greater in the ultimate

tensile strength [77,134]. For all conditions, ductility is reduced to

very low levels due to localization of plastic flow at shear bands

[77,78,133-135], a phenomenon also known as channeling. The decrease

in ductility is much greater for the initially more ductile recrystallized material. Irradiation causes stress-relieved and recrystallized materials to become more nearly equal in both strength and ductility compared to the substantial difference in unirradiated materials [77]. The textural anisotropy in deformation behavior is retained after irradiation [77,78, 133,134].

Residual stress is affected by irradiation. At relatively low fluences residual stress levels are reduced to low ($\leq$14 MPa) values by irradiation induced stress relaxation [83,85].

2.3   Analysis of Iodine SCC Processes and PCI Solutions

Three topics are covered in this section. They are SCC

phenomenology, remedies, and models and are depicted in relation to the

other PCI failure topics in Fig. 1.1. The treatment is introductory in

nature since analysis of specific issues is deferred until the

Discussion, Section 7.

2.3.1   SCC Phenomenology

Roberts et al. [136] and Cox and Wood [12] present a

mechanistically based model for PCI failures consisting of four stages:

oxide penetration, crack formation, crack propagation, and cladding

rupture. The first two steps comprise crack intiation while the later

two constitute crack propagation. It is critical to remember that

environment, stress, and material condition contribute to each step in

the cracking process. Both laboratory and service failures must be

evaluated from this point of view. The observations from service

failures must be consistent with any mechanistic model that is

proposed.

The oxide cracking step in crack initiation appears to be

accomplished quite readily. A thin oxide (<.5 μm) is readily penetrated

by iodine without the application of stress. Strain is necessary to

crack a thicker oxide, but the amount is low and does not limit initia-

tion [75]. In oxygen containing environments, oxide cracking limits

initiation if a competition exists between chemical attack and

repassivation. This is not generally the case in a fuel rod where the

oxygen potential is very low. Thick oxide layers several microns in thickness are normally present on the fuel rod ID surface.

The crack formation stage involves the initiation of a crack nucleus, i.e. a small crack, in the metal surface. The role of materials variables is important since analysis of the initiation is normally reported in terms of a microstructural feature such as intermetallic and inclusion particles, intergranular sites, pits and flaws, hydrides, and transgranular sites. The reported behavior tends to be confusing and contradictory so consideration is delayed until the Discussion, Section 7. Initiation that is clearly intergranular in character is often (but not always) observed in recrystallized material in both irradiated and unirradiated condition [76,78,118].

Crack propagation occurs primarily by cleavage near the basal plane complemented by ductile tearing and fluting. In some cases intergranular propagation is observed [12,118]. Crack growth occurs normal to the applied tensile stress and crack branching is sometimes observed at high stress levels. The appearance of fracture surfaces from power reactor failures, laboratory tests on irradiated material, and laboratory tests on unirradiated material are indistinguishable indicating that the mechanism for propagation is potentially the same.

Cladding rupture occurs when the ligament between the crack tip and tube OD reaches plastic instability and fails by shear. The crack opening at the tube OD is low, i.e. "pinhole" failure, at low stress and is large, characterized by a short axial split, at high stresses. This process is modeled by Smith [137]. Service cracks are almost exclusively pinhole type failures.

2.3.2   Remedies

To alleviate the PCI problem one or more of the three necessary conditions for stress corrosion cracking, i.e. stress, environment, and material susceptibility, must be negated. The remedies are evaluated in this context. Two classes of potential "fixes" are being considered: coatings and barriers, and fuel redesign.

The coatings and barriers are discussed in Section 2.2.3.5.1 so they are only summarized here. The graphite coatings [12,83] were originally intended to reduce the frictional stress on the cladding by acting as a lubricant, however, recent work [99] indicates that the graphite is more likely to function as a chemical barrier. Siloxane is a chemical barrier. The metal barrier coatings [76] under consideration are copper and pure zirconium. The copper is immune to SCC so it functions as relatively inert barrier to fission products. The pure zirconium liners are susceptible to SCC but a greatly reduced level so they represent a change in the material susceptibility characteristics.

Several modifications to existing fuel design are being considered [138]. The present geometry of chamfered edges, dished ends, and low height to diameter ratio is designed to reduce local stresses on the cladding. The new designs are annular pellets, differential enrichment, additives, large grain size, and sphere-pac fuel. The intent is to reduce the release of fission gases, and therefore fission products to the clad. Annular pellets and differential U^{235} enriched pellets (high toward the outside and low at the center) lower the pellet temperature reducing fission product release. The additives and large grain size create a fuel microstructure which better retains fission products.

Sphere-pac fuel [139] should reduce the stresses imposed on the cladding. Reductions in fuel pin diameter are intended to reduce the temperature gradient in the fuel.

2.3.3   Models

Two distinctly different approaches are taken for modeling PCI behavior and predicting fuel rod failure. Probabilistic models [140-142] use operating data such as power histories, temperatures, and fuel rod design and operating variables. A statistical model is constructed to predict a failure probability which is matched to a data base of actual behavior. Materials variables and PCI mechanics are usually not considered in model development.

Mechanistic models attempt to simulate actual PCI behavior considering fuel behavior including fission produce release, cladding mechanical properties, and the mechanics of the fuel cladding interaction. Some models consider only the material behavior [106,107,136, 143-145] and can be used as a component in a fuel element failure code. An alternate approach is incorporation of a failure criteria into a general fuel performance analysis code [146]. Many of the models are based, at least in part, on fracture mechanics principles [106,107,136, 144,145].

Table 2.1

Threshold Iodine Concentrations for Stress Corrosion Cracking

System	Lowest Iodine Quantity to Cause Cracking	Threshold	Range of Iodine Concentrations*	$T(°C)$	Type of Test	Comment	Ref
Static	$5x10^{-6}$ gm/cm^2	No	$5x10^{-6}$ - $3x10^{-3}$	360, 400	Tube pressur.	No concentration effect	[116]
Static	$3x10^{-6}$ gm/cm^2	Yes	$1x10^{-6}$ - $1x10^{-4}$	400	Tube pressur.	Threshold independent of stress and deformation rate	[81]
Static	$1x10^{-5}$ gm/cm^2	Yes	$1x10^{-7}$ - $1x10^{-4}$	350	Tube pressur.		[81]
Static	$6x10^{-5}$ gm/cm^2	No	$6x10^{-5}$ - $6x10^{-3}$	320	Tube pressur.	No concentration effect	[109]
Static	$2x10^{-5}$ gm/cm^2	No	$2x10^{-5}$ only	340	Tube pressur.		[86]
Static	$3x10^{-5}$ gm/cm^2	Yes	$1x10^{-5}$ - $3x10^{-3}$	300	Split ring	Iron "catalyst" is present	[82]
Flowing	0.03 Pa	No	0 - 40 Pa	317	Tube indentor		[75]
Flowing	4 Pa	No	4 - 875 Pa	350	Fuel swelling simulation	No concentration effect	[18]

* Concentration expressed in gm/cm^2 unless otherwise noted

Table 2.2

Melting Points (T_m) and Vapor Pressure at 300°C for

Several Metal Iodides

Material	T_m (°C)	$\log P_{MI_X}$ (atm) at 300°C	Ref.
ZrI_4	499[*]	−2.11	53,94
FeI_2	587	−8.42	95
Al_2I_6	191	−0.80	95
CsI	620	(−9.70)	94
CuI	588	−	94
CdI_2	390	−	94

*Sublimation temperature

TABLE 2.3   SUMMARY OF TEST METHODS FOR IODINE STRE   (

TYPE OF TEST	AECL (a)	GE (b)	EPRI (c)	KWU (d)	Bettis (e)	Videm and Lunde [86,117-120]	Garlick et al [80,85]	Une [83,90,91]	van der Schaaf [84]	Rosenbaum [5,6]	Wilson et al. [121]	TYPICAL DATA OBTAINED
CONSTANT DISPLACEMENT												
1. Split ring	X								X		X	t_f
2. Differential thermal expansion mandrel					X		X	X		X		t_f, ϵ_f^p
CONSTANT STRESS												
1. Internal tube pressurization			X	X	X		X	X			X	σ vs t_f, ϵ_f
2. Clad segment		?	X		X							σ vs t_f
3. Indentor			X						X			Crack frequency vs indentor load
4. Uniaxial tension							X	X	X	X		
CONSTANT EXTENSION RATE												
1. Fuel swelling simulation	X	X					X	X				ϵ_f^p vs $\dot\epsilon$, ϵ_f^p
2. Clad segment		X										ϵ_f^p vs $\dot\epsilon$, ϵ_i^p
3. Plane strain plate specimen		X										σ_f, displacement at failure
4. Uniaxial tension		X							X			σ vs ϵ
CRACK GROWTH												
1. Fracture mechanics specimen	X		X									$\dfrac{da}{dt}$ vs K, K_{ISCC}
2. Tubing								X				$\dfrac{da}{dt}$ vs K

(a) AECL is Atomic Energy of Canada, Ltd. and represents Cox, Wood, and co-workers at Chalk River Nuclear Laboratory [12, 44, 82, 83, 100-102]

(b) GE is General Electric Company and represents work done at GE Corporate Research and Development Center and Nuclear Energy Division [18, 43, 74, 76-79, 96-98,103]

(c) EPRI is the Electric Power Research Institute which has sponsored research at NASA-Ames, Argonne National Laboratory, and SRI International [19, 75, 92, 104-107, 109-114]

EST METHODS FOR IODINE STRESS CORROSION CRACKING OF ZIRCALOY

Rosenbaum [5,6]	Wilson et al. [121]	TYPICAL DATA OBTAINED	ADVANTAGES	DISADVANTAGES
	X	t_f	Simple test, good for screening	Stress relaxation above 300°C; no failures without "catalysts"
X		t_f, ϵ_f^p	Simple test, good for screening; test at high temperature with proper mandrel	Test chemistry complicated by mandrel; do not know stress and strain distribution; stress relaxation; mandrel masks ID surface; no control over strain rate; stress range limited
	X	σ vs t_f, ϵ_f	Stress state well characterized; multi-axial stress state representative of fuel cladding; large strains can be applied	Pressurization system needed; bulging can occur at high strains; no localized stresses.
		σ vs t_f	Stress applied over localized region; machine notch or fatigue crack can be introduced.	Local strain distribution uncertain
		Crack frequency vs indentor load	Characterize initiation sites; localized plastic stress and strain; biaxial stress state	Stress state and strain distribution poorly known; no control over strain rate.
X			Simple test	No SCC failures in iodine
		ϵ_f^p vs $\dot\epsilon, \epsilon_f^p$	Local stresses typical of application	Strain distribution not known; must be analyzed by finite element methods
		ϵ_f^p vs $\dot\epsilon, \epsilon_f^p$	Good screening test for both materials and environmental variables; local stress and strain; requires little material	Local strain and strain rate uncertain because of small, irregular gage size
		σ_f, displacement at failure	Plane strain stress state; good screening test for environmental variables	Plate material might be metallurgically different from cladding; cracks can be initiated at edges of gage section
		σ vs ϵ	Simple test, good for screening	No multiaxial stress state
		$\dfrac{da}{dt}$ vs K, K_{ISCC}	Plane strain loading conditions; data can be used for fracture mechanics design and modelling	Microstructure in crack growth direction of plate different from tubing; long crack not representative of application
		$\dfrac{da}{dt}$ vs K	Material representative of service material	Uncertainty about applying fracture mechanics to thin gage section

co-workers

ate Research
, 96-98,103]

search at
, 92,

(d) KWU is Kraftwerk Union AG and denotes work done at that company [38, 81, 115]

(e) Bettis is Westinghouse, Bettis Atomic Power Laboratory and represents work at that laboratory [87, 89, 116]

TABLE 2.4   COMPILATION OF ZIRC...

TYPE OF TEST Specimen Type Investigator or Laboratory (a)	DATA COLLECTED	Iodine Concentration	Metal Iodides	Hydrogen	Oxygen (air)	Water vapor	Liquid metals	Heat treatment	Texture
CONSTANT DISPLACEMENT									-
Split Ring									
AECL	σ_1 vs t_f	[82]		[82,101, 102]	[83]		Cs[83]	[82,83]	[82]
van der Schaaf [84]	-	X							
Wilson et al. [121]	-								X
Differential Thermal Expansion Mandrel									
Bettis [81]	σ_1 vs t_f						Cs		
UKAEA	σ_1, t_f							[80,85]	[85]
Une [88]	ϵ_f, t_f	X			X			X	
Rosenbaum [6]	-	X							
CONSTANT STRESS									
Internal Pressurization									
EPRI	σ vs t_f, ϵ_f	[109]						[111,113]	[109,110]
KWU	σ, t_f, ϵ_f	[38,81]			[38]	[38]			[81]
Bettis	σ vs t_f, ϵ_f	[87,89,116]		[87]		[87]	Cs [87,89]	[116]	
UKAEA [85]	σ vs t_f, ϵ_f							X	
Videm and Lunde	σ vs t_f, ϵ_f	[86,120]	[86]	[86,120]	[86]			[86]	
Wilson et al. [121]	σ vs t_f								X
Clad Segment									
GE [74]	σ vs t_f						Cs,Cd		
KWU [81,115]	ϵ vs t at const. σ	X							
Indentor									
EPRI	crack freq. vs ϵ_p	[75]						[75]	[114]
Van der Schaaf [84]	force to crack	X						X	
CONSTANT EXTENSION RATE									
Uniaxial Tension									
GE [43,97,98]	σ vs displacement						X		
Swelling Simulation									
UKAEA [85]	cracked/not cracked							X	
Une [90,91]	$\dot{\epsilon}_{avg.}$, ϵ_f							X	
AECL	t_f, $\dot{\epsilon}$, ϵ load vs ϵ_f						Cs[44],Cd[99]		
	ϵ_f core displ. rate	[18]	[18]				Cd[18,76]		
Plane Strain Clad Segment									
GE	ϵ_f vs $\dot{\epsilon}$, σ vs ϵ							[74,77]	
Une [91]	ϵ_u, $\epsilon_{0.9}$ vs $\dot{\epsilon}$	X			X	X		X	
Plane Strain Plate Specimen									
GE	σ vs ϵ [78], σ vs displ.[79], red. in thick. at failure [91,103]				[79]		Cd [74]		[103]
CRACK GROWTH									
Fracture Mechanics Specimen									
AECL [44,82,100]	da/dt vs K, K_{ISCC}						Cs [44]		
EPRI [92]	K_{ISCC}				[X]				
Tubing									
Videm and Lunde [117-119]	da/dt vs K							X	

(a) See Table 2.3 for explanation of laboratories

) Surface Condition	Oxide	Pickling	Mech. polish, honing, sand blast, shot peen	Pre-flaws, scratches	EXPERIMENTAL FACTORS POSSIBLY AFFECTING CHEMISTRY	COMMENTS
[3]	[82]	[83]		[101]	Add iron or air as catalysts	No failures without catalysts, no failures in liquid Cs [83]
	X				Add iron in one batch	No failures
		X			Add iron	One of three lots fail
	[80]				Stainless steel mandrels	No failures in some tests [87]
					Brass, aluminum and stanless steel mandrels	
					Al alloy, brass, and stainless steel mandrels	Crack initiated at tube OD
	X				Stainless steel mandrel	
		[111,113]		[104]	Iron transported from fittings to specimen surface	Biaxial tests [112]
		[81]			Break iodine ampoule with stainless steel ball [81]	Calculate $\dot{\varepsilon} = \varepsilon_f/t_f$
	.89]				Air not removed before pressurization in some tests [87]	No failures in Cs tests
					Steel volume displacing mandrel	
	[86,120]	[120]	[86]		Moisture and air often not removed prior to test	
			X			
				X	Flowing Ar + I_2 stream	
					Stainless steel test chamber	Split ring test, separates initiation and propagation
	[75]	[114]	[114]		Flowing Ar + I_2 stream	Examine crack initiation sites; test tube and sheet
	X				Stainless steel test chamber	Indentor forces crack to propagate through specimen
					Cs, Cs/Cd, solid and liquid Cd	Screen several environments for cracking susceptibility [43]
					Aluminum and stainless steel mandrel	Compression of mandrel necessary to fail low strength cladding
X	X				Al plug with Al_2O_3 annulus	
99]					Al plug with Al_2O_3 annulus, stainless steel ram	Strain rate calculated from test machine cross bend speed
					Zirconium core, WC inserts, Al_2O_3 annulus (17-7 pH	
76]		[18]		[18]	stainless steel for Cd tests); flowing Ar+I_2 stream	Strain rate calculated from test machine crosshead speed
					Flowing Ar + I_2 stream	Localized ductility specimens
						Study stress ratio effects, including uniaxial tension
					Flowing Ar + I_2 stream	
					Steel loading bolt	DCB specimens
					Other environments were I_2+Fe, I_2+Cd, ZrI_4, Br_2 and Cl_2	WOL specimens; troughs on fracture surface perpendicular to crack growth direction
						Fatigue pre-cracked specimens

Figure 2.1

Model for PCI Cracking of Zircaloy Fuel Cladding
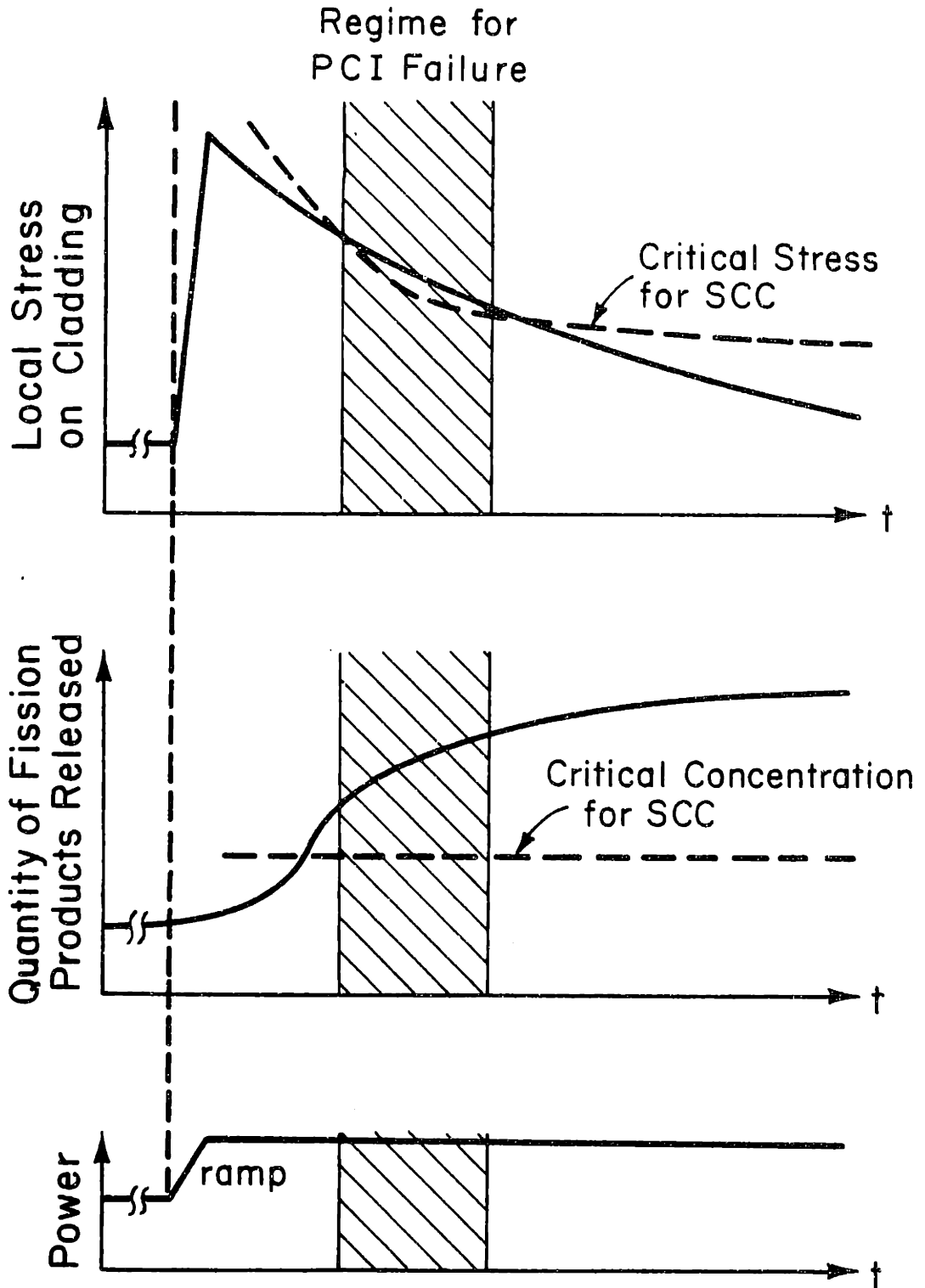
Figure 2.2

Variation in Oxygen Potential with x for $(U_{1-q}, Pu_q)O_{2+x}$ at 700°C
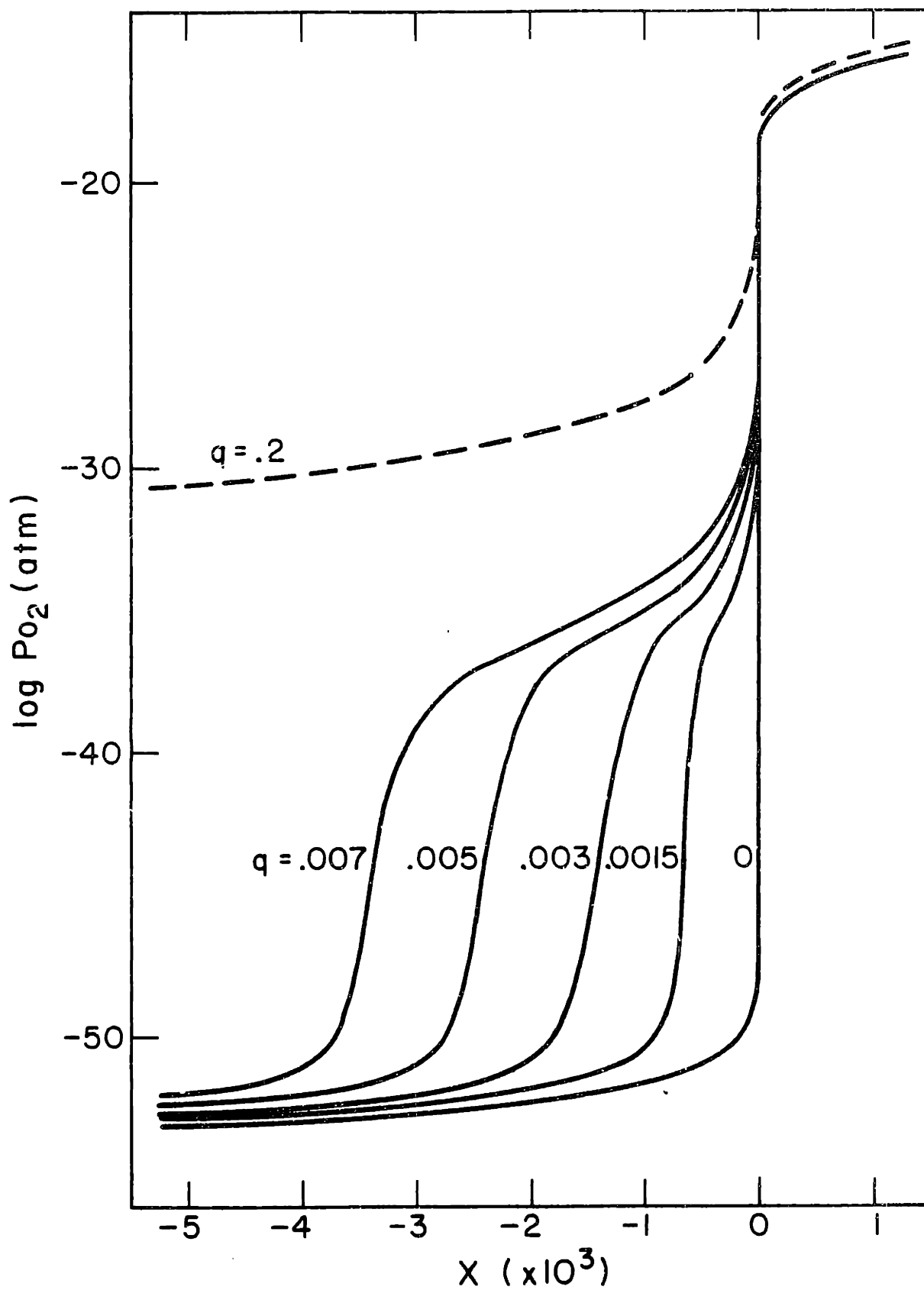
Fig. 2.3   Compositions of Zr/I Phase Stability

Bar represents the composition range studied. Open areas give compositions of homogeneous solid solution while cross-hashed regions are two phase.
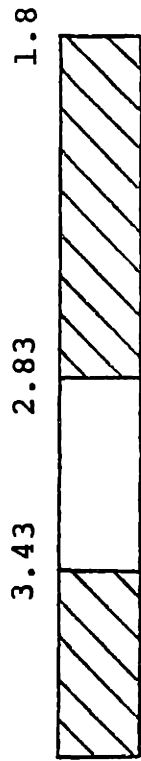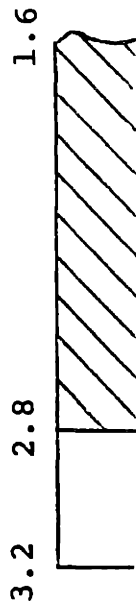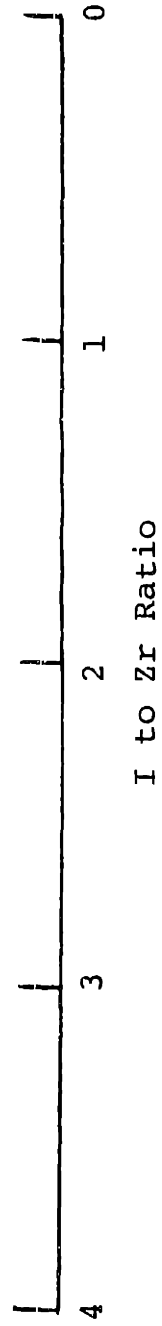
Figure 2.4

Regions of Stability for Zirconium Iodide Phases
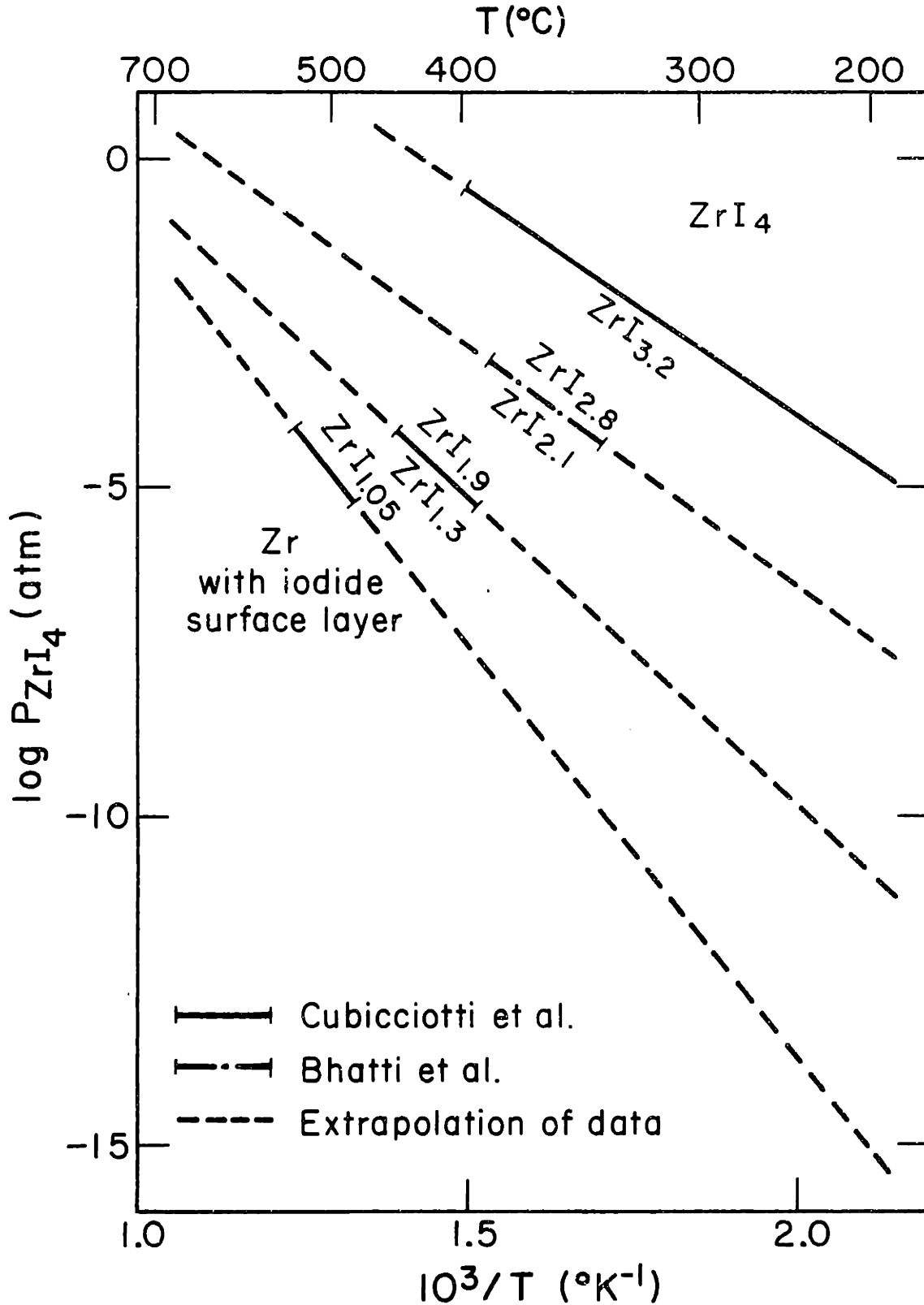
Figure 2.5

Free Energy of Formation versus Temperature for
Several Metal Iodides
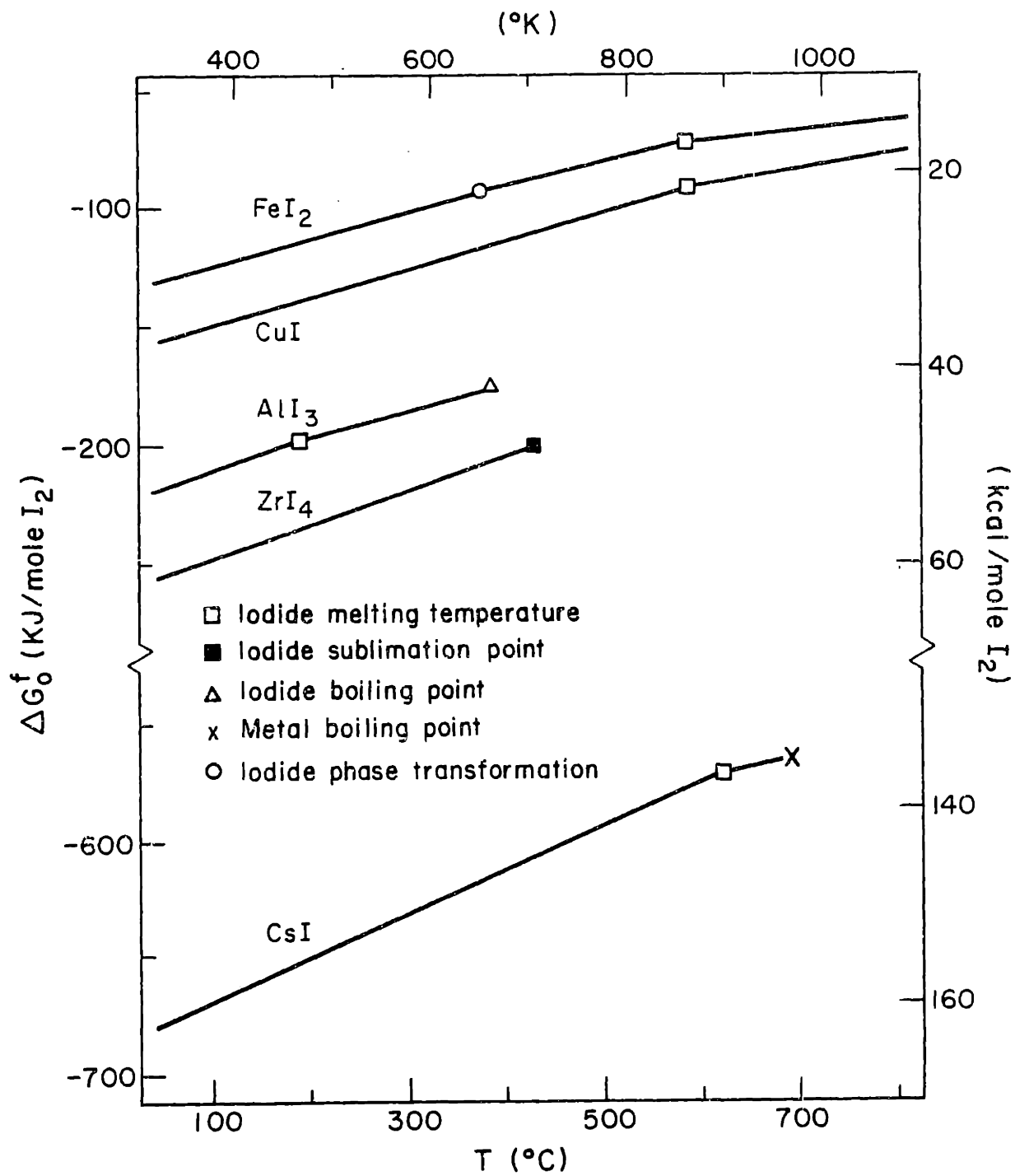
Figure 2.6

Vapor Pressure versus Temperature for Several Metal Iodides
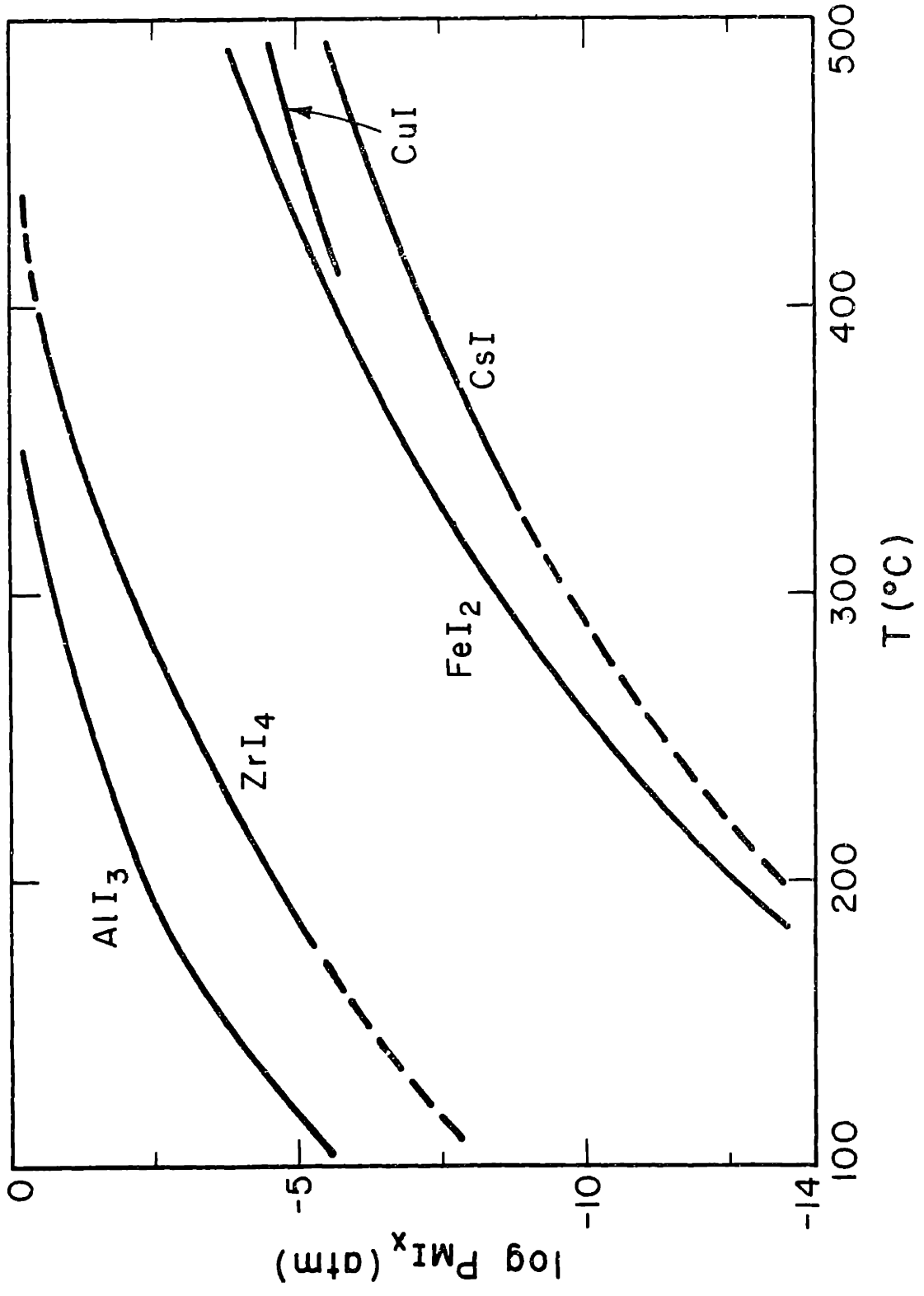
Figure 2.7

Loading Schemes for Stress Corrosion Cracking Tests
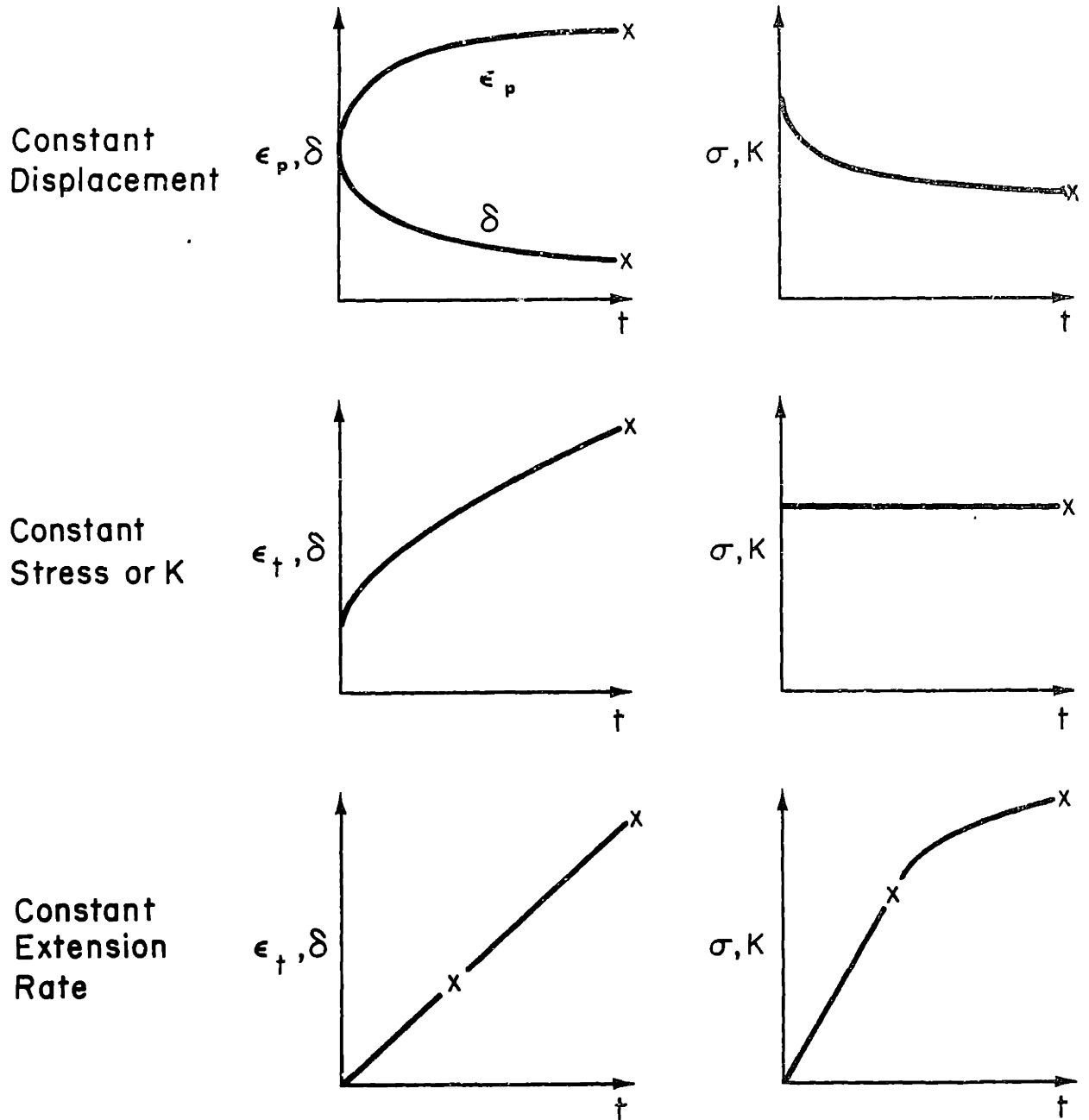
3.   MATERIALS FOR EXPERIMENTAL PROGRAM

The materials chosen for this program are nominally 1.27 cm

Zircaloy plates and several lots of Zircaloy-2 reactor grade cladding

tubes.   The plate materials remain from an Electric Power Research

Institute program and have received considerable characterization

[19, 129].   The tubing lots are provided by Exxon Nuclear Company, Inc.

from standard production lots used in fuel rod fabrication.   A critical

microstructural aspect in all these materials is the crystallographic

texture.   An introduction to texture and to quantitative texture numbers

is presented.   The plate and tubing materials are then characterized.

3.1   Texture

3.1.1   Background and Description of Techniques

Crystallographic texture refers to the preferred orientation

of grains in a solid that deviates from a random distribution.   It is

analyzed by the x-ray diffraction techniques of inverse pole figure and

direct pole figure [147, 148].   Experimental details are provided in

Appendix B.   An inverse pole figure is a plot of the intensities of all

diffracting planes in a particular sample direction on a stereographic

projection.   For HCP materials such as Zircaloy, a segment of the

standard (0002) projection is used.   A General Electric XRD-5 diffracto-

meter is used to obtain the data which are reduced and plotted as

approximate lines of isointensity.

A pole figure maps the statistical distribution of the normals to a given {hkil} plane of a polycrystalline sample. It shows the extent and direction of preferred orientation on a polar stereographic projection. For Zircaloy basal, or (0002), pole figures are normally constructed since this is the unique direction in the HCP crystal structure. With one additional pole figure, usually [10$\bar{1}$0], the texture is fully defined by knowing the rotation about the basal pole. Experimentally, the Schultz reflection technique [149] is used. A specimen is simultaneously tilted and rotated about its normal on a Siemens Pole Figure Diffractometer to sample all directions for the desired pole. The intensity data are corrected, normalized, and plotted on the polar stereographic projection.

For plate materials, inverse pole figures are usually determined in the three principal directions. Pole figures are plotted for several through thickness locations. For tubing materials, both inverse and direct pole figures are determined for radial samples at several locations through the wall thickness.

3.1.2 Texture Numbers

Crystallographic texture is quantified by the calculation of texture numbers [148]. The Kearns texture parameter f_i [148, 150, 151] represents the resolved fraction of basal poles in a reference direction, i. In integral form, f_i is defined as:

$$f_i = \int_0^{\pi/2} I_\phi \sin\phi \, \cos^2\phi \, d\phi \qquad (3\text{-}1)$$

where I_ϕ is the pole density at a tilt angle, ϕ from the reference direction, i, averaged over all rotations about that reference direction. The integration, therefore, considers poles over the entire stereographic projection. The value of f_i varies between 0 and 1 indicating perfect alignment of basal poles perpendicular and parallel to the ith direction, respectively. For a random texture $f = 1/3$ in each of the three ortho-gonal directions in a sample. The sum of f_i's in three orthogonal directions in any sample, textured or random, equals unity. The f_i values are calculated from inverse pole figure data by the method of Kearns [150].

The texture numbers F_T [131, 148] and $(SD)_T$ [148] are used to characterize the basal pole texture in the R-T plane. F_T is scaled to give limiting values of 1.0 for a radial basal pole texture and -1.0 for a tangential basal pole texture. The standard deviation $(SD)_T$, is a measure of the dispersion of basal poles in the R-T plane. $(SD)_T$ reaches a limiting value of 0.303 for a uniform basal pole distribution in the R-T plane. The mathematical definitions of these quantities are:

$$F_T = \int_{-\pi/2}^{\pi/2} I(\phi) \cos 2\phi \, d\phi \bigg/ \int_{-\pi/2}^{\pi/2} I(\phi) \, d\phi \qquad (3-2)$$

$$(SD)_T = [2nd \text{ moment} - (1st \text{ moment})^2]^{1/2} \qquad (3-3)$$

$$\text{where} \quad 1st \text{ moment} = \int_{-\pi/2}^{\pi/2} I(\phi) \sin\phi \, d\phi \bigg/ \int_{-\pi/2}^{\pi/2} I(\phi) \, d\phi \qquad (3-4)$$

$$\text{2nd moment} = \int_{-\pi/2}^{\pi/2} I(\phi) \sin^2\phi \, d\phi \Bigg/ \int\!\!\int_{-\pi/2}^{\pi/2} I(\phi) \, d\phi \qquad (3\text{-}5)$$

3.2   Plate Materials

The materials used in this study are plates of Zircaloy-2 and Zircaloy-4 whose ingot compositions and fabrication schedules are given in Appendix C. The primary difference between the fabrication routes is the final rolling treatment. Plate 9912 is rolled to give a tube (±40°) texture. Plate 9908 is warm cross-rolled to give a normal (0°) texture. Each plate receives two separate final heat treatment steps. The stress-relief treatments product a recovered microstructure. The full anneals give a recrystallized microstructure. The characteristics of each plate are summarized as follows:

- 9908-3A : 0° texture, stress relieved;

- 9908-3B : 0° texture, recrystallized;

- 9912-SR : ±40° texture, stress relieved;

- 9912-RX : ±40° texture, recrystallized.

The plates are referred to by the above designation or by a shorthand designation: 0°-SR, 0°-RX, ±40°-SR, and ±40°-RX.

The stress-relieved treatment results in recovery but not recrystallization so the microstructure remains essentially cold-worked. The grains are flattened with the smallest grain dimension measured through the plate thickness or short transverse direction. For both stress-relieved plates, that grain dimension is 4-6 μm. The length and width dimensions are more difficult to measure due to the cold work

so the scatter in values is greater, however, the ranges are 20–25 μm in the longitudinal and 12–15 μm in the transverse direction. Recrystallization grain size in both plates is 8–10 μm.

Figs. 3.1 and 3.2 present basal pole figures for plates 9908-3A and 9908-SR near the center of the respective plates. Texture numbers are given in Table 3.1. Additional pole figures, normal-transverse (N-T) scans, and inverse pole figures for near surface and near mid-thickness in each plate are collected in Appendix B. A through-thickness f_N plot, and axial and transverse inverse pole figures are also included. All texture plots for recrystallized material are relegated to Appendix B because they are similar to the stress-relieved material.

3.3   Tubing Materials

3.3.1   General Characteristics

Three lots of reactor grade Zircaloy-2 tubing are selected for study. The nominal dimensions of the as-received Supplier A and B materials are 10.9, 12.8, and 0.95 mm (0.429, 0.504, and 0.037 inch) for the inside diameter (ID), outside diameter (OD), and wall thickness, respectively. Chemical composition for both lots are given in Appendix C. The third lot, termed 1340, has nominal dimensions of 12.0, 14.3, and 1.17 mm (0.472, 0.564, and 0.046 inch) for the ID, OD, and wall thickness, respectively. All lots meet or exceed the standard quality control standards with regard to final dimensions, chemical composition, mechanical properties, surface finish, hydride orientation, and steam corrosion.

The final pickling for as-received (AR) material results in a substantial difference in ID surface finish between Supplier A and Supplier B. The surface of Supplier A is comparatively smooth with particles protruding as shown in Fig. 3.3 (a). The particles are identified by energy dispersive x-ray analysis on the scanning electron microscope (SEM) to be primarily second phase particles (Zr/Fe/Ni/Cr) with occasional inclusions (Zr/Ca/Al/K). The AR surface of Supplier B, Fig. 3.3 (b) contains two pit populations. The large pits probably result from either gouging of the ID surface during the final tube making pass or selective local attack during pickling. The second pit population is composed of small pits (~ 0.5 μm diameter) resulting from selective removal of second phase particles.

3.3.2   Texture

The following basal pole figures are presented:

•Fig. 3.4 - ID surface of supplier A;

•Fig. 3.5 - 0.10 mm from the ID surface of supplier A;

•Fig. 3.6 - ID surface of supplier B;

•Fig. 3.7 - 0.10 mm from ID surface of supplier B;

•Fig. 3.8 - 0.17 mm from ID surface of lot 1340.

Texture numbers for all locations are given in Table 3.2. Kearn's numbers, f_r, for suppliers A and B are plotted versus wall thickness in Fig. 3.9. The remaining pole figures, radial-tangential (R-T) scans, and inverse pole figures are found in Appendix B.

3.3.3   Additional Processing and Characterization

To measure the hoop residual stress, ~1.3 cm lengths of tubing are slit axially and the resulting dimensional changes converted into residual stress values. The formula [152] for the maximum hoop stress is:

$$\sigma_{max} = \frac{Et}{1-\nu^2} \frac{D_m^1 - D_m^o}{D_m^1 D_m^o} \tag{3-6}$$

where E is Young's modulus, t is the wall thickness, ν is Poisson's ratio, and D_m^o and D_m^1 are the mean tubing diameter $(\frac{OD - ID}{2})$ before (^{o}super-script) and after (^{1}superscript) slitting. It is important to note that these residual stress values assume a linear stress gradient across the wall of the cladding tube. Both linear [90] and non-linear [82] gradients are reported depending on the processing history of the material. Residual stress values are given in Table 3.3 for the AR condition tubing where straightening stresses are present and for the same tubing following a 500°C stress-relief anneal for two hours (SR condition). The AR residual stress values are much higher in Supplier A than in Supplier B but fall to approximately the same low value following the SR treatment.

In addition to the AR surface condition, two additional surface conditions are developed. A pickling (45% H_2O, 45% HNO_3, 10% HF) operation, (P), of the AR materials removed 37-50 μm of metal giving the surfaces shown in Fig. 3.3 (c) and 3.3 (d) for Suppliers A and B, respectively. Both surfaces are now indistinguishable with a population of only small pits. Because no large pits formed during pickling, it is likely that Supplier B large pit population of Fig. 3.3 (b) is a

consequence of the tube making operation. A final surface treatment is honing (H) with a hone made of a bonded coarse grit. Tube ID surface receives multiple passes over the hone which is cooled and lubricated by a light oil. Approximately 0.5 μm is removed leaving an ID surface with distinct circumferential scratches. A stress-relief anneal and pickling follow the honing operation. The H + SR + P surface is somewhat rougher than a pickled surface and is between Supplier A and B as-received material in terms of roughness. Table 3.4 summarizes the important features of ID surface condition.

Table 3.1

Texture Numbers for Zircaloy Plates

| Texture Number* | Plate and Heat Treatment | | | |
| | 9908 | | 9912 | |
	3A	3B	SR	RX
f_N	.70	.67	.56	.59
f_T	.19	.21	.33	.32
f_L	.09	.09	.08	.07
F_T	.460	.416	-.018	.203
$(SD)_T$	.239	.252	.243	.251

*Normal values taken near mid-thickness of plate

Table 3.2

Texture Numbers for Zircaloy Tubing

Lot Designation	Location	Texture Numbers		
		f_r	F_T	$(SD)_T$
Supplier A	ID surface	0.628	0.264	0.243
	0.10 mm from ID surface	0.647	0.329	0.241
	0.47 mm from ID surface	0.625	0.263	0.247
	0.10 mm from OD surface	0.594	0.167	0.258
Supplier B	ID surface	0.538	0.161	0.247
	0.10 mm from ID surface	0.550	0.152	0.269
	0.47 mm from ID surface	0.543	0.119	0.274
	0.10 mm from OD surface	0.498	0.125	0.278
Lot 1340	ID surface	0.595	0.192	0.251
	0.18 mm from ID surface	0.582	0.124	0.244
	0.71 mm from ID surface	0.524	-0.011	0.245
	0.10 mm from OD surface	0.497	-0.027	0.254

Table 3.3

Residual Stress Data for Tubing Materials

Supplier	Condition	Residual Stress at Tube ID (ksi)	(MPa)
A	AR	-15.9	-110
	SR	- 3.0	- 21
B	AR	- 2.7	- 19
	SR	- 1.5	- 10

*Assume linear stress gradient across tube wall.

Table 3.4

Surface Condition for Supplier A and Supplier B Tubing

As-Received (AR)

Supplier A: Smooth (4μm peak-to-peak)*
                     Second phase and inclusion particles
                        imbedded in surface

Supplier B: Rough (9μm peak-to-peak)
                     Pitted surface
                        A) Large pits   10-20μm
                        B) Small pits   0.5-1μm

Pickled (P)
Both Suppliers: Smooth (approaching Supplier A
                        As-Received.
                     Small pit population   0.5-1μm

Honed + Pickled (H+P)
Both Suppliers: Rougher than pickled only surfaces
                        (intermediate between suppliers
                        A and B As-Received)
                     Small pit population 0.5-1μm

*After Syrett et al., J. Nucl. Mater., 92 (1980) 102
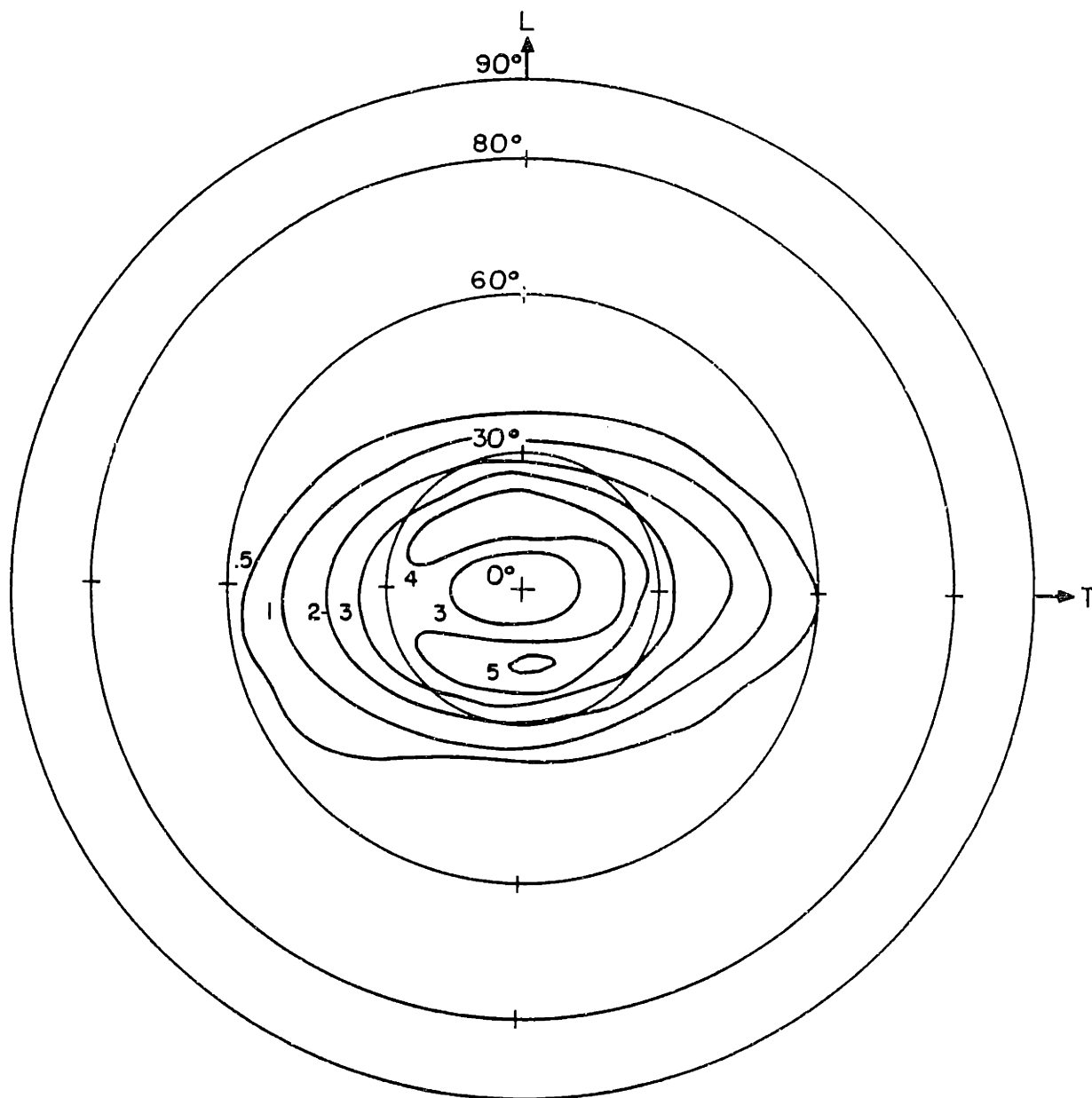
Fig. 3.1

Basal pole figure for Zircaloy-2 plate 9908-3A,
stress-relieved at 497°C for 4 hours
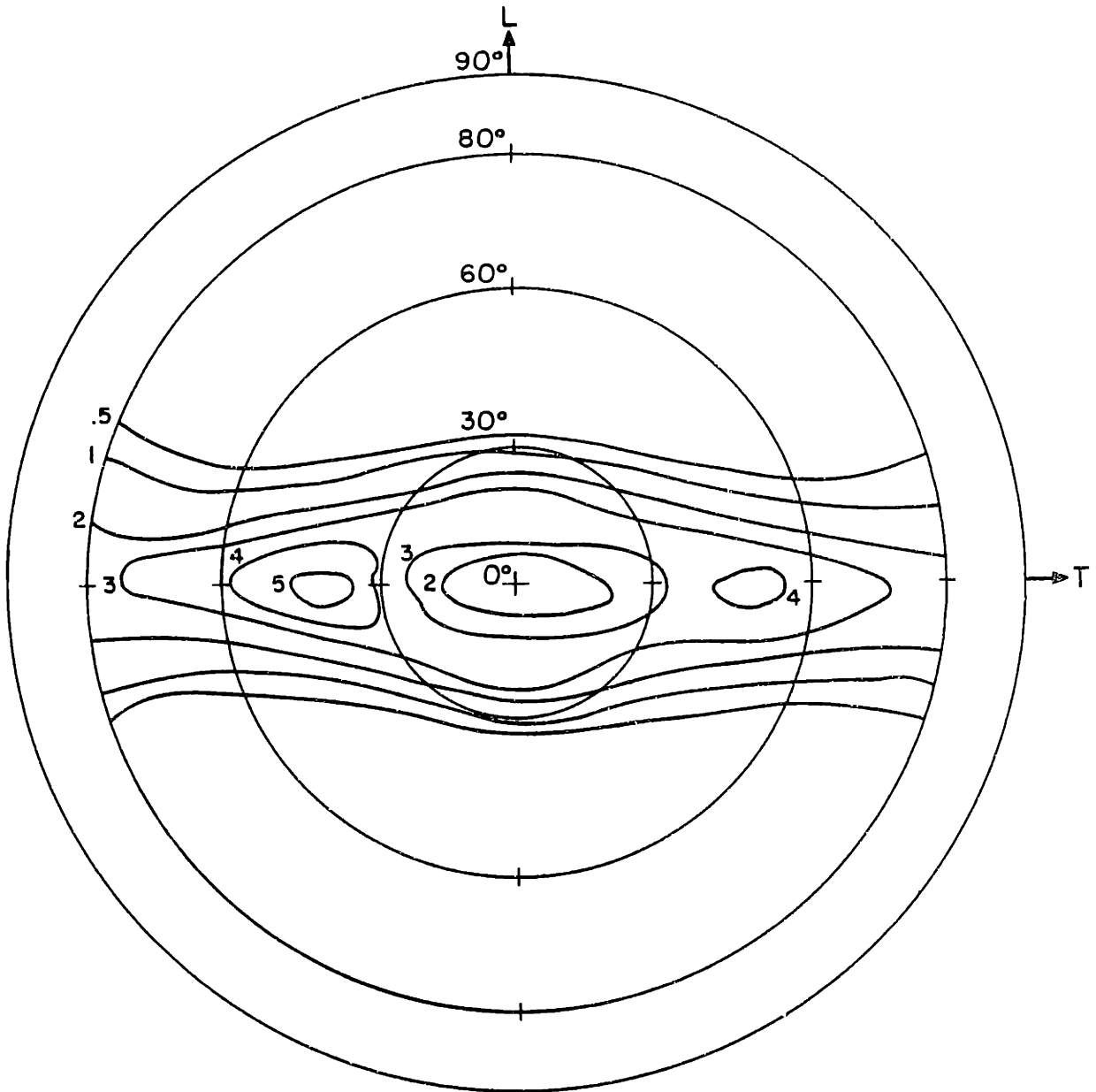
Fɪɢ. 3.2

Basal pole figure for Zircaloy-4 plate 9912-SR,
stress-relieved at 485°C for 4 hours

Fig. 3.3   SEM micrographs of the ID surfaces for supplier A and supplier B cladding in the as-received and pickled conditions.
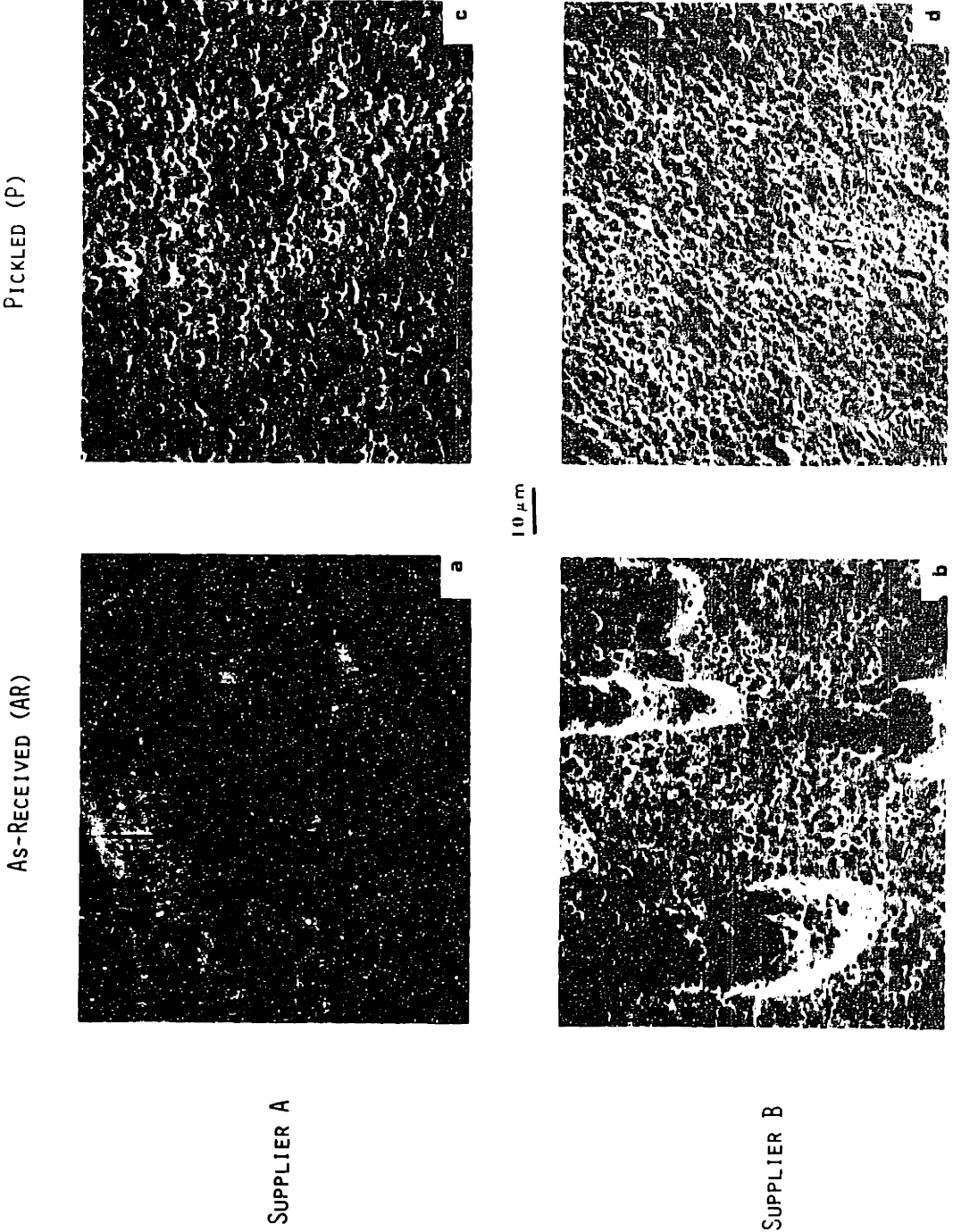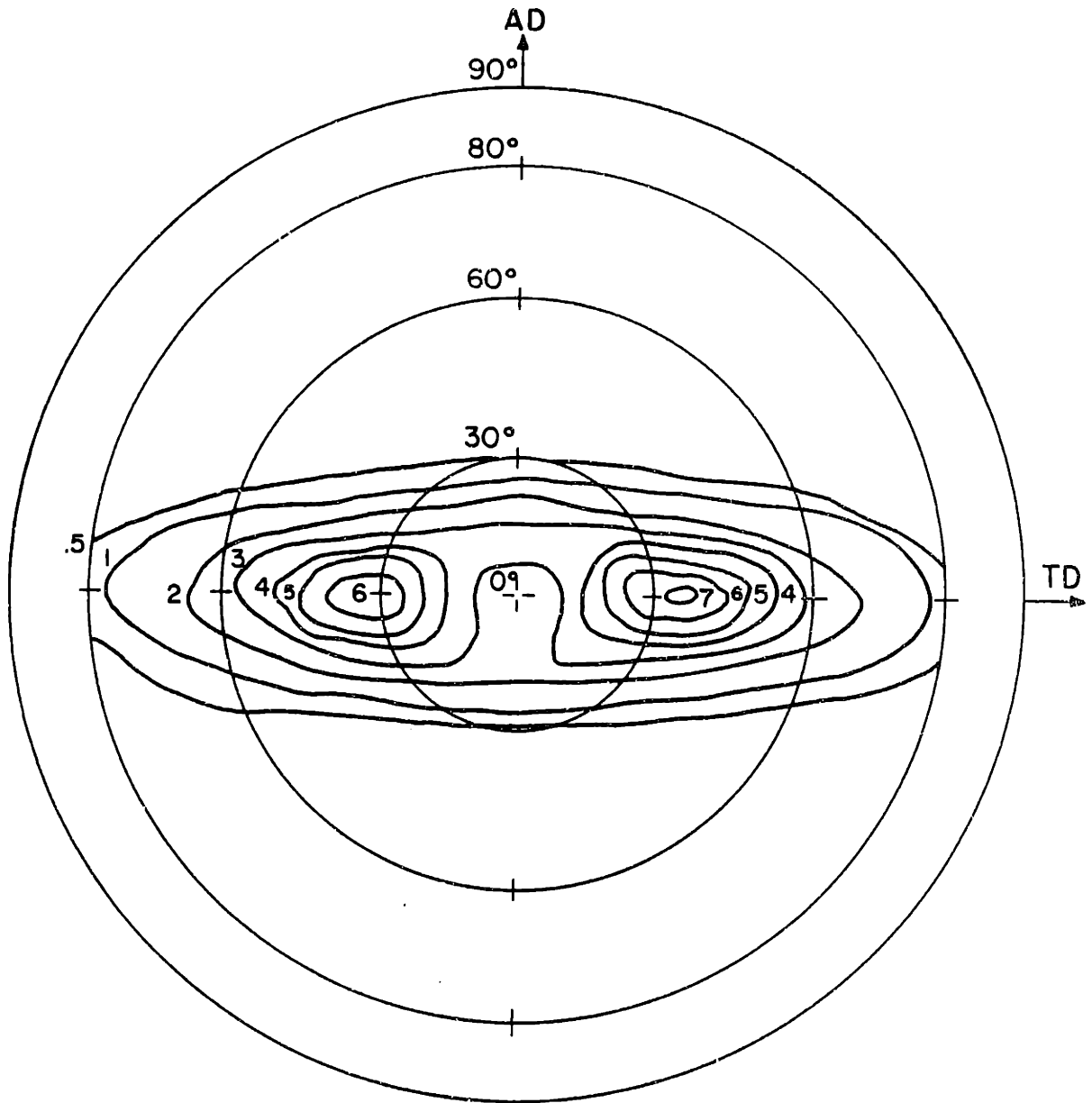
Basal Pole Figure for Supplier A Tubing, ID Surface

Figure 3.4
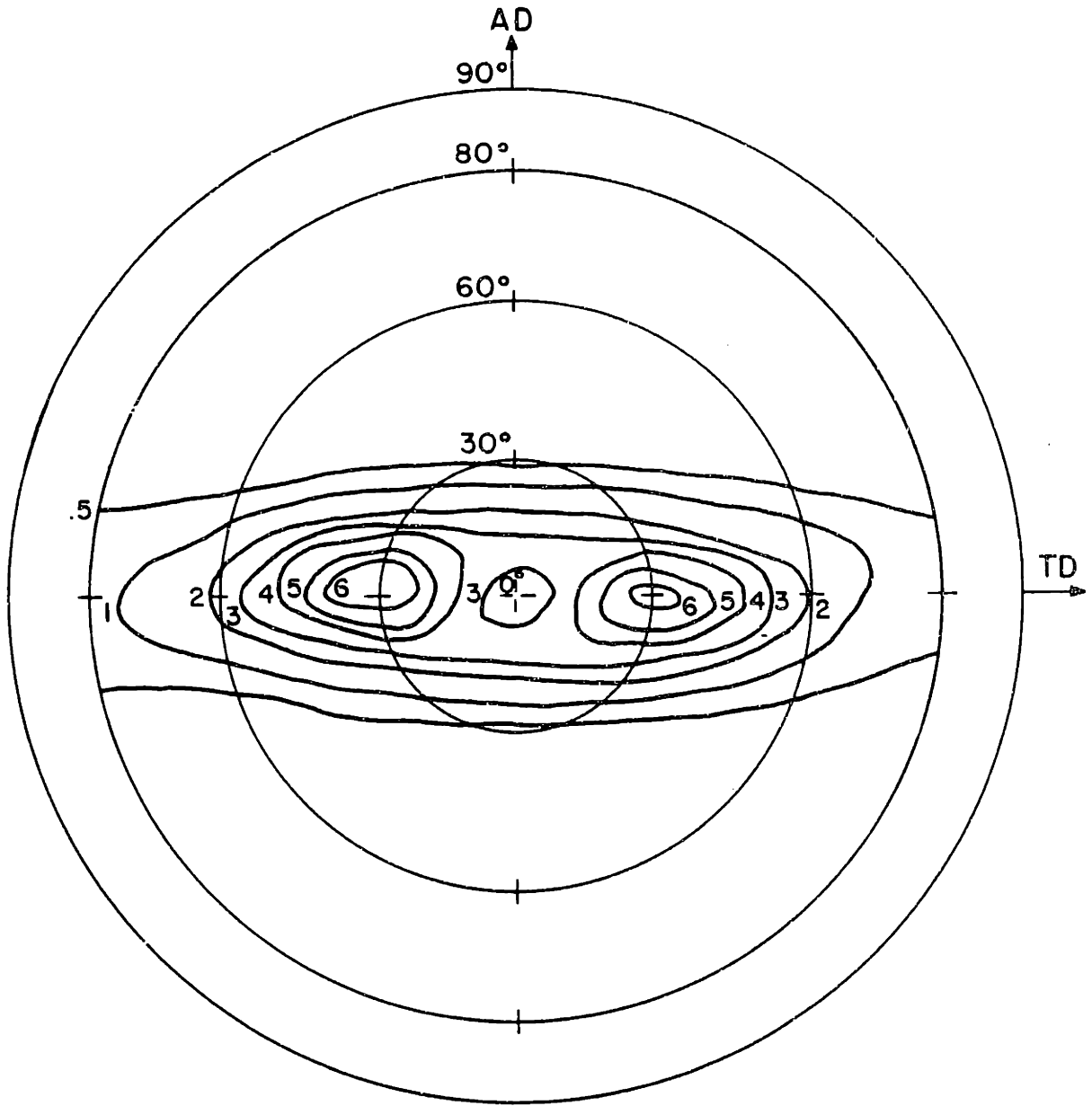
Basal Pole Figure for Supplier A Tubing, 0.1mm from Tube ID

Figure 3.5
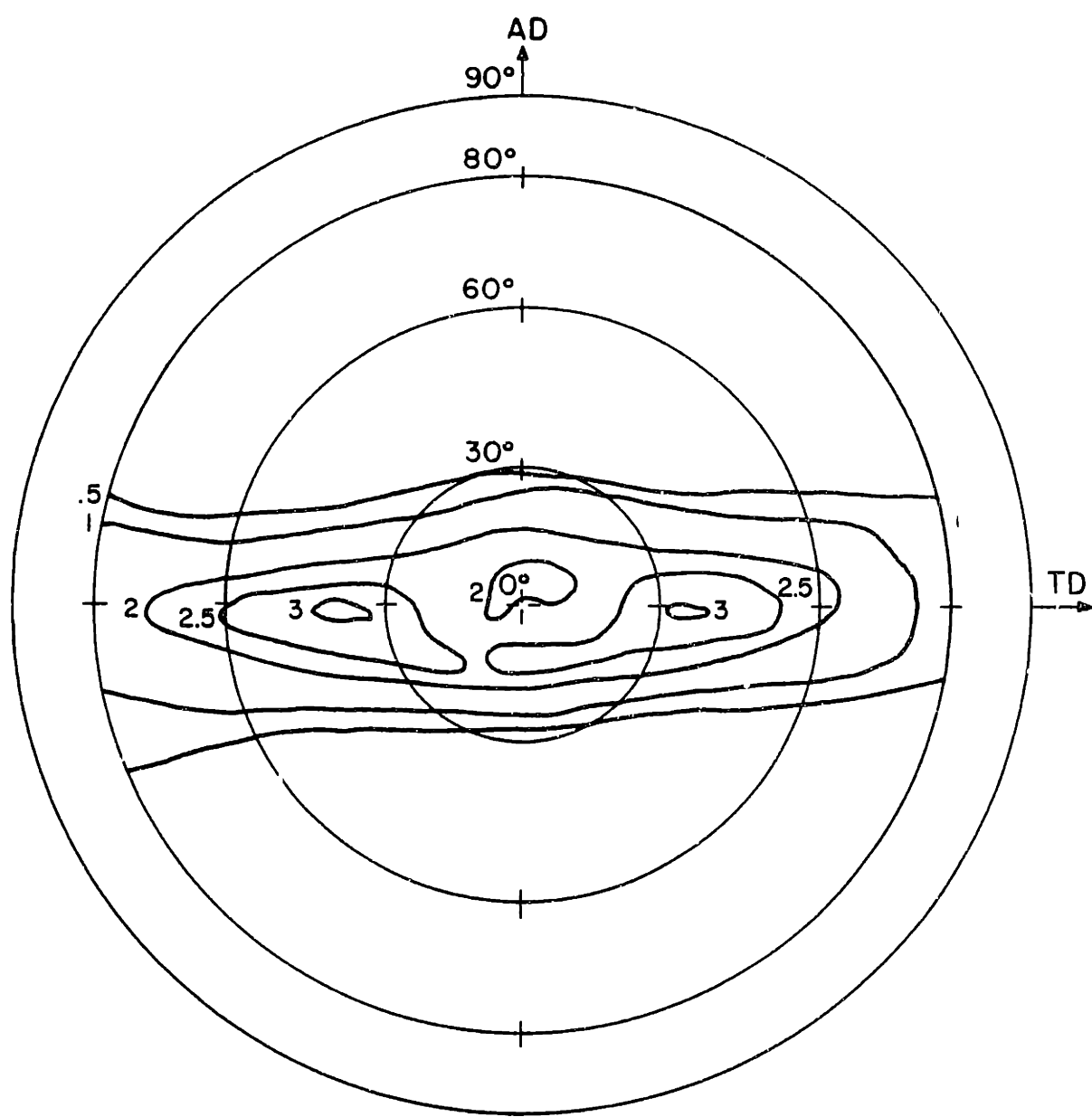
Basal Pole Figure for Supplier B Tubing, ID Surface

Figure 3.6
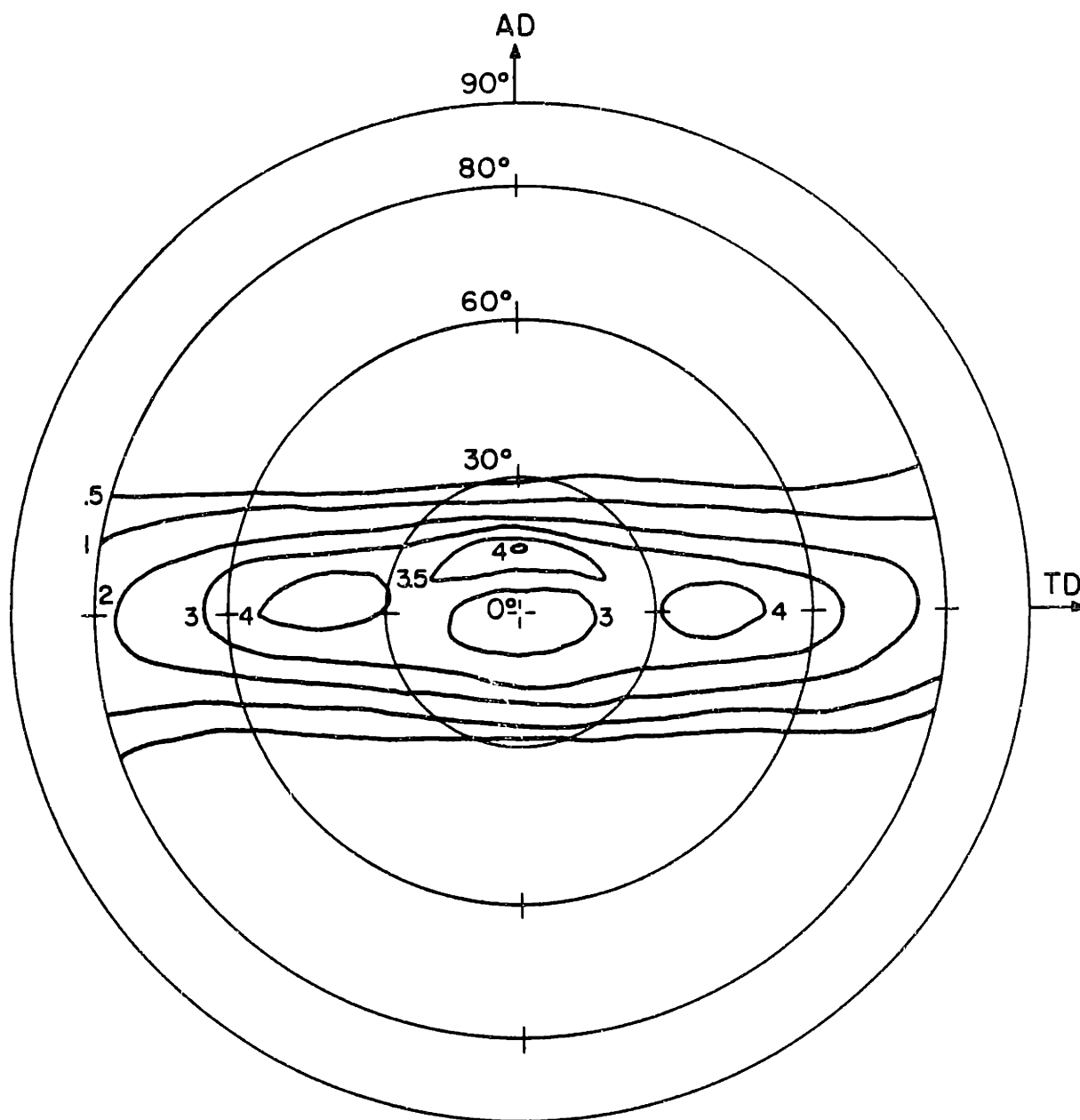
Basal Pole Figure for Supplier B Tubing, 0.1mm from Tube ID

Figure 3.7

Figure 3.8 Through-Thickness Texture Numbers for Tubing
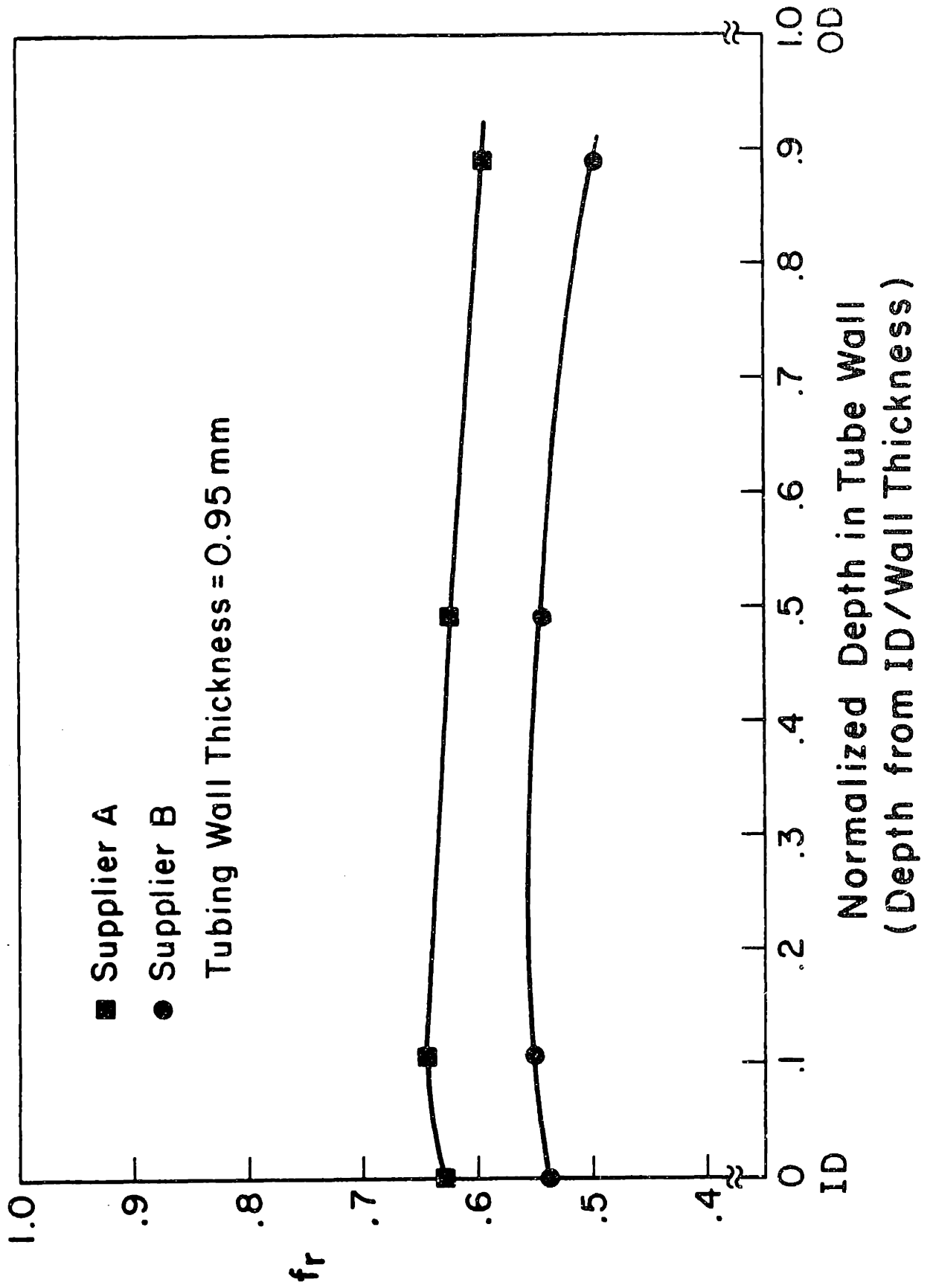
4. EQUIPMENT AND TEST PROCEDURES

4.1 Crack Arrest Tests

4.1.1 Apparatus

Tests are conducted under carefully controlled environmental conditions. Argon gas (99.999% minimum) is passed through a desiccating column (anhydrous $CaSO_4$), then through a column of iodine crystals (reagent grade, >99.8%). Any residual water vapor from the iodine column is removed by a molecular sieve (Linde 4A) heated to $1555\pm5°C$ to permit passage of the iodine [153]. Excess iodine is condensed in a column surrounded by a controlled temperature bath to achieve the desired iodine partial pressure. Only materials known to be inert to iodine attack are used in the test system construction: glass, teflon, and viton O-rings. The system in shown in Fig. 4.1.

4.1.2 Specimens

Two types of fracture mechanics specimens are used in this program: the double cantilever beam (DCB) and the wedge opening load (WOL). The DCB specimens for the early phase of the program have dimensions of 12.6 mm width by 12.6 mm height (2h) by 25.4 mm length with a machined notch 12.6 mm long. Loading is accomplished by inserting a Zircaloy-2 wedge into the machined notch at the front face of the specimen. Later tests use a slightly modified DCB specimen which has a total length of 40.6 mm with machined bolt holes for loading. The specimens are loaded by two opposing molybdenum alloy (TZM) bolts.

The WOL specimens [154,155] are made to "$\frac{1}{2}$ T" dimensions by appropriate scaling from a larger specimen size to 12.6 mm thickness. They are loaded by a TZM bolt and loading tup configuration [155]. Specimen drawings are shown in Fig. 4.2.

4.1.3 Procedures

All specimen surfaces are polished through 600 grit SiC paper. The surface for observation of the propagating crack receives additional polishing by a one micron alumina slurry followed by a fine silica suspension. Specimens are pre-notched with a 0.2 mm diamond string saw to a depth of 0.8 - 1.0 mm. Wedge-loaded DCB specimens are tested in the as-notched condition where stress corrosion cracks are allowed to "pop-in" from the string saw cut. Bolt loaded DCB and WOL specimens are pre-cracked in fatigue. The maximum stress intensity during pre-cracking is always less than half the initial K of SCC exposure.

For wedge-loaded DCB specimens, initial displacement, δ_i is measured directly at the front face with a micrometer accurate to ± 0.005 mm. For bolt-loaded DCB specimens, displacement is measured at the front face and load line displacement is calculated knowing the pre-fatigue crack length. Stress intensity for DCB specimens is calculated from the expression [156,157]:

$$K = \delta Eh[2h(a + 0.6h)^2 + h^3]^{1/2} \Big/ 4[(a + 0.6h)^3 + h^2a]$$

$$\cdots\cdots (4\text{-}1)$$

where E is Young's modulus and a is the crack length measured from the load line. This formulation is found to agree quite well with other compliance equations [158].

For WOL specimens, displacement is monitored by a clip gage mounted on attachable tungsten carbide knife edges. Clip gage accuracy is better than ± 0.0025 mm. Specimen compliance, $(BE\delta/P)$ is determined by the specimen geometry and clip gage location (i.e. point of measure-ing δ) where B is the specimen width, E is Young's modulus, δ is the displacement, and P is load. Compliance as a function of crack length is calculated for the applicable clip gage location using the equations of Saxena and Hudak [159]. The stress intensity is then calculated from the crack length and displacement. The K-calibration expression [159] (applicable for 0.20 < a/W < 0.8, where W is the length of specimen ahead of the loading line) is:

$$\frac{K}{P}BW^{\frac{1}{2}} = \frac{2 + a/W}{(1 + a/W)^{3/2}} \left\{ 0.8072 + 8.858 \left(\frac{a}{W}\right) - 30.23 \left(\frac{a}{W}\right)^2 + 41.088 \left(\frac{a}{W}\right)^3 - 24.15 \left(\frac{a}{W}\right)^4 + 4.951 \left(\frac{a}{W}\right)^5 \right\} \quad (4-2).$$

The resulting K values are in good agreement with K's calculated using the equations of Nowak and Rolfe [155].

The specimens are pre-loaded at room temperature in air to an initial opening, δ_i. Most specimens are exposed to 4 Pa of iodine carried in a high purity argon gas stream at 300°C. Exposure times vary from 46 to 284 hours. Propagation of the stress corrosion cracks is monitored visually; however, crack velocities are not measured. Most tests are not terminated until several days after propagation of the crack has apparently stopped. This should be sufficient to achieve slow crack growth (Region I behavior) and subsequent crack arrest. Upon termination of the test, the specimen is removed from the test chamber and is washed in methanol to remove most zirconium iodide reaction product. The final opening, δ_f, is determined from measurements before and after unloading of the specimen similar to the procedure for initial loading of the specimen. The final opening is less than the initial opening due to stress relaxation in the arms of the DCB and WOL specimens. The relaxation does not affect calculation of the final K value since the final opening value, δ_f, is accurately determined. The beam relaxation and possible crack closure effects are discussed in Appendix D.

Fracture surfaces are opened by loading to failure or by extending the crack by fatigue. Crack lengths are measured along the specimen edges and at the center of the crack front by a traveling microscope accurate to ±0.005 mm. The values of crack length, a, for Eqs. (4-1) and (4-2) represent an average of the above measurements when crack bowing is present.

In several DCB specimens of recrystallized material, the fatigue pre-crack did not remain in the plane of loading. The subsequent stress corrosion cracks propagate normal to the loading direction

in the proper plane. To insure that accurate K values are calculated for these specimens, the equations of Mostovoy et al. [159] are used to account for DCB arms of unequal height. This corresponds to a more general form of Eq. (4-1). The results for these specimens agree with the results of specimens with equal arm heights.

The SCC fracture surfaces are examined optically at low magnification and by scanning electron microscopy (SEM) at high magnification. Fracture appearance in the SEM is analyzed in terms of texture, microstructure, and heat treatment.

4.2 Tube Pressurization Tests

4.2.1 Equipment

Internal gas pressurization SCC tests are performed with the test system shown schematically in Fig. 4.3. A complete description with photographs and detailed operating instructions is presented in Appendix E. High purity (>99.999%) argon is pumped into a reservoir using a compressed air driven gas booster pump. System capability is approximately 76 MPa (11,000 psi). The closed end loading gives a hoop to axial stress ratio of two to one. Results are reported as applied hoop stress.

Specimens are ∿15 cm long with a ∿5 cm gage section where ∿0.25 mm is removed from the tube OD decreasing the hoop stress ∿17%. Prior to testing, all specimens are cleaned with methanol and dried. Circumferential scribe lines are placed at three OD locations on the reduced section and carefully measured by a micrometer accurate to ±0.0025 mm. The ID and OD away from the gage section are also measured.

4.2.2   Procedures

Specimen assembly involves a series of steps. The rear end plug is inserted and the end is sealed by a Swagelok end cap. For SCC tests, 10 ±1 mg of reagent grade iodine crystals (>99.8%) are weighed on an analytical balance and placed inside the tubing specimen with a two segment volume displacing mandrel of Zircaloy rod. This quantity of iodine corresponds to approximately 1×10^{-4} gm/cm^2 which is in the middle of iodine concentration ranges considered by other investigators, Table 2.1. The front end plug is inserted and the front end sealed to a Swagelok fitting. Exploded and assembled views of the specimen are shown in Appendix E. The assembly is then connected to the pressurization system and purged of residual air and water vapor by repeated low pressure pressurization and venting (8-10 times). A thick walled pipe encloses the specimen assembly for safety reasons. An argon cover gas (>99.7% purity) is flowed through the chamber to minimize oxidation of the specimen OD. Temperature is monitored and controlled by a Chromel/Alumel thermocouple which touches the specimen at approximately the center of the gage section. Heatup time is ordinarily 180 min. When the test temperature is reached, the specimen is pressurized from the reservoir by bleeding the argon gas through a micrometering valve while pressure is monitored by an in-line pressure transducer. Stress is calculated from the formula:

$$\sigma = \frac{D_{ID}^2 + D_{OD}^2}{D_{OD}^2 - D_{ID}^2} \, p \qquad (4\text{-}3)$$

where D_{ID} and D_{OD} are the ID and OD diameters, respectively, and p is the

pressure inside the specimen. Time is monitored by a timer which is shut

off by specimen failure. After the failed specimen cools, it is

disassembled and the internal mandrels are removed. The specimen is

cleaned with methanol and D_{ID} and D_{OD} values are measured at the location

of failure and at the scribe lines.

One gas pressurization test is used to expose unstressed

cladding segments to the same environment encountered by the cladding ID.

The purpose is to identify the surface sites most susceptible to iodine

attack by analyzing the same surface locations before and after iodine

exposure. Four cladding segments $\sim$1.3 cm in length are loaded into an

internal gas pressurization test specimen with iodine. The samples are

from Supplier A and B tubes in both AR and AR + P surface conditions.

The ID surface of each specimen is marked with a small punch indentation

and examined near that point by SEM prior to exposure. The specimen

reaches 320°C in 115 min and is held at this temperature and low argon

pressure for 180 min. The clad segments are then removed, cleaned, and

examined by SEM near the mark location.

4.2.3   Examination of Failed Specimens

Several techniques are used to examine a representative

sample of failed SCC specimens. An 1.0-1.5 cm long annular section of

tubing which contains the crack is cut from the remainder of the specimen.

This ring is sectioned axially to give two half circular arcs, one

containing the through wall crack at the bottom of the arc. An SEM

photomontage of the ID surface of the crack is made, typically at 100X

magnification. The specimen is then broken open at liquid nitrogen

temperature to reveal the fracture surface. Macrophotographs of the through wall crack are taken at 40X. SEM examination of the crack surface identifies the fracture features. For selected specimens a 1000X photo-montage is taken across the fracture face from the ID to the end of the SCC region near the OD. During all SEM evaluations features of interest are frequently examined at higher magnification. The half circular ring opposite from the main crack is sectioned in the tangential plane, mounted, and polished metallographically to expose the tube wall directly opposite from the crack. The circumference along the tube ID is carefully analyzed at 500X and 1000X for incipient cracks which are counted and measured for depth of penetration into the tube wall. In several cases, an entire tube cross-section away from the crack but still in the reduced section, is evaluated metallographically.

4.3   Split Ring Tests

Three separate sets of tests are done on the split ring design. The initial specimen design involves a $\sim$1.3 cm length of cladding with a gap of 10.54 mm (0.415 in). The expression for maximum stress at the cladding ID is derived from mechanics principles and is verified by strain gage measurements which are given in Appendix F. The maximum stress is:

$$\sigma_{max} = \frac{0.79 \; Et\delta}{D_m^2} \qquad (4-4)$$

The terms are defined in Eqn. (3-6). Some specimens are scratched with a sharp scribe. All tests are performed in the apparatus used for the crack arrest tests. The specimen remains outside the hot zone during

heat-up and purging with the Ar+I$_2$ gas stream. After the temperature is stabilized, the sample is pulled into the hot zone to commence the test. After a predetermined period of time, the specimen is removed and examined for cracks visually and in the SEM for some specimens.

The first and second sets of experiments test the lot 1340 tubing material. The first set of tests is constant deflection. The temperature range is 300°-350°C, and the iodine partial pressure is 4 or 40 Pa. The second set of tests is constant load run in the loading fixture shown in Fig. 4.4. The fixture is Zircaloy and the spring is Type 302 stainless steel with an impervious gold coating. The temperature is 325°C, and the iodine partial pressure is 40 Pa.

The third set of split ring tests is done on Suppliers A and B cladding. Cladding segments ∿1.3 cm long are slit axially with a 1.6 mm wide slow speed cut-off wheel. A Zircaloy wedge is pressed into the narrow slot to give the desired opening, δ. The maximum tensile stress occurs at the clad ID opposite the wedge. The hoop stress is calculated by:

$$\sigma_{max} = \frac{4Et\delta}{3\pi(1-\nu^2)D_m^0 D_m^1} \tag{4-5}$$

where the terms are defined for Eqn. (3-6). The equation differs from Eqn. (4-4) because the slot size is much smaller. It is also predicted by the method developed in Appendix F. The iodine partial pressure is 4 Pa, and test temperatures of 300°C and 320°C are used.
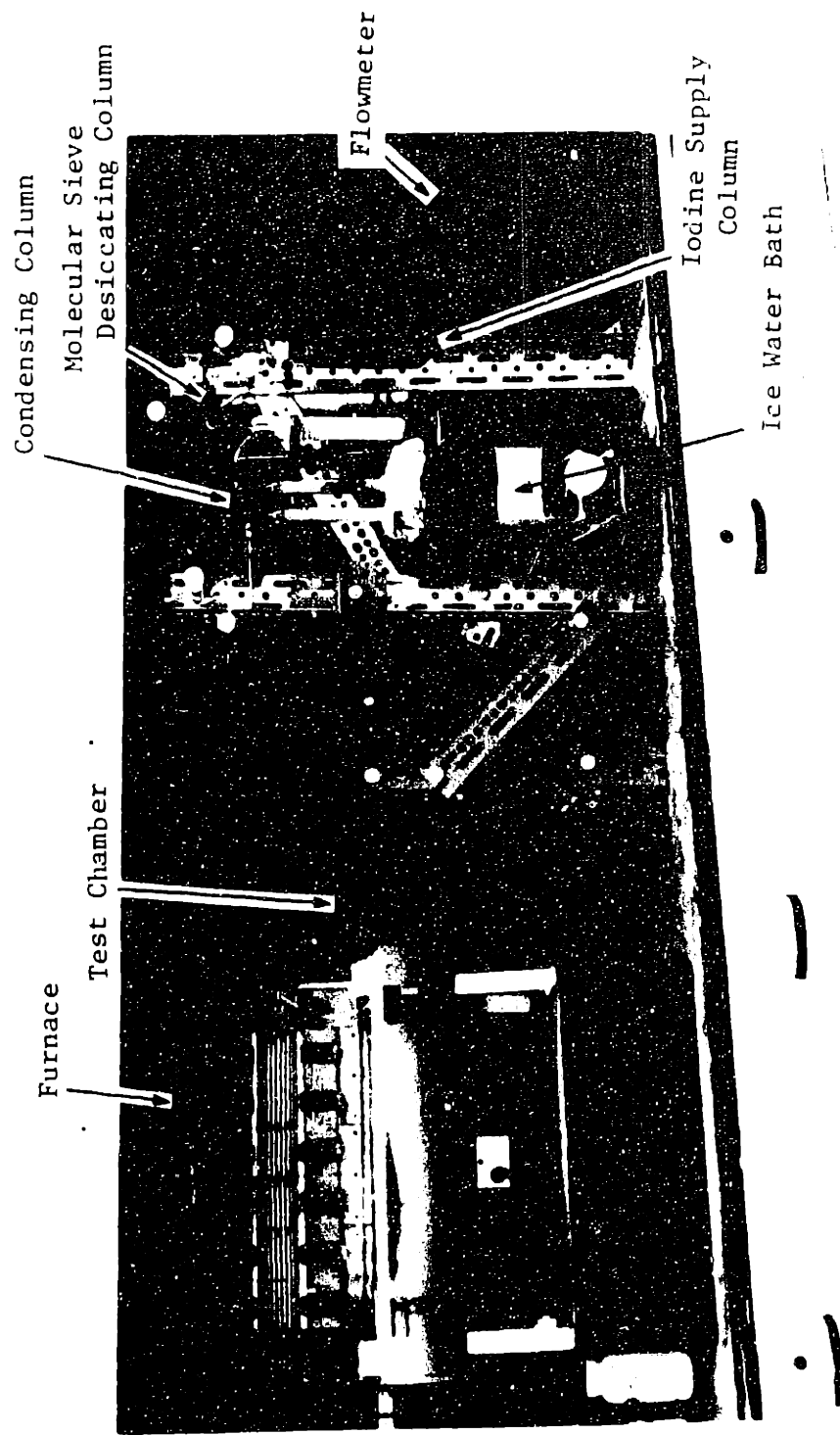
Figure 4.1   Controlled Atmosphere System for Tests in a Flowing Ar + I_2 Environment

Figure 4.2.   Drawings of Fracture Mechanics Specimens
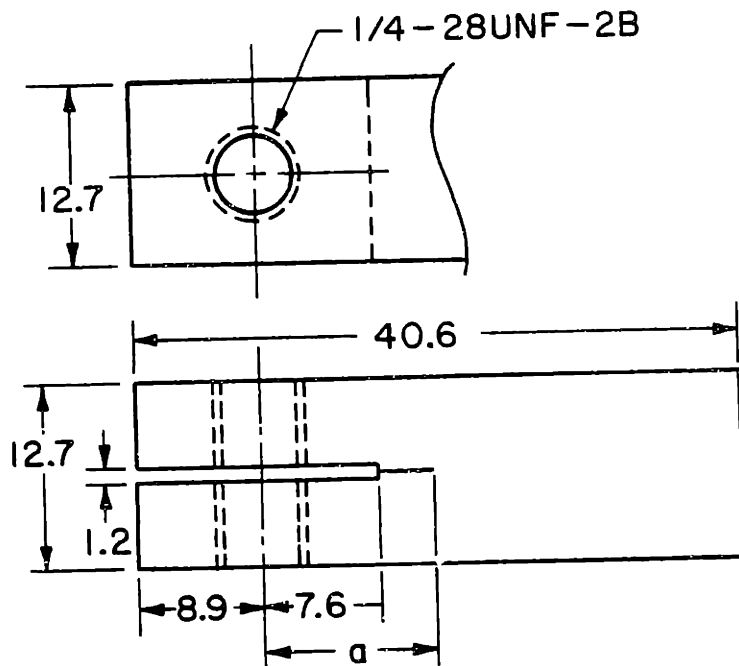
a) Bolt loaded double cantilever beam (DCB) specimen
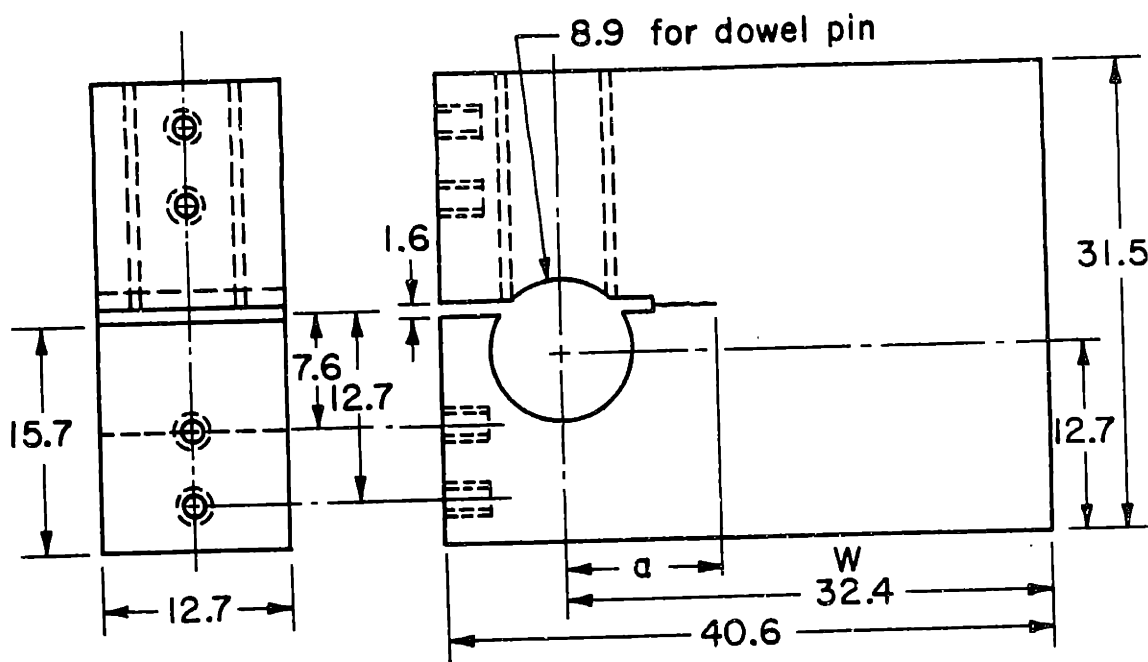
b) Bolt loaded wedge opening load (WOL) specimen
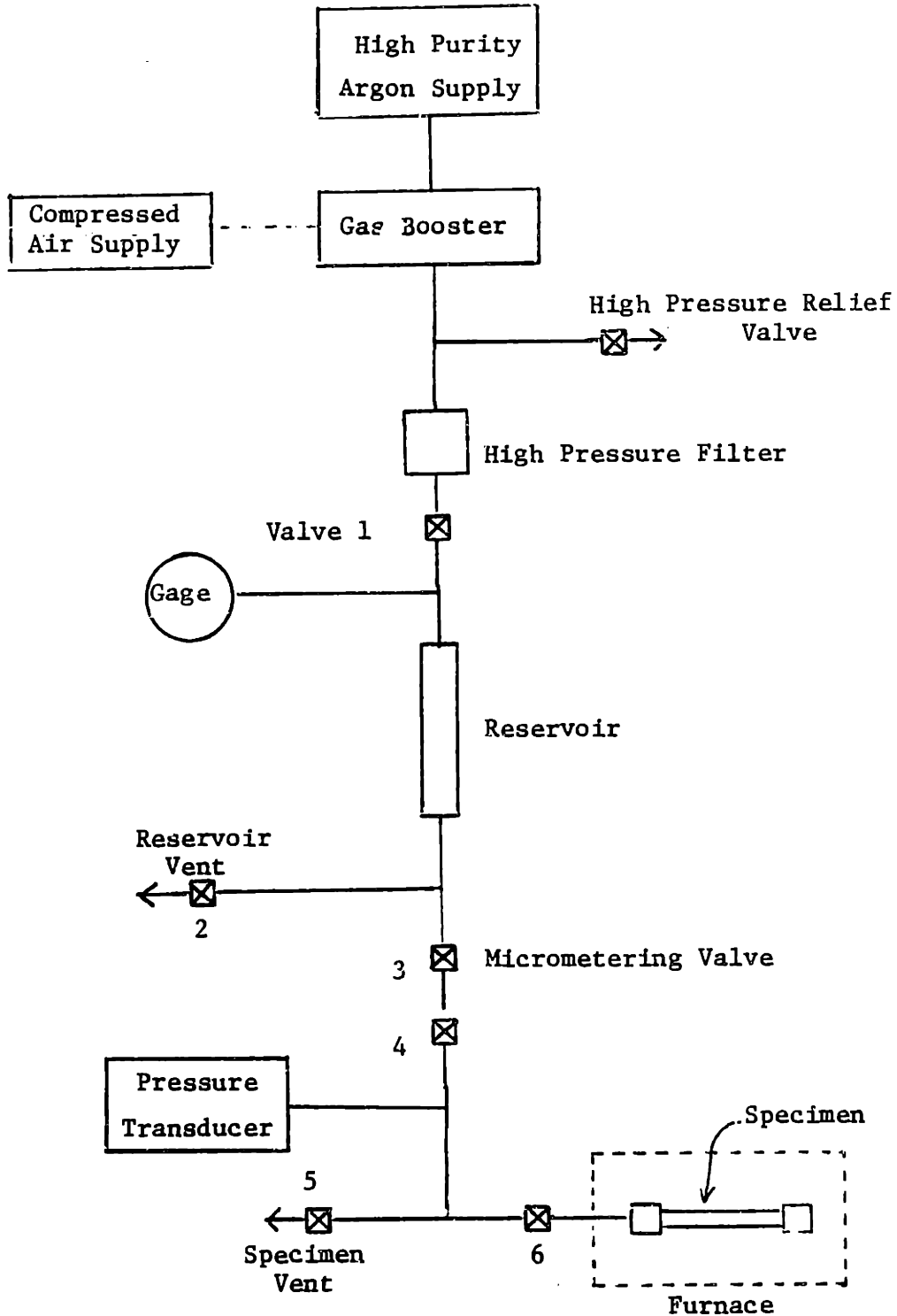
Schematic Drawing of Tube Pressurization Facility

Figure 4.3
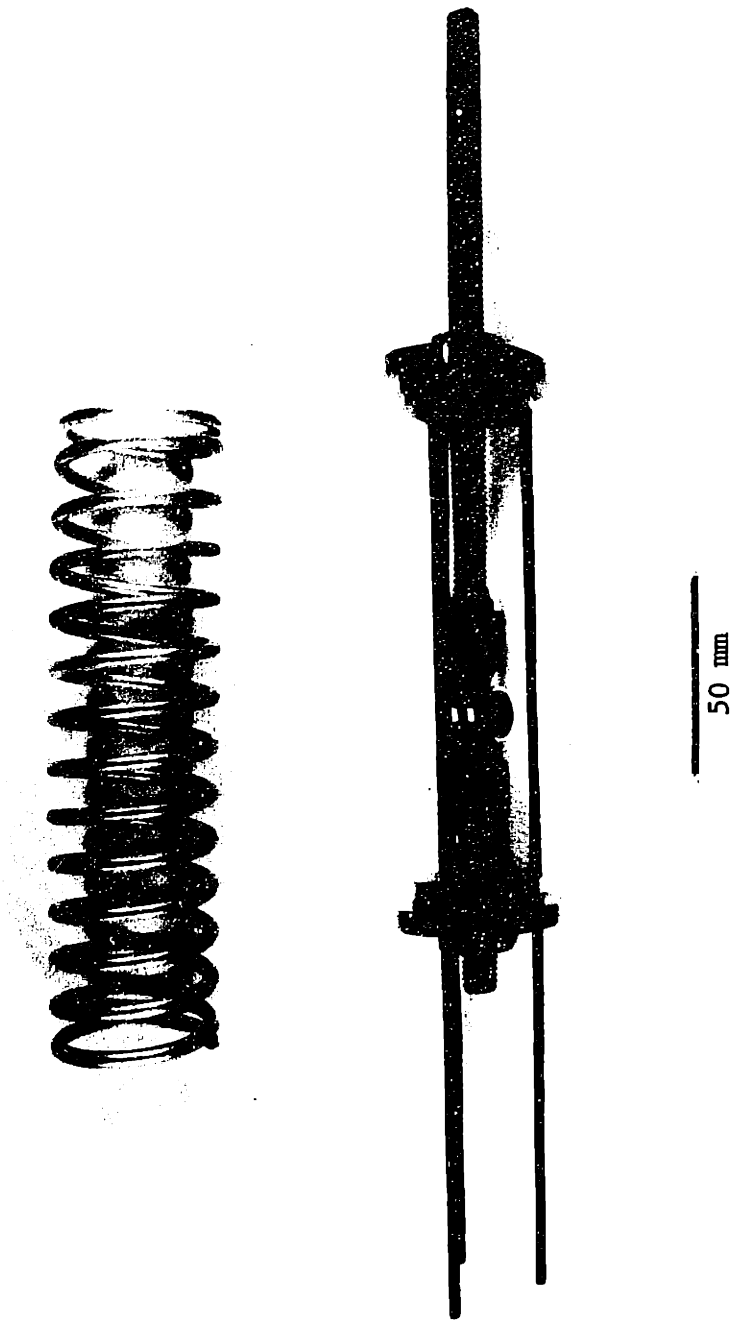
Figure 4.4   Constant Stress Zircaloy Loading Fixture with Specimen and Gold Coated
Stainless Steel Spring

5. PLAN OF WORK

5.1 Crack Arrest Tests

The purpose of the crack arrest tests is to study the iodine SCC propagation behavior of Zircaloy under conditions where complications due to crack initiation are absent and stress and stress intensity fields ahead of the crack front are well defined. By appropriate choice of plate texture, specimen orientation, and heat treatment, both the texture and microstructure ahead of the propagating crack are controlled and their effects studied in a systematic manner.

The fracture mechanics specimens are machined from different orientations in the plate as shown schematically in Fig. 5.1. In the designation of orientation, the first letter gives the direction of specimen loading (i.e. crack opening) while the second letter indicates the direction of crack growth, e.g. an NT specimen is loaded in the normal direction with crack propagation in the transverse direction.

From Fig. 5.1 it is evident that four specimen orientations are possible. Four plates are considered as introduced in Section 3.2. The test matrix for the crack arrest test is:

	NL	NT	TL	LT
0°-SR	(2)	X	X	
0°-RX	(2)	(2)	X	
±40°-SR	X	X	(3)	X
±40°-RX		(3)	X	

Numbers in parenthesis indicate the number of specimens from a given plate and orientation greater than one. DCB specimens are used in NL,

NT, and some TL orientations. WOL specimens are used for LT and some TL orientations.

5.2 Tube Pressurization Tests

Fig. 5.2 shows the test matrix for the internal gas pressurization tests. The test matrix is designed to isolate the effects of the following materials variables on SCC behavior: surface condition, heat treatment which influences the strength and residual stress, and crystallographic texture. For each material condition, AR, AR+P, SR+P, and H+SR+P, from two to seven specimens are tested to develop a stress versus time to failure curve for each material condition of each supplier which extends from the short time rupture strength to a "threshold" stress where time to failure is at least one day and is often several days. All tests are done at 320°C.

Fig. 5.3 gives a test matrix where tubing wall thickness is the key variable. Tests at a given condition (nominal wall thickness/ nominal stress and supplier) are done in duplicate. The nominal stresses as chosen to give short times to failure (<2 hr) and long times to failure (>12 hr) for the "high" and "low" stresses, respectively.

Finally, four tests are run at 390°C rather than 320°C. The material condition depends on what specimens are available. Stresses are chosen to give "short" and "long" times to failure.
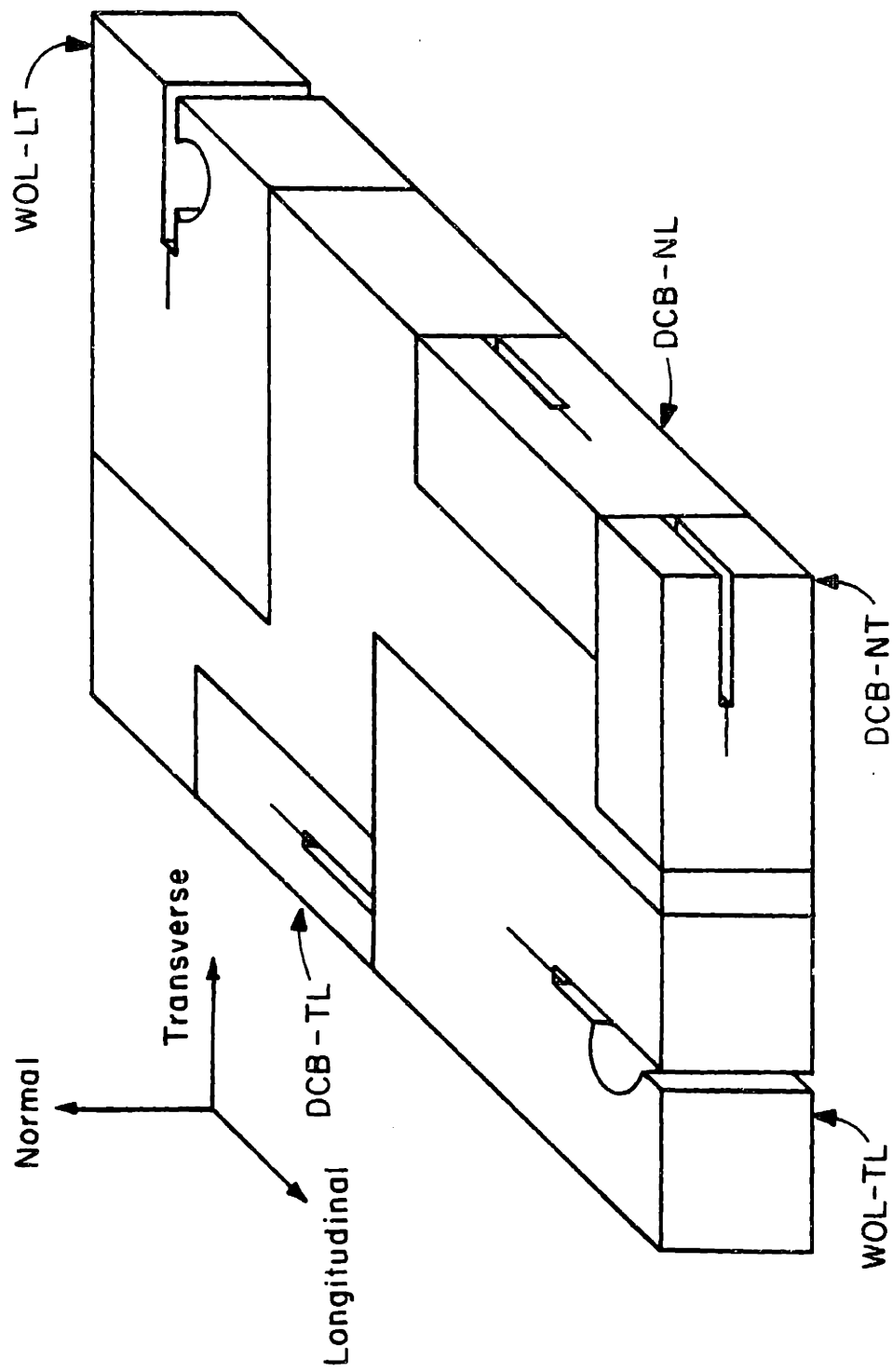
Orientations and Designations of Fracture Mechanics Specimens
Figure 5.1

Figure 5.2

TEST MATRIX FOR ZIRCALOY-2 TUBING

HEAT TREATMENT
(STRENGTH, RESIDUAL STRESS)
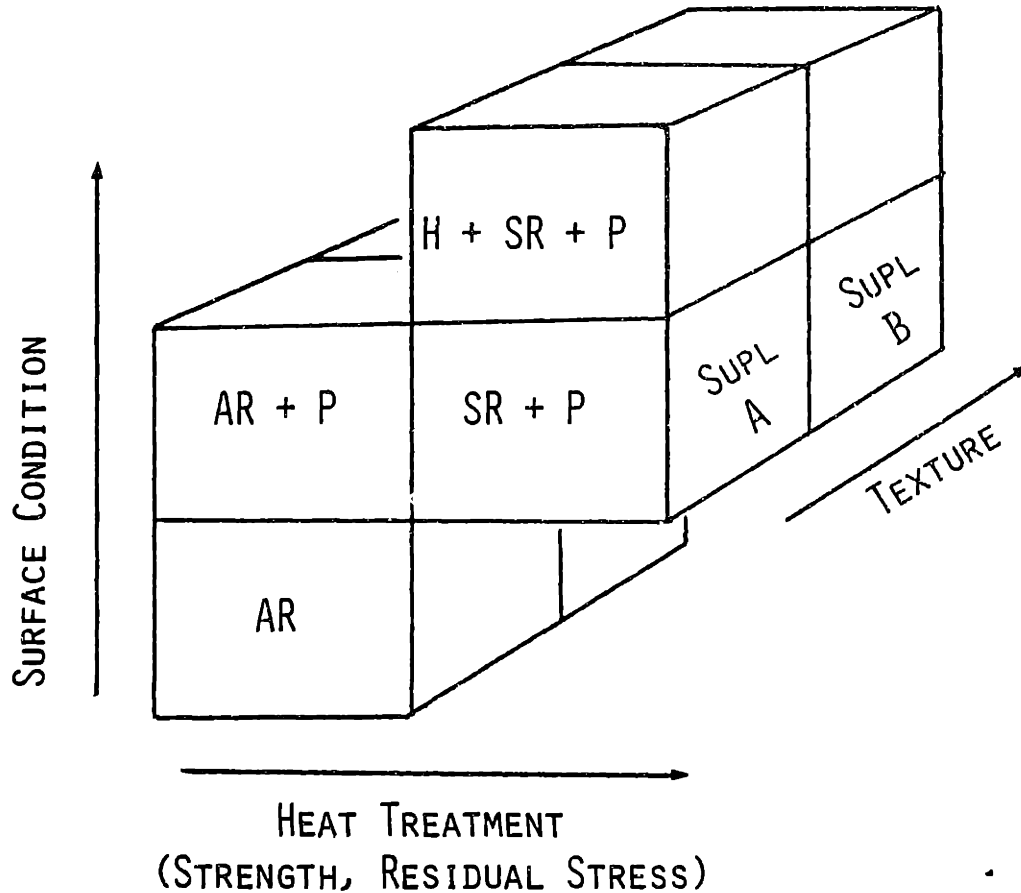
AR = AS-RECEIVED

P = PICKLED, 37-50 MICRONS REMOVED
FROM TUBE ID

SR = STRESS-RELIEVED AT 500°C/2 HR

H = HONED WITH COARSE GRIT, ~13 MICRONS
REMOVED FROM TUBE ID

TEST TYPE : INTERNAL GAS PRESSURIZATION
TEST TEMPERATURE : 320°C

Figure 5.3

TEST MATRIX FOR VARIABLE WALL THICKNESS SPECIMENS
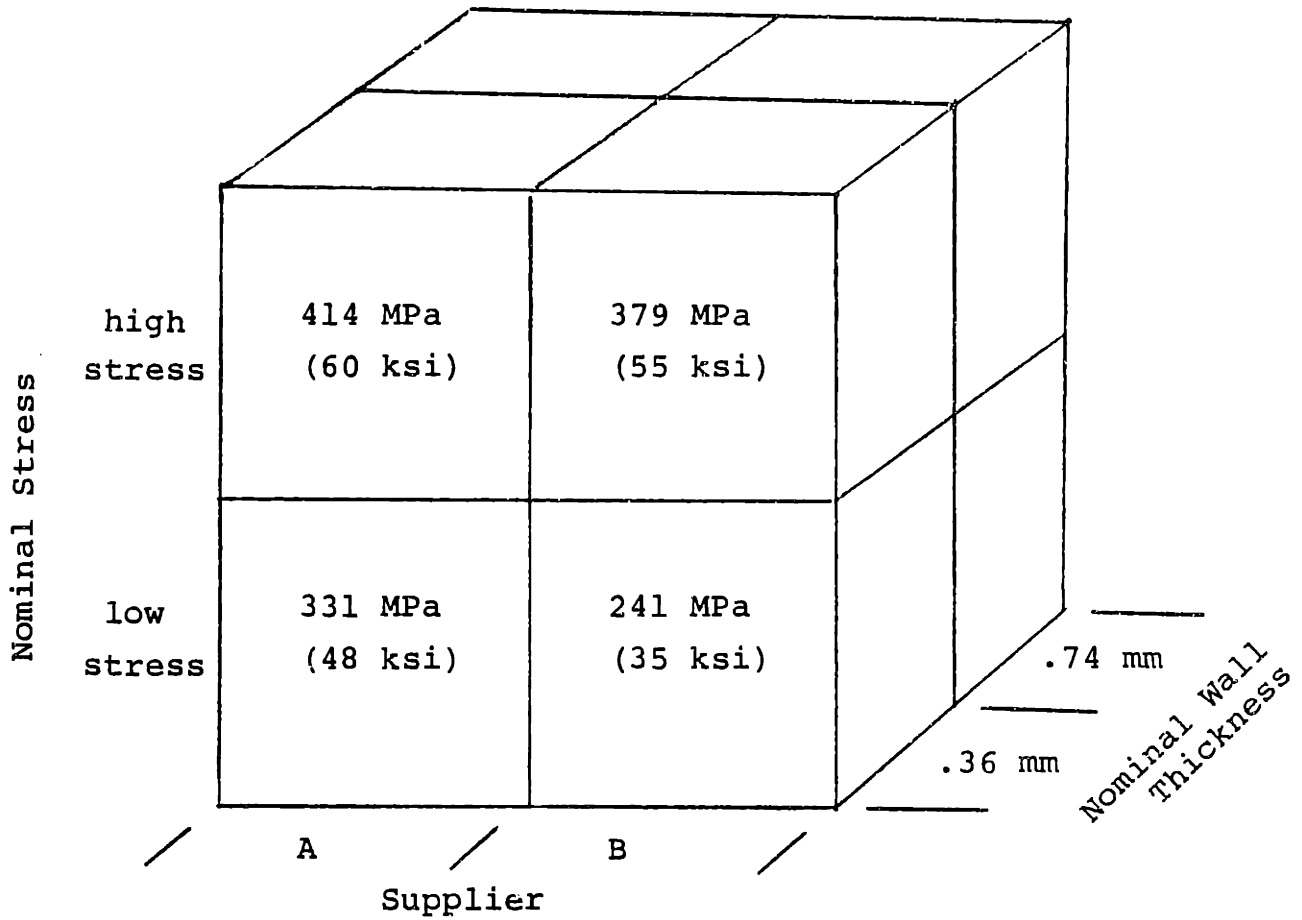
Material Condition: SR + P

Test Temperature: 320°C

6. RESULTS

6.1 Crack Arrest Tests

6.1.1 $K_{I_{SCC}}$ Behavior

The K values at crack arrest, K_f, are given in Table 6.1.
No crack propagation occurs below K_f so this quantity is termed $K_{I_{SCC}}$.
It is plotted against the texture parameter f in Fig. 6.1, and the data
are listed in Table 6.2. The f-parameter is measured along the direction
of crack opening, thus the pertinent f for various specimen orientations
sketched in Fig. 5.1 is:

$$f = \begin{cases} f_N & \text{for NL and NT} \\ f_T & \text{for TL} \\ f_A & \text{for LT} \end{cases} \qquad (6\text{--}1)$$

6.1.2 Fractography

An important complement to the $K_{I_{SCC}}$ versus f behavior is the
fractography from various specimen orientations. Fig. 6.2 shows macro-
photographs from three of the four possible orientations: NL, LT, and
TL, for stress-relieved material. Fractography from the NT specimens is
very similar to the NL. The following three figures present SEM fracto-
graphs for each specimen orientation at higher magnification:

- o Fig. 6.3 - DCB-NL specimen;

- o Fig. 6.4 - WOL-LT specimen;

- o Fig. 6.5 - WOL-TL specimen.

The fracture surface for recrystallized material is shown for a NL orientation in Fig. 6.6.

Examples of the fluting [108] are also observed. Figs. 6.7 and 6.8 present fluting fractographs observed in the SCC and ductile regions, respectively.

All fractographs are chosen because they are demonstrative of the behavior for a particular specimen orientation and/or are representative of features seen in a particular class of specimens, e.g. stress-relieved versus recrystallized. The Discussion section relates the $K_{I_{SCC}}$ versus f relationship to the fracture features in terms of texture, crack velocity, and microstructure.

6.2 Tube Pressurization Tests

6.2.1 Burst and Creep Rupture

Ramp to failure and creep rupture results are listed in Table 6.3. Ramp tests take 3-5 minutes to complete. Burst strength represents the ultimate tensile strength of the material and is calculated by Eqn. (4-3) from diameter values measured adjacent to the failure location to minimize the influence of local strain in the region of tube rupture. Creep rupture tests (stress versus time to failure) are done prior to any iodine tests in the test system. The data are plotted on Figs. 6.9 and 6.10 for comparison with the iodine SCC results of suppliers A and B, respectively. The error bars have two sources: slight pressure fluctuation due to leaks at fittings and dimensional changes due to cladding creep. Uniform strain represents the maximum strain in the gage section

away from the failure location which has a large amount of local strain associated with the penetration of the tubing wall.

6.2.2   Iodine SCC

The stress versus time to failure results for the text matrix in Fig. 5.2 are presented in Figs. 6.9-6.11. The data are tabulated in Table 6.4. Data for all material conditions of Supplier A and B cladding are presented in Figs. 6.9 and 6.10, respectively, with burst and creep rupture results included for comparison. Fig. 6.11 compares the stress/ time to failure data for the AR condition of both suppliers. Curves for the tests at SRI International [111] performed on the same tubing at the same temperature and with the same type of test, but with a larger quantity of iodine (250 mg I_2 versus 10 mg I_2 in the present tests) are also shown.

Strain in percent is defined as:

$$\epsilon = \frac{D_{OD}^f - D_{OD}^i}{D_{OD}^i} \times 100 \tag{6-2}$$

where D_{OD}^f and D_{OD}^i are the final and initial outside diameters, respectively. They are measured at the same location on the specimen corresponding to the location of failure if no local ductility increase occurs and at a location near the failure if any ballooning is present. Accuracy is judged to be ±0.03% except when tube ovality is present which lowers accuracy to ±0.05%. The average strain rate is calculated as:

$$\dot{\epsilon}_{avg} = \frac{\epsilon}{t_f} \tag{6-3}$$

Figs. 6.12 and 6.13 present ε and $\dot{\varepsilon}_{avg}$ versus t_f, respectively. Data from all material conditions of both suppliers are included.

The results for the variable tube wall thickness test matrix shown in Fig. 5.5 are tabulated in Table 6.5. Data for the four tests at 390°C are presented in Table 6.6.

6.2.3   Failure Examination

6.2.3.1   Sample Plan

The sampling scheme for the iodine SCC tests is shown in Fig. 6.14. The tests, arranged by supplier and surface condition, are listed by stress. All examinations are indicated in a shorthand code next to the specimen. Due to the large number of failed SCC specimens, it is not feasible to examine every specimen. The alternate approach is to design a sampling matrix emphasizing the following comparisons:

- specimens from the same supplier with the same material condition at high stress (short time to failure) and low stress (long time to failure);

- specimens from the same supplier with different material conditions at approximately the same stress; emphasis is placed on AR and SR + P conditions since σ versus t_f behavior differs the most within one supplier (see Figs. 6.9 and 6.10);

- a stress level of $\sim$340 MPa ($\sim$50 ksi) which is common to both suppliers and all material conditions;

- analysis of anomalous samples such as fractures outside the specimen reduced section (A-6, A-24, B-13, and B-19)

and duplicate specimens with different times and strains at

failure (A-22, A-24).

The presentation of fractographic results utilizes the matrix in Fig. 6.14.

Emphasis is given to fracture features common to most samples.

6.2.3.2   Fractography

The ID surface of a through wall crack from specimen A-27 is

shown in Fig. 6.15(a). Several features should be noted. Below the

main crack, a large secondary crack (A) and smaller secondary cracks (B)

away from the primary cracks are observed. The region of different

contrast at the opposite end of the main crack (labeled C) is shown at

higher magnification in Fig. 6.15(b) to be composed of many small cracks.

The crack opening at the tube ID varies with stress and

plastic strain. This effect is quanitified by defining a crack opening

angle (COA) as:

$$COA = \tan^{-1} \left(\frac{ID \ surface \ opening}{wall \ thickness}\right) \qquad (6\text{-}4)$$

Since COA is calculated for through wall cracks, its usefulness as a

fracture mechanics parameter is limited. It is intended to be used to

compare the plastic contribution to crack opening for many tests on the

same basis. The formula is applicable to specimens where at least 75%

of the through wall propagation is SCC, and where the crack penetrated

the tube OD by either a pinhole or tight slit, i.e. the ID opening is

much larger than the OD opening. Tests at the highest stress (>440 MPa)

do not meet these criteria. COA is plotted against stress in Fig. 6.16.

An attempt to plot COA versus plastic strain at failure gives significantly greater data scatter.

At stresses above 350 MPa, many ID surface secondary cracks beyond the ends of the main crack are observed. The main crack has a thumbnail shape as shown in Fig. 6.17(a). Below 350 MPa secondary cracking is much less prevalent, and the crack shape as seen in Fig. 6.17(b) is best represented by a partial ellipse with the maximum crack length, 2c, located at a depth one-quarter to one-third of the wall thickness. Although supplier A specimens are used as examples, the observations apply equally to supplier B cladding.

Fracture surfaces are presented in Figs. 6.18-6.20 for samples A-27, B-12, and B-28, respectively. The photomontages are taken near the center of the crack and extend from the ID to approximately the end of the SCC region near the OD. The fracture appearance depends more on the stress level than on the time to failure. Samples A-27 and B-12 are typical of the high stress (345 MPa) failures while sample B-28 is representative of low stress (221 MPa) failures.

6.2.3.3 Metallography

The specimens examined by metallographic cross-section for tests at 320°C are indicated in the sample plan of Fig. 6.14. Specimens tested at 390°C, Table 6.6 are also examined. The cracks in each cross-section are counted and their depths are measured. The results are presented as histograms in Figs. 6.21 and 6.22 for the 320°C and 390°C specimens, respectively. Fig. 6.23 shows several cracks from 390°C test specimens. The short cracks (<5 μm) in Figs. 6.23(a) and (c) are straight and propagate normal to the hoop stress. The direction of crack

propagation is radial on the macroscopic scale for deeper cracks (>10 μm), but a crack changes direction during propagation on the microscopic (i.e. grain to grain) scale. This behavior is more pronounced in supplier A, Fig. 6.23(b), than in supplier B, Fig. 6.23(d). The long cracks (>40 μm) in supplier A tubing are branched. The supplier A cracks exhibit more crack opening than cracks in supplier B cladding consistent with the COA results in Fig. 6.16.

6.3 Split Ring Tests

6.3.1 Lot 1340 Material

The split ring test results under both constant deflection and constant load conditions are reported in Table 6.7. The severity of the test conditions increases with subsequent tests by the introduction of notches, use of the constant load fixture which reduces the stress-relaxation, and the presence of iron which is reported to be a "catalyst" for iodine SCC [82]. No failures or incipient cracks are detected under any conditions. Iodine attack is found in specimens examined by SEM. Creep plastic strain is accumulated in the surface layer of all specimens.

6.3.2 Supplier A and Supplier B Materials

Several constant deflection split ring tests are performed. The purposes are: 1) to determine if the lot 1340 split ring specimens did not fail due to inherent SCC resistance of the material or due to experimental factors such as stress relaxation in the specimens, and 2) to initiate cracks for subsequent SEM characterization. The test

conditions and results are listed in Table 6.8. No specimens failed by
through wall cracking, however, microcracks are observed in supplier B
specimens, Fig. 6.24, but not in supplier A specimens.

Table 6.1

Results of SCC Crack Propagation Tests Using Fracture Mechanics Specimens

Specimen (1)	P_{I_2} (Pa)	T (°C)	Time of I_2 Exposure (hrs)	Length of SCC on Specimen (mm)	Initial δ_i (mm)	Initial K_i (MPa√m)	Final δ_f (mm)	Final K_f (MPa√m)	$\dfrac{\delta_f}{\delta_i}$
Stress-Relieved									
9912-SR-WOL-LT-1	40	325	46	–	.502	34.6	.381	–	.76
9908-3A-DCB-TL-25	4	300	257	.15	.386	23.2	.292	17.3	.76
9912-SR-DCB-T1-17	4	300	261	2.90	.282	23.6	.165	9.8	.59
9912-SR-WOL-TL-2	4	300	209	1.70	.369	27.9	.267	14.6	.72
9912-SR-WOL-TL-3	4	300	261	5.08	.357	28.9	.236	15.7	.66
9912-SR-DCB-NL-2	4	300	115	7.52	.305	20.1	.122	4.0	.40
9912-SR-DCB-NT-15	4	300	281	8.53	.241	15.0	.178	4.6	.74
9908-3A-DCB-NL-4	4	300	113	14.35	.381	28.2	.203	4.6	.53
9908-3A-DCB-NL-11	4	300	255	6.81	.292	16.7	.208	6.8	.71
9908-3A-DCB-NT-12	4	300	255	13.49	.292	16.1	.155	3.5	.53
Recrystallized									
9908-3B-DCB-TL-23	4	300	284	0	.340	22.4	.175	11.6	.51
9912-RX-DCB-TL-21	4	300	284	<.25	.516	29.8	.213	12.3	.41
9912-RX-DCB-NT-19	4	300	264	4.88	.384	22.6	.196	7.0	.51
9912-RX-DCB-NT-20	4	300	284	1.83	.292	23.1	.183	7.7	.63
9912-RX-DCB-NT-24	4	300	257	3.53	.343	22.1	.180	7.5	.52
9908-3B-DCB-NL-7	4	300	190	8.84	.480	30.7	.137	4.7	.29
9908-3B-DCB-NL-5	4	300	115	9.42	.422	27.9	.203	6.4	.48
9908-3B-DCB-NT-18	4	300	264	6.17	.366	24.6	.175	6.5	.48
9908-3B-DCB-NT-22	4	300	284	4.83	.351	20.1	.190	5.9	.54

(1) Specimen designation

```
9912 - SR - DCB - NL - 1
                      └─ specimen number
                └─ specimen orientation, see Fig. 5.1
          └─ specimen design; DCB = double cantilever beam, WOL = wedge opening load
     └─ heat treatment:  SR=485°C/4 hrs; RX=625°C/4 hrs; 3A=497°C/4 hrs; 3B=567°C/2 hrs.
└─ plate type:  9912 is Zircaloy-4 with a ±40° texture, 9908 is Zircaloy-2 with a 0° texture;
                see Figs. 3.1 and 3.2 and Appendix B.
```

Table 6.2

$\underline{K_{I_{SCC}}}$ versus Texture Number, f, for Stress-Relieved

and Recrystallized Materials

Specimen	f	Value or Range $K_{I_{SCC}}$ (MPa$\sqrt{m}$)
Stress-relieved		
9908-3A-DCB-TL-25	0.19	17.3
9912-SR-DCB-TL-17	0.33	9.8
9912-SR-WOL-TL-2	0.33	14.6
9912-SR-WOL-TL-3	0.33	15.7
9912-SR-DCB-NL-2	0.56	4.0
9912-SR-DCB-NT-15	0.56	4.6
9908-3A-DCB-NL-4	0.70	4.6
9908-3A-DCB-NL-11	0.70	6.8
9908-3A-DCB-NT-12	0.70	3.5
Recrystallized		
9908-3B-DCB-TL-23	0.21	>22.4
9912-RX-DCB-TL-21	0.32	12.3
9912-RX-DCB-NT-19	0.59	7.0
9912-RX-DCB-NT-20	0.60	7.7
9912-RX-DCB-NT-24	0.59	7.5
9908-3B-DCB-NL-7	0.67	4.7
9908-3B-DCB-NL-5	0.67	6.4
9908-3B-DCB-NT-18	0.67	6.5
9908-3B-DCB-NT-22	0.68	5.9

Table 6.3

Tube Burst and Creep Rupture Data

Supplier	Heat Treatment	Rupture Strength (MPa)	(ksi)	Time to Failure (min)[1]	Uniform Strain(%)
A	AR	527	76.4	ramp	1.8
		540	78.3	ramp	2.2
		465+8	67.5+1.1	384.5	2.9
		441+3	64.0+0.5	3689.5	4.3
		421+14	61.1+2.0	100014.1(nf)	-
	SR	445	64.5	ramp	4.5
		447	64.9	ramp	1.8
B	AR	474	68.7	ramp	0.81
		465	67.5	ramp	1.0
		463	67.2	ramp	-
		432+5	62.7+0.7	138.7	1.4
		416+19	60.4+2.7	10000.0(nf)	-
	SR	443	64.3	ramp	2.3
		465	67.4	ramp	2.5

(1)ramp indicates constant loading (pressurization) rate to failure, duration 3-5 minutes.

(nf)means no failure for specimen.

Table 6.4

IODINE SCC DATA FOR INTERNAL GAS PRESSURIZATION TESTS AT 320°C

Condition[1]	Sample[2]	Stress (MPa)	(K_{si})	Time to Failure (min)	Strain at Failure (%)	Comment
AR	A-12	476	69.1	143.1	1.9	
	A-11	421	61.1	340.7	0.78	
	A-15	345	50.0	634.2	0.53	
	A-17	343	49.8	809.0	0.37	
	A-18	314	45.5	1788.1	0.35	
	A-16	272+5	39.5+0.7	8600	0.37	No failure
AR+P	A-23	474	68.7	108.9	1.14	
	A-19	421	61.0	243.7	0.74	
	A-21	390	56.5	413.1	0.39	
	A-20	349	50.6	2157.4	0.51	
	A-24	333	48.3	1906.6	0.35	Fail ¼" outside reduced section
	A-22	325	47.1	2280.4	0.33+0.03	Fail outside reduced section
SR+P	A-28	423	61.3	287.5	1.9	
	A-26	403	58.5	405.7	1.68	Several cracks penetrate wall
	A-27	345	50.0	1390.4	0.60	
H+SR+P	A-5	366	53.1	140.5	1.0	
	A-6	310	45.0	1141.9	<0.53	Fail outside reduced section
	A-9	292	42.3	2088.0	0.47	
	A-10	276	40.0	5680.0	0.66	
AR	B-10	435	63.1	48.3	0.59	
	B-12	347	50.3	99.7	0.20	
	B-13	283	41.1	276.9	--	Fail $\frac{11}{16}$" outside reduced section
	B-14	277	40.2	261.7	0.14	
	B-15	242	35.1	1098.9	0.09	
	B-16	225	32.6	2067.8	0.07	
	B-18	208	30.2	2715.0	0.10	
	B-19	165	24.0	1463.9	--	Fail near end fitting

Table 6.4 (continued)

Condition[1]	Sample[2]	(MPa)	(ksi)	Time to Failure (min)	Strain at Failure (%)	Comment
AR+P	B-20	413	59.9	75.7	0.43	
	B-21	345	50.1	179.2	0.16	
	B-22	275	39.9	540.6	0.10	
	B-26	220	31.9	2430.0	0.09	
SR+P	B-25	418	60.6	53.1	0.92	
	B-24	345	50.0	217.6	0.32	
	B-27	276	40.0	892.9	0.14	
	B-28	221	32.0	5334.5	0.10	
H+SR+P	B-6	376	54.5	50.1	0.49	
	B-7	310	44.9	426.1	0.20	

Notes

[1] AR = As received

 P = Pickled, 37-50 microns removed

 SR = Stress-received at 500°C for 2 hours

 H = Honed, coarse grit, ~13 microns removed

[2] Samples listed as "A" are Supplier A (Sandvik)

 Samples listed as "B" are Supplier B (Wolverine)

Table 6.5

Iodine SCC Tests for Tubing Specimens with Different Wall Thicknesses

Nominal Stress			Nominal 0.74 mm (29 mil) Wall				Nominal 0.36 mm (14 mil) Wall			
Supplier	(MPa)	(ksi)	Specimen	t_f(min)	$\dot{\varepsilon}$(%)	σ(MPa)	Specimen	t_f(min)	$\dot{\varepsilon}$(%)	σ(MPa)
A	414	60	A-30	108.0	>0.96	412	A-34	23.2	>0.33	421
			A-31	64.3	>1.33	424	A-35	2.3	≥3.2	419
	331	48	A-32	788.3	0.61	334	A-36	891.4	0.50	331
			A-39	1015.5	0.45	338	A-37	928.7	0.74	338
B	379	55	B-29	32.0	0.57	377	B-31	75.4	0.30	383
			B-30	27.6	0.27	379	B-32	105.1	0.28	383
	241	35	B-33	1304.8	<0.08	243	B-36	2132.8	0.11	250
			B-35	1301.1	0.08	240	B-37	892.1	0.20	347

Material Condition: SR+P

Test Temperature: 320°C

Table 6.6

Iodine SCC Tests on Tubing at 390°C

Supplier	Condition	Sample	Stress (MPa)	(ksi)	Time to Failure (min)	Strain at Failure (%)
A	AR	A-33	283	41.0	320.0	1.31
	SR+P	A-38	252	36.6	377.1	1.26
B	AR	B-34	223	32.3	163.0	0.26
	SR+P	B-38	138	20.0	6900(nf)	
			169	24.5	2700(nf)	
			210	30.4	3300(nf)	
			238	34.5	209.8	1.24

Table 6.7

Split Ring Tests for Lot 1340 Zircaloy-2 Tubing in Flowing Iodine Environment

Specimen Number	Type of Test[1]	T(°C)	P_{I_2} (Pa)	Initial Stress[2] (MPa)	(ksi)	Time of Exposure (min)	Final Stress[2] (MPa)	(ksi)	Comment
1	CD	350	40	440	63.8	240	194	28.2	
2	CD	350	40	432	62.6	240	220	31.9	
3	CD	350	40	457	66.3	60	262	38.0	
4	CD	300	4	473	68.6	1440	327	47.4	
5	CD	300	4	583	84.5	3900	256	37.2	Pickle 50μm, .10mm deep notch, wrap specimen in Fe wire
6	CL	325	40	503	73.0	1110	483	70.0	
7	CL	325	40	461	66.8	720	445	64.5	
8	CL	325	40	295	42.8	1200	292	42.3	.20 mm deep notch
9	CL	325	40	469	68.0	2440	463	67.1	.13 mm deep notch
10	CL	325	40	539	78.2	2400	518	75.1	Fe wire placed next to specimen ID surface

(1) CD = constant deflection; CL = constant load

(2) Stress values are based on fully elastic conditions. No corrections are made for yielding or creep.

Table 6.8

Constant Deflection Split Ring Tests in 4 Pa (0.03 torr)

Flowing Iodine Environment

Supplier	Condition	Temperature (°C)	Initial Stress (MPa)	(ksi)	Time of Exposure (min)	Final Stress (MPa)	(ksi)	Microcracks Observed
A	AR	320	374	54.3	300	265	38.5	No
	AR+P	300	379	54.9	360	295	42.8	No
B	AR	320	367	53.3	300	242	35.1	Yes
	AR+P	300	387	56.1	360	284	41.2	Yes
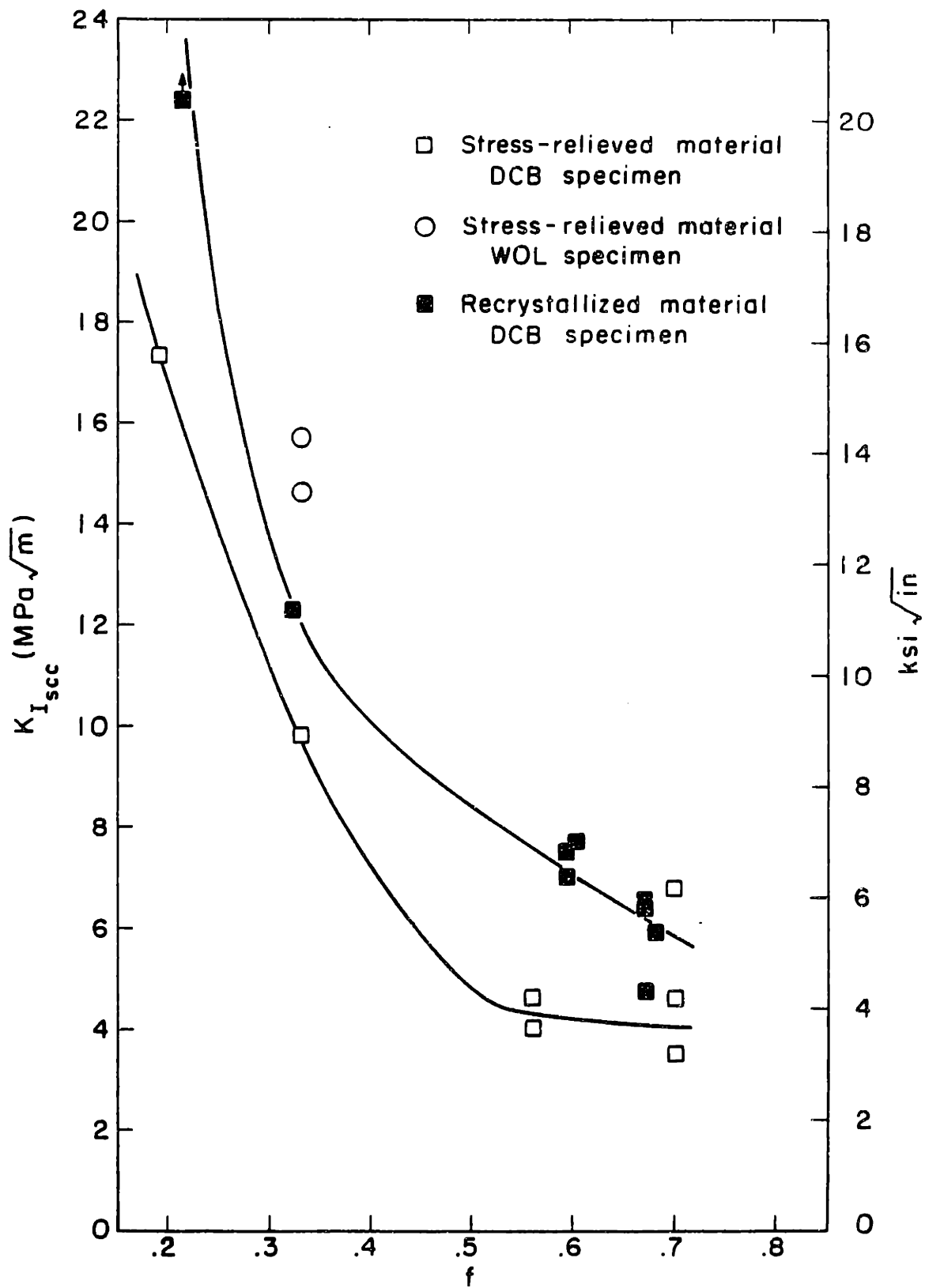
Effect of crystallographic texture on $K_{I_{scc}}$ in Zircaloy

FIG. 6.1
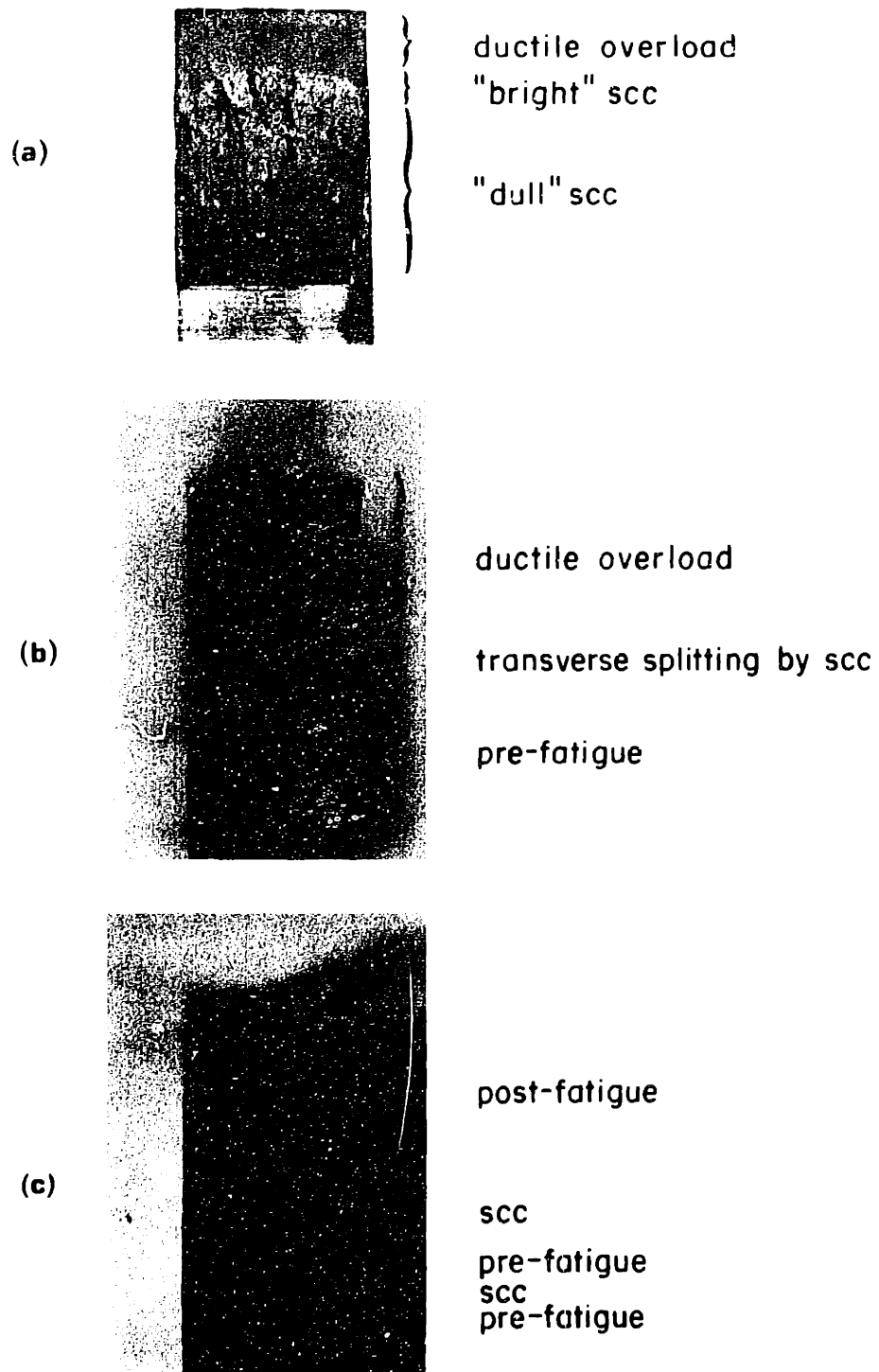
Fig. 6.2   Macrophotographs of SCC specimens.   (a) DCB-NL
showing "bright" and "dull" SCC reaions.
(b) WOL-LT showing transverse splitting.
(c) WOL-TL showing banded SCC region.   Actual
width of all specimens is approximately 12.6 mm.
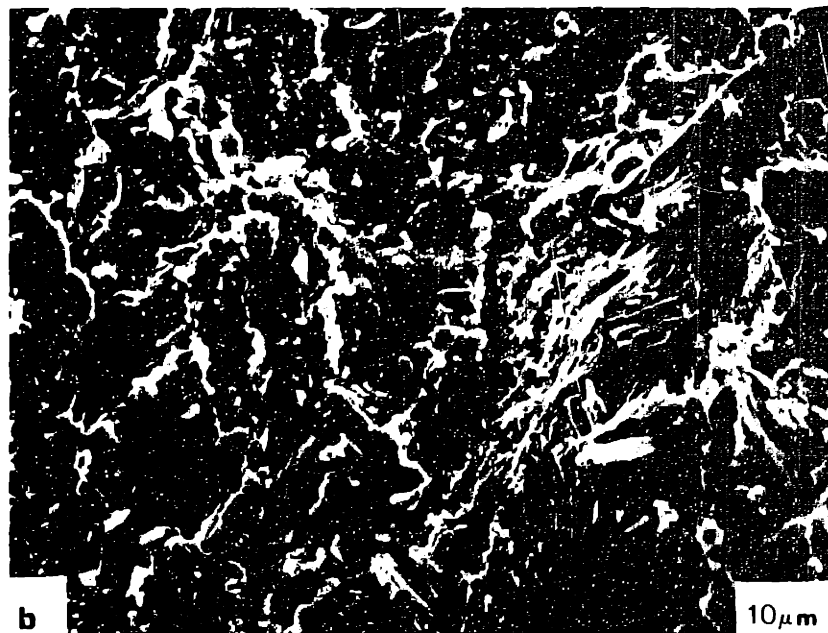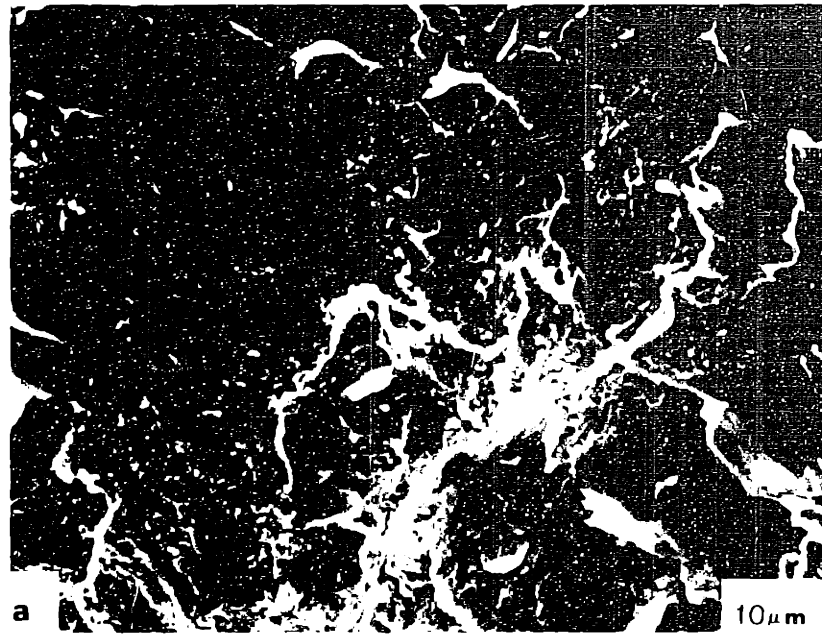
Fig. 6.3   SEM micrographs of DCB-NL specimen of stress-
relieved material showing a) "bright", and
b) "dull" regions of SCC propagation

Fig. 6.4   Low magnification SEM micrograph of WOL-LT
            specimen showing end of pre-fatigue region and
            SCC-induced transverse splitting.
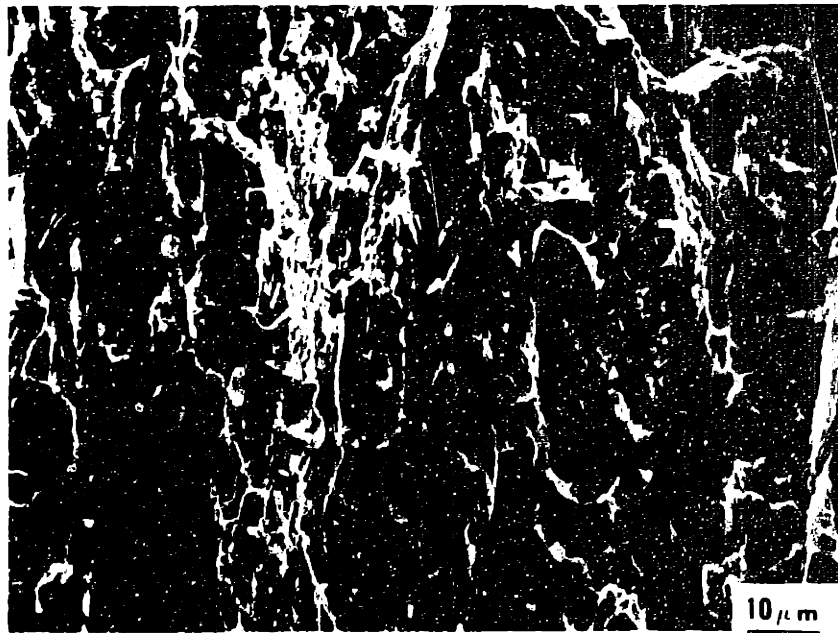
Fig. 6.5   SEM micrograph from TL specimen showing
            narrow, elongated cleavage facets with
            tearing between facets.
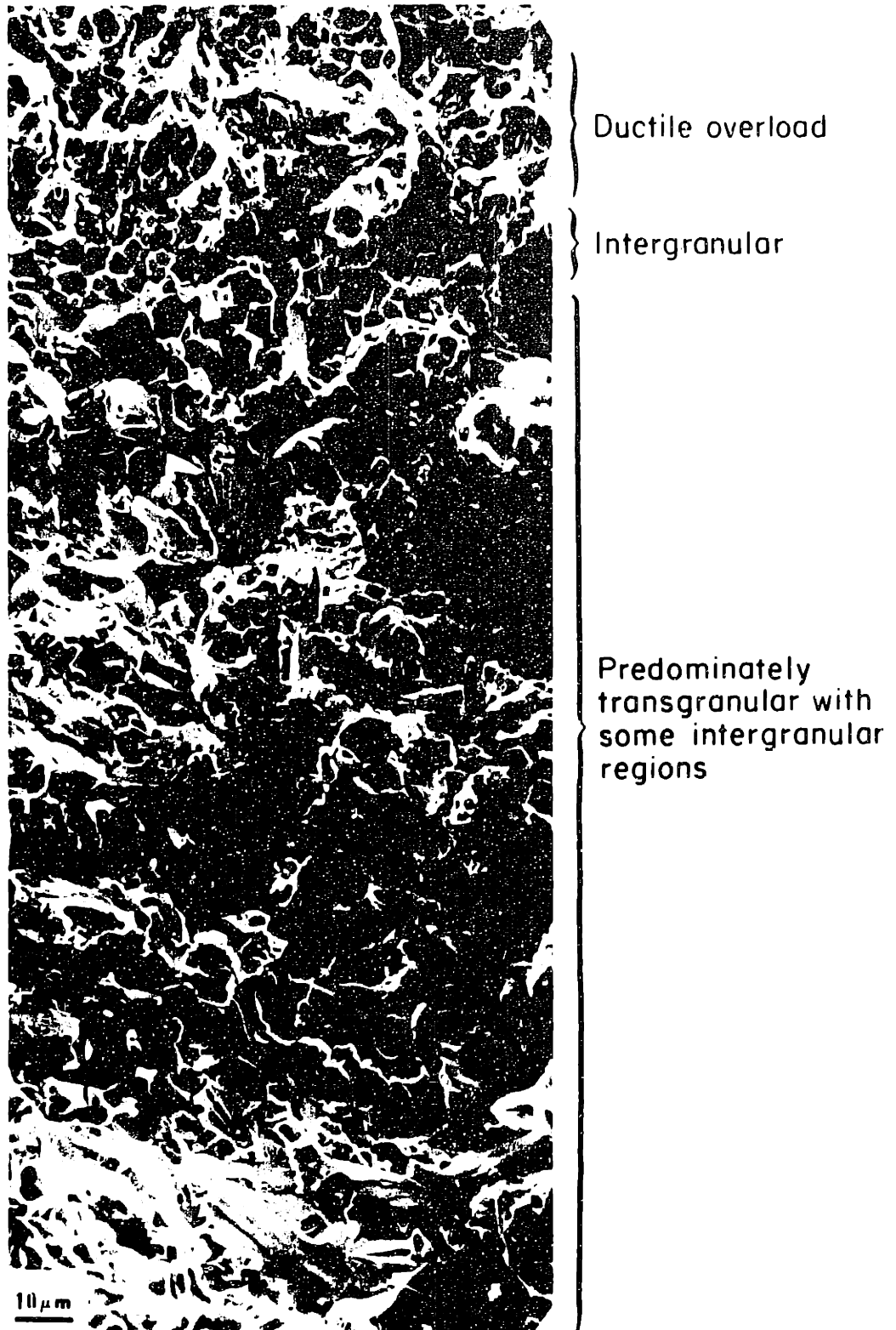
Fig. 6.6 Fracture surface from recrystallized material showing the transition from mixed intergranular/ transgranular to fully intergranular propagation.
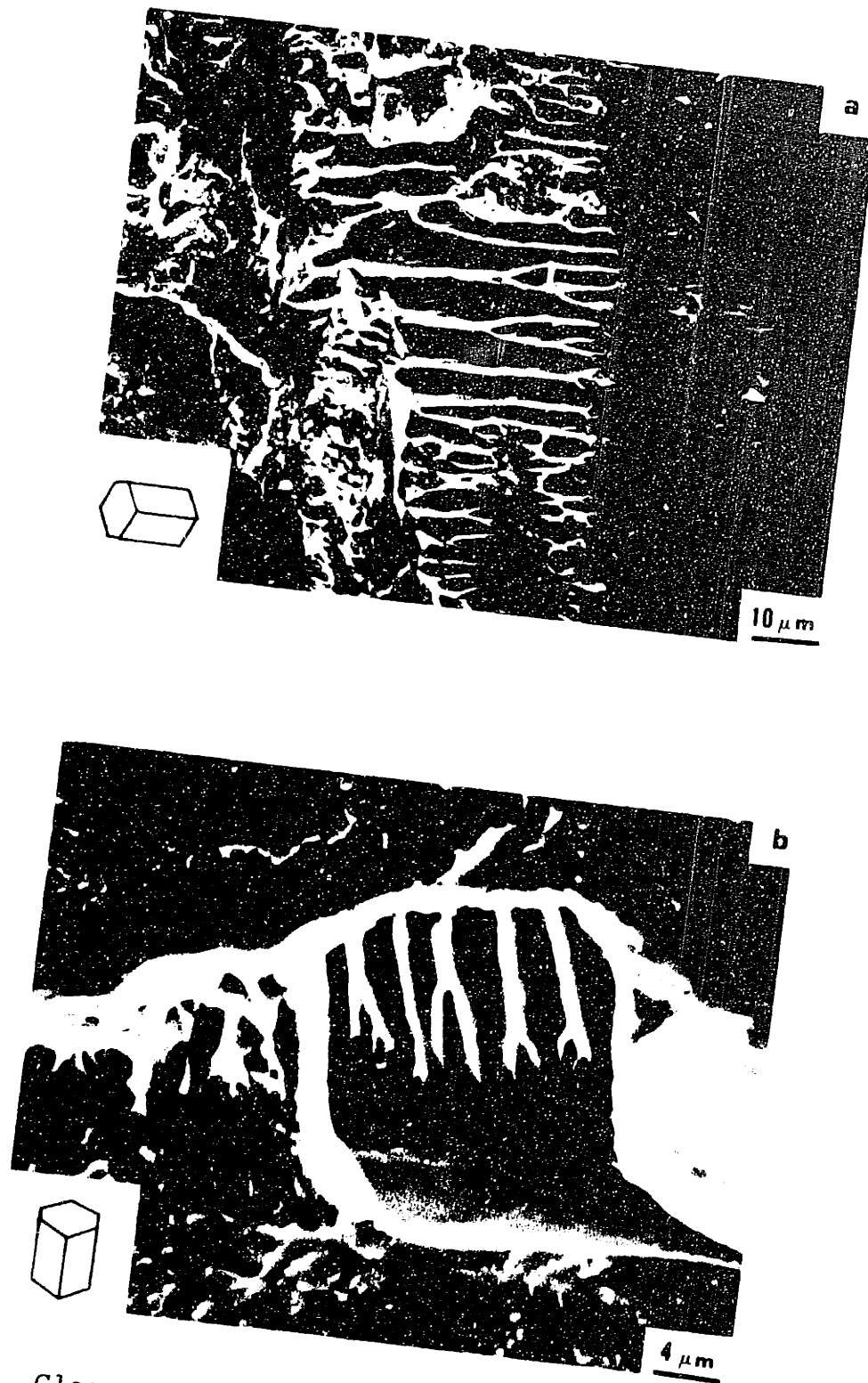
Fig. 6.7   Cleavage and fluting features from the SCC
region.   (a) NL specimen orientation.
(b) NT specimen orientation.

Fig. 6.8 Ductile overload failure from areas immediately beyond SCC regions. (a) Dimples in a 0°-NL specimen. (b) Mixture of dimples and flutes parallel to the direction of crack growth in a 0°-NT specimen. (c) Flutes perpendicular to the direction of crack growth in a ±40°-NL specimen. (d) Flutes parallel to the direction of crack growth in a ±40°-NT specimen.
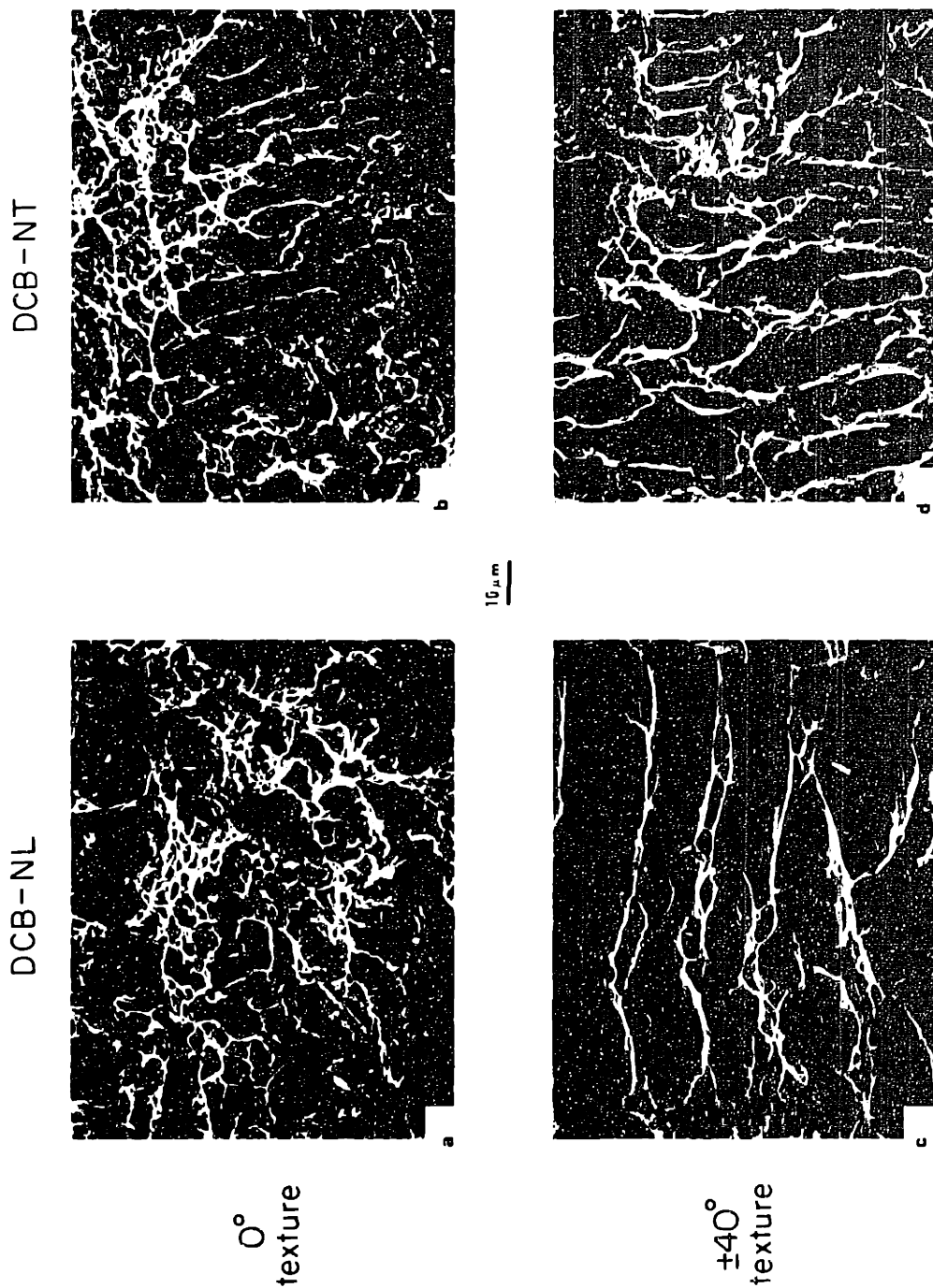
FIGURE 6.9   HOOP STRESS VERSUS TIME TO FAILURE FOR SUPPLIER A TUBING AT 320°C
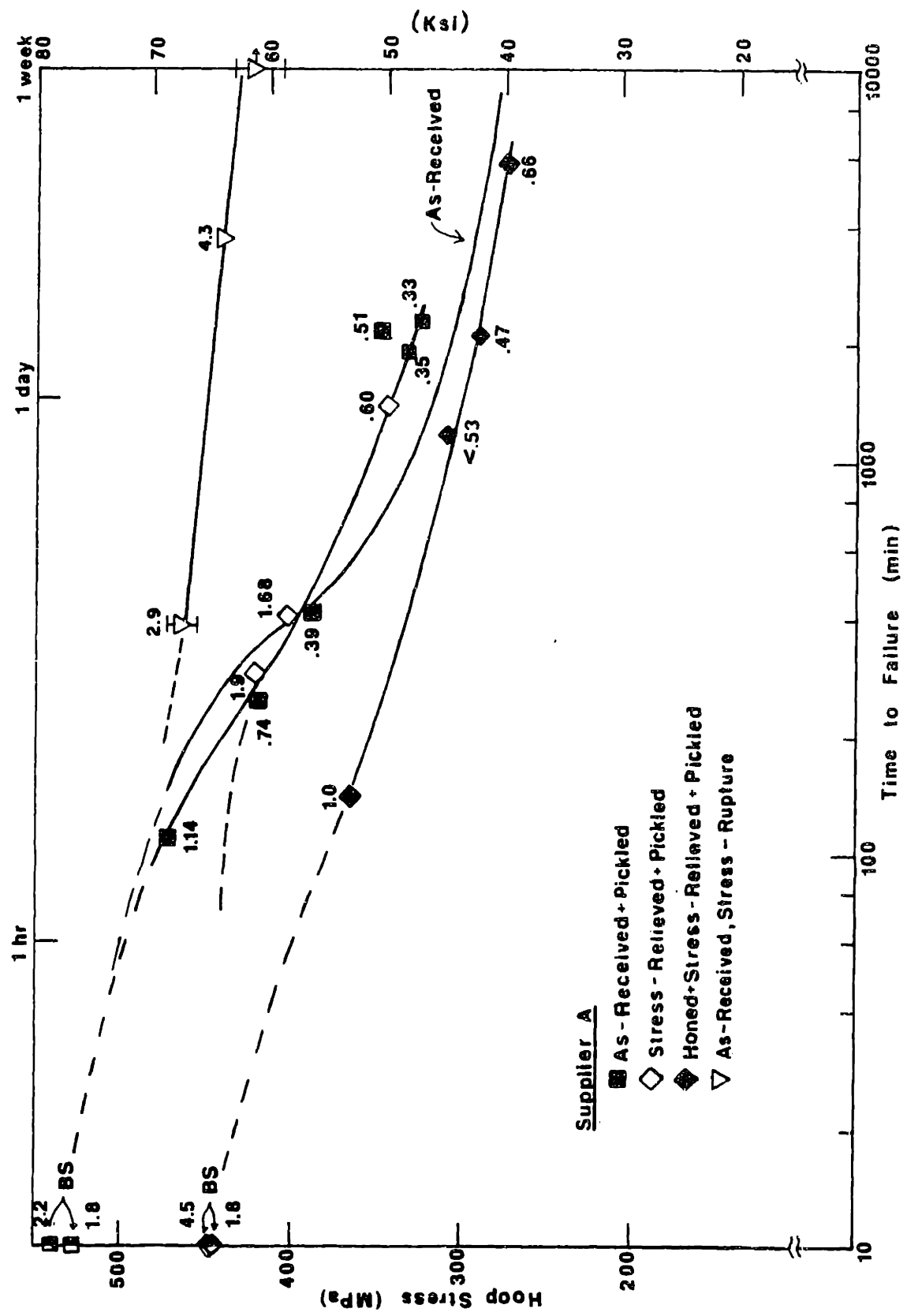
FIGURE 6.10   HOOP STRESS VERSUS TIME TO FAILURE FOR SUPPLIER B TUBING AT 320°C
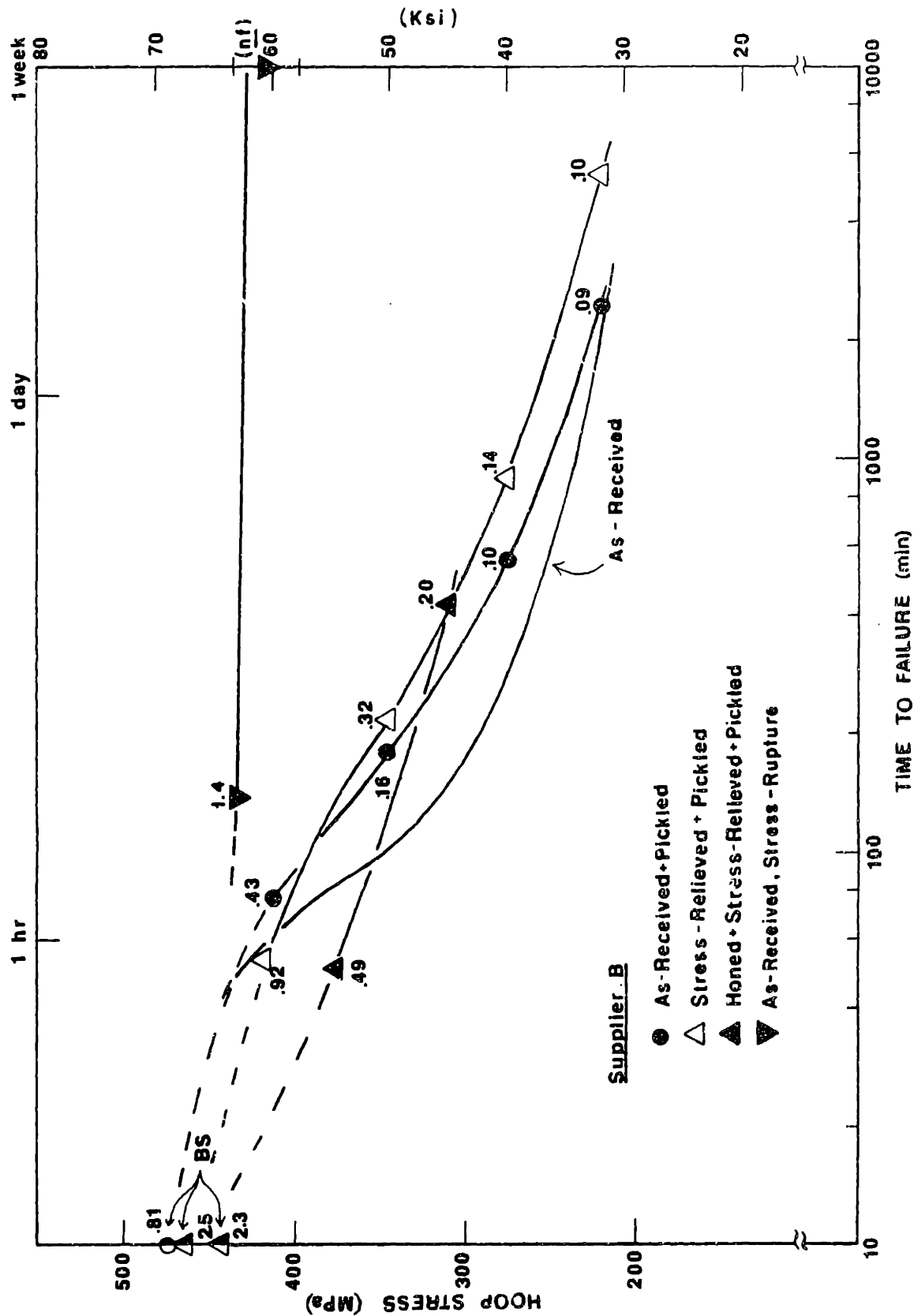
FIGURE 6.11 COMPARISON OF SUPPLIER A AND SUPPLIER B IN THE AR CONDITION AT 320°C
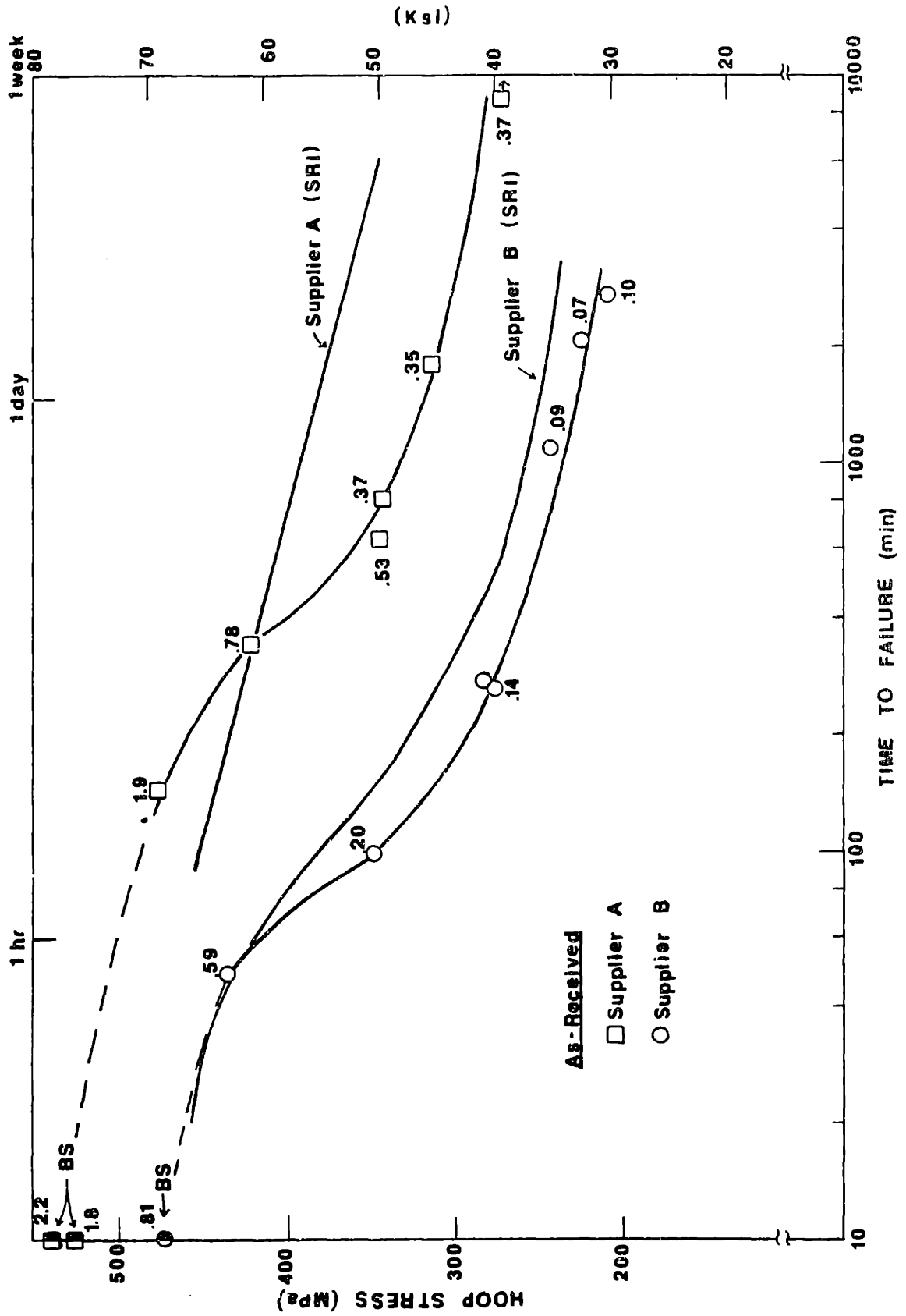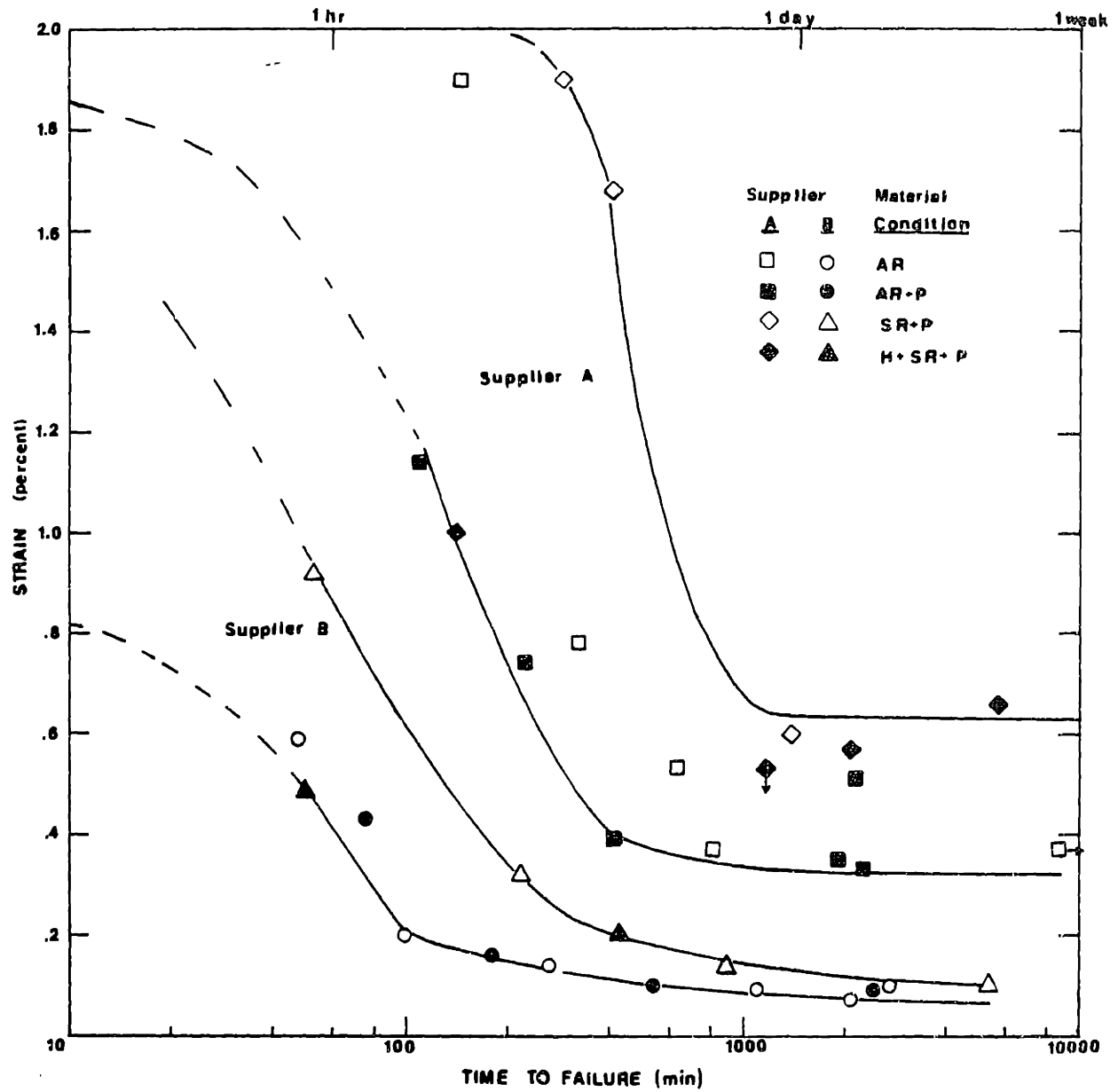
FIGURE 6.12   PLASTIC STRAIN VERSUS TIME TO FAILURE FOR IODINE SCC TESTS AT 320°C
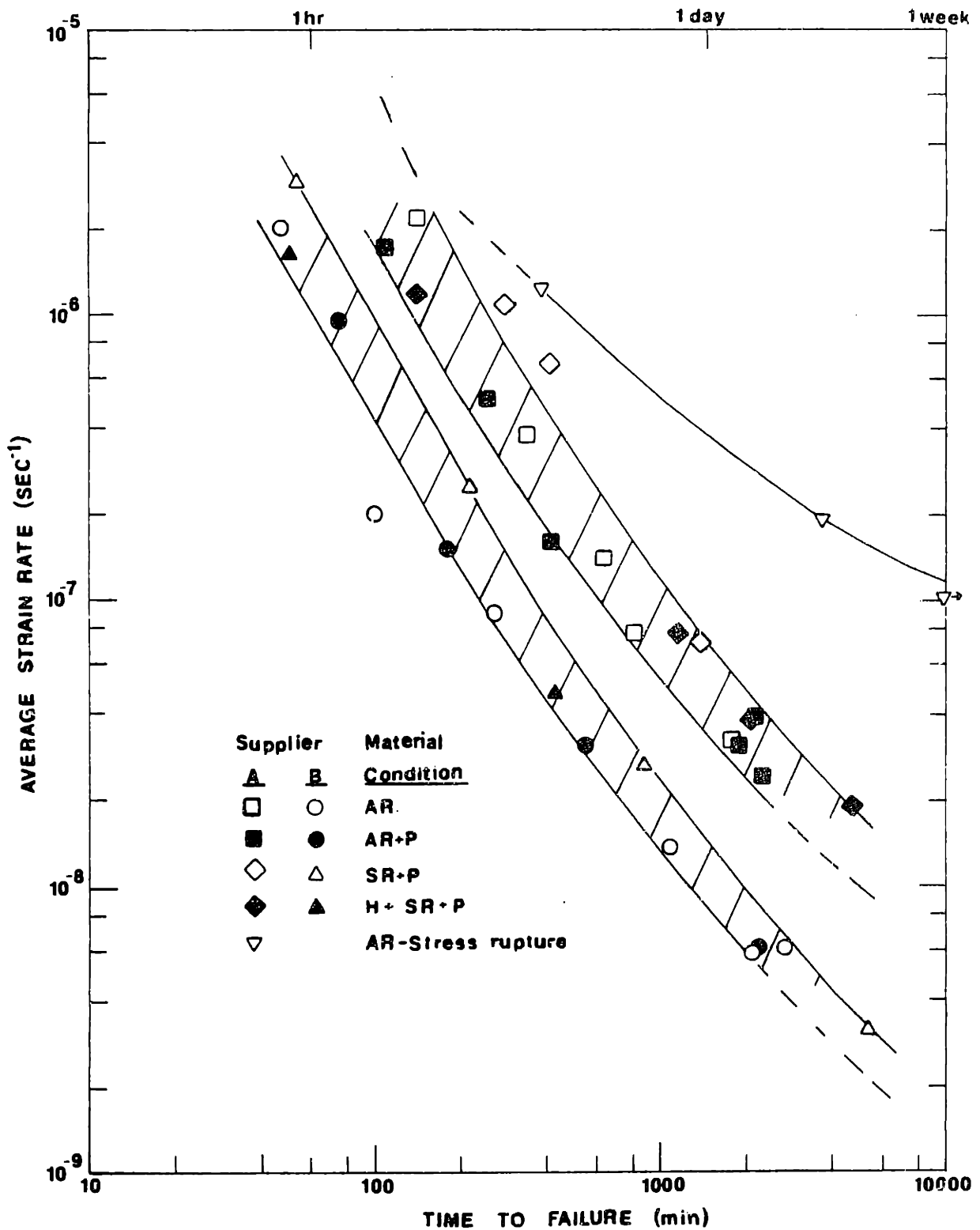
Figure 6.13

Average Strain Rate versus Time to Failure for Tests
at 320°C

Figure 6.14

Sampling Plan Summary for Iodine SCC Tests at 320°C

M·aterial   Condition

Figure 6.15

SEM micrographs of failure site from tube pressurization specimen.

a) A through-wall iodine SCC crack is seen from the ID surface of specimen A-27. Large (A) and small (B) secondary cracks are evident.

b) The region of different contrast (C) in a) is shown at higher magnification to be composed of numerous small cracks.

Fig. 6.16 Correlation Between Hoop Stress and Crack Opening Angle for 320°C Tests
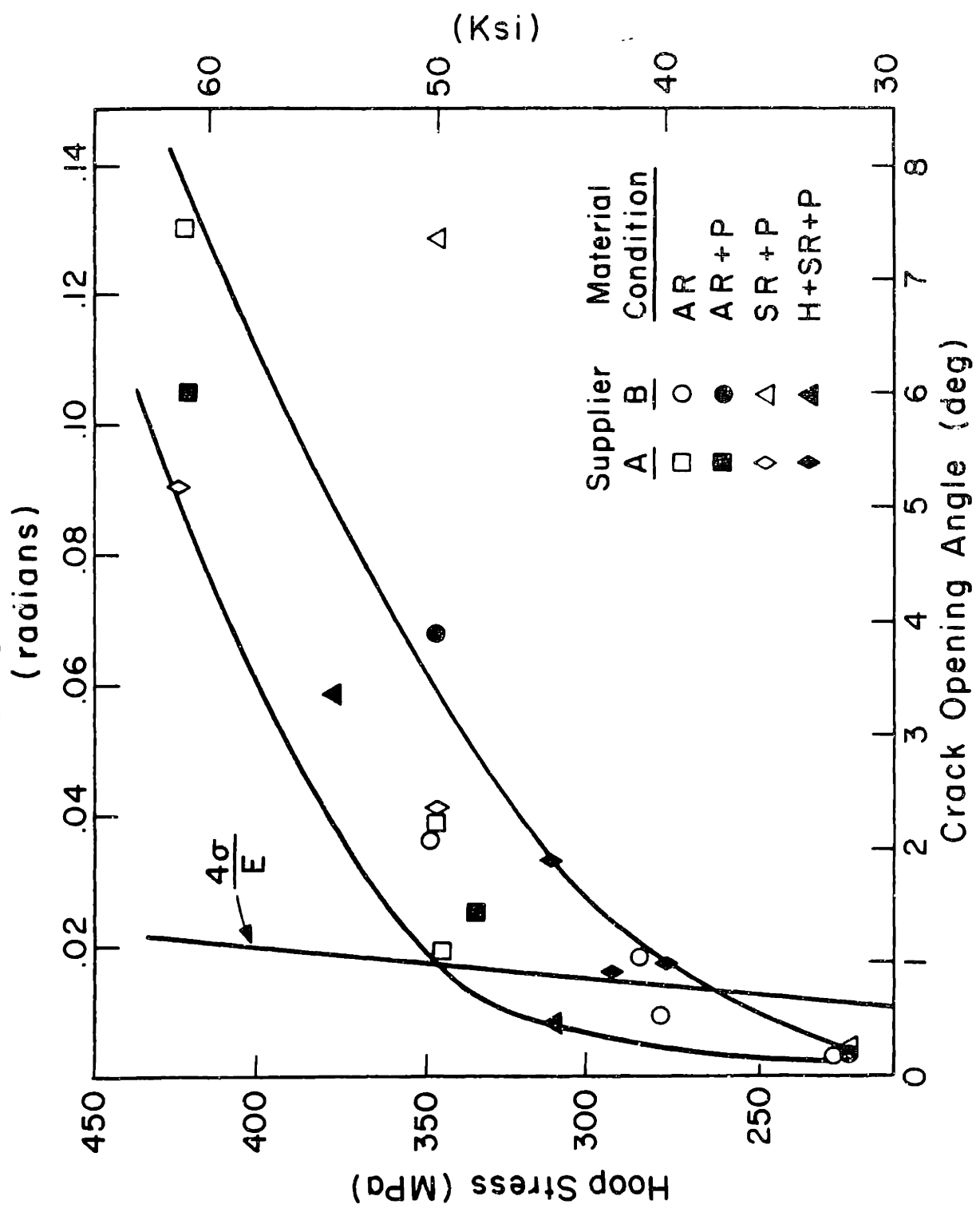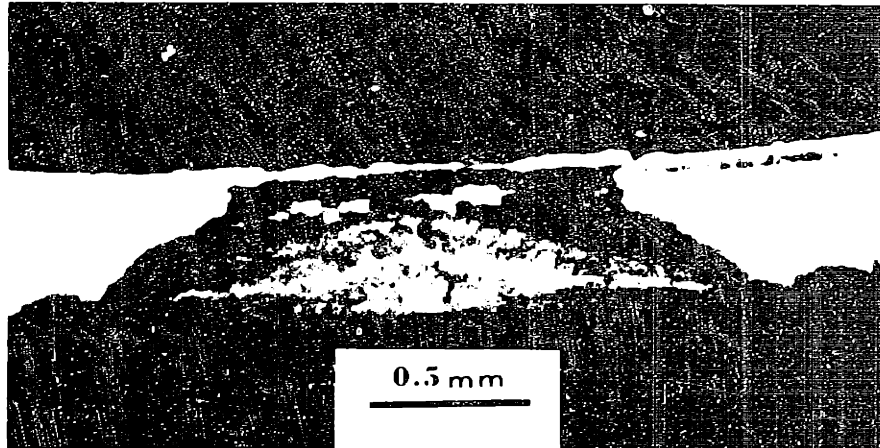
a) Specimen A-11 σ = 421 MPa t_f = 340.7 min.
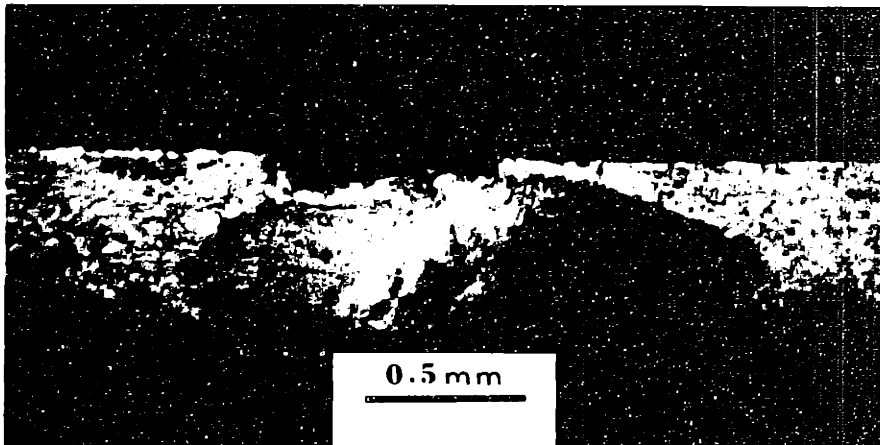
b) Specimen A-15 σ = 345 MPa t_f = 634.2 min.

Figure 6.17

Macrophotographs of supplier A specimens showing well defined regions of stress corrosion crack propagation.

Figure 6.18

SEM composite of the fracture surface
for specimen A-27
    SR+P condition
    σ ≈ 345 MPa
    t_f = 1390.4 min.
    ε = 0.60%
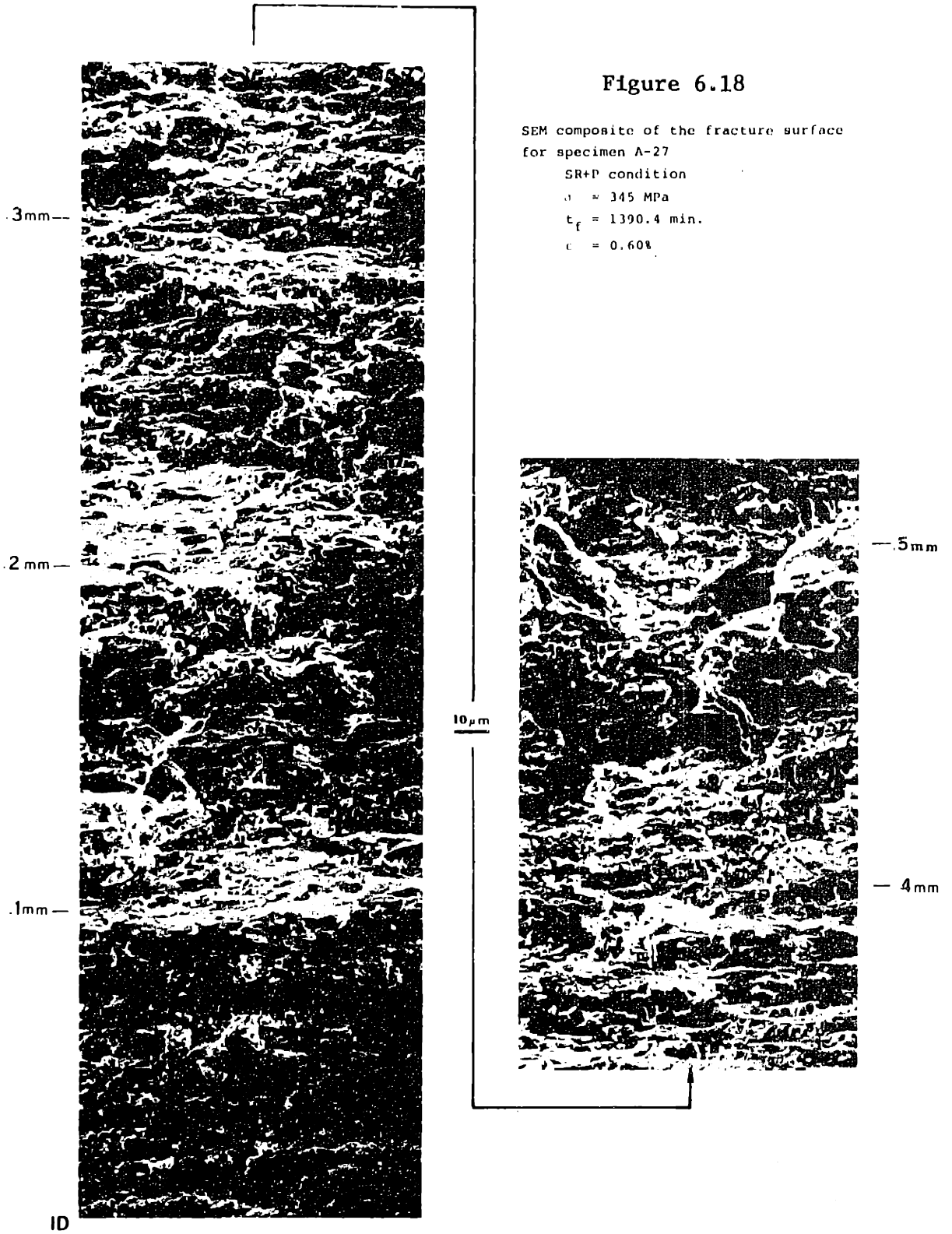
Figure 6.19
SEM composite of the fracture surface for specimen B-17
AR condition
= 347 MPa
t_f = 99.7 min.
= 0.20%

.3mm —

.2mm —

.1mm —

10μm

— 6mm

— .5mm

— .4mm

ID

.3 mm —

.2 mm —

.1 mm —

ID

10 μm

Figure 6.20

SEM composite of the fracture surface
for specimen B-28

SR+P condition

' = 221 MPa

t_f = 5334.5 min.

ɩ. = 0.10%

—.5 mm

—.4 mm
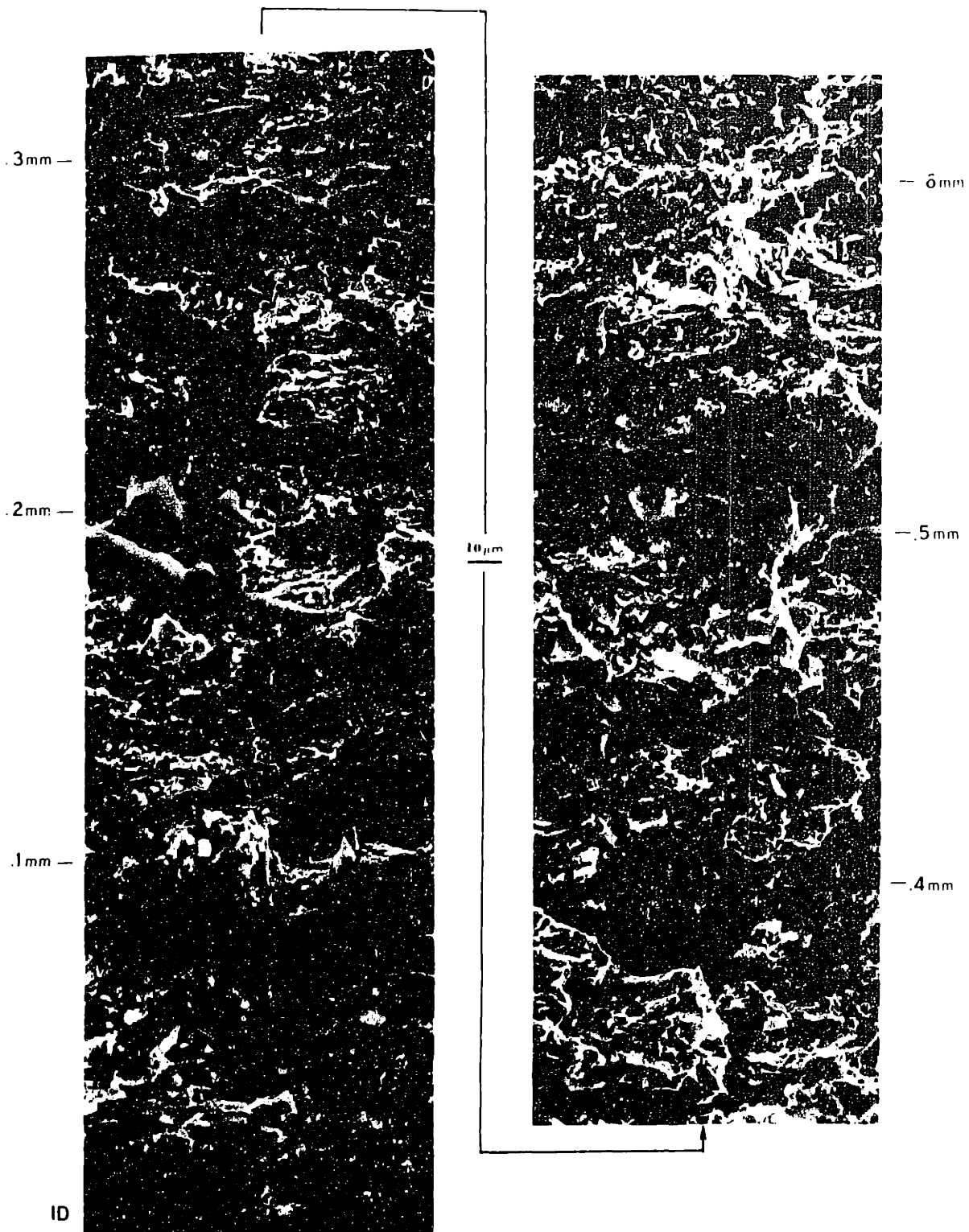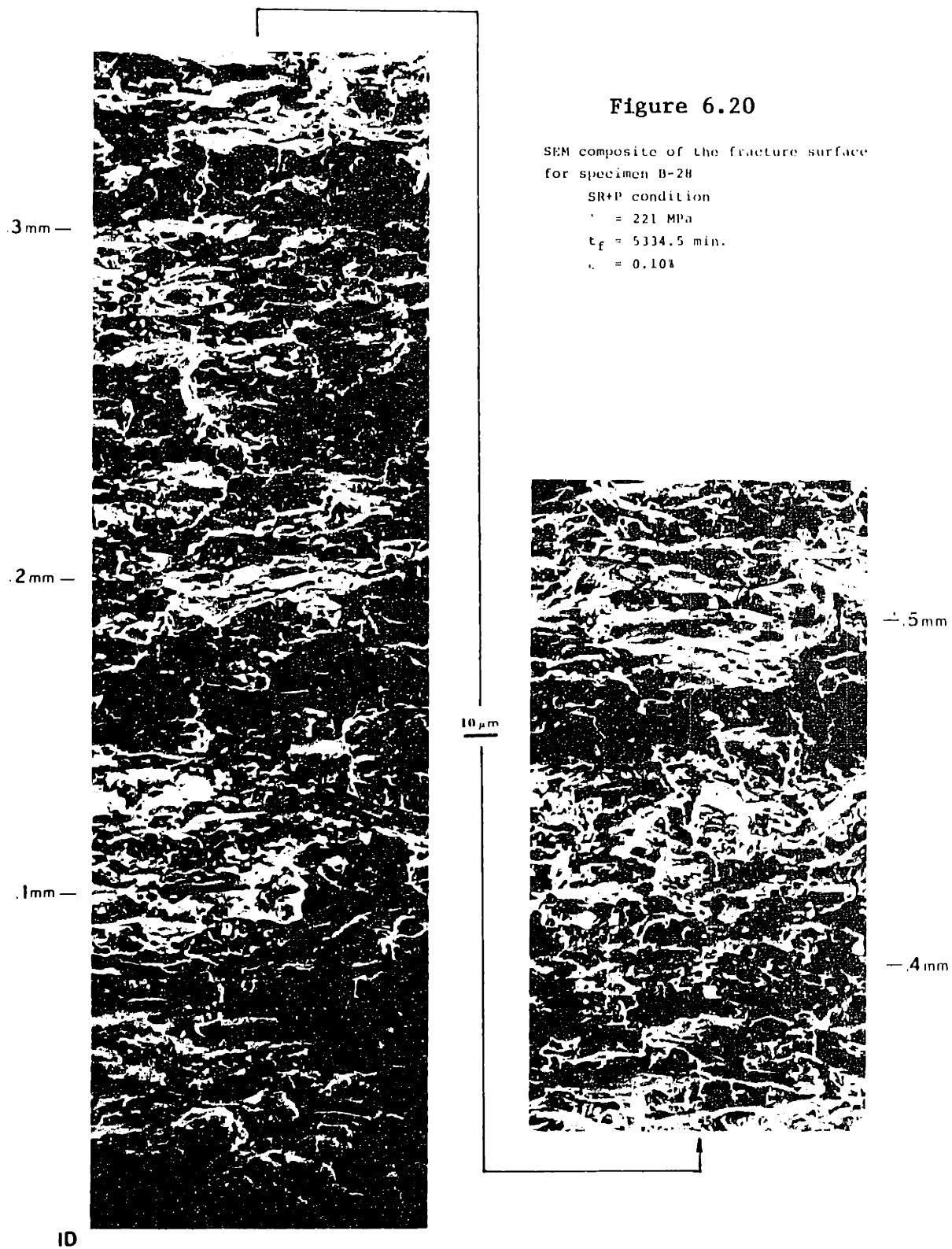
Figure 6.21

Distribution of Incipient Microcracks for Failed Iodine SCC Specimens Tested at 320°C

Specimen & Condition		σ (MPa)	t_f (min)	ε_f (%)	Deepest Crack (μm)
A-11	AR	421	340.7	0.78	7
A-28	SR+P	423	287.5	1.9	18
A-15	AR	345	634.2	0.53	7
A-27	SR+P	345	1390.4	0.60	3
B-12	AR	347	99.7	0.20	4
B-24	SR+P	345	217.6	0.32	3
B-16	AR	225	2067.8	0.07	2

Number of Cracks Counted in Metallographic Section *

Crack depth (μm)

*Metallographic section is half the tube circumference opposite the crack that propagated to failure
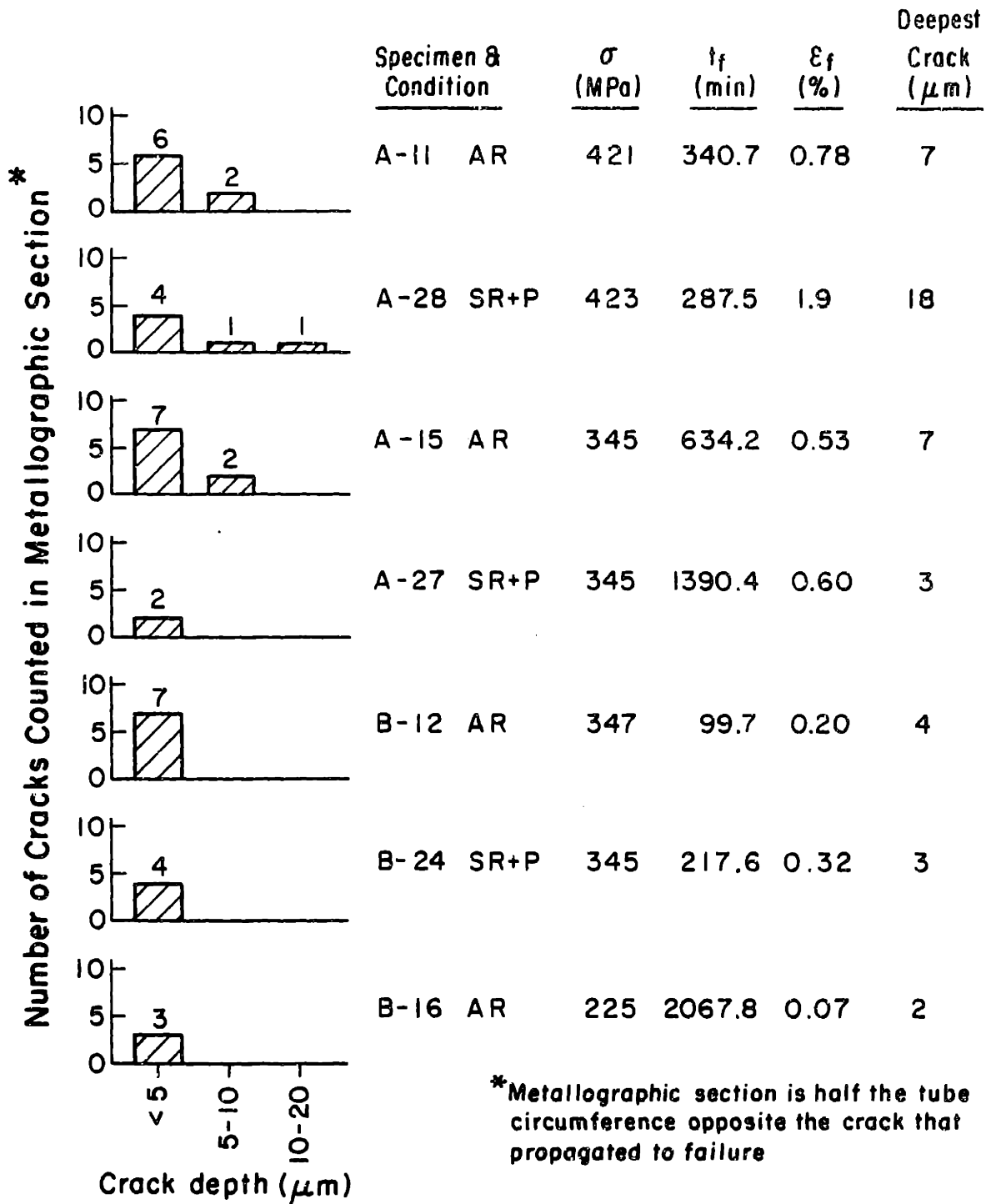
Figure 6.22

Distribution of Incipient Microcracks for Failed
Iodine SCC Specimens Tested at 390°C

Specimen & Condition	σ (MPa)	t_f (min)	ε_f (%)	Deepest Crack (μm)
A-33 AR	263	320.0	1.31	340
A-33 AR	283	320.0	1.31	43

Full tube circumference examined
~40 mm from failure site

A-38 SR+P	252	377.1	1.26	6
B-34 AR	223	163.0	0.26	39
B-34 AR	223	163.0	0.28	4

Full tube circumference examined
~20 mm from failure site

B-38 SR+P	138	6900 (nf)		
	169	2700 (nf)		
	210	3300 (nf)		
	238	209.8	1.24	19
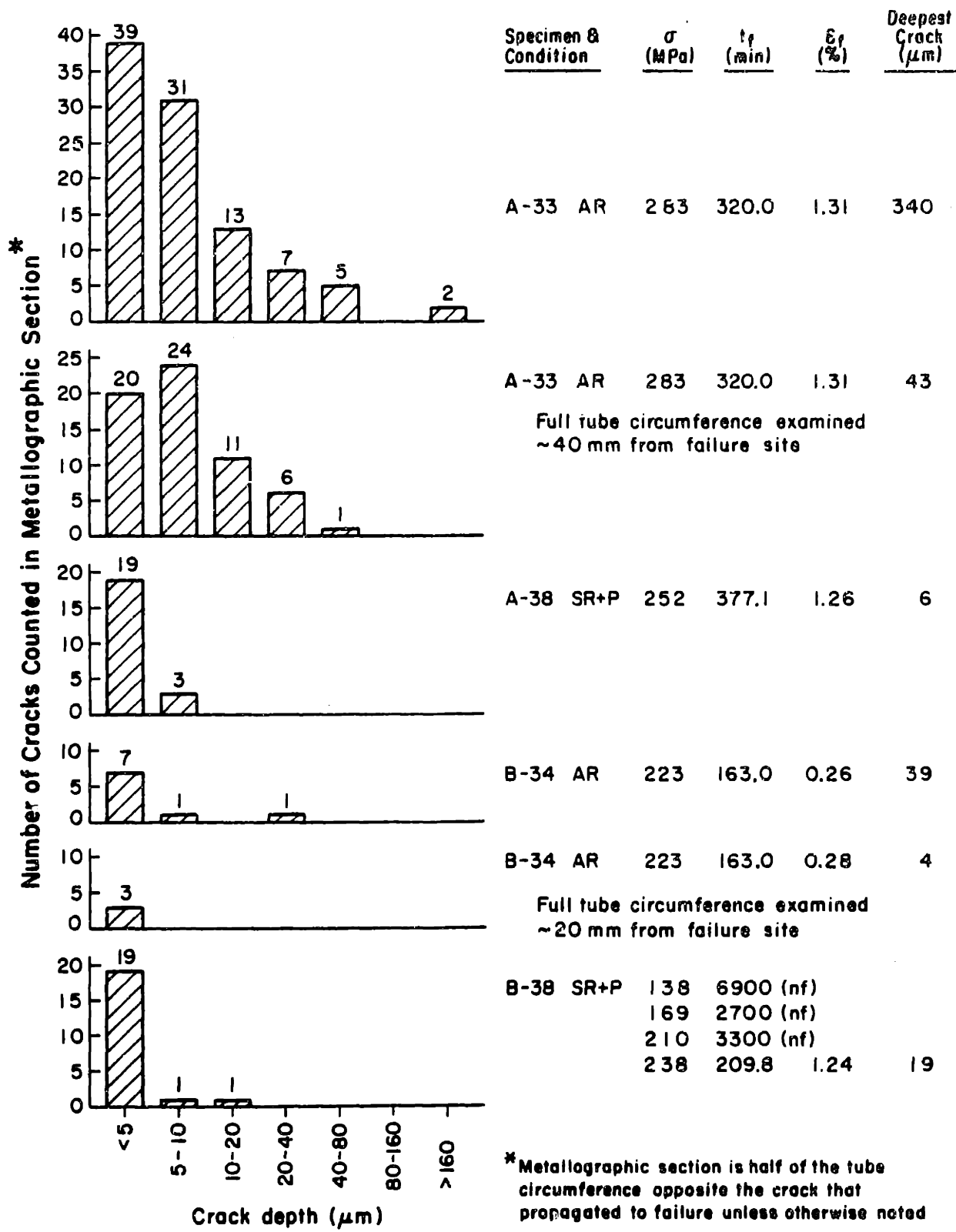
*Metallographic section is half of the tube
circumference opposite the crack that
propagated to failure unless otherwise noted

Incipient cracks revealed in metallographic cross-sections of tubing specimens
from tests at 390°C

Figure 6.23
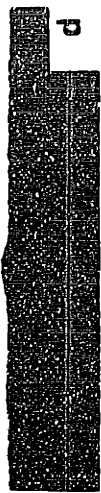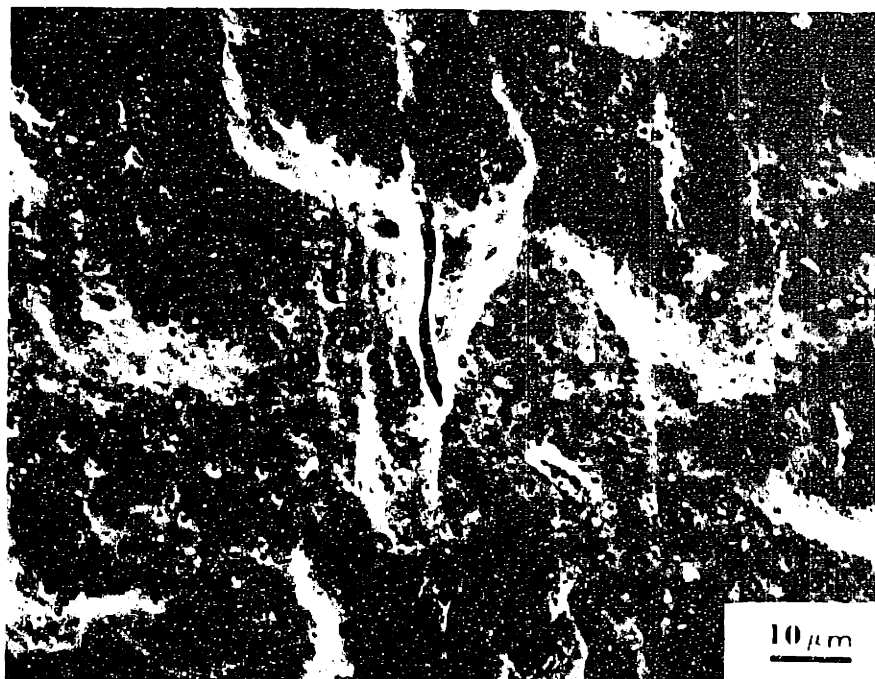
Figure 6.24

SEM micrograph of the ID surface of a split ring test
specimen is shown. The supplier B cladding in the
as-received condition is exposed to a flowing
argon + 4Pa (.03 torr) iodine gas stream at 320°C
for 300 minutes. A microcrack is evident in the
center of the micrograph.

7. DISCUSSION

7.1   Crack Propagation and Crack Arrest in Fracture Mechanics Specimens

7.1.1   Explanation of K_{ISCC} versus f Behavior

The curve of K_{ISCC} versus f is shown in Fig. 6.1. Decreasing f in the crack opening direction results in a higher value of K_{ISCC}. Cleavage, which is the principal mode of crack propagation, is known to occur along planes near the basal plane [81,105] so specimen orientations with high values of f (f > 0.55) have basal poles favorably aligned for cleavage. As f decreases, fewer basal planes are oriented for easy cleavage so K_{ISCC} increases due to the higher stress necessary both for propagation along less favorably oriented cleavage planes and for ductile processes such as tearing and fluting. The curve for recrystallized materials lies above the curve for stress-relieved materials. The higher K_{ISCC} values at similar texture are probably related to the lower strength and higher toughness of this microstructure. No effect is evident due to the slight compositional differences between Zircaloy-2 and Zircaloy-4 [109].

The data in Table 6.2 indicate that reproducibility for a particular specimen type and orientation is good. In the ±40° material which is tested with both WOL and DCB specimens, K_{ISCC} values are lower for DCB specimens compared to WOL specimens although the fractography reveals similar features. This issue is considered further in Appendix D.

The present results are compared with a limited number of studies by other investigators. Cox [100] reports a K_{ISCC} of 9 MPa$\sqrt{m}$

for a NL specimen orientation in a 40% cold-worked Zircaloy-2 plate with a $\pm 30°$ (tube) texture that is roughly equivalent to the 9912 plate. The tests are performed with a static environment in a sealed test capsule at 300°C. This K_{ISCC} exceeds the value for the $\pm 40°$-NL specimens. The large discrepancy between the results in this study and Cox's data cannot be accounted for by minor differences in texture and microstructure. Differences in test technique (static capsule versus flowing system) might be postulated as causing significant differences in the test environment. The static system favors formation of solid lower iodides (ZrI, ZrI_2) with a lower equilibrium P_{ZrI_4} [56,66] than the flowing system where constant iodine replenishment results in continued reaction with the Zircaloy surface and in higher solid iodides (ZrI_3) with a higher iodine activity as I_2 and ZrI_4. The flowing system behavior is consistent with experimental observations of iodide coating of specimens and profuse ZrI_4 formation. The K_{ISCC} difference then might be attributed to P_{ZrI_4} effects.

Wachob and Nelson [92] report a K_{ISCC} of 10 MPa$\sqrt{m}$. A WOL-TL specimen is tested on Zircaloy-4 plate (stress-relieved at 497°C for 4 hours, $f_T = 0.34$) so the material condition is very similar to the TL specimen in $\pm 40°$ plate. The test with iodine alone is performed in a sealed, static capsule at 360°C for 677 hours. This K_{ISCC} was lower than the values of 14.6 and 15.7 MPa$\sqrt{m}$ for WOL-TL specimens reported in Table 6.1. The difference might be due to the 60°K difference in test temperature and the iodine chemistry discussed previously which is also strongly dependent on temperature [66].

Videm and Lunde [117-119] test fatigue pre-cracked tubing reporting a K_{ISCC} of 4-5 MPa√m at a test temperature of 349°C. The material had a ±30° basal pole texture giving an f-parameter in the range of 0.3-0.4 for propagation of through-wall cracks. The markedly low K_{ISCC} values for this texture are probably related to the application of fracture mechanics to the propagation of short cracks through thin-walled tubing. It is doubtful that their simplified elastic fracture mechanics analysis applies to this case. A more elegant fracture mechanics analysis accounting in detail for the thumbnail crack geometry, the transition from shallow to deep cracks, back wall effects, and possible deviation from plane strain loading conditions is necessary. Videm and Lunde also note that the apparent K_{ISCC} is slightly lower for tubing recrystallized at 570°C than for tubing stress-relieved at 520°C. This observation contradicts the trend presented in Fig. 6.1.

Although no data are available concerning the effect of texture on SCC propagation in Zircaloy, work in titanium alloys, a system very close metallurgically to the zirconium alloys, is available. Dawson and Pelloux [161] describe the texture effect on corrosion fatigue of α and α/β titanium alloys. They find that basal plane alignment parallel to the applied stress lowers, but does not eliminate cracking susceptibility. Larson and Zarkades [16] tested DCB specimens of titanium in methanol/HCl solution and find a marked decrease in K_{ISCC} with increased alignment of basal planes parallel to the direction of crack growth while no effect on K_{IC} is noted. Definite parallels exist between the observations in the titanium system and the results for Zircaloy because of the near basal plane mode of cleavage fracture. The micromechanisms of fracture are probably different since environmental failure of titanium alloys is

attributed to hydrogen embrittlement while mechanisms other than hydrogen

embrittlement are postulated for Zircaloy in gaseous iodine [12].

7.1.2   Fractography

7.1.2.1   Stress-relieved material

The K_{ISCC}-texture relationship shown in Fig. 6.1 is best

understood by a detailed study of the fracture surfaces from the differently

textured specimens. In this section the fracture features are related to

texture, to crack velocity, and to the threshold stress intensity K_{ISCC}.

The fractography from the NL/NT, LT, and TL specimens of stress-relieved

material is considered in that order.

Fig. 6.2(a) shows a macrophotograph of a DCB-NL specimen of

stress-relieved material. The SCC surface appears brighter and more

reflective at the location just preceding the location of crack arrest.

Fig. 6.3(a) presents SEM fractographs from the "bright" region. The direc-

tion of propagation is from bottom to top on all SEM fractographs. Crack

propagation in the "dull" region, Fig. 6.2(b), proceeds at relatively high

velocity and at K values appreciably above K_{ISCC}. The facet size approxi-

mates the grain size which is difficult to determine in the heavily

deformed and twinned microstructure of the stress-relieved material. The

high crack velocities at high stress intensity cause appreciable tearing

between facets. Crack propagation in the "bright" region is at lower

velocity and at K values approaching K_{ISCC}. The lower energy cleavage

failure occurs along a cleavage plane common to several grains to give

cleavage facets much larger than the grain size. The same "dull" to

"bright" transition is observed in specimens from the NT orientation.

A dramatic example of the texture effect on crack propagation is evident from a test on the WOL-LT specimen. Macroscopic channels form ahead of the pre-fatigue crack, Fig. 6.2(b). Examination of the fracture surface in Fig. 6.4 reveals no brittle crack propagation in the plane and direction of macroscopic crack growth. The pole figure, Fig. 3.2, indicates no basal poles near the rolling (crack opening) direction accounting for the lack of cleavage in the direction of macroscopic crack growth. The cleavage crack growth, which is perpendicular to direction of macroscopic crack growth, occurs along basal plane approximately parallel with the plate surface consistent with the observed basal pole texture. Opening of the troughs results from the transverse stress component of the plane strain stress state in the specimen. No estimate of stress intensity is possible since the formation of deep troughs relaxes the plane strain stress state and makes assignment of a crack length impossible.

The TL specimens are better oriented for crack propagation than LT specimens since basal planes with poles near the transverse plate direction are favorably oriented for cleavage. The grains in stress-relieved material are flattened by the plate rolling process resulting in the macroscopic banded appearance shown in Figure 6.2(c). "Fingers" of favorably oriented grains cleave ahead of the main crack front. At higher magnification, the cleavage facets appear long and thin as seen in Fig. 6.5. This contrasts with the wide facets in the NL or NT specimens. Since the f-parameter is lower for TL than NT and NL specimens, fewer grains are well oriented for cleavage so more tearing between grains is evident. The greater microscopic irregularity of the

the fracture surface is a consequence of cleavage across grains having basal planes misoriented with respect to the macroscopic crack growth plane. These higher energy fracture processes are responsible for the high K_{ISCC} values. More tearing is present at high K than near K_{ISCC} in TL specimens, but the differences are less pronounced than in NL and NT specimens. The fractographic features in the TL specimens are consistent with the observations of Wachob and Nelson [92].

7.1.2.2   Recrystallized Material

Recrystallized material in the NL and NT orientations exhibits transgranular features similar to the stress-relieved material. Discrete facets with edge tearing at high K change to larger cleavage facets with less tearing as K_{ISCC} is approached. The facets are regularly shaped due to cleavage across the relatively equiaxed grains. An additional feature is the presence of intergranular facets which are most common at low K values near crack arrest. Most annealed material shows mixed intergranular/transgranular features with a greater degree of transgranular faceting as shown in Fig. 6.6. A transition in fracture mode to completely intergranular is also possible very near K_{ISCC}. The fractography substantiates the observations of Videm and Lunde [117-119] who noted an intergranular-mixed intergranular/transgranular-transgranular sequence with increasing K.

7.1.2.3   Ductile Processes

Several ductile failure modes are available to complement the transgranular cleavage process. Cox [100] has identified three such

failure modes:

1. Clean separation along grain boundaries;

2. Ductile tearing at or near grain boundaries giving a disordered or "torn" appearance, and

3. Fluting.

All three types of features are observed in the crack propagation specimens. Furthermore, it is possible to assign the conditions of K and crack velocity favoring each mode.

The "torn" appearance between cleavage facets, shown in Figs. 6.3(b) and 6.5, is a high K phenomenon. It is observed in the TL specimens having a relatively high K_{ISCC} compared to the NL and NT specimens and in the high K/high crack velocity regime in the NL and NT specimens. The clean separation along grain boundaries is noted at lower K values as K_{ISCC} is approached. This is reflected in the reduced incidence of tearing and by the large cleavage zones shown in Figs. 6.3(a) and 6.6.

Flutes are regions of ductile channels between widely spaced cleavage planes. The striated appearance is crystallographic in origin resulting from slip on the $\{10\bar{1}0\}<11\bar{2}0>$ system. The ridges are defined by the intersection of such slip planes. They are parallel to each other and are normal to the basal plane with matching peak-to-peak on opposite faces [108].

Two distinct instances of fluting are observed. Small, widely spaced regions with flutes occur in the SCC region. Examples are shown in Fig. 6.7 for both NL and NT specimens. Fluting also occurs in the ductile overload region beyond the SCC surfaces. Examples for the

NL and NT orientations in both 0° and ±40° plates are given in Fig. 6.8.

Texture and microstructure have a very strong influence on the occurrence of the flutes. SCC flutes in the ±40° texture are more common than similar fluting features in the 0° texture material. The NL and NT specimen orientations have a microstructure with grains flattened by the plate rolling process so the cleavage facets are not "widely spaced" suppressing the development of flutes. Clean separation of adjacent facets or a slightly "torn" appearance is most commonly observed.

Specimen orientation and texture control the morphology of the flutes that are observed in the SCC region. Fig. 7.1(a) is a schematic diagram of the formation of the flute striations in the NL orientation. The basal pole texture and crystallographic nature of the flutes result in ridges and valleys perpendicular to the direction of crack propagation. This is readily observed in Figs. 6.7(a) and 6.8(c). Figure 7.1(b) is a similar sketch for the NT orientation where the ridges and valleys are now parallel to the direction of crack propagation as seen in Figs. 6.7(b) and 6.8(b), (d) for the SCC and ductile flutes, respectively. Ductile flute formation is favored in NT specimens and in ±40° material.

Several observations are relevant to features associated with the SCC flutes. As the flutes begin to form, the spacing between ridges is small. The ridges then coalesce to form coarser flutes as the length of the fluted region increases. Fractographic evidence for this process is shown in Fig. 6.7. The SCC flutes start at a 1-2 μm ridge-to-ridge spacing. The flute spacing after coalescence is found to vary according to the length of the fluted region. Qualitatively similar behavior is observed in the ductile flutes.

The fracture process requiring the least energy to accomplish crack propagation is cleavage. The ductile processes of fluting, tearing, and dimple formation can also be distinguished by the relative amounts of energy required to complete the separation process. In the SCC region, fluting is seen primarily near the point of crack arrest, i.e. Region I. This indicates that fluting is a lower energy process than the ductile tearing processes that also complement cleavage.

Fluting is preferred at low strain rates. This is demonstrated by the observation of flutes at low crack growth rates in SCC. Prism, or $\{10\bar{1}0\}<11\bar{2}0>$, slip is activated at a critical resolved shear stress (CRSS) much lower than the CRSS for any $<c+a>$ slip system at room temperature and at 300°C [163-165]. At low strain rate, and thus at low stress, dislocation glide occurs almost exclusively on prism planes where the flutes develop along intersecting prism planes. The fine flutes coalesce to form larger flutes, and the material between them necks to a knife edge. Ductile flutes in Zircaloy have also been observed in plane strain tension tests [165].

No evidence exists to confirm or reject an environmental contribution to the fluting process. However, the observations reported here indicate that fluting is more likely to be a purely mechanical process. In the ductile region, the occurrence of fluting in titanium alloys is related to absorbed oxygen and hydrogen in an aqueous environment [166]. A similar phenomenon is less plausible in Zircaloy because an aqueous environment is not present to facilitate hydrogen uptake. Therefore, the ductile fluting process is probably a purely mechanical effect dependent on texture and strain rate similar to fluting in the SCC region.

7.2   Comparison of SCC Behavior in Supplier A and Supplier B
       Tubing

The results in Figs. 6.9-6.11 reveal a substantial effect of some materials variable(s) on SCC susceptibility. The test matrix in Fig. 5.2 is designed to separate the difference in iodine SCC susceptibility using the following comparisons:

1. Heat Treatment: AR + P versus SR + P

2. Surface Condition: AR versus AR + P

    SR + P versus H + SR + P

3. Texture: Supplier A versus supplier B, the same material

    condition.

Synergistic interactions among any of the above materials variables are also possible. Each factor will be considered separately in the following discussion. The behavior discussed here is integrated with the results and observations of other investigators to understand the role of materials variables on both initiation and propagation. Subsequent sections provide separate discussion of the initiation and propagation stages of SCC.

7.2.1   Heat Treatment

The 500°C/2 hr stress-relief treatment has two effects: 1) a reduction of residual stresses from the tube straightening operation as indicated in Table 3.3 and 2) a change in mechanical properties indicated by a minor reduction in burst strength and probable increase in creep rate. The reduction in burst strength is greater in supplier A than the negligible difference in supplier B, Table 6.3. For comparable stress and time to failure in SCC, the strain at failure is greater for

the SR + P than for the AR + P in both suppliers, Fig. 6.12. The difference is much more pronounced in supplier A indicating a change in the creep properties; the higher creep rate produces more creep strain over a given period of test time. The behavior is consistent with the heat treatment of the materials following the final tube forming operation. Supplier B tubing is known to receive a higher temperature stress-relief treatment than the supplier A tubing so its mechanical properties are less affected by the 500°C/2 hr anneal. A similar trend in mechanical properties with heat treatment is demonstrated by Videm and Lunde [86].

The stress versus time to failure behavior for the AR + P and SR + P conditions is essentially the same for supplier A, Fig. 6.9, and is only slightly different for supplier B, Fig. 6.10, indicating a negligible effect of residual stress on SCC behavior. The creep strain accumulated by the specimen relieves the residual stress for strain greater than the maximum residual strain (residual stress/Young's modulus) [167]. This corresponds to .09% for supplier A/AR condition and .02% for supplier B/AR. The implication is that residual stress is eliminated early in the lifetime of any specimen.

7.2.2   Surface Condition

7.2.2.1   Pickling

The effect of a pickling operation on SCC behavior of as-received material is minimal. The supplier A specimens for the AR and AR + P conditions have very similar times to failure at a given stress indicating that the different surface conditions shown in Figs. 3.3(a)

and 3.3(c) do not affect SCC behavior. A modest different in stress

versus time to failure between the AR and AR + P conditions in supplier

B is evident in Fig. 6.10. In the AR condition the surface with the

large pits, Fig. 3.3(b), has a lower time to failure at a given stress

than the AR + P condition, Fig. 3.3(d). SEM observations of incipient

cracks reveal that many initiate from the large pits, e.g. the crack

shown in Fig. 6.24. These conclusions disagree with other studies where

a substantial increase in time to failure with pickling is found in split

ring tests [82] and in tube pressurization tests [86].

7.2.2.2   Honing

The most substantial effect of material condition on SCC

behavior for both suppliers is observed in the honed, stress-relieved,

and pickled specimens. The difference between SR + P and H + SR + P

samples clearly indicates an effect of the mechanical removal of material

by honing which carries through subsequent stress-relief and pickling

steps. The differences are most prevalent in the high stress specimens

A-5 and B-6. Supplier B remains more susceptible than supplier A in

the H + SR + P condition.

The honed surface is the least well characterized by any

condition considered in this study since the depth and extent of "damage"

is not known. Most likely, a thin layer of heavily worked, gouged metal

is present with less deformation as depth from the ID surface increases.

The surface roughness is greater for the H + SR + P condition than the

AR + P condition, Table 3.4. To obtain a qualitative measure of the

residual cold-work, line broadening measurements on the $\{10\bar{1}3\}$ peak are

reported in Table 7.1. Greater peak width is associated with increased residual levels of cold-work [168]. It is evident that the values for the H + SR + P surfaces are greater than for the SR + P only.

7.2.3 Texture

Residual stress and surface finish have a negligible effect on SCC susceptibility so texture must be considered as the explanation for the large difference in behavior between supplier A and supplier B cladding. The potential effect of an anomalous ID surface texture is precluded since none is found in the texture evaluation of Figs. 3.4-3.7 and pickling does not significantly alter the susceptibility of the two suppliers.

Supplier A (f_r = 0.63 at ID surface) has a significantly more radial basal pole texture than supplier B (f_r = 0.54 at ID surface). Fig. 7.2 shows the radial-tangential (R-T) scan for ID surface samples of both suppliers. The peak intensity is at $\phi \sim 35°$ for both suppliers but is sharper and more intense for supplier A. The basal pole intensity at high tilt angles ($\phi > 70°$), where planes are well oriented for transgranular cleavage, is greater for supplier B. Figure 7.3 compares the textures in another way. Inverse pole figure data for radial samples are used to construct a plot of cumulative basal pole volume fraction versus α. The angle α = ($90° - \phi$) is measured from the edge of the inverse pole figure, i.e. α = $0°$ corresponds to ϕ = $90°$ from the radial direction and α = $90°$ corresponds to ϕ = $0°$. Since the basal poles are most strongly concentrated near the R-T plane, α is a good (but not exact) approximation of the angle measured from the tangential direction toward the radial direction, i.e. the complementary angle to ϕ in the R-T

scan. Fig. 7.3 shows that a much larger volume fraction of grains have basal poles near the tangential direction for supplier B tubing than for supplier A tubing. For example, approximately twice the volume fraction of grains in supplier B tubing have basal poles oriented within 35° of the tangential direction than in supplier A tubing (0.36 versus 0.18).

Two tube pressurization studies on materials with various textures [113,121] prove that the more radial basal pole texture has both a higher threshold stress and a longer time to fracture at any stress above threshold than tubing with more tangentially oriented basal poles. This is the exact trend observed for suppliers A and B. Later discussion separates the effect of texture on the initiation and propagation stages of iodine SCC.

The largest variations in the stress versus time to failure for either supplier are between groups of samples with the same material/ surface condition. Fig. 6.11 includes SRI, International test results [111] on the same A and B cladding lots in the AR condition. The difference within the supplier A data is particularly evident. Results are available for two groups of SR + P specimens. Group 1 specimens are tested as part of the test matrix in Fig. 5.2. An additional set of specimens, Group 2, is received at a later time for the test matrix in Fig. 5.3. Fig. 7.4 shows within lot variation in SCC behavior. The processing steps and material characteristics discussed previously (residual stress, surface condition, deformation characteristics) could not cause the magnitude of the observed differences since they have been shown to have a marginal effect on SCC susceptibility. This leaves within lot texture variation as the most likely explanation. The f_r

numbers are determined for each group and the results are indicated on Fig. 7.4. The trend in SCC results for within lot texture variation is consistent for supplier A, but not supplier B.

A texture effect on mechanical properties is evident from the iodine SCC results. The substantial difference in SCC susceptibility between supplier A and B is reflected in the plots of strain and average strain rate versus time-to-failure, Figs. 6.12 and 6.13, respectively. To understand this behavior, information on the creep behavior of these materials is required. Fig. 7.5 shows creep curves at 138 MPa (20 ksi) and 300°C [169]. Supplier B is much more creep resistance than supplier A because the more transverse texture has a lower transverse creep strain. The same trend in creep behavior with texture is observed over the temperature range 300°C [170] to 400°C [76,169]. For a comparable time-to-failure, texture causes supplier B specimens to accumulate less creep strain which gives a lower average creep rate. Fig. 7.5 shows that both lots experience a decreasing creep rate with time in the transition from primary to secondary creep behavior, therefore, Eqn. (6-3) is only an approximation of the actual creep behavior. Within one supplier an effect of the SR heat treatment is evident where higher strains (and therefore average strain rates) are generally observed in the heat treated material. This trend is opposite to the trend observed by Kallstrom et al. [151] and could be due to differences in prior material processing steps such as degree of cold work and stress relief anneals.

7.3   Split Ring Test

The most critical question relative to the split ring tests is why the specimens do not fail. For constant deflection specimens, failure in the split ring test is known to depend on both the stress relaxation behavior and the inherent susceptibility of the material [101,112]. To a first approximation the failure criteria is that the stress remain high enough for a length of time sufficient for the failure curve to be reached. The yield stress and stress relaxation behavior control the stress level. The material condition ("susceptibility") determines the location of the failure curve. A comparison of the initial and final stress values for suppliers A and B, Table 6.9, shows that the amount of stress relaxation is only slightly greater for supplier B than supplier A. The failure curves from the tube pressurization tests are very different as seen in Figs. 6.9-6.11. For the times and stresses attained in split ring tests of Supplier A, it is clear that these specimens remained far from the failure curve, therefore, the absence of SCC cracks is expected. The same conclusion is reached for the lot 1340 material. The stress relaxation significantly lowers the stress particularly at the higher temperatures. The texture resembles the more resistent supplier A than the supplier B. For supplier B split ring tests, the time and stress levels approach the failure curve of this more susceptible material. Therefore, the detection of microcracks is not surprising.

No failure occurs in the lot 1340 material in the constant load tests which are a more severe loading condition. A combination of specimen response to stress and of the material resistance to SCC are probably responsible. Plastic creep strain is accumulated at the location of

highest stress which decreases the maximum tensile stress level at the clad ID. The constant load imposes a bending moment that remains essentially constant whereas the bending moment decreases in the constant deflection specimens. Thus, the maximum stress at the clad ID decreases, but a lesser amount than the constant deflection case. The calculated plastic strain at the ID surface after the specimen is unloaded is only slightly greater for the constant load specimens compared to the constant deflection tests. The important point is that the elastic stresses given in Tables 6.7 and 6.8 decrease due to plasticity and creep relaxation which delays the initiation stage, particularly in material that is relatively immune to iodine SCC.

7.4   Iodine SCC Phenomenology

7.4.1   Analysis of Crack Initiation

The crack initiation process has two stages: 1) penetration of iodine through the surface oxide film to the underlying metal and 2) formation of a microcrack or "crack nucleus". Consideration of initiation in terms of the three requirements for SCC is appropriate here. The iodine environment attacks the Zircaloy surface ultimately forming condensed iodides. Stress and strain affect the crack initiation steps by fracturing any thick oxide coatings to permit iodine penetration and by opening the initial crack nucleus. The relevant materials variables are surface finish, texture, and heat treatment which influence the initiation site.

Before further discussion of crack initiation can proceed, it must be determined what feature on the tube ID can be considered as

a crack. Examination of failed specimens by metallography identifies cracks two microns in depth. SEM observation of the ID surface detects incipient secondary cracks on the order of four microns in length as seen in Fig. 6.15(b). An "initiated crack", therefore, is established by the time a depth of one grain is reached.

7.4.1.1 Iodine Attack

Iodine penetration occurs readily in the tube pressurization tests. The very thin air formed film on the surface is penetrated without the application of strain [12]. The ID surface of the samples and unstressed cladding segments reveal slight pitting. Hydrolysis of residual iodides occurs at the end of the test when specimens are opened to the air indicating complete reaction of the initial iodine charge.

The iodine exposure of unstressed cladding segments indicates that iodine attack occurs preferentially at particles. Fig. 7.6 shows the series of steps starting with general attack of some regions of the surface. If particles are present in that region of general attack, localized attack occurs along the matrix/particle interface resulting in final removal of the particles. STEM analysis of second phase particles shows that Zr, Cr and Fe are present. Very few particles are found to contain any Ni which is also known to be present in certain types of intermetallic particles [171]. No localized attack is evident at pre-existing pits (0.5 - 1 μm in size). The behavior described here is observed in both suppliers in both the as-received and pickled surface conditions. The behavior of slotted ring specimens exposed to a flowing iodine environment is similar. At 40 Pa (0.3 torr) extensive pitting

and attack at particles is seen. At 4 Pa (0.03 torr) much less attack is observed but cracking still occurs as seen in Fig. 6.24.

7.4.1.2   Initiation Sites

Although preferential attack is noted at particles, an extensive search for microstructural features contributing to or causing initiation reveals no feature that is conspicuous in the initiation region for any crack in either supplier A or supplier B. Several initiation sites are reported in other studies:

1. Intermetallic and inclusion particles [75,117];

2. Intergranular sites [12,75,76,78,86,116-118];

3. Pits and flaws [12,79,114,116,117,121];

4. Hydrides [102];

5. Transgranular sites [18,116,118].

The variety of sites underscores the complexity of the initiation problem. Different material conditions and surface conditions influence the initiation process, but no micromechanistic understanding exists to develop a unified view from the various observations. A detailed discussion of the effects of particular surface and material conditions on initiation site is presented in Appendix G.

7.4.1.3   Texture

Since a strong texture effect is observed in both the crack propagation tests and the tube pressurization tests, special consideration is given to the role of texture in crack intiation. An experiment by Peehs et al. [81] is particularly relevant here. A tube is machined from

heavily textured plate giving a strong circumferential texture gradient.
It is tested by tube pressurization with some iodine. Fig. 7.7 shows
that microcracks are formed preferentially where basal poles are located
50° to 75° from the radial direction. Very few microcracks form where
basal poles are normal to the tube surface. This microcrack distribution
indicates that crack initiation depends on texture. The split ring test
results are consistent with this hypothesis since microcracks, as seen in
Fig. 6.24, form in the more tangentially oriented supplier B material
while no microcracks form in supplier A material for equivalent test
conditions (temperature, time, environment, material condition, and
initial stress). If a strong tangential texture is more susceptible to
cracking, then more cracks should be observed in the metallographic cross-
sections of supplier B than supplier A (Figs. 6.21 and 6.22). This is not
the case since the trend reveals a slightly higher microcrack density in
supplier A than in supplier B. At higher stresses, the relatively rapid
times to failure in supplier B might preclude the development of
significant numbers of microcracks, i.e. rapid propagation and failure
occurs before sufficient strain/time are able to nucleate additional
cracks.

7.4.2   Analysis of Crack Propagation

Since ample fractographic evidence of SCC features is available
for both tubing and fracture mechanics specimens, a comparison of
features is useful. The mechanistic models of several investigators are
critically evaluated. Crack propagation behavior for both fracture
mechanics specimens and tubing tests is analyzed in terms of some of

these models. Finally, the crack intiation and crack propagation stages of SCC are bridged by analyzing the relative lengths of time that a tubing specimen spends in each regime.

7.4.2.1   Relation of Fractography to Texture

Fractographic features in many studies of recrystallized tubing follow the sequence of intergranular propagation near the initiation site to transgranular propagation as crack growth proceeds [76,78, 118]. This sequence can be explained by results from fracture mechanics specimens. The value of K is low for a shallow crack, even when a rather high nominal stress is imposed on the tube. As the crack grows under constant stress, K increases. Qualitatively, the sequence of "low K"-intergranular and "high K"-transgranular corresponds to the fractography observed in the crack arrest tests and crack growth tests through the tube wall of Videm and Lunde [118].

The texture effect on crack propagation is discussed in Section 7.1.2. Observations from tubing specimens are consistent with the crack arrest results. It is important to remember that specimen orientation for the fracture mechanics specimens, Fig. 5.1, differ from the crack path through the tubing wall. Tubing cracks represent a TN orientation which could not be tested.

Examination of the fracture surfaces from tubing in Figs. 6.18-6.20 provides further evidence of a stress and texture dependent on crack propagation. Figs. 6.18 and 6.19 are micrographs of specimens from suppliers A and B, respectively, at approximately 345 MPa (50 ksi). Neither surface is macroscopically flat and both show cleavage features

with small facets and tearing between facets. Fluting features are seen

occasionally. Figs. 6.19 and 6.20 compare supplier B at two stress

levels, 345 MPa and 221 MPa (32 ksi), respectively. The specimen at

lower stress has larger cleavage facets with less tearing between facets

and with a more macroscopically flat surface than the higher stress

specimen. The stress intensity and crack velocity is lower for any given

crack length at 221 MPa than at 345 MPa. The difference in failure

appearance is analogous to the behavior in the fracture mechanics

specimen. High K/high velocity produces small cleavage facets and

tearing between facets while low K near K_{ISCC}/low velocity produces

larger cleavage facets and less tearing between facets.

The texture effect is also shown by the metallographic examina-

tion of incipient cracks. The cracks in supplier B samples, Fig. 6.23,

propagate on a microscopic (grain to grain) scale that is more normal to

the applied hoop stress than supplier A samples. This behavior is

related to the larger volume fraction of basal planes with proper orienta-

tion for cleavage, i.e. near radial, as shown in Fig. 7.3.

The texture effect is expected to be most critical for short

cracks. Once nucleated, a short crack might arrest if it encounters

grain(s) not well oriented for cleavage. This is one explanation for the

somewhat larger number of incipient cracks in supplier A at 320°C and the

tendency to have cracks in the 5-20 μm range. Alternatively, a crack

nucleated in material well oriented for cleavage tends to propagate

readily. If this situation is to apply to supplier B material, initiation

must be somewhat difficult, particularly at low stress/long time to

failure to account for the small number of incipient cracks observed at

320°C.

7.4.2.2   <u>Modeling SCC Behavior</u>

A mechanistic model must incorporate a variety of factors
relating to both the mechanics and the materials aspects of SCC.
Several features are considered.

1. Crack geometry – tubing cracks have a short length with
    thumbnail configuration;

2. plasticity – near the failure threshold, the crack propaga-
    tes under elastic conditions, however, both short term
    and creep plastic deformation become important as the
    yield stress is approached;

3. texture – from previous discussion, this materials
    variable · has a strong influence on both initiation and
    propagation;

4. fracture surface appearance – observations from both
    fracture mechanics specimens and tubing tests indicate
    that intergranular, cleavage, and ductile features depend
    on both crack velocity and texture;

5. initiation versus propagation – the failure time of a
    smooth specimen is the sum of these two components.

Five mechanics-based models for iodine SCC of Zircaloy are
summarized. Other models exist for predicting cladding behavior under
fuel rod operating conditions where a wide range of conditions and
phenomena are considered [136,146,172], e.g. temperature, variable
stress, variable fission product (iodine) concentration, irradiation,
etc. The models considered here would be a part of such a code. The
approach, assumptions, essential features, regions of validity, and

shortcomings are discussed. The results of this experimental program are then analyzed in terms of these models.

7.4.2.2.1 Description of Models

Five models are described below in brief fashion. Table 7.2 compares all the models both on the basis of approach and on several attributes considered in each model. General comments on several model characteristics from Table 7.2 are presented.

Propagation. Most models assume growth from a pre-existing defect or "crack nucleus" but do not consider the formation of the crack.

Threshold, Growth above Threshold. All models predict this behavior.

Plasticity. Only two models [8,144] are applicable above the yield stress. Both reach the same result that an increment of strain in the plastic regime produces twice the crack opening as is provided by an equivalent increment of strain in the elastic regime.

Crack Geometry. Most models do not explicitly consider the corrections to fracture mechanics calculations that account for the thumbnail crack geometry of a partial through wall crack. Corrections for front free surface, back free surface, finite width, and plastic zone could be made from available empirical correlations [175-177]. Such corrections are also applicable above the yield stress [178]. For the geometry of interest, a correction on $K = \sigma\sqrt{\pi a}$ is typically less than 20% [143,177].

Fit to Data. Only Kreyns et al. [145] attempt to fit their model to experimental data. The approach used in most other models is

to make a calculation of a threshold parameter (J, K, or δ) using typical values for model parameters and comparing the calculated threshold value with experimental results.

The five models are introduced in subsequent discussion. The general approach and some key equations are presented, but the reader is advised to consult the reference for a detailed treatment of a particular model.

Smith and Miller [173]. The crack model is shown in Fig. 7.8. A COD approach is used. Cleavage failure occurs readily at an opening, δ_c, leaving an unfailed region, a. This region supports a fraction of the yield stress qY where $q = 3 q_f$, q_f being the fraction of fluted grains and Y is the yield stress. The region of partial cohesion fails at an opening, δ_f. Plastic and elastic zones are located ahead of the region of partial cohesion. This basic model is applied to both propagation from a crack and from an ID surface flaw. Minor modifications are made by Smith [174] to explicitly consider a texture effect. The physical model is consistent with observations of cleavage complemented by more difficult plastic processes. Fluting is observed only to a limited extent so δ_f should apply to ductile processes in general which include tearing as well as fluting. A threshold stress for propagation as a fraction of yield stress is calculated, however, the "fracture process zone" is calculated to be 200-300 μm.

Tomkins and Gittus [144]. An elastic-plastic model using a COD approach based on the Bilby-Cottrell-Swinden(BCS) crack model [179] is proposed. The governing equation is:

$$\delta = \frac{2AaT}{\pi E} \ln \left[\sec \left(\frac{\pi \sigma}{2T} \right) \right] + \frac{Aa\varepsilon_p}{(n+1)} \tan \left(\frac{\pi \sigma}{2T} \right) \qquad (7\text{-}1)$$

where a is crack length, A is a constant, T is the ultimate strength, E is Young's modulus, σ is stress, ε_p is plastic strain, and n is work hardening exponent. A significant plastic term is assumed to be present but does not occur at low stresses in susceptible material such as supplier B cladding or in irradiated material [110]. At threshold, δ, σ, and ε_p assume critical values of δ_{ISCC}, σ^*, and ε_p^*. The crack growth model requires continued plastic straining to maintain the crack opening above δ_{ISCC}.

Adams, Baty, and Murty [143]. This model is unusual among the five being considered since it deals strictly with crack initiation. Initiation is assumed to occur by cleavage along basal planes in properly oriented grains at a particular threshold stress. Texture is considered explicitly in the model. The basal plane distribution is weighted according to the applied stress state to calculate a susceptibility parameter, S, which is assumed to be inversely proportional to failure time to a first approximation. Plotting normalized stress versus 1/S gives a diagram similar to σ versus t_f data, but with a strong texture dependence. Crack propagation is not considered. No process other than cleavage is modeled which excludes any plastic deformation contribution

to initiation. A final objection centers around the reciprocal relation-ship between S and t_f which is only hypothetical at this time.

Kreyns, Spahr, and McCauley [145]. A fracture mechanics (K) approach to crack propagation is used. Cracks are assumed to grow from pre-existing surface defects (pits and gouges) with no incubation time. The power law crack growth data of Wood [82] are used to predict σ versus t_f results by the Bettis investigators [116]. This model represents the only attempt to consider the tubing/thumbnail crack geometry and to predict experimental data. Several weaknesses are evident. Although cracks are observed to initiate from surface imperfectsion (e.g. Ref. [116] and supplier B/AR), the effect on SCC susceptibility is small as demonstrated by supplier B cladding. The application of fracture mechanics to a shallow, blunt notch is very dubious. The K_{ISCC} values of ~32 MPa$\sqrt{m}$ used by these investigators was later corrected by Cox to a value of 9 MPa$\sqrt{m}$ [100]. The assumption of no incubation time was not verified. In conclusion, the good fit of model to data should be viewed with skepticism until several critical model assumptions are confirmed.

Garlick and Gravenor [8]. This model explores the application of the J-integral to the SCC problem, but only extends the use of K into the regime of small plastic strains. Equations for J_{ISCC} are developed and a framework to consider crack growth above J_{ISCC} is introduced. The authors attempt no model development beyond this point.

7.4.2.2.2 Modeling Experimental Data

The crack arrest data from fracture mechanics specimens are analyzed in terms of the model of Smith and Miller [173]. The K_{ISCC} values for stress-relieved specimens are used to calculate δ_{ISCC} using the relationship:

$$\delta_{ISCC} = \frac{K_{ISCC}^2}{E\sigma_y} \qquad (7-2)$$

δ_{ISCC} is plotted against f in Fig. 7.9 analogous to the K_{ISCC} versus f plot in Fig. 6.1.

The crack opening displacement consists of both a cleavage and a plastic contribution. The cleavage contribution is calculated from the model of Gell and Smith [180]. For cleavage facets ahead of the crack tilted at an angle ϕ from the macroscopic crack growth direction, the cleavage depends on ϕ as:

$$\sigma_c \propto \sec^2 \frac{\phi}{2} \qquad (7-3)$$

Since COD is proportional to stress squared, the relationship for crack opening normalized to the perfect cleavage case is:

$$\frac{\delta}{\delta_{f=1}} = (\sec^2 \frac{\phi}{2})^2 \qquad (7-4)$$

Kearns [150] defines an effective tilt angle from the f parameter as

$$\phi_{eff} = \cos^{-1} \sqrt{f} \qquad (7-5)$$

substitution of Eqn. (7-5) into Eqn. (7-4) yields the dependence of cleavage crack opening on texture:

$$\frac{\delta}{\delta_{f=1}} = (\frac{2}{1 + \sqrt{f}})^2 \qquad (7-6)$$

Assuming $\delta_{f=1} = 0.33$ µm to match δ_{ISCC} values at high f, δ is plotted as $\delta_{cleavage}$ in Fig. 7.9. This analysis predicts that misorientation of cleavage facets has a secondary effect on δ_{ISCC}. The conclusion is that the plastic processes are primarily responsible for the increase in δ_{ISCC} at $f \leq 0.5$. Fractography supports this conclusion since higher levels of tearing between cleavage facets are observed on fracture surfaces at lower f values. Fig. 6.3 shows that crack opening (as measured by K) above threshold produces substantially more tearing than δ at the threshold.

The propagation of through-wall cracks is modeled using a stress intensity approach. The basic equations and definition of addition terms are:

$$K = M_e \sigma \sqrt{\pi \frac{a}{Q}} \qquad (7-7)$$

$$M_e = M_1 + (\sqrt{Q \frac{c}{a}} - M_1) (\frac{a}{t})^p \qquad (7-7a)$$

$$Q = 1 + 1.47 (\frac{a}{c})^{1.64} - 0.212 \frac{\sigma^2}{\sigma_y^2} \qquad (7-7b)$$

$$p = 2 + 8 (\frac{a}{c})^3 \qquad (7-7c)$$

$$M_1 = 1.13 - 0.1 (\frac{a}{c}) \qquad (7-7d)$$

The empirical correction factors are due to Neuman [177]. The parameters are defined such that M_e is the elastic magnification factor which considers both front and back face corrections; M_1 is the front face correction; 2c is the surface crack length; a is the depth of the surface crack; and t is the wall thickness. The corrections not considered are a shell curvature effect [181] and collateral aligned cracks [115] which are observed in fractography.

The specimen case that is evaluated is the growth of a surface crack, $\frac{a}{c} = 0.5$, near the threshold stress through the wall of supplier A (331 MPa) and supplier B (221 MPa). The result is plotted in Fig. 7.10. K and δ are calculated from Eqns. (7-7) and (7-2), respectively. Elastic fracture mechanics is not valid until the crack penetrates ∿40% of the tube wall. Less plastic contribution to δ is predicted from Fig. 7.9 for supplier B than supplier A. Careful analysis of the tubing fractography in Figs. 6.18-6.20 shows that this is the case.

7.4.2.3   Relative Initiation and Propagation Times

The separation of time to failure in smooth specimens is an important consideration. Other investigators have attempted such a separation by direct or indirect means. Peehs et al. [81] find that approximately 55% of a ∿3 hr split ring test at 400°C is consumed by incubation followed by an enhanced deformation period which is correlated with crack propagation. A tube pressurization test by Peehs et al. [115] at 400°C and 225 MPa showed a strong acoustic emission signal within the first 20 minutes of the 600 minute test which is interpreted as crack initiation. Videm and Lunde [117] test smooth and precracked cladding

segments of recrystallized material at 340°C. They conclude that roughly three-quarters of the lifetime is consumed by crack initiation for times to failure in the approximately range 30-1200 minutes and that the initiation fraction of life increases as the temperature decreases. In this study the large number of microcracks observed 390°C compared to 320°C indicates that cracks initiate more readily at high temperature.

At 320°C analysis of the limiting cases must be used to define the relative initiation and propagation fractions of lifetime. If initiation occurs readily and most of life is spent in propagation, many microcracks would be evident. This is clearly not the case. If initiation requires most of specime life, very few microcracks would be present and crack opening angle would be small since little plastic strain would accumulate during propagation to open the crack. Supplier A and supplier B must be compared separately regarding this point. Few microcracks are found in supplier A but several have propagated beyond a depth of one or two grains. A relatively large crack opening angle is shown in Fig. 6.16. A best guess is that crack initiation occurs in the middle third of specimen lifetime. Few microcracks are also found in supplier B. Crack opening angles decrease with stress. However, the total creep strain also decrease, so this trend is not unexpected. At high stresses (>345 MPa), the COA is comparable to supplier A despite lower strain at failure and shorter lifetime so initiation occurs quite rapidly, probably at less than half the lifetime. At low stress (<300 MPa) both strain and COA are small so a judgement is not clearcut. More time is spent in propagation at lower stress than at high stress on an absolute scale based on a comparison of fractography in Figs. 6.19 and

6.20.   Considering the limited number of microcracks formed over the length of time for the low stress tests, initiation is possibly delayed to later in life, possibly until the order of two-thirds of lifetime is accumulated. It is again emphasized that this qualitative separation of initiation and propagation times is inferred from observations rather than direct experimental measurement of these times.

In conclusion, initiation requires a substantial fraction of the reported times to failure with the possible exception of the high stress levels in susceptible (supplier B) material. This conclusion is supported by the tests on tubing of different wall thicknesses, Table 6.5, where no consistent difference in time to failure emerges between the two wall thicknesses. An important point is that the absolute times for initiation must be quite different for the two suppliers to account for the appreaciable differences in lifetime. Some, but not all, the difference can be justified on the basis of variation in the rate of crack propagation between supplier A and supplier B.

7.4.3   Role of Stress and Strain

7.4.3.1   Mechanical Variables

Controversy exists regarding the mechanical variable that controls SCC susceptibility. A particular study might conclude that any one of the loading variables of stress, strain, strain rate, or stress intensity is responsible for iodine SCC failure. Such an approach is overly simple considering the complexity of both Zircaloy mechanical properties and the SCC process. Stress, strain, and strain rate not independent; they are linked by the flow and creep properties of the

material which are a function of prior cold-work, annealing conditions, and texture.

The role of stress, strain, strain rate and stress intensity must be evaluated in terms of the critical steps in the SCC process:

1. crack initiation (film rupture and crack formation), and

2. crack propagation (environmentally assisted growth of the flaw to a critical size and final ductile rupture).

Previous attempts to correlate SCC behavior with mechanical variables have not separated mechanical loading effects on these steps. This is one explanation for the poor correlation of failure time with strain and strain rate, i.e. values for total strain at fracture and for "average" strain rate do not provide any insight into the potentially different processes occurring during initiation and propagation. It is probable that no single mechanical parameters controls SCC behavior for all stresses and during all stages of cracking. The key to resolving the effect of mechanical load is an understanding of the local mechanical and chemical processes that contribute to cracking. Subsequent discussion considers initiation and propagation separately.

7.4.3.2   Microstructural Mechanism for Crack Initiation

An evaluation of the initiation process must incorporate several observations: many microstructural features associated with initiation, a texture effect, and a temperature dependence. Plastic deformation is know to be a prerequisite for initiation, therefore, slip might be the key factor leading to initiation at any number of potential sites. Peehs et al. [115] noted extensive microcracking at 400°C where

creep rates are expected to be rapid. At high strain levels, increase microcracking is demonstrated both in the tubing cross-section (Figs. 6.21 and 6.22) and the plastic zones at the end of tubing surface cracks. (Fig. 6.15). Gangloff and Coffin [18] report a strain threshold and more numerous cracking with increased strain levels above the threshold. An additional requirement is strain localization which is necessary to build up local stress levels at potential initiation sites. Slip band formation due to channeling is observed to cause intergranular crack initiation in irradiated material [21]. In another case intergranular microcrack formation is inferred from difference in slip behavior in grains adjacent to microcracks [79].

The dual requirements of strain accumulation and strain localization are capable of explaining texture, heat treatment, and irradiation effects on initiation. The role of texture is two fold: it promotes larger plastic strain at a given stress for radial textures, and it provides tangential basal poles properly oriented for transgranular initiation in the more tangential textures. The cleavage event leading to initiation could result from local stress buildup similar to the case of intergranular initiation. As annealing temperature increases, larger initiation strains are necessary to cause strain localization. For recrystallized material, several percent strain is required to cause cracking since a dislocation structure capable of supporting local stress concentration must be established. This is supported by observations on recrystallized material [75,79]. Intense slip bands, or channels, are know to develop when recrystallized and irradiated Zircaloy is strained a small amount which accounts for the reduced strain to failure in SCC. Although stress

concentration is required for crack initiation by cleavage (consider the model of Baty et al. [143]), plastic strain accumulation is the critical microstructural event.

The site that is activated depends on several factors: texture, surface condition, flaws, pits, second phase particles, and intermetallic particles, microstructure (cold-worked versus recrystallized), residual cold work in cold-worked and stress-relieved material, and irradiation. With sufficient strain and strain localization, the easiest site is activated followed by secondary sites. This accounts for the observation of several types of sites on the same specimen and for changes in the type of site with stress level [75,117].

7.4.3.3   Crack Propagation

At appreciable crack size, crack propagation is controlled by a fracture mechanics based parameter. The study of Videm and Lunde [117] provides critical experimental verification. A crack of ~50 μm is able to propagate below the stress threshold for unflawed specimens. The apparent stress threshold decreases with increase flaw size indicating a K controlled process. Fig. 7.10 predicts that crack growth near the stress threshold is K controlled when a crack size of 300 μm is reached. This critical crack size is reduced at higher stress values.

Experimental observations show that a "crack" is identifiable when a depth of only one or two grains is reached. An important question is what mechanical variable controls the growth of this crack nucleus from a depth of several microns where strain/stress are controlling to the order of 100 microns where fracture mechanics is applicable. Smith

and Miller [173] model this behavior based on a COD approach. A basic assumption is that a plastic zone and multi-axial elastic stress state form ahead of a surface flaw. From a mechanics standpoint, this assumption is questionable. As a short crack grows, the stress concentration should increase providing a transition to a crack that can be analyzed by linear elastic fracture mechanics.

7.4.3.4   Threshold Behavior

A popular mechanism for analyzing the SCC behavior is consideration of threshold values below which no cracking occurs. Stress, strain, strain rate, and stress intensity thresholds are reported. A problem with the threshold concept is that materials and testing variables often have a substantial influence on the threshold values. Stress thresholds are sensitive to texture [this study, 113], heat treatment [86,109], test temperature [109], and surface condition [113]. The minimum strain at failure is sensitive to small changes in heat treatment as shown in Fig. 6.12 as well as test temperature [86,109]. K_{ISCC} is very texture dependent as seen in Fig. 6.1.

Another issue is whether threshold behavior is initiation or propagation controlled. For the low test temperatures, the process is clearly initiation controlled. Few microcracks are observed near the threshold in the tube tests at 320°C. Cox and Wood [12] report that cracking occurs at temperature down to 210±20°C while crack propagation is pre-cracked specimens in iodine is measurable at room temperature. At higher temperatures ($\geq$350°C), the choice of initiation or propagation is less clear cut. Initiation occurs more readily based on the observation of many microcracks [this study, 109,115] and rapid initiation

times [81,115]. Non-propagating cracks are reported below the threshold
stress [75,117]. This indicates that propagation is more limiting at
high temperature than at low temperature. Failure might ultimately be
initiation controlled at very long times as indicated by the low
threshold stresses for very long term (>5,000 hr) tube pressurization
tests [116].

7.4.4 Role of Irradiation

Several effects of neutron irradiation are noted in SCC tests.

1. Threshold stress values decrease as irradiation dose
   approaches saturation [82,83,106,107,120].

2. SCC susceptibility is substantially increased compared to
   unirradiated material.

3. Stress versus time to failure and ductility values are
   similar when irradiated stress-relieved and irradiated
   recrystallized materials are compared [77,106,107,120].

4. Macroscopic strain at failure is greatly reduced by
   irradiation [77,78,120].

5. The fractographic features for irradiated material resemble
   the features in comparable unirradiated material.

The increased susceptibility of irradiated material is
explained by enhanced crack initiation. Lee and Adamson [78] show that
localized flow by dislocation channeling is responsible for crack initia-
tion. Adamson [103] observes that 60° material is slightly more
susceptible than 0° and 25° material in constant extension rate tests.
Tube pressurization tests on irradiated material [106,107] show that
different materials and heat treatments approach the same stress
threshold.

Little is known about the texture effect on cracking of irradiated Zircaloy. The crack initiation step is consistent with the model of local strain concentration presented previously. Since channeling is texture dependent [78], initiation would also be expected to have some texture dependence. The cleavage and tearing morphologies in crack propagation in irradiated material should retain a texture dependence similar to unirradiated material. Mechanical properties retain a texture dependence following irradiation [77,78,133,134]. Although the critical tests on irradiated material have not been done, a texture effect should be retained following neutron irradiation.

Table 7.1

Line Broadening Measurements on the $\{10\bar{1}3\}$ Peak

for Suppliers A and B Material

Material Condition	$\{10\bar{1}3\}$ Peak Width at Half the Maximum Intensity (radians)	
	Supplier A	Supplier B
AR	7.68×10^{-3}	7.16×10^{-3}
SR+P	6.35×10^{-3}	6.63×10^{-3}
H+SR+P	7.33×10^{-3}	7.75×10^{-3}

Table 7.2

SUMMARY OF THE CHARACTERISTICS OF SEVERAL SCC MODELS

Authors	Reference	Approach						Model Attributes						
		σ_{crit}	COD	J-integral	K	Initiation	Propagation	Plasticity	Threshold	Crack growth above threshold	Crack growth kinetics	Thumbnail crack geometry	Texture	Fit to data
Smith and Miller	[173,174]		X				X		X	X			X	
Tomkins and Gittus	[144]		X				X	X	X	X	X			
Adams, Baty, and Murty	[143]	X				X			X	X			X	
Kreyns et al.	[145]				X		X	X	X	X	X	X		
Garlick and Gravenor	[8]			X			X	X	X	X	X			X

Fig. 7.1 Schematic diagram representing the relative orientation between cleavage facets (C) and flutes (F) for (a) the NL specimen orientation, and (b) the NT specimen orientation. The direction of macroscopic crack propagation is indicated on the cleavage facets of the top view. HCP cells give the basal pole orientation relative to the principal directions in the plate.

(a)

(b)
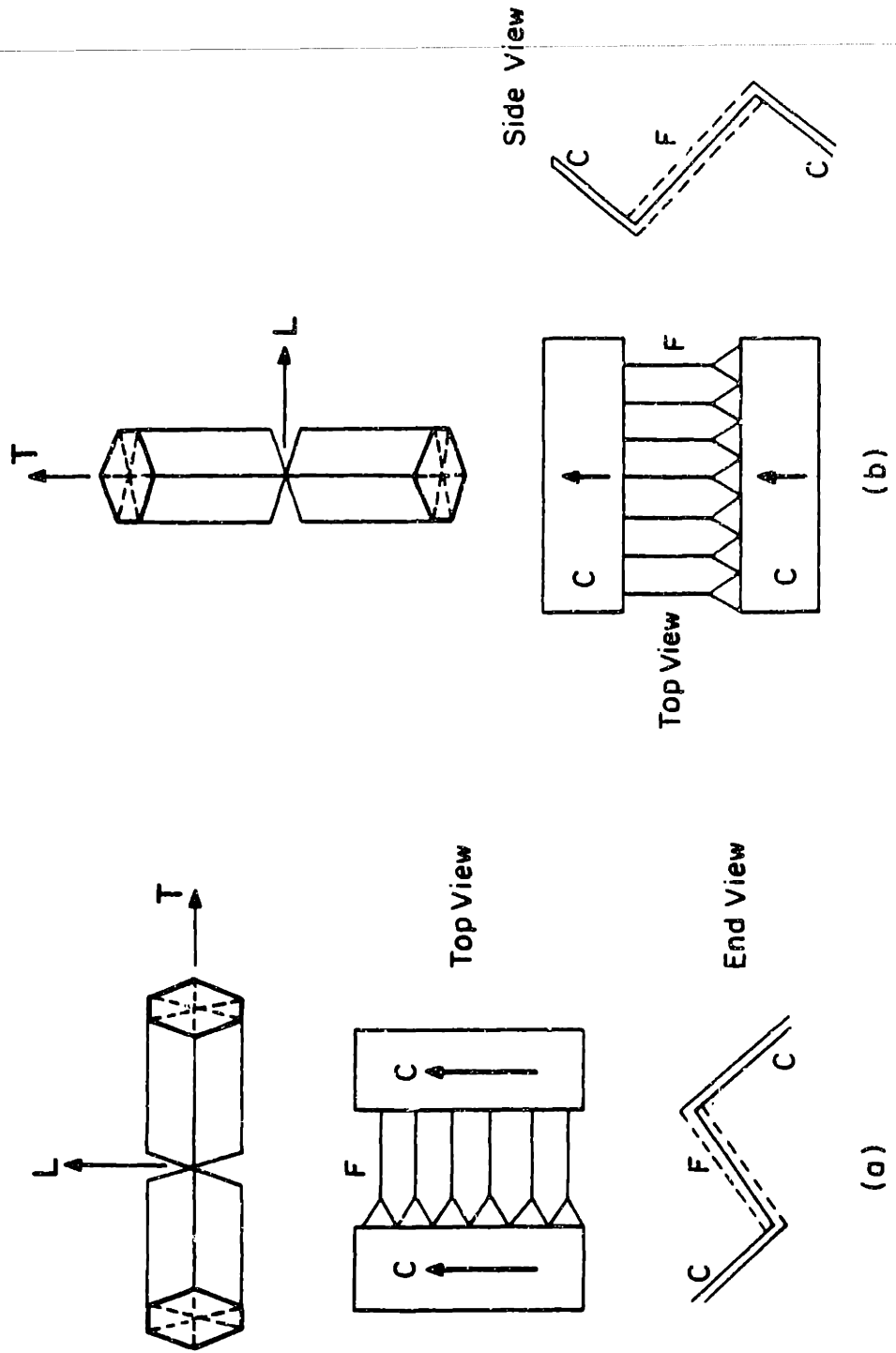
RADIAL-TANGENTIAL SCAN FOR

+   SUPPLIER A   ID SURFACE
☆   SUPPLIER B   ID SURFACE

FIGURE 7.2
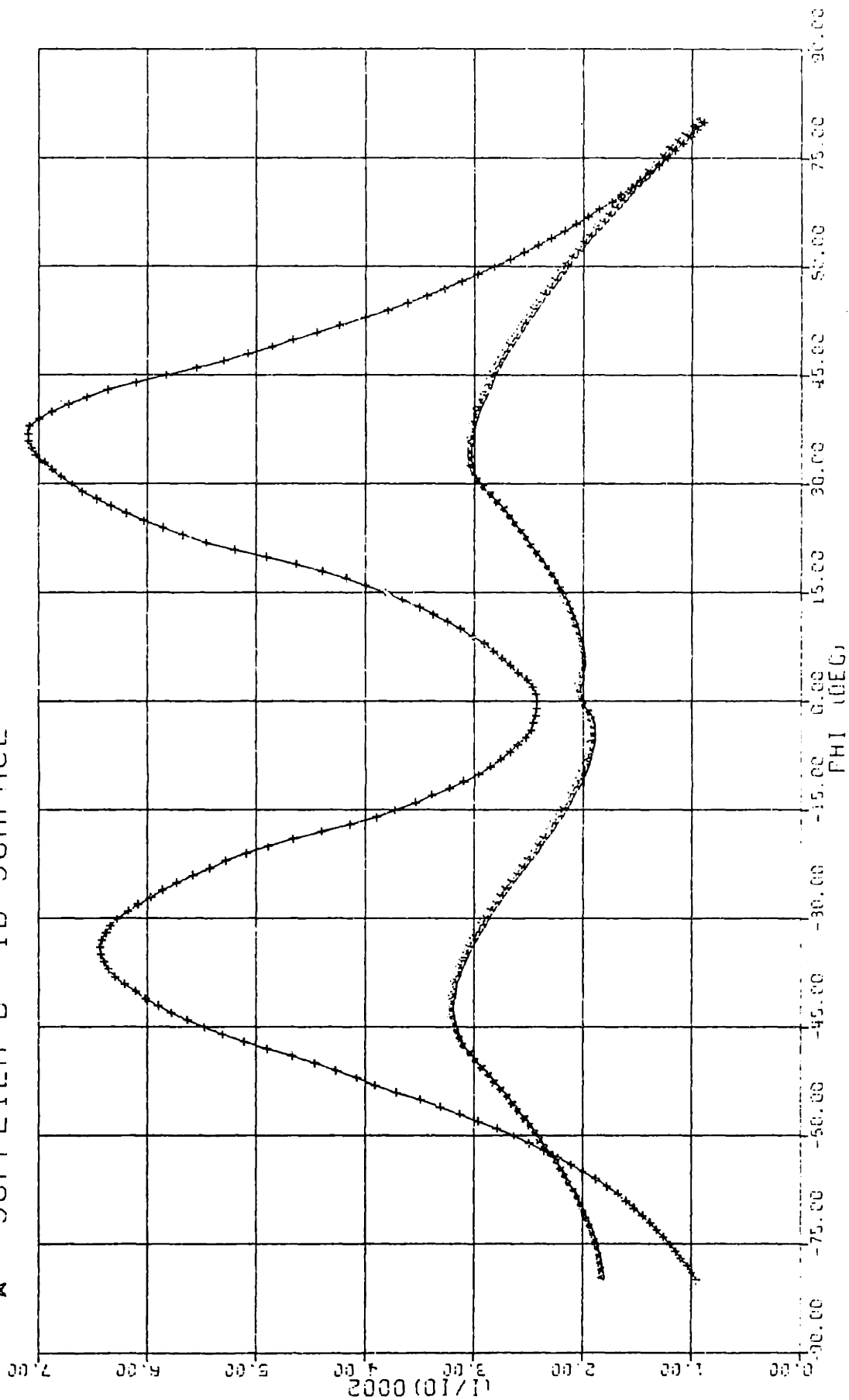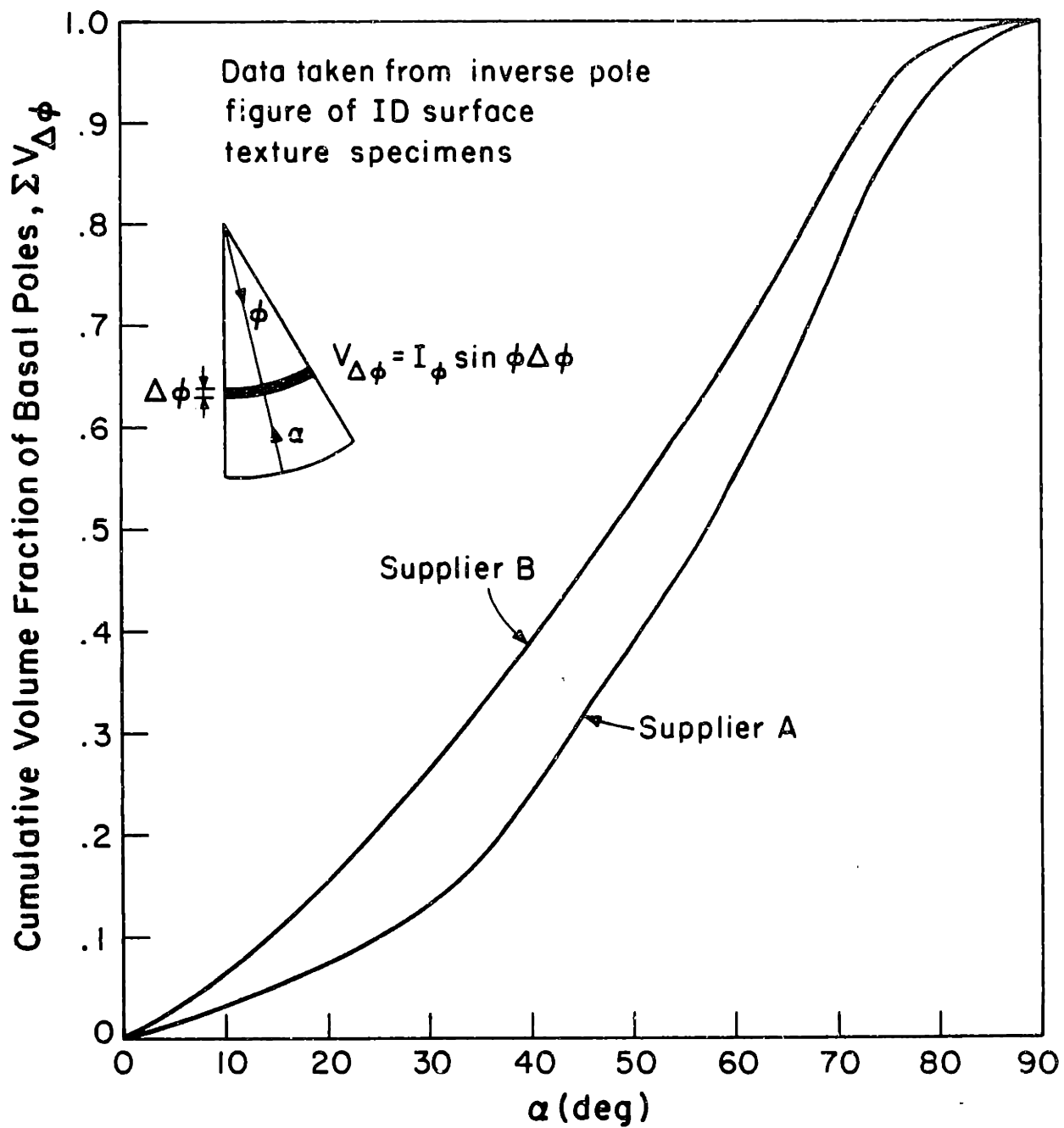
Figure 7.3

Variation of Basal Pole Volume Fraction with Tilt Angle

Figure 7.4

Comparison of Hoop Stress versus Time to Failure for Two Different Specimen Groups at 320°C
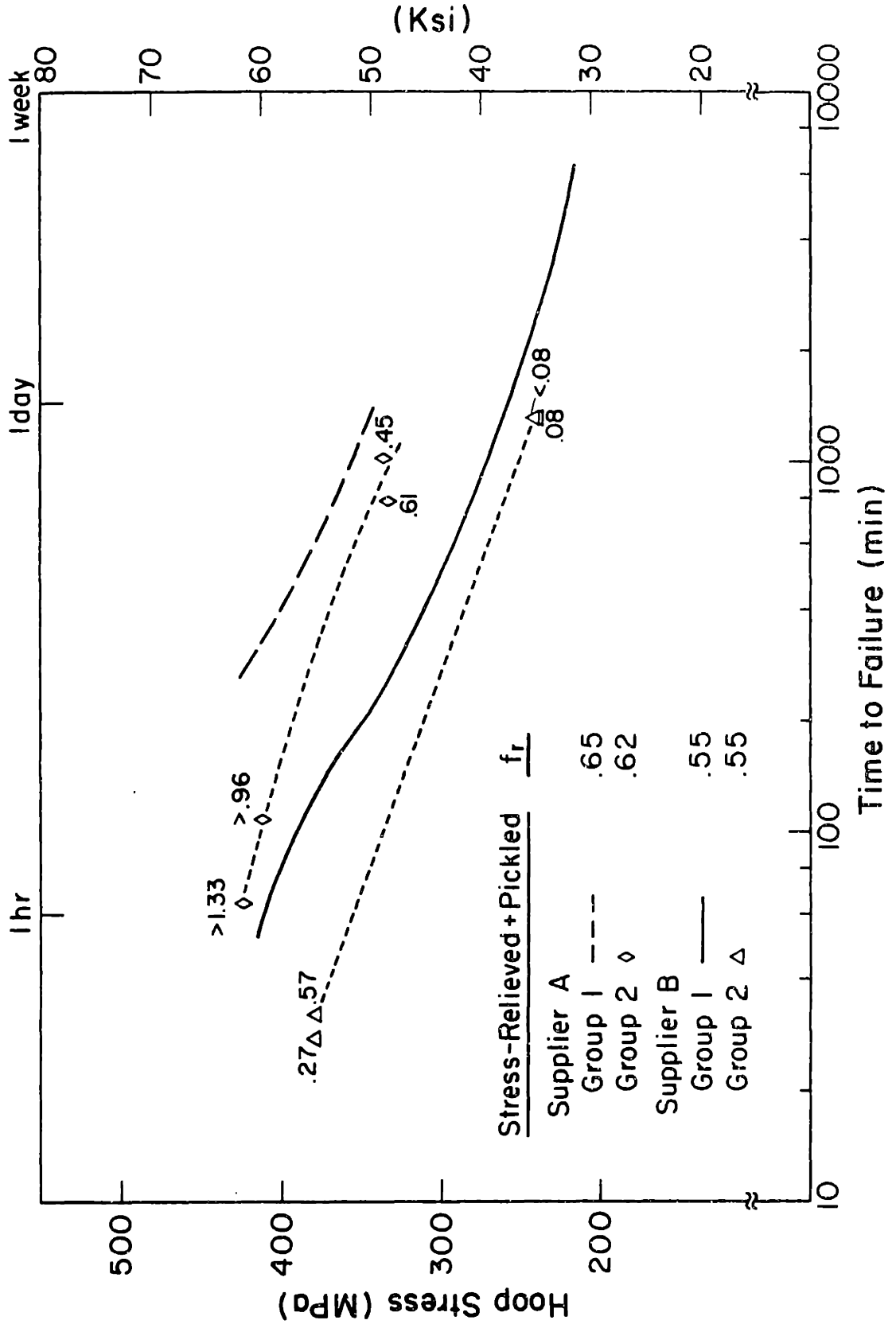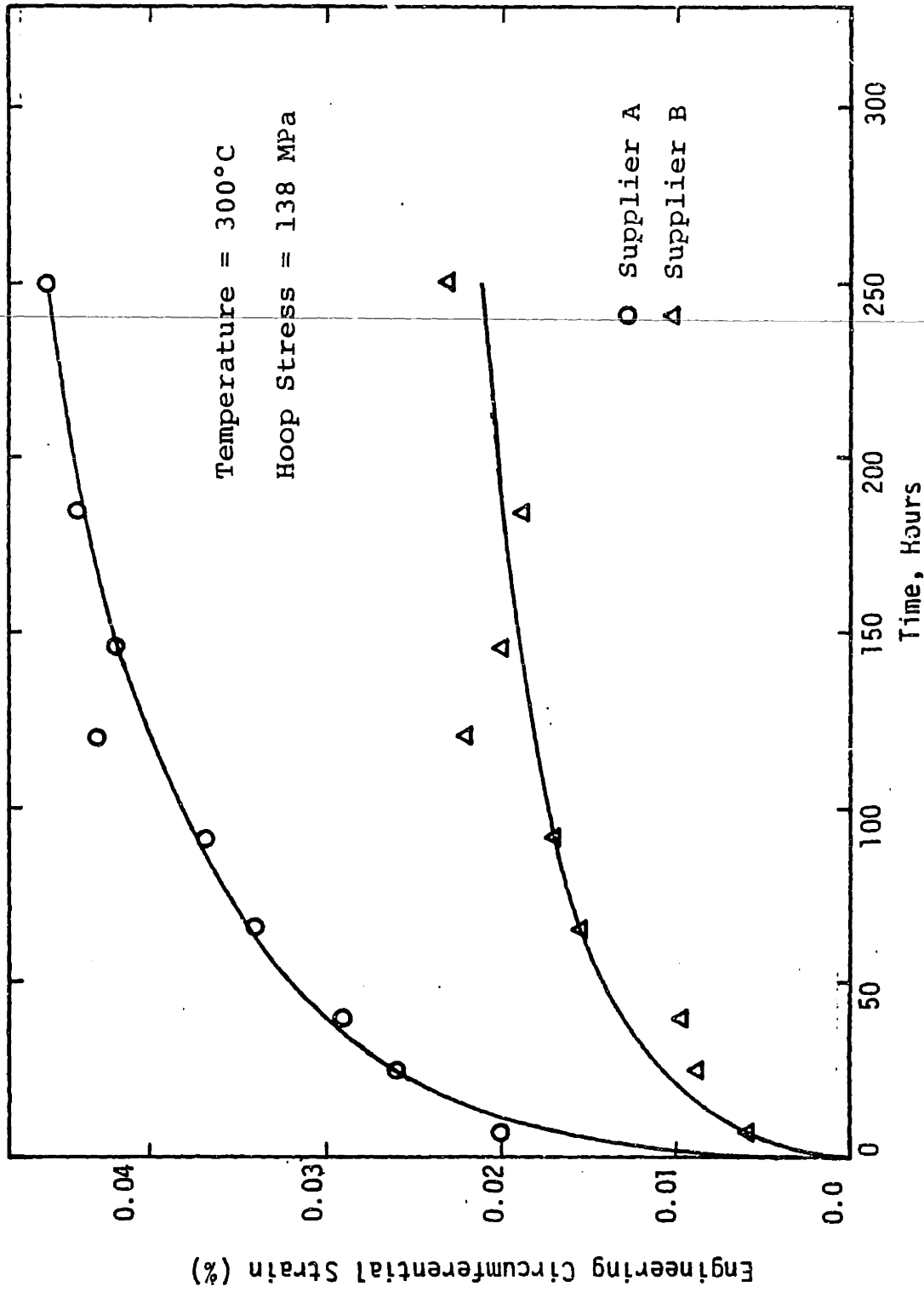
Fig. 7.5 BIAXIAL CREEP TEST RESULTS PLOTTED AS CIRCUMFERENTIAL STRAIN VERSUS TIME FOR TESTS AT 300°C AND 138 MPa (20 KSI)

Figure 7.6

Unstressed supplier B cladding material in the pickled
condition is exposed to the iodine environment present
in a tube pressurization test at 320°C. Features of
interest are regions of general attack (A), local
attack at particles (C) where the particles are finally
removed from the surface (B), and pre-existing pits
that exhibit no localized attack (D). Energy dispersive
analysis of the particles reveals Zr, Cr, and Fe to be
present.
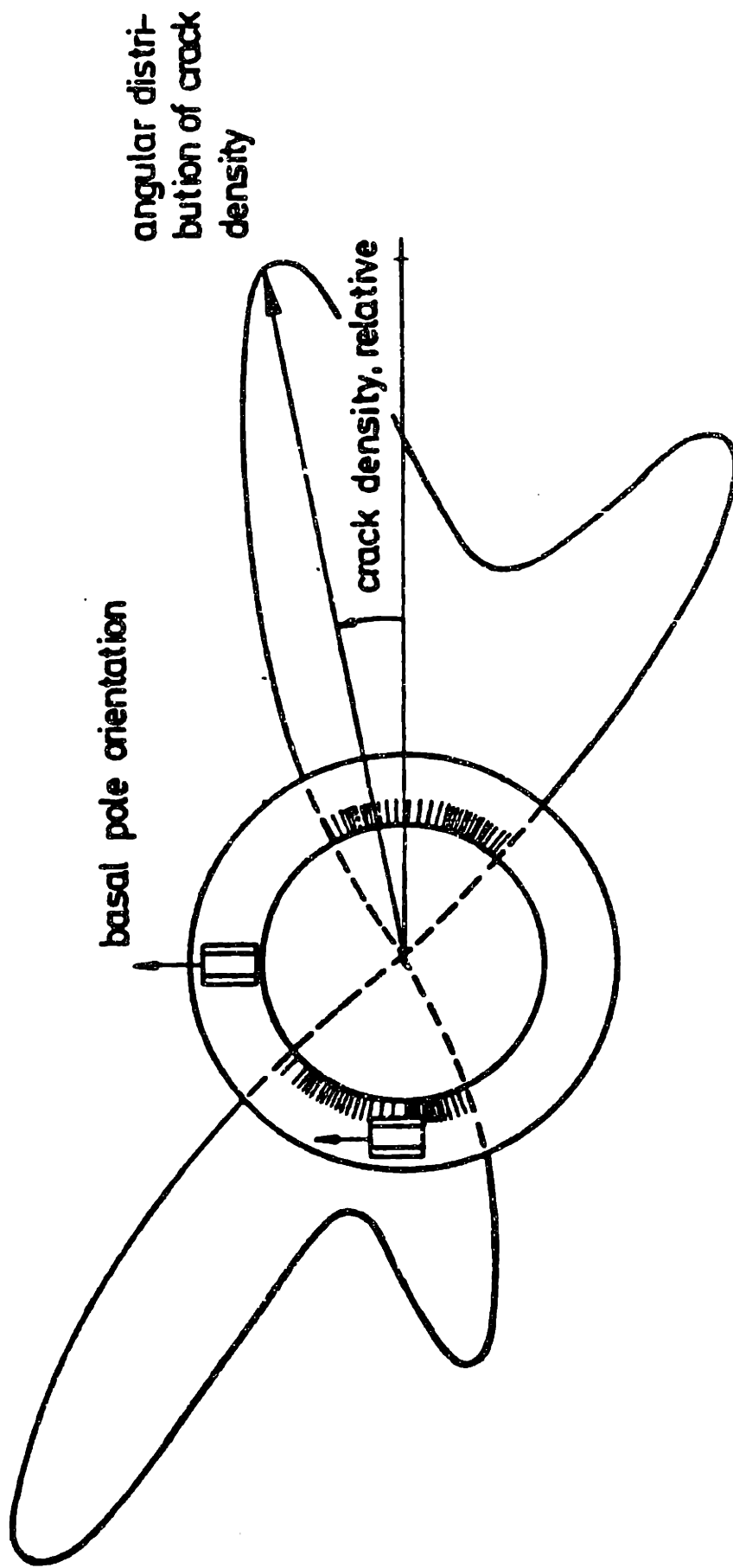
Fig. 7.7   Influence of Basal Pole Orientation on Iodine SCC Susceptibility for Tubing Machined from Textured Plate; after Peehs et al., ASTM STP 681, p. 244, 1979.
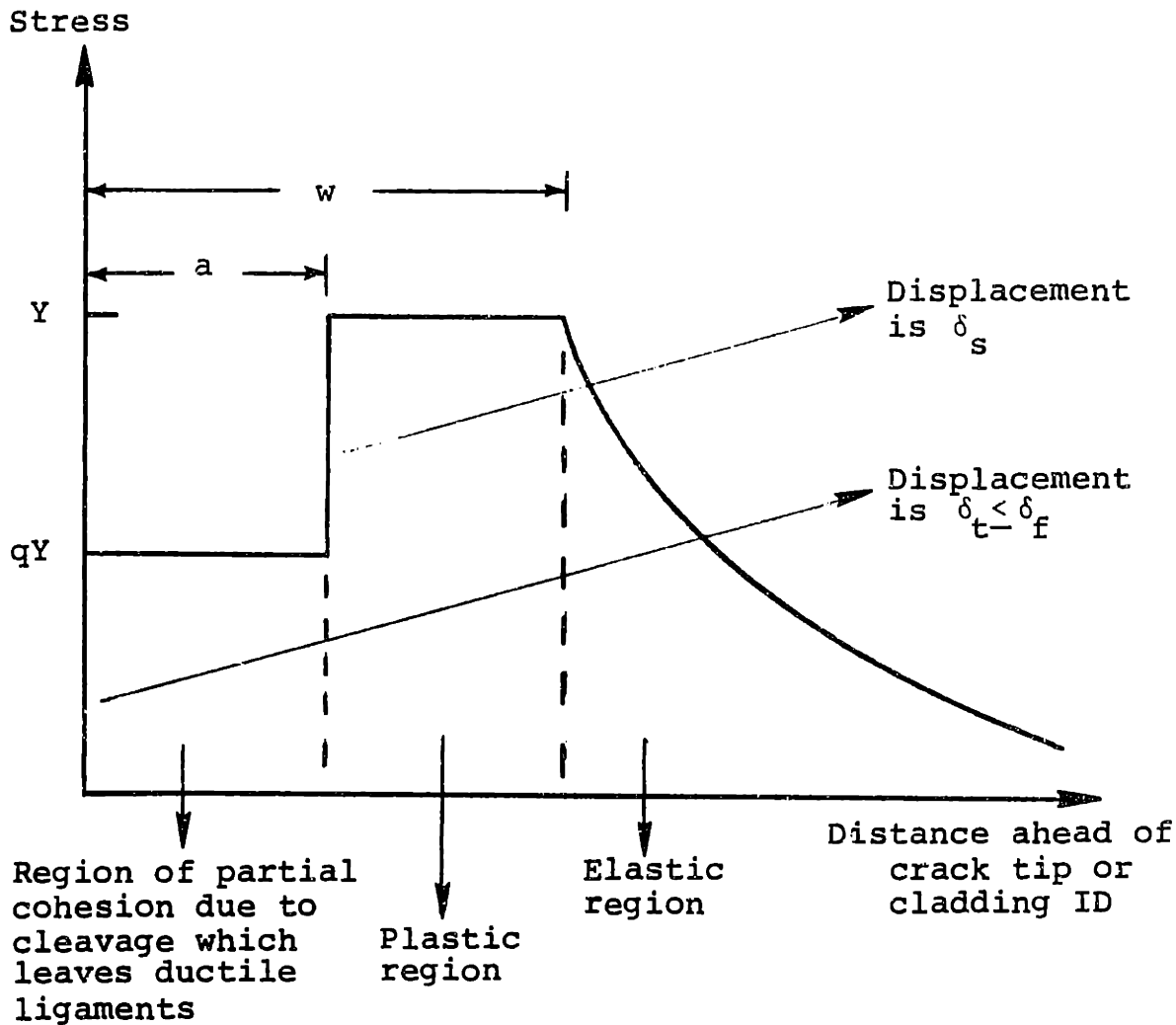
Figure 7.8

Idealized Model of Smith and Miller [173] for Propagation
of Iodine SCC Cracks
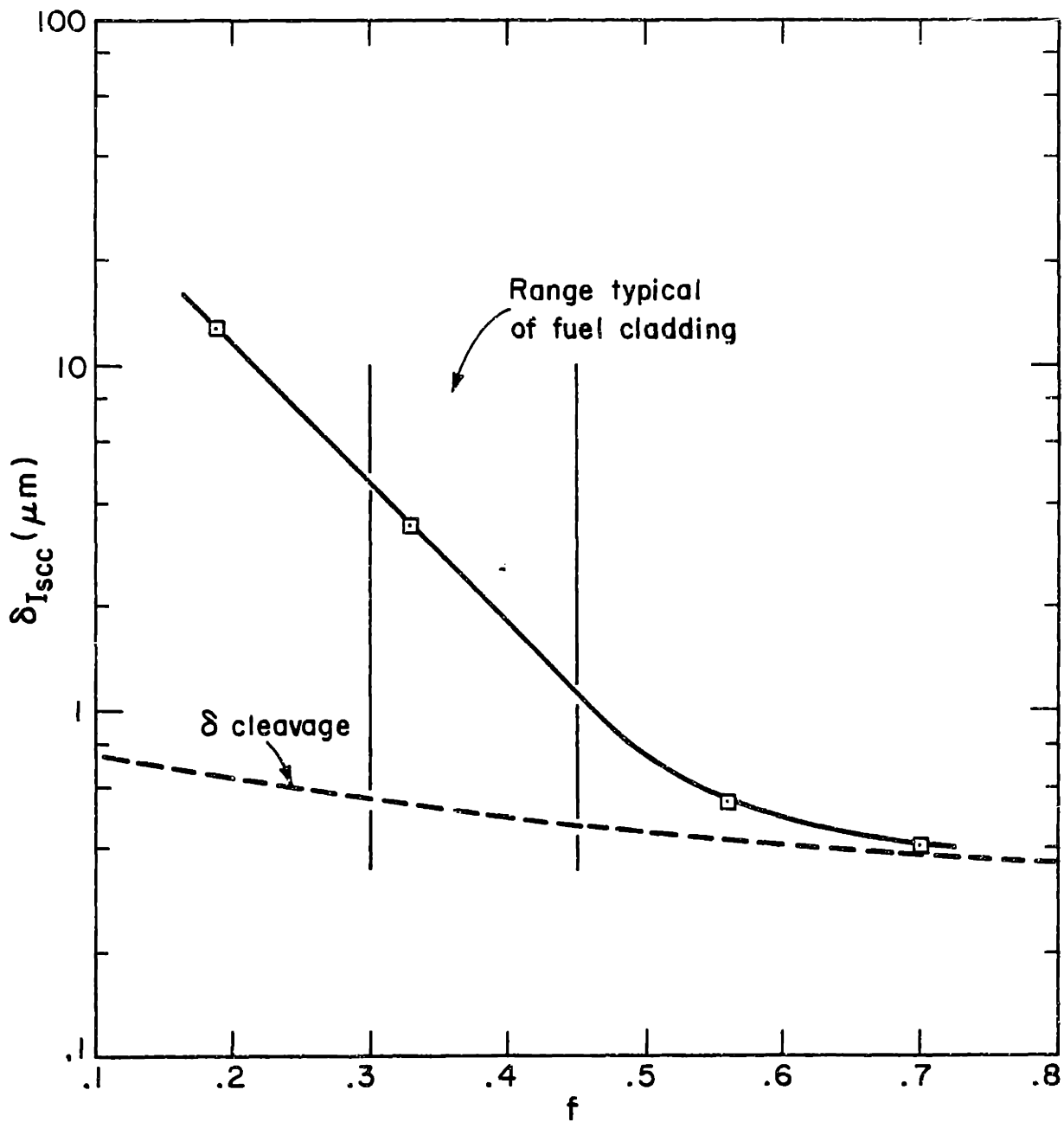
Figure 7.9

Effect of Crystallographic Texture on δ_{ISCC} in
Stress-Relieved Zircaloy

Figure 7.10
Calculated K Profiles Through the Tube Wall for Near Threshold
Stress Levels in both Supplier A and Supplier B
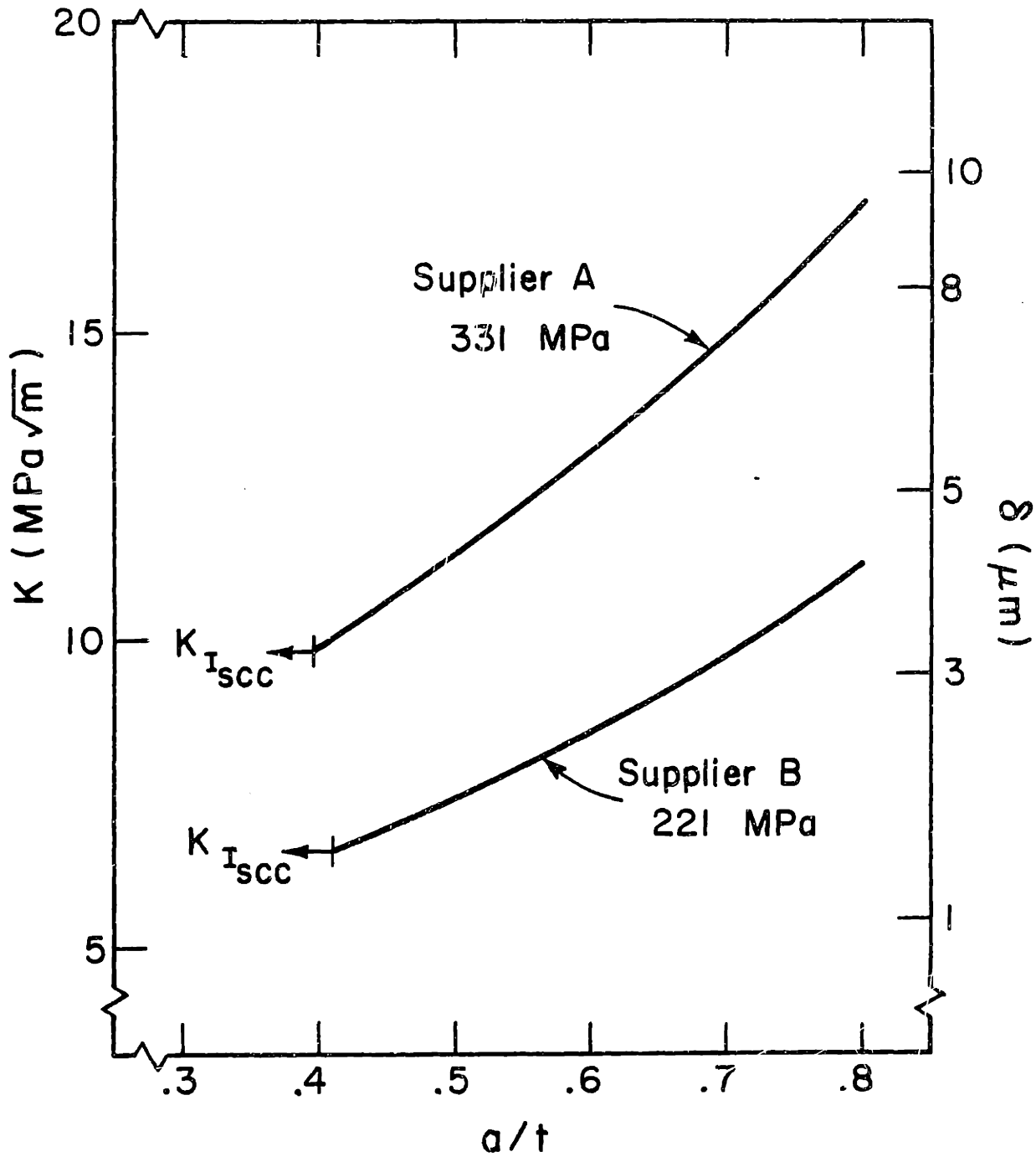
8. SUMMARY AND CONCLUSIONS

The stress corrosion cracking behavior of Zircaloy in an iodine environment is considered. The experimental program is composed of two principal sections:

1. SCC propagation in fracture mechanics specimens at 300°C in a 4 Pa flowing iodine environment is studied. The variables are crystallographic texture, heat treatment, and microstructure.

2. Tube pressurization tests on two different lots of Zircaloy-2 cladding tubes are used to generate stress versus time to failure behavior. The test matrix is designed to separate the effects of texture, heat treatment, residual stress, and surface finish on the iodine SCC susceptibility. Iodine concentration is approximately 10^{-4} gm/cm^2 and test temperature is 320°C, although some tests are performed at 390°C.

The conclusions are listed below:

1. Texture has a strong influence on K_{ISCC}. As the resolved fraction of basal poles parallel to the direction of crack opening decreases, K_{ISCC} increases from 4 MPa√m at f = 0.70 to 17 MPa√m at f = 0.19. Comparing recrystallized and stress-relieved material with essentially the same texture, K_{ISCC} is greater for the recrystallized material, e.g. 6.3 MPa√m at f = 0.67 versus 4 MPa√m at f = 0.70 for stress-relieved material.

2. The principal mode of crack propagation is transgranular cleavage near the basal plane. Several ductile modes of separation compliment the cleavage process. High crack velocity and/or K promotes tearing of ductile ligaments between cleavage facets which are on the order of the grain size. At low K near K_{ISCC} very little tearing is observed and cleavage zones larger than the grain size are common, particularly for specimens with a low K_{ISCC}. Fluting is also preferred in the low K/low crack velocity regime. In recrystallized material regions of inter-granular propagation are observed and a transition to completely intergranular failure is possible near K_{ISCC}.

3. In tube pressurization tests of cladding from two different suppliers, a substantial difference in stress versus time to failure behavior is due to texture where a more tangential texture results in shorter time to failure at a particular stress and a lower threshold stress. Other materials variables, such as surface finish and stress-relief heat treatment temperature have a smaller, second order effect on SCC. Residual stress at the levels found in these two lots has no effect on SCC susceptibility.

4. A consistent interpretation of many observations of crack initiation is possible if strain accumulation and strain localization are necessary steps in the initiation process. Lifetime is initiation limited at 320°C, but initiation occurs more readily at 390°C. Further work is

necessary to quantitatively separate the initiation and propagation fractions of lifetime.

5. Model predictions indicate that the ductile processes are responsible for the high K_{ISCC} at low f in the crack opening direction where misoriented cleavage planes make only a secondary contribution. The fractography in both the fracture mechanics tests and tube pressurization tests are consistent with this interpretation. More ductile tearing is observed at higher K values in fracture mechanics specimens. The crack path in tubing depends on texture and stress where high stress/high K activate more of the ductile processes than low stress/low K.

9. SUGGESTIONS FOR FUTURE WORK

Additional work would be useful to answer several questions concerning the initiation and propagation of iodine stress corrosion cracks. A more exact separation of the life fraction spent in initiation and in propagation is very desirable. This would require experimentally a knowledge of when the crack forms during the test. Both the texture and temperature effects on initiation could be resolved. The initiation sites are more easily characterized from small incipient cracks rather than large cracks on failed specimens.

Several aspects of crack propagation should be studied. Crack velocity measurements are obtainable from two sources. Fracture mechanics specimens give data under well defined conditions of K and crack length where linear elastic fracture mechanics (LEFM) applies. Crack growth kinetics can be evaluated from a properly planned test matrix. Tubing samples are also useable for crack velocity measurements as demonstrated by Videm and Lunde [118]. Improvements in crack growth modeling would aid in analysis of tubing data. The problem of short crack growth in tubes before LEFM is applicable should be addressed.

Since texture strongly influences both initiation and propagation of cracks, more mechanical property data such as burst and creep are needed to correlate with tubing materials involved in studying texture effects. This could help explain the strain and strain rate versus time to failure data.

The effects of several materials variables need additional characterization. Very little data are available on materials containing

dissolved hydrogen. Irradiated materials require further study,
particularly with regard to texture effects and separation of initiation/
propagation stages of SCC. The exact role of mechanical surface treatments
on SCC susceptibility is ambiguous at the present time.

Appendix A

Modeling of Oxygen Potential over LWR Fuel

This appendix presents a model for oxygen partial pressure over $(U_{1-q}, Pu_q)O_{2+x}$ as a function of temperature. Values of q, the fraction of plutonium, are low for LWR fuels being limited to 0.01 - 0.015 at end of life. Yittrium and the rare earths are also dissolved in the urania matrix [36] at quantities of 0.01 - 0.012 at end of life [39]. These small values of q will be shown to have a very large effect on the oxygen partial pressure over the fuel. The quantity x is the deviation from stoichiometry and can be greater or less than zero.

Blackburn [35] originally developed the model for oxygen partial pressure over UO_{2+x} based on the thermochemical properties of pure oxides. For values of $x < 0$, U^{+4} is reduced to U^{+2} by the reaction:

$$U^{+4} + O^{-2} = U^{+2} + \frac{1}{2} O_2(g) \qquad (A-1)$$

The law of mass action for this reaction gives:

$$K^U_{2,4} = \exp[-78.3 \times 10^3/T + 13.6] = \frac{P_{O_2}^{1/2} [U^{+2}]}{[O^{-2}][U^{+4}]} \qquad (A-2)$$

For values of $x > 0$, U^{+4} is oxidized to U^{+6} by the reaction:

$$U^{+6} + O^{-2} = U^{+4} + \frac{1}{2} O_2(g) \qquad (A-3)$$

The law of mass action gives:

$$K^U_{4,6} = \exp[-(16.4 \times 10^3/T) + 5.0] = \frac{P_{O_2}^{1/2} [U^{+4}]}{[O^{-2}][U^{+6}]} \qquad (A-4)$$

Johnson et al. [37] give similar equations for plutonia where it is necessary to consider the cations Pu^{+2}, Pu^{+3}, and Pu^{+4}. The reactions and mass action expressions are:

$$2Pu^{+4} + O^{-2} = 2Pu^{+3} + \frac{1}{2} O_2(g) \tag{A-5}$$

$$2Pu^{+3} + O^{-2} = 2Pu^{+2} + \frac{1}{2} O_2(g) \tag{A-6}$$
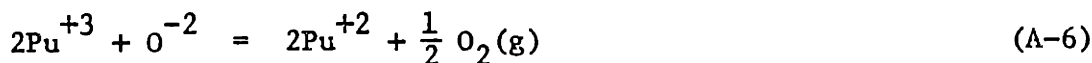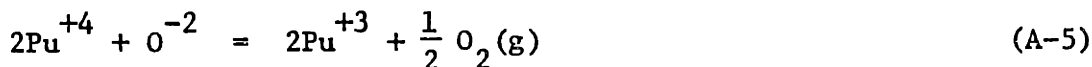
$$K^{Pu}_{3,4} = \exp[-(50.8 \times 10^3/T) + 10.4] = \frac{P^{1/2}_{O_2} [Pu^{+3}]^2}{[O^{-2}][Pu^{+4}]^2} \tag{A-7}$$

$$K^{Pu}_{2,3} = \exp[-(92.6 \times 10^3/T) + 21.4] = \frac{P^{1/2}_{O_2} [Pu^{+2}]^2}{[O^{-2}][Pu^{+3}]^2} \tag{A-8}$$

For the mixed oxide, additional equations are provided by the stoichiometric relationships:

$$[U^{+2}] + [U^{+4}] + [U^{+6}] = 1 - q \tag{A-9a}$$

$$[Pu^{+2}] + [Pu^{+3}] + [Pu^{+4}] = q \tag{A-9b}$$

and the electroneutrality condition is:

$$[O^{-2}] = 2 + x = [U^{+2}] + [Pu^{+2}] + \frac{3}{2} [Pu^{+3}] + 2[U^{+4}] +$$

$$2[Pu^{+4}] + 3[U^{+6}] \tag{A-10}$$

Olander [36] outlines a procedure for solving these equations for P_{O_2}. Using Eqns. (A-2), (A-4), and (A-7) - (A-10), P_{O_2} is expressed in terms of T, q, and x. The result is a complicated equation in P_{O_2}, T, q, and x. A computer solves iteratively for P_{O_2} at various values of x with T and q held constant. T and q are varied to cover the range of interest and to generate sufficient data for Figs. 2.2, A.1, A.2, and A.3.

Calculations based on the model are qualified against results from fuel compositions for which experimental data exist: UO_{2+x} [35] and $[U_{0.80}, Pu_{0.20}]O_{2+x}$ [33]. Since the computer calculated values agree for these two extreme cases, oxygen partial pressures can be calculated for the lower values of q relevant to LWR fuel.

Oxygen partial pressure is plotted as a function of x at various temperatures for UO_{2+x} in Fig. A.1. It is evident that P_{O_2} is very sensitive to stoichiometry near x = 0 and drops precipitously for x < 0 because it is difficult to reduce uranium to the +2 valence state. Fig. 2.2 is similar to Fig. A.1 except lines of constant q are drawn at a single temperature, 700°C. The results for $(U_{0.8}, Pu_{0.2})O_{2+x}$ are also given. For small hypostoichiometric deviations, the plutonium tends to act as a buffer retarding the sharp drop in oxygen partial pressure. Even small quantities of Pu are effective in raising P_{O_2} as shown in Fig. A.2. Finally, Fig. A.3 plots P_{O_2} versus temperature for various q values in stoichiometric $(U_{1-q}, Pu_q)O_2$. This figure is significant because it shows how oxygen partial pressure is increased substantially for stoichiometric fuel with even small Pu additions.

This analysis is simplified in that it deals only with the heavy metal ions uranium and plutonium and assumes that urania and plutonia form an ideal solution, i.e. obey Raolt's law. This is a reasonable first order assumption since these compounds exhibit complete solid solubility. A set of equations similar to Eqns. (A-7) - (A-10) would be used for Ce which is also an electron donor. The analysis is simplified for a cation with only one valence state such as yittrium or neodymium since Eqns. (A-5) - (A-8) are not necessary and the stoichiometric relationships and electroneutrality conditions are also simplified.

The number and complexity of the equations is greater when multicomponent systems such as $(U, Pu, Ce, \ldots)O_{2 \pm x}$ are considered.

The primary point of this analysis is that the presence of small amounts of Pu and/or rare earth elements significantly alters the oxygen potential over the fuel at compositions near stoichiometry. At a given oxygen potential, a lower O/M ratio corresponds to the release of oxygen from the fuel. This factor must be considered in an oxygen balance of the fuel.
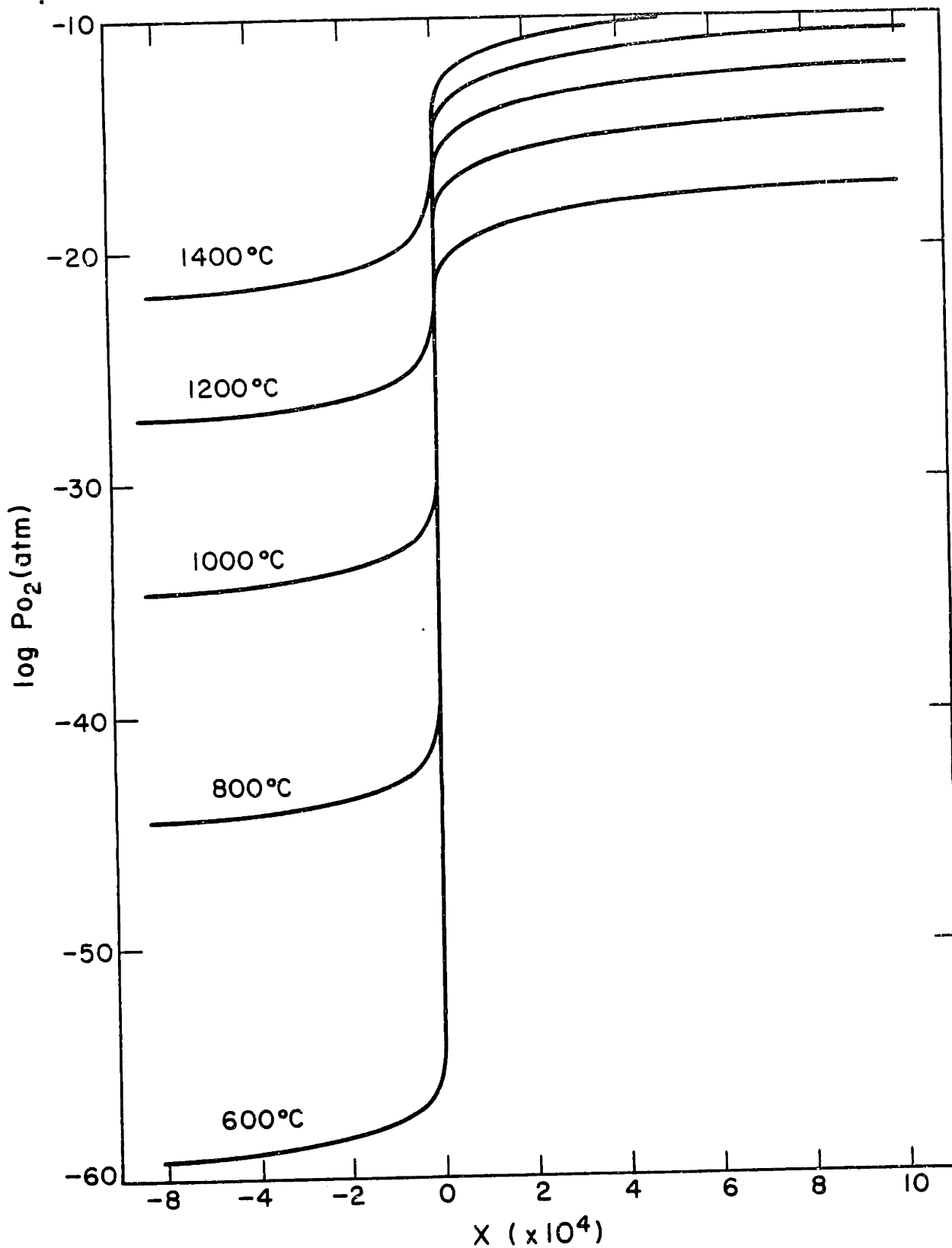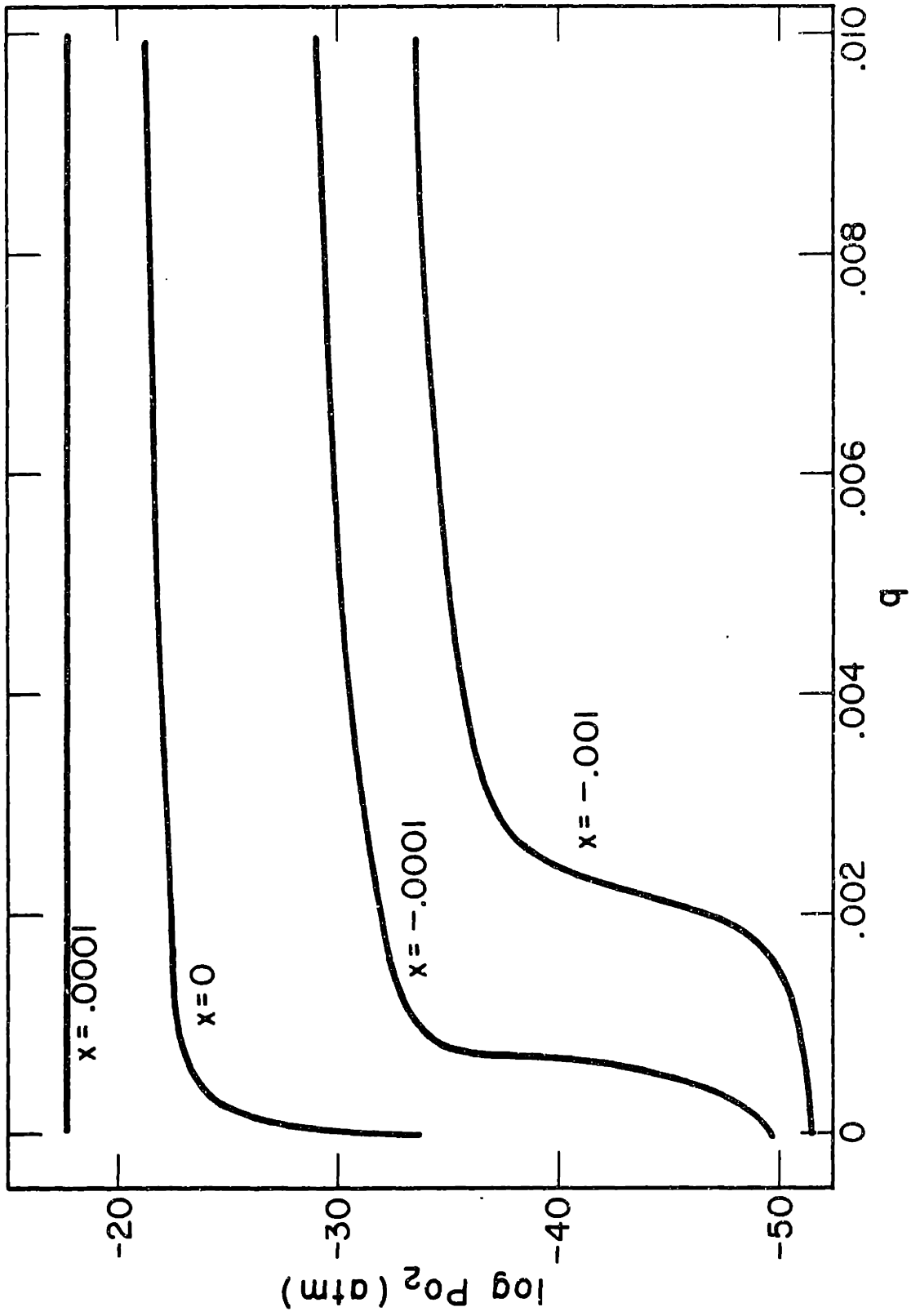
Figure A.1
Variation of P_{O_2} with x at Various Temperatures for UO_{2+x}

Figure A.2

Variation in Oxygen Potential with Plutonium Content for $(U_{1-q}, Pu_q)O_{2+x}$
at 700°C for Various x Values
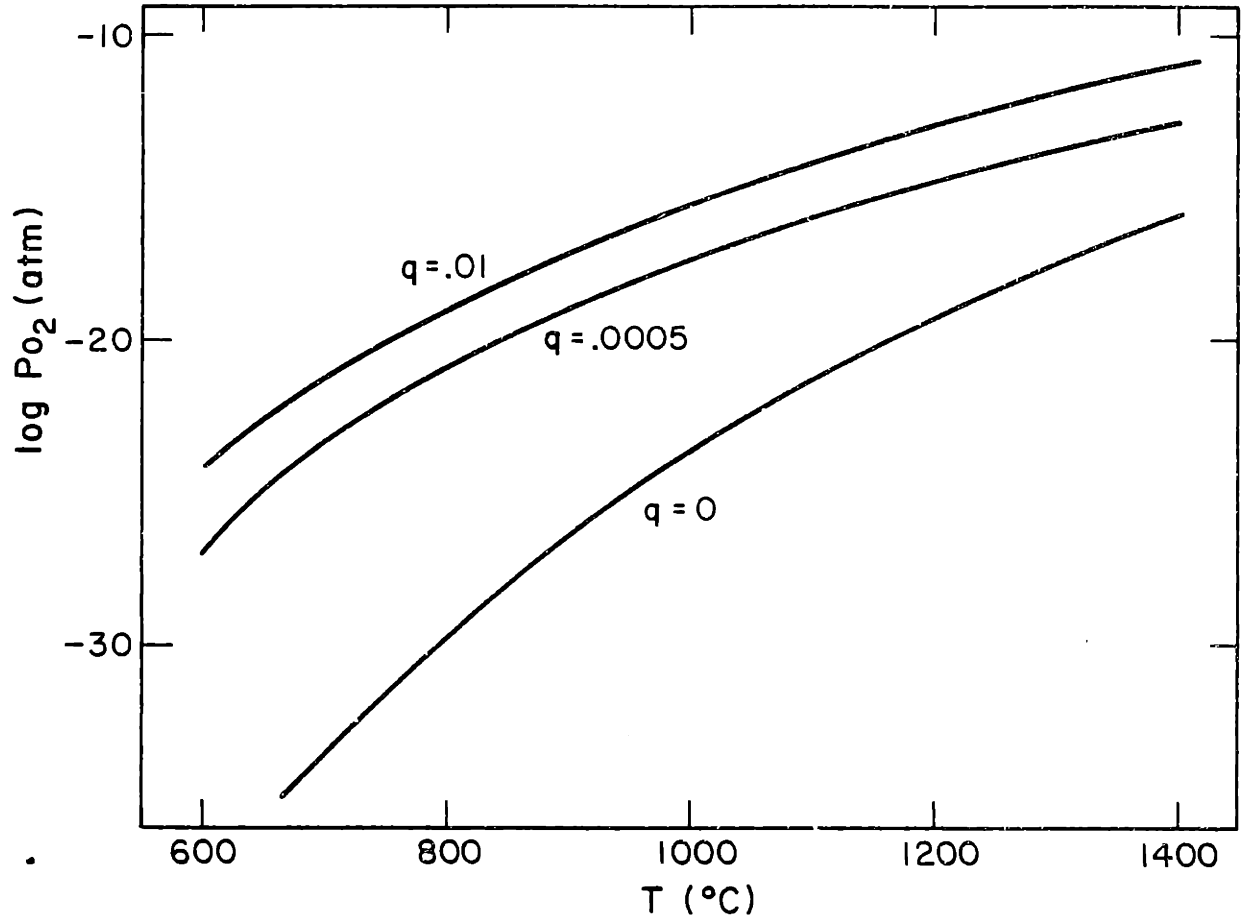
Figure A.3

Variation in P_{O_2} with Temperature for Various q Values in $(U_{1-q}, Pu_q)O_2$

Appendix B

.

Procedures for Crystallographic Texture Determination and

Texture Results for Experimental Materials

B.1 Experimental Procedures

B.1.1 Specimen Preparation

B.1.1.1 Plate Samples

The 9908 and 9912 plate materials are ~1.27 cm thick. Pieces
~2.5 cm square are cut through the thickness with a slitting saw to give
four specimens. Two sections each are cut from the axial and transverse
directions to make composite samples from these directions. All
specimens are polished through 600 grit SiC paper and pickled (45% H_2O,
45% HNO_3, and 10% HF) to remove approximately 80 μm of material. The
result is an axial composite specimen, a transverse composite specimen,
and four through-thickness specimens or eight surfaces that are available
for texture analysis.

B.1.1.2 Tubing Samples

Annular sections of tubing are machined from the ID, mid-wall, and
OD of the tube. The dimensions are 0.2 mm wall-thickness and 2.5 cm
length. The specimens are pickled to a thickness of 80 μm so that they
can be unrolled elastically and attached to a stiff plexiglass backing
with contact cement. The ID surface sample is made by closing off the
tube ID with rubber stoppers and thinning only the outside of the specimen
blank. Locations of the through-wall specimens are listed in Table 3.2.

B.1.2 Inverse Pole Figures

An inverse pole figure is constructed from a Bragg diffraction
scan of a specimen. Ni filtered Cu K_α radiation is used. The range of
2θ coverage is 30° to 141° which is sufficient to record eighteen

possible peaks. The beam slit is 3° and the receiving sl.t is 0.2°.

The peaks are integrated with a planimeter and the data are used to

calculate texture coefficients for each {hkil} plane by the formula:

$$T_{c\{hkil\}} = \frac{I_{\{hkil\}}\big/I_{o\{hkil\}}}{\frac{1}{N}\sum_{1}^{N}(I_{\{hkil\}}\big/I_{o\{hkil\}})} \qquad (B-1)$$

where I is the integrated area (intensity), I_o is the relative intensity

for a random sample [B1], and N is the number of reflections, usually

eighteen. The $T_{c\{hkil\}}$ values are plotted on a segment of the standard

(0002) projection and approximate isointensity lines are drawn.

The f-parameter texture number is calculated from the inverse

pole figure data using the method detailed by Kearns [150]. A computer

program is used to calculate both T_c values and f_i from the integrated

peak intensities [147].

B.1.3 Pole Figures

Data for direct pole figures are obtained by simultaneously

tilting the specimen while rotating it about its axis. Tilt angles from

0° to 80° are used in pole figure construction. Experimentally, Ni fil-

tered Cu K_α radiation is used. The specimen is tilted at 1°/min and

rotated at 72°/min which gives a spiral path with a 5° pitch on the

polar stereographic projection.

The pole figure is prepared by subtracting background radiation

and correcting the data for geometric defocusing [B2]. The defocusing

factors are listed elsewhere [147]. The reference intensity is at 0°

tilt or the center of the pole figure where the actual intensity equals

the T_c value for that reflection. Data normalization proceeds from the center of the pole figure outward by plotting lines of isointensity. Almost all pole figures presented here are (0002) pole figures.

Another useful plot of texture information for basal pole figures is the radial-tangential (R-T) scan (normal-transverse or N-T in plate). The data are obtained from discreet points on the pole figure diffract-ometer scan, curve fit by hand, and plotted by computer from values every degree in tilt angle. This information is also used to generate the F_T and $(SD)_T$ texture numbers [147].

B.2 Texture Results

B.2.1 Plate Material

A plot of through-thickness f_N values for all four plate conditions is shown in Fig. B.1. Selected pole figures, N-T scans, and inverse pole figures are presented in Figs. B.2 through B.20.

B.2.2 Tubing Material

Pole figures, R-T scans, and inverse pole figures are given in Figs. B.21 through B.34. All three lots of material: supplier A, supplier B, and lot 1340, are represented.

References

B.1 E. F. Sturchen and W. G. Duke, AEC DP-607 (1961).

B.2 W. P. Chernock and P. A. Beck, J. Appl. Phsy., 23 (1952), 341.

Figure B.1

Plot of Through-Thickness Texture Number, f_N, for Plate Materials
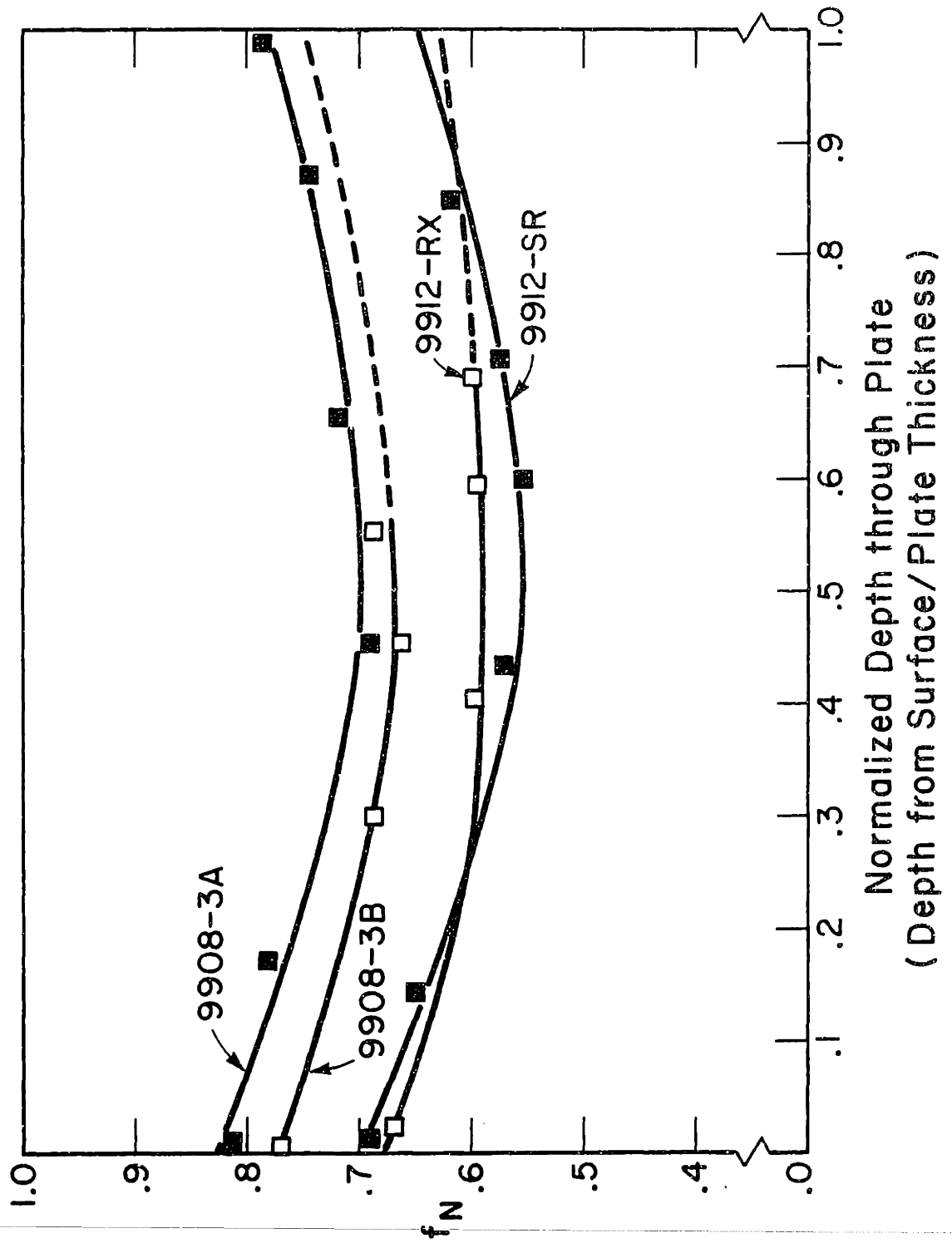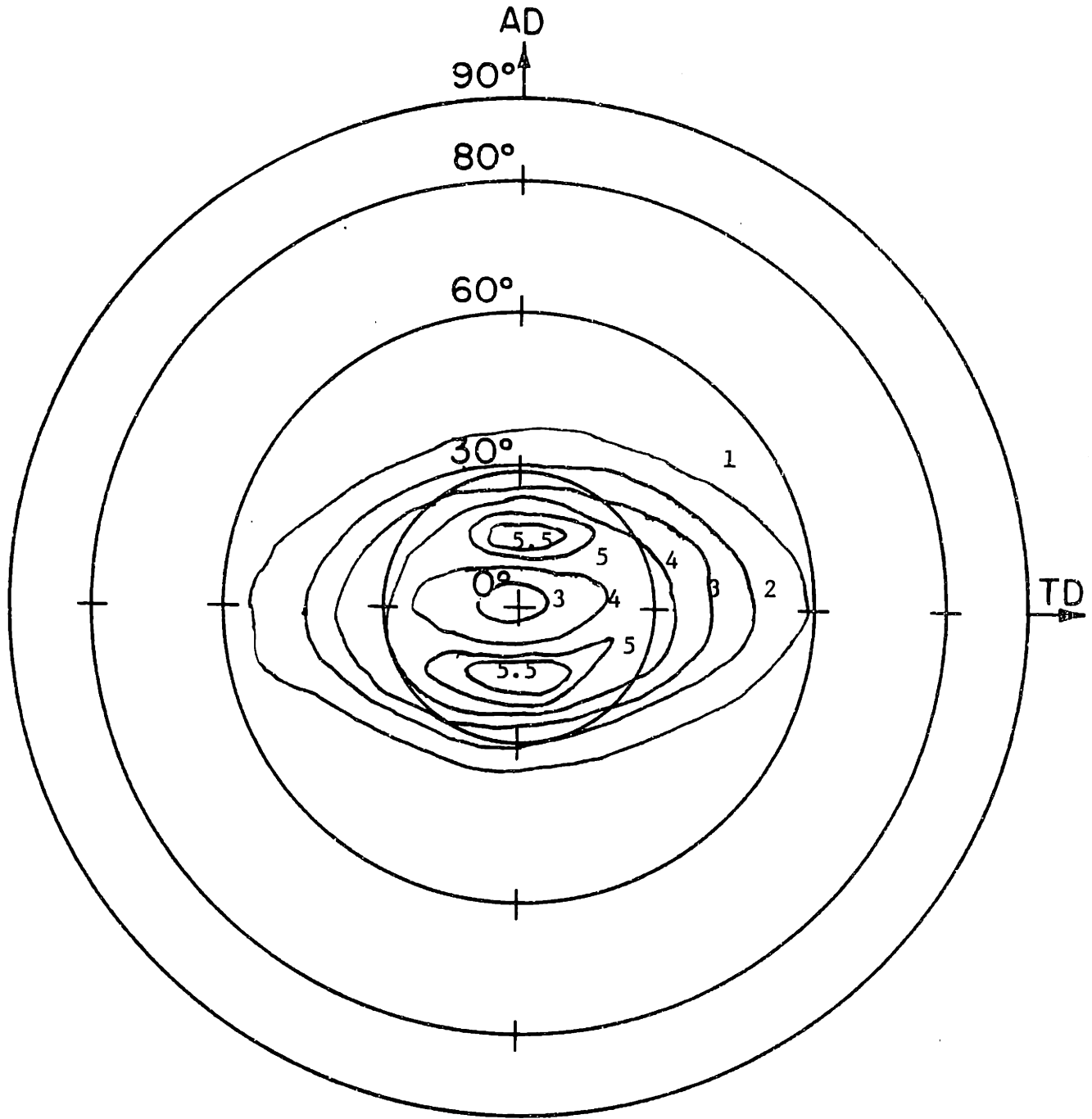
Figure B.2

Basal Pole Figure 0.15 mm from Surface of Plate 9908-3A

FIGURE B.3
TRANSVERSE-NORMAL SCAN FOR
PLATE 9908-3A, 6.05 MM FROM TOP OF PLATE
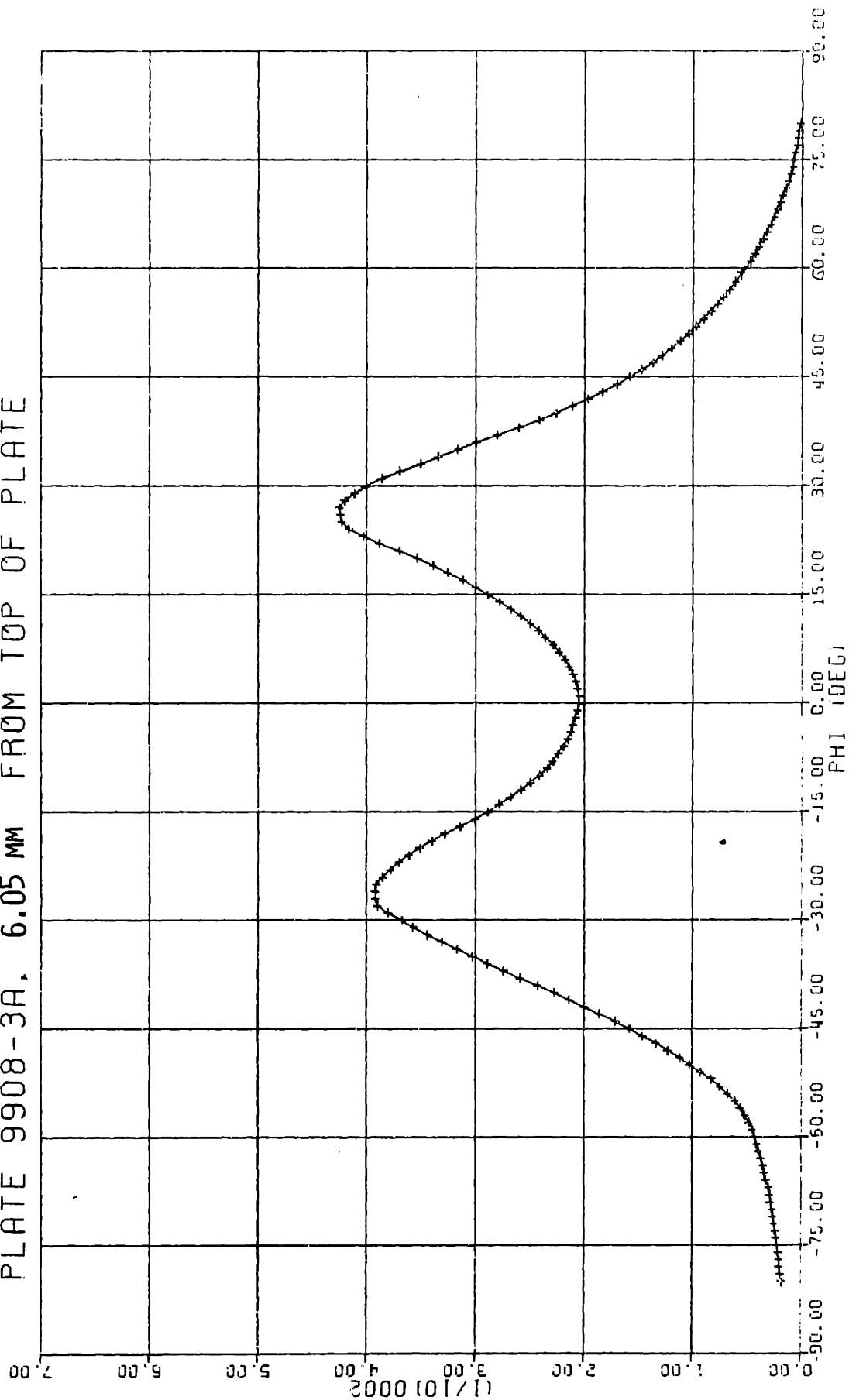
Figure B.4

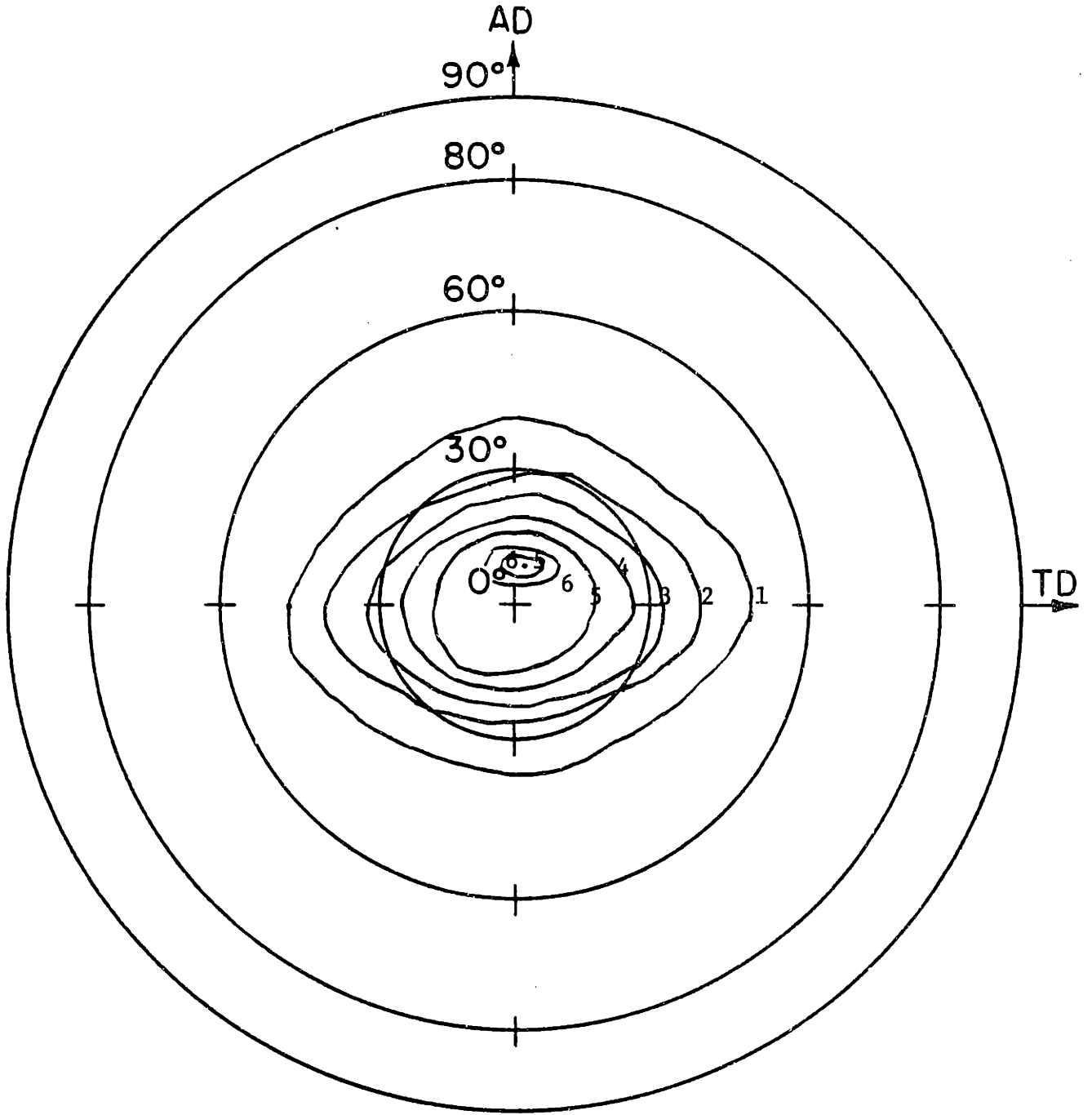Inverse Pole Figure 6.05 mm from Surface of Plate 9908-3A
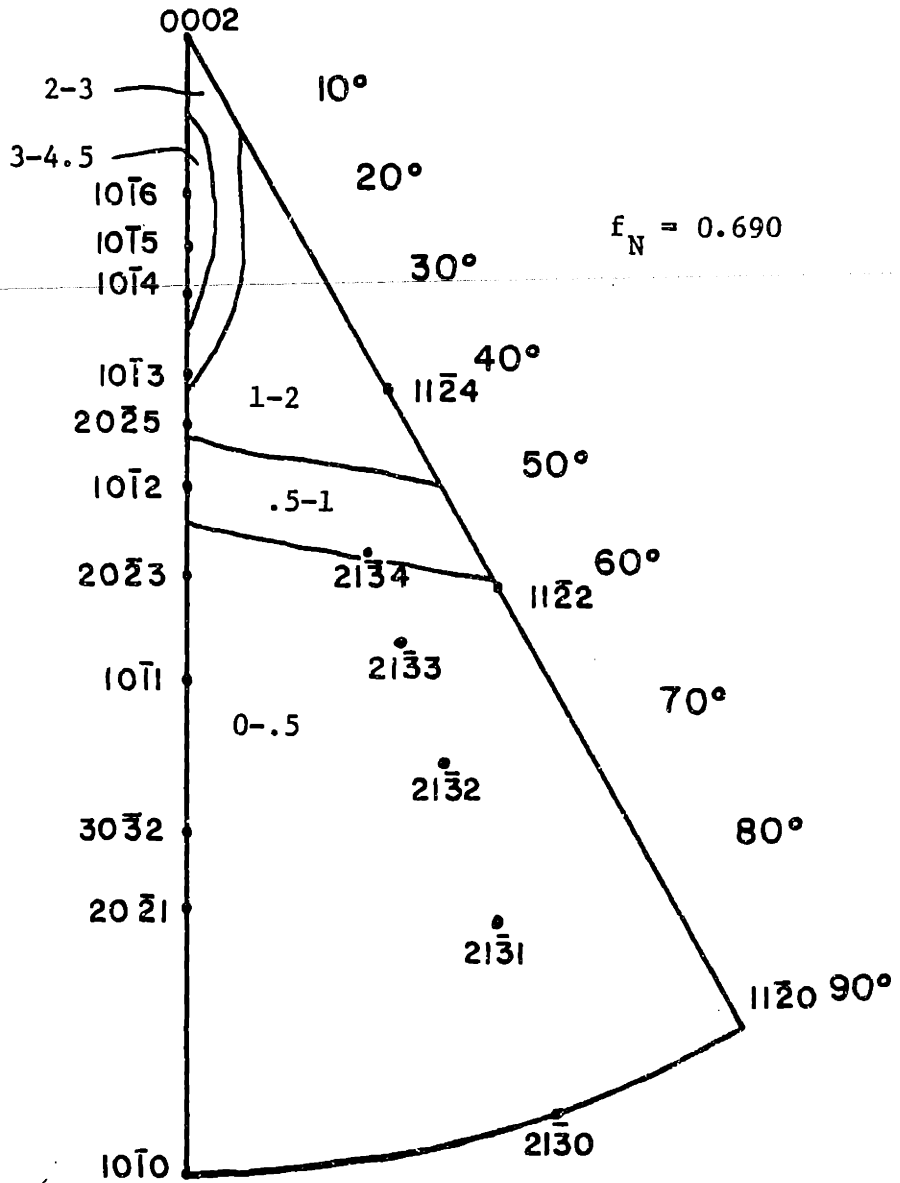
Figure B.5

Basal Pole Figure 8.66 mm from Surface of Plate 9908-3A

Figure B.6

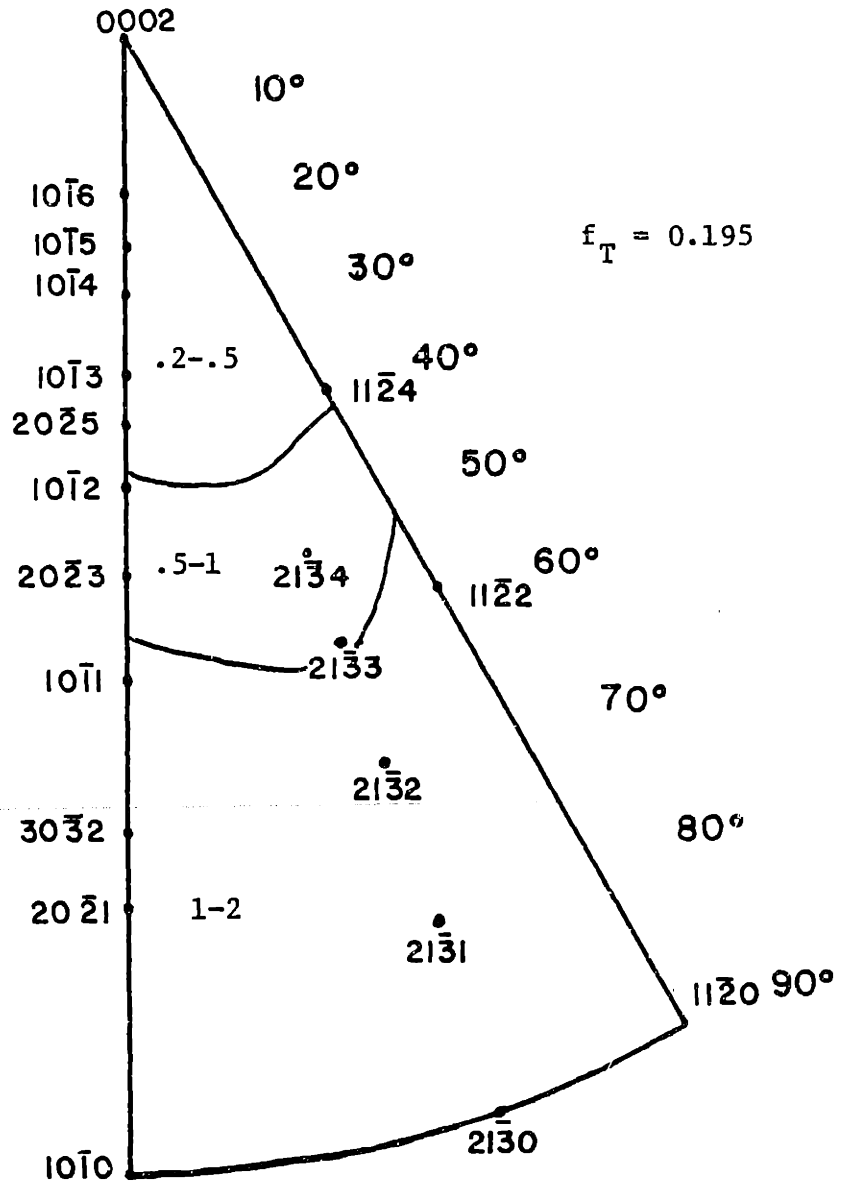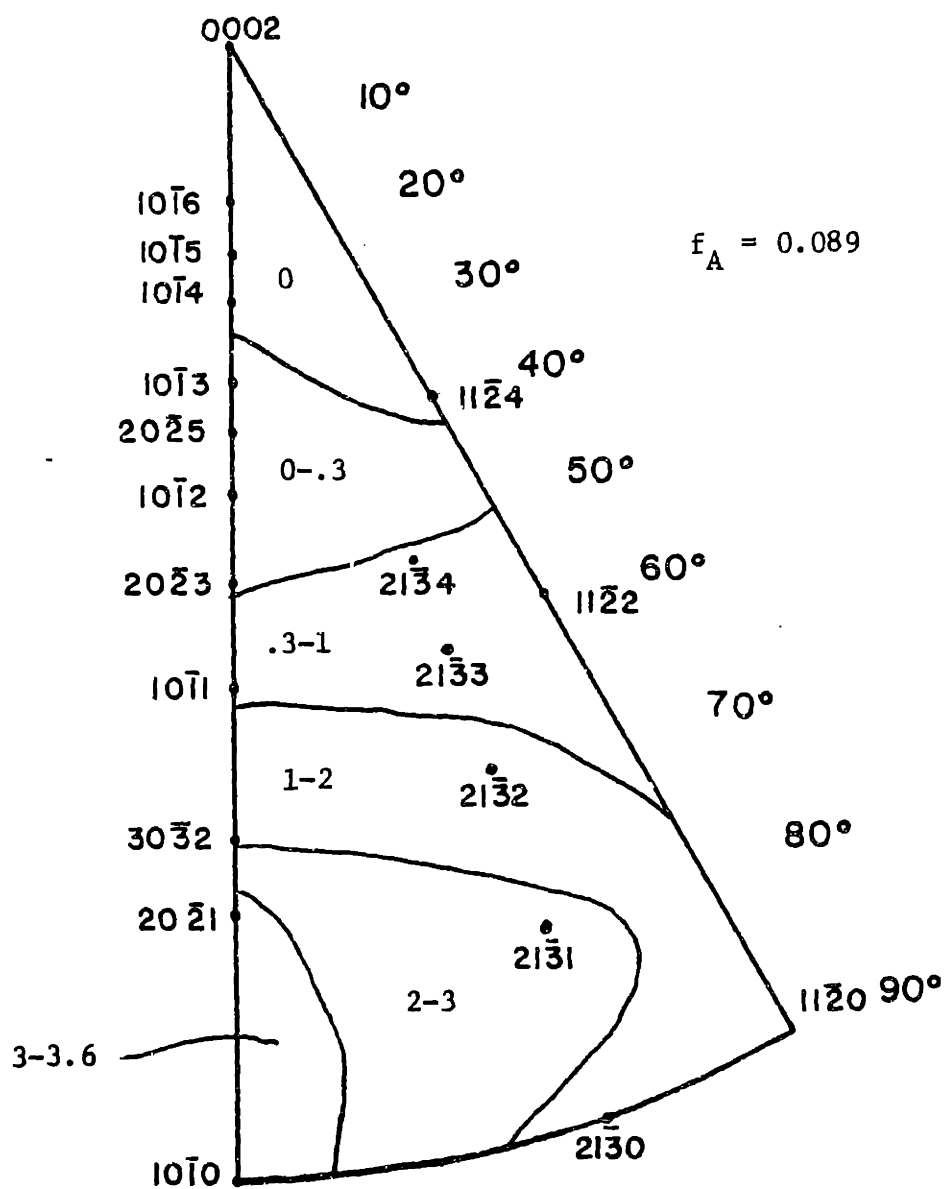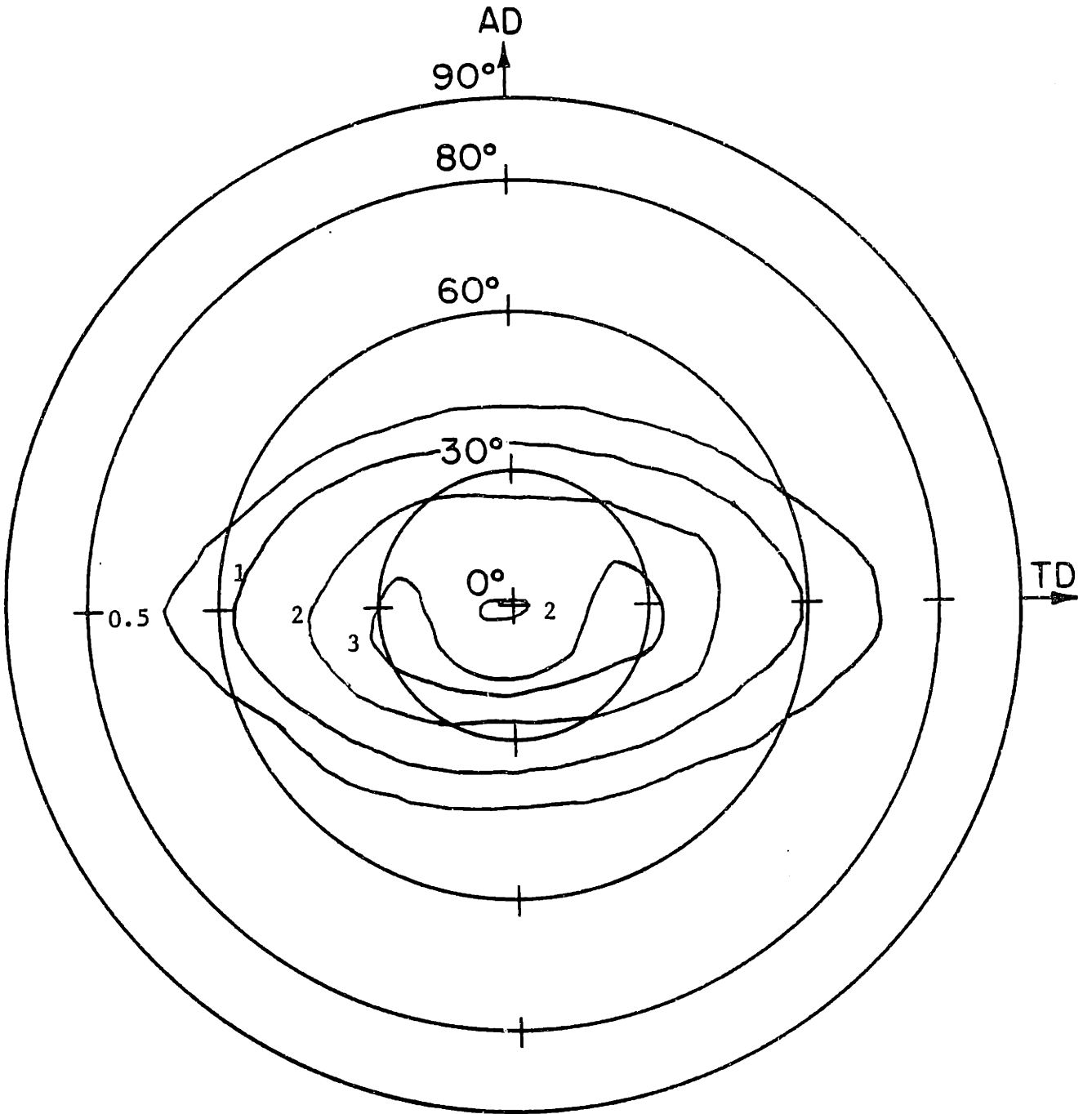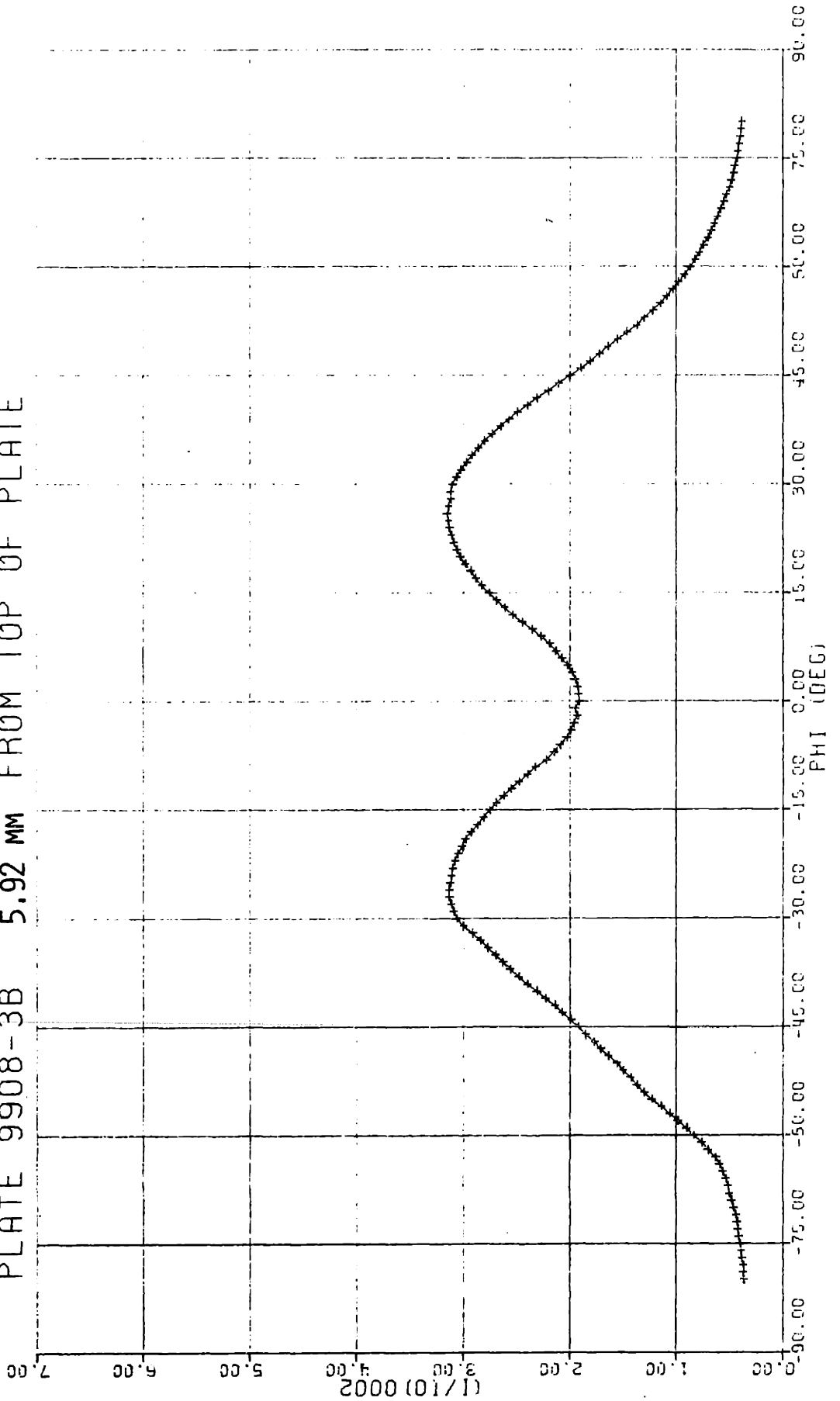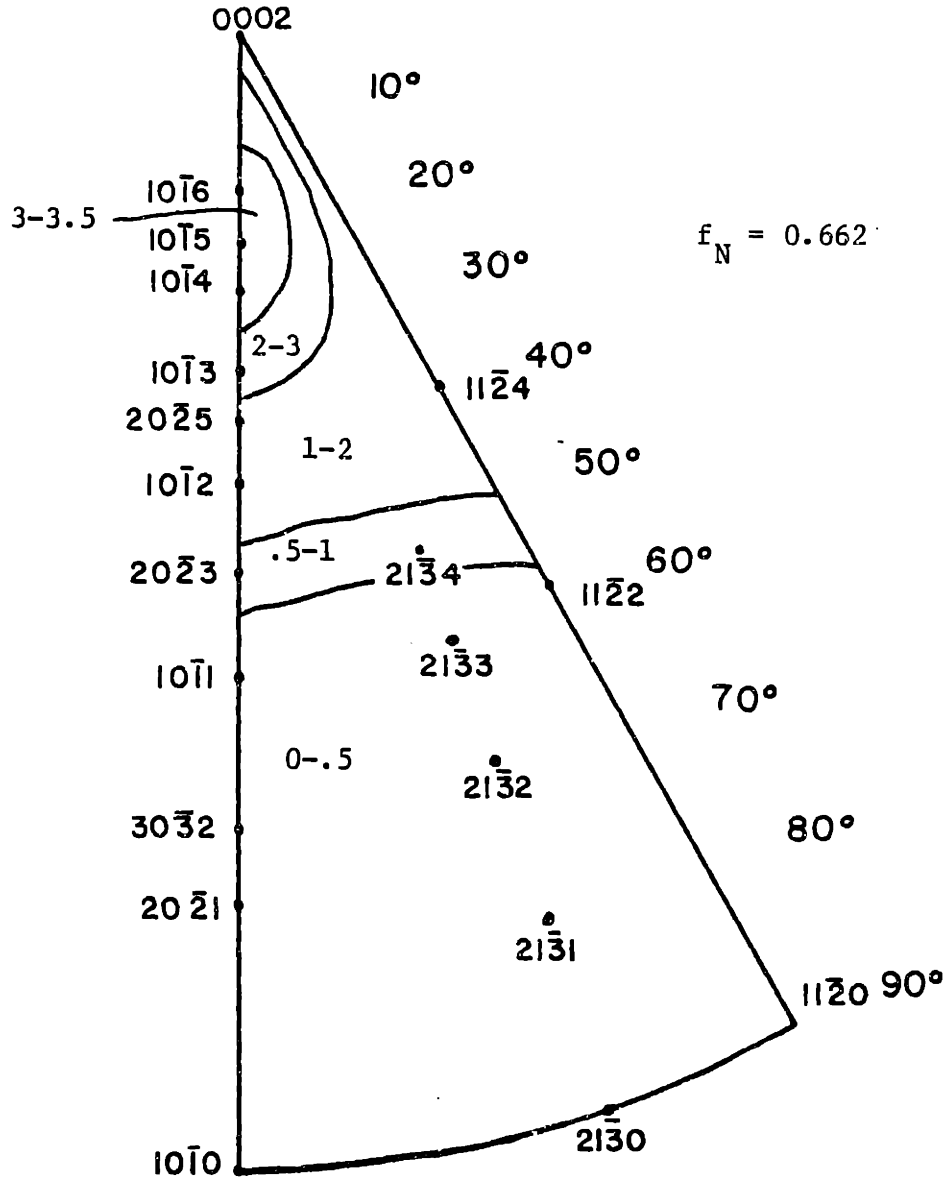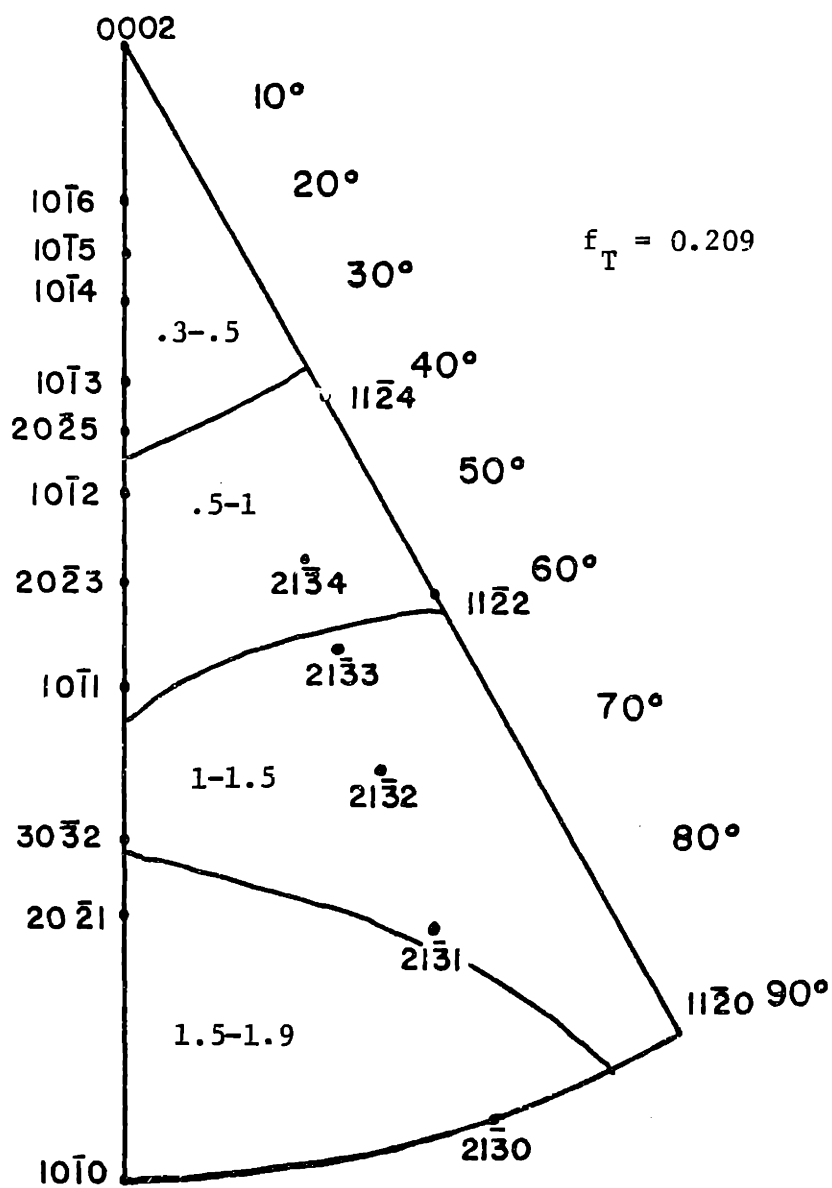Inverse Pole Figure from Transverse Direction of Plate 9908-3A

Figure B.7

Inverse Pole Figure from Rolling Direction of Plate 9908-3A

Figure B.8

Basal Pole Figure 5.92 mm from Surface of Plate 9908-3B

Figure B.9

TRANSVERSE-NORMAL SCAN FOR
PLATE 9908-3B   5.92 MM   FROM TOP OF PLATE

Figure B.10

Inverse Pole Figure 5.99 mm from Surface of Plate 9908-3B

Figure B.11

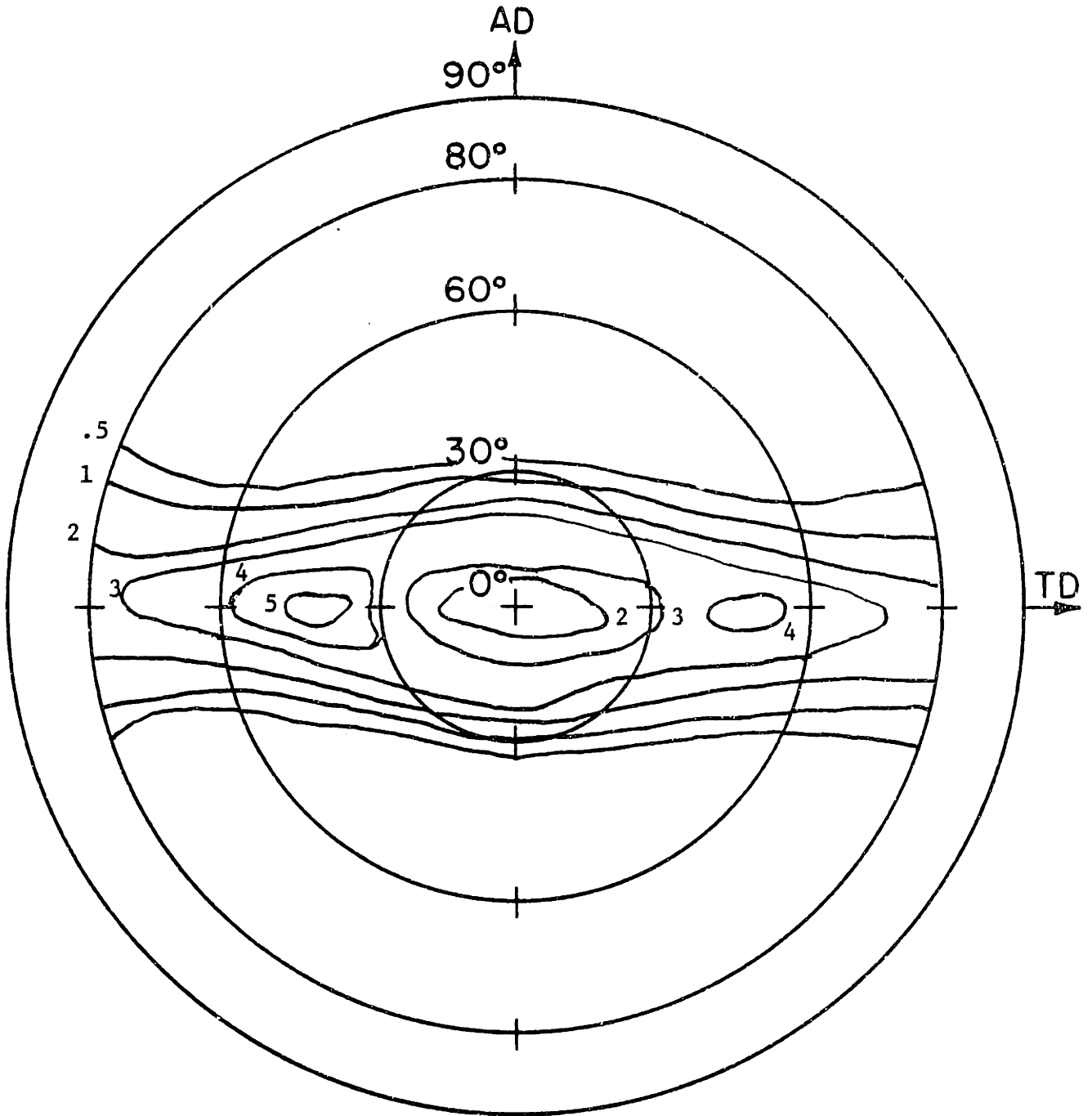Inverse Pole Figure from Transverse Direction of Plate 9908-3B

Figure B.12

Basal Pole Figure 7.85 mm from Surface of Plate 9912-SR

FIGURE B.13

TRANSVERSE-NORMAL SCAN FOR
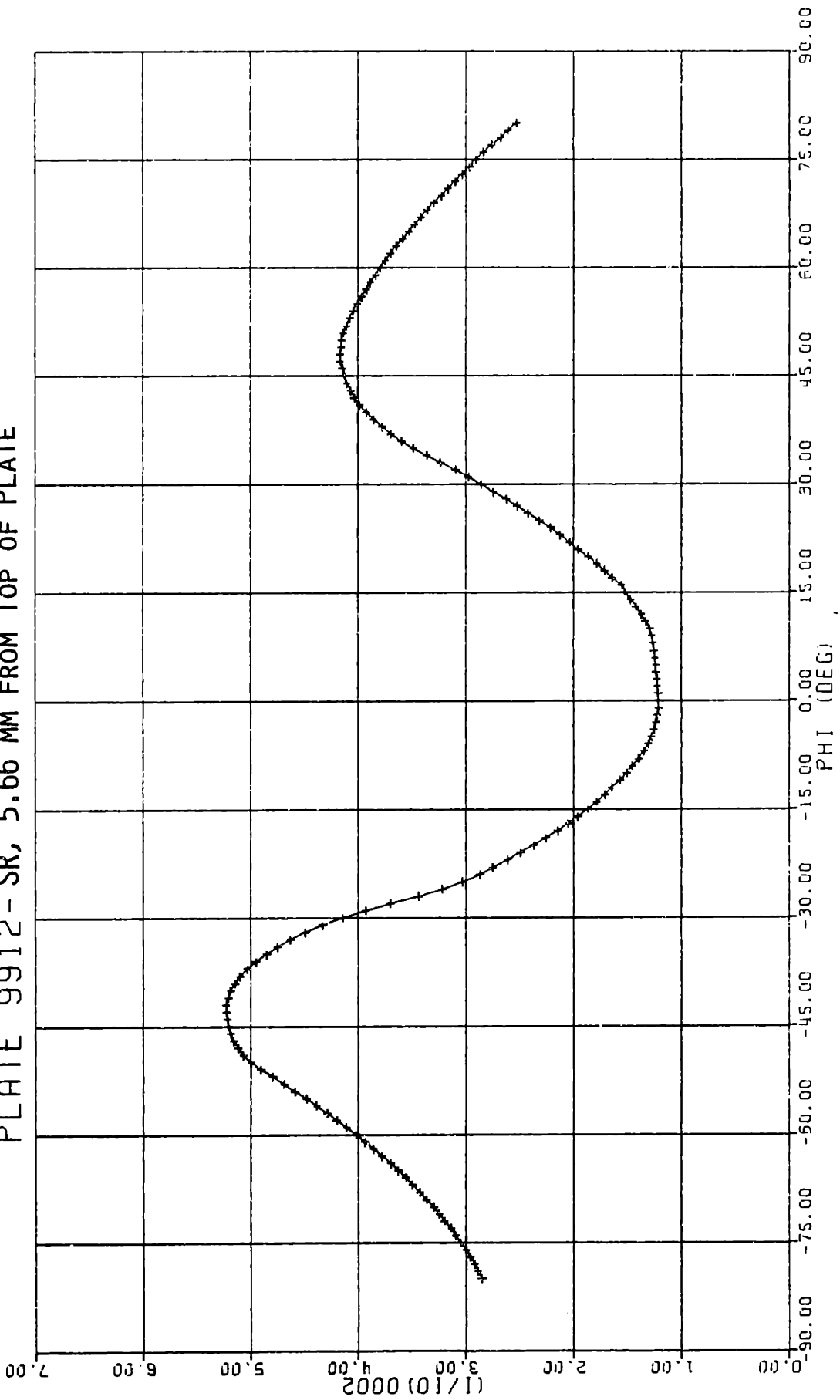PLATE 9912-SR, 5.66 MM FROM TOP OF PLATE

Figure B.14

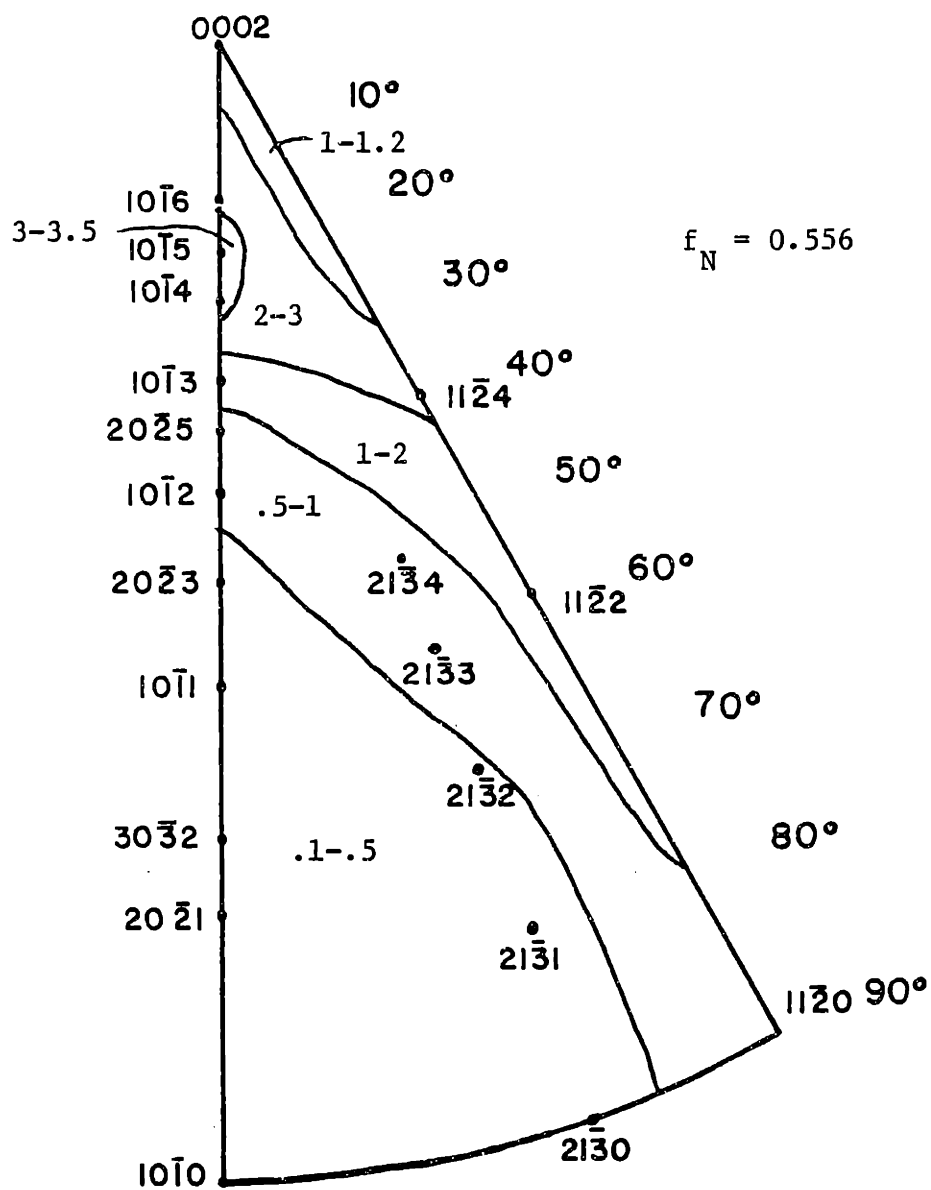Inverse Pole Figure 7.85 mm from Surface of Plate 9912-SR

Figure B.15

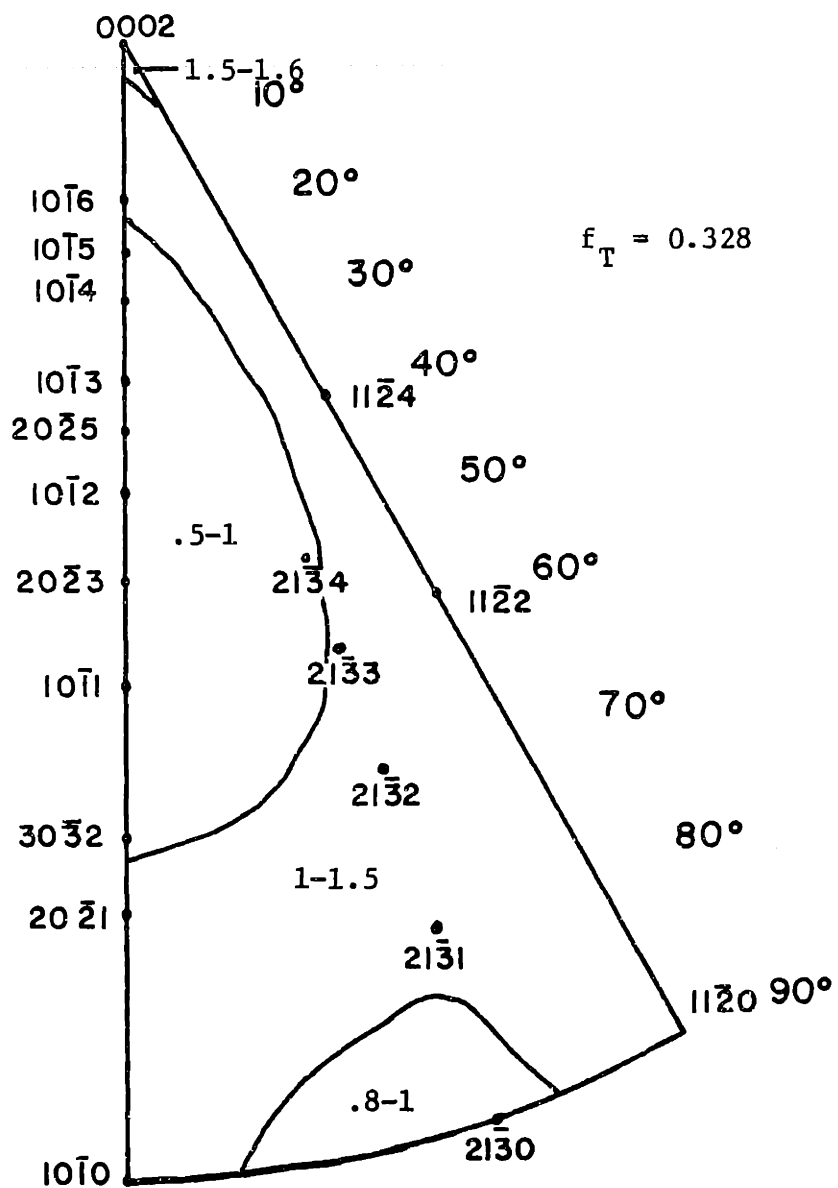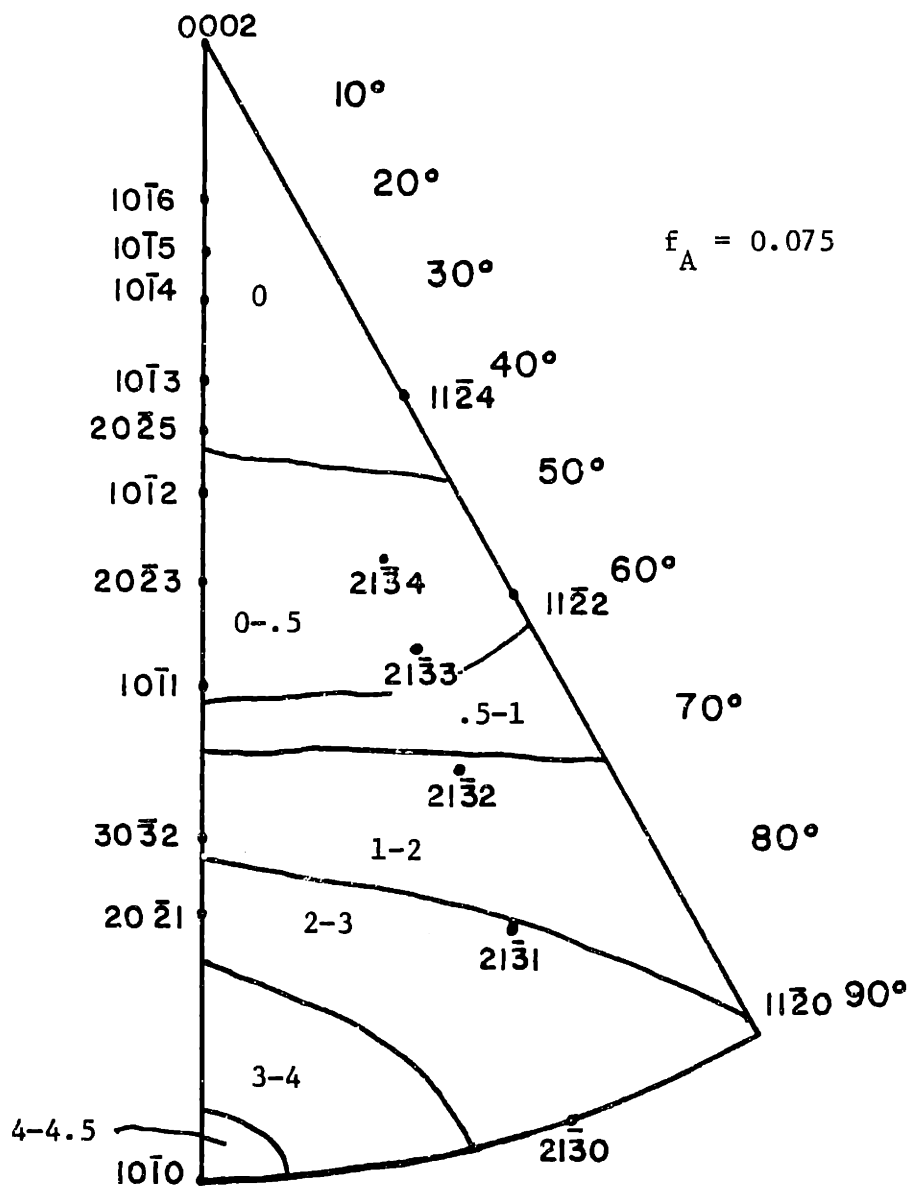Inverse Pole Figure from Transverse Direction of Plate 9912-SR

Figure B.16

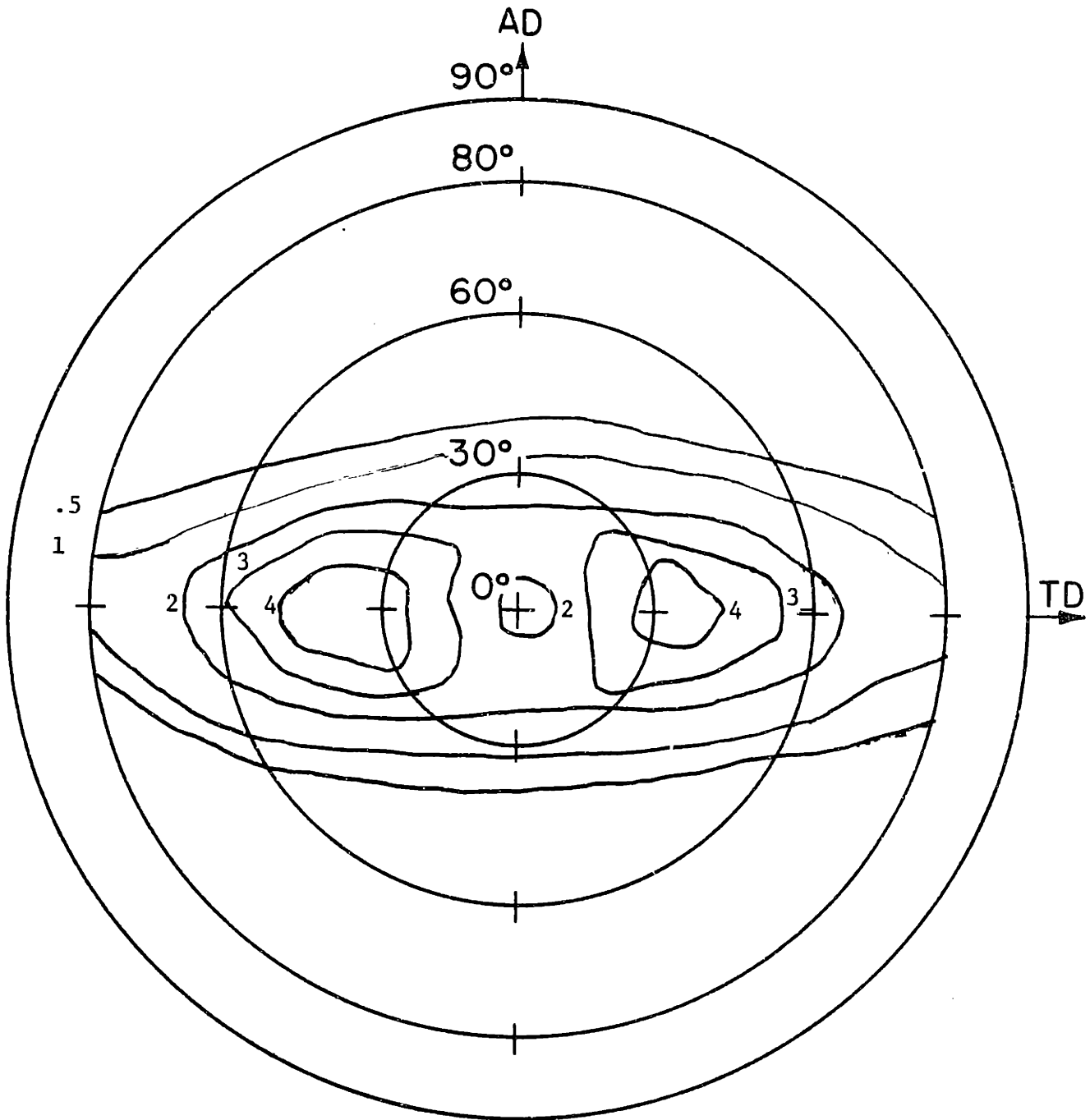Inverse Pole Figure from Rolling Direction of Plate 9912-SR

Figure B.17

Basal Pole Figure 7.77 mm from Surface of Plate 9912-RX

Figure B.18

Inverse Pole Figure 7.77 mm from Surface of Plate 9912-RX
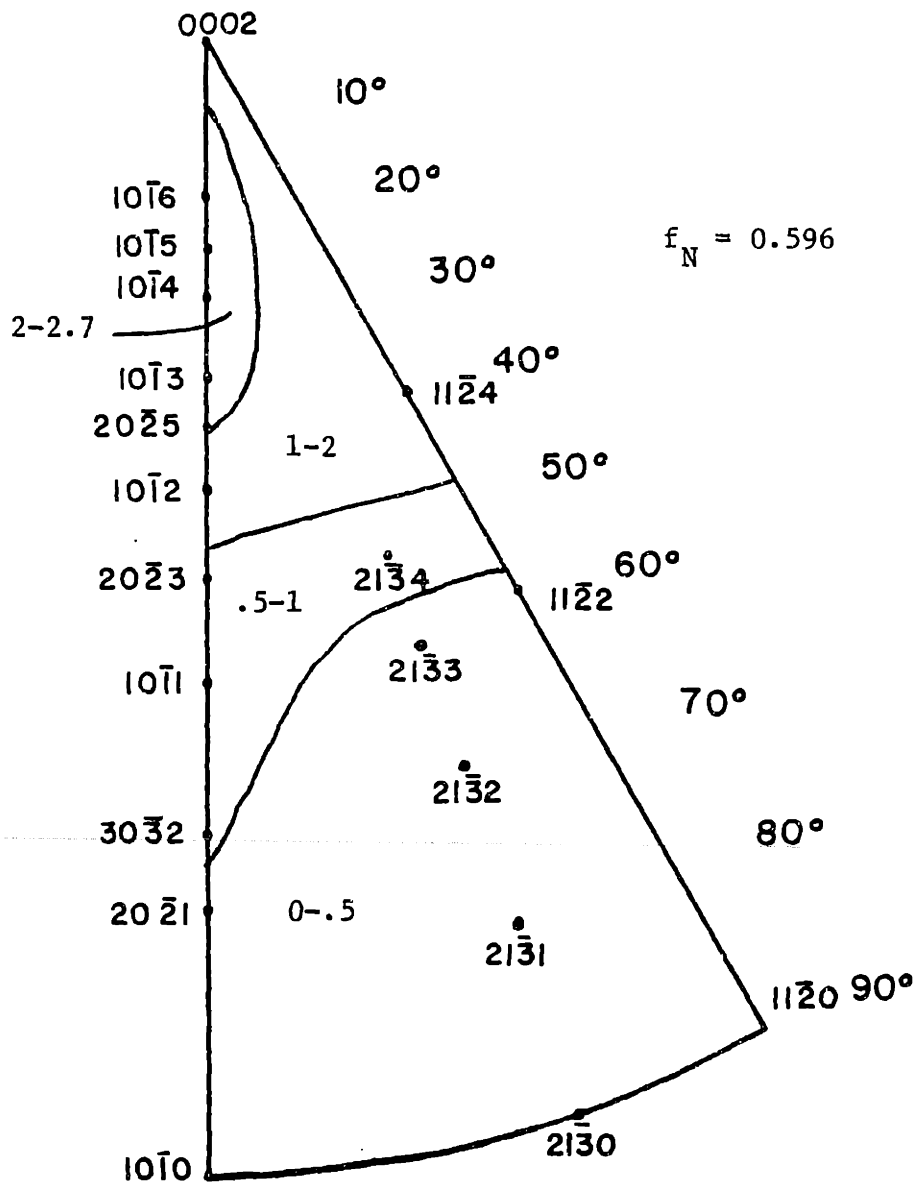
Figure B.19

Inverse Pole Figure from Transverse Direction of Plate 9912-RX
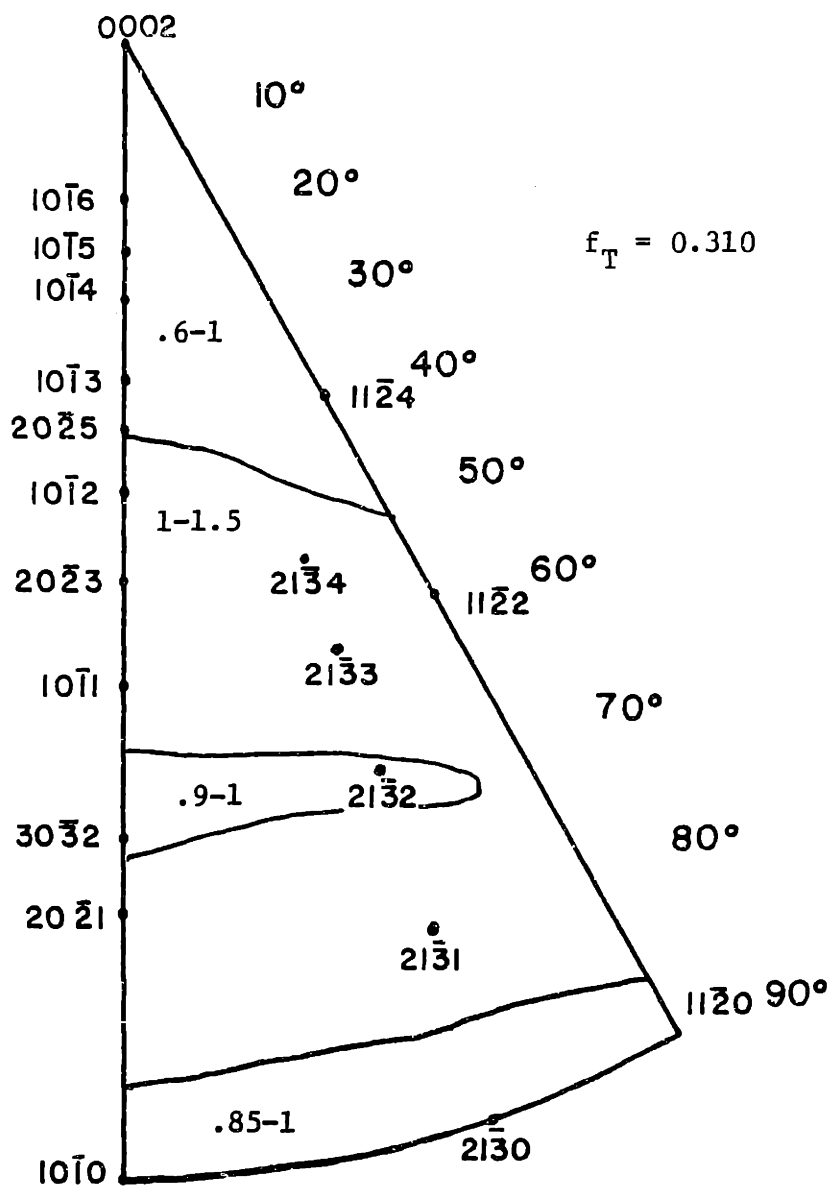
Figure B.20

Inverse Pole Figure from Rolling Direction of Plate 9912-RX
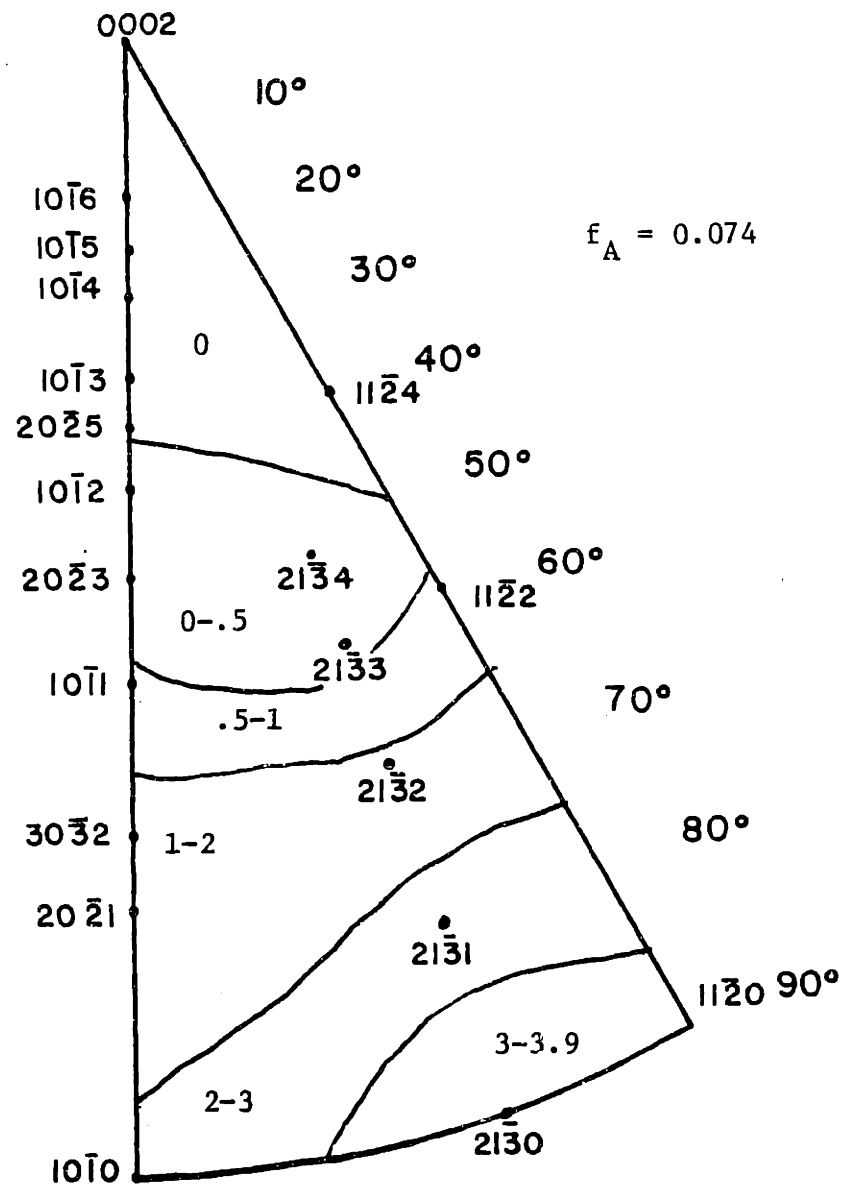
Figure B.21

Basal Pole Figure 0.47 mm from OD of Supplier A Tubing

Figure B.22

{10$\bar{1}$0} Pole Figure 0.47 mm from OD of Supplier A Tubing

Figure B.23

Inverse Pole Figure 0.47 mm from OD of Supplier A Tubing
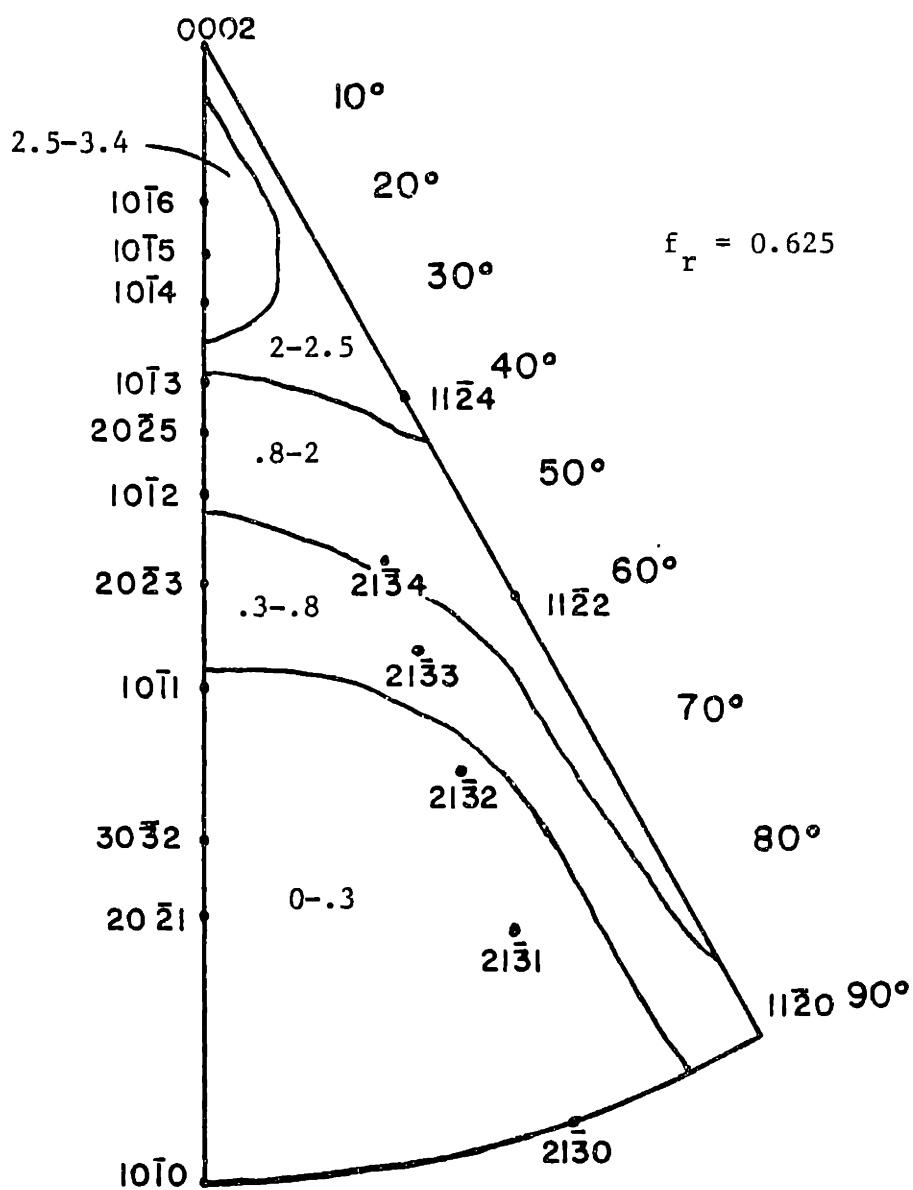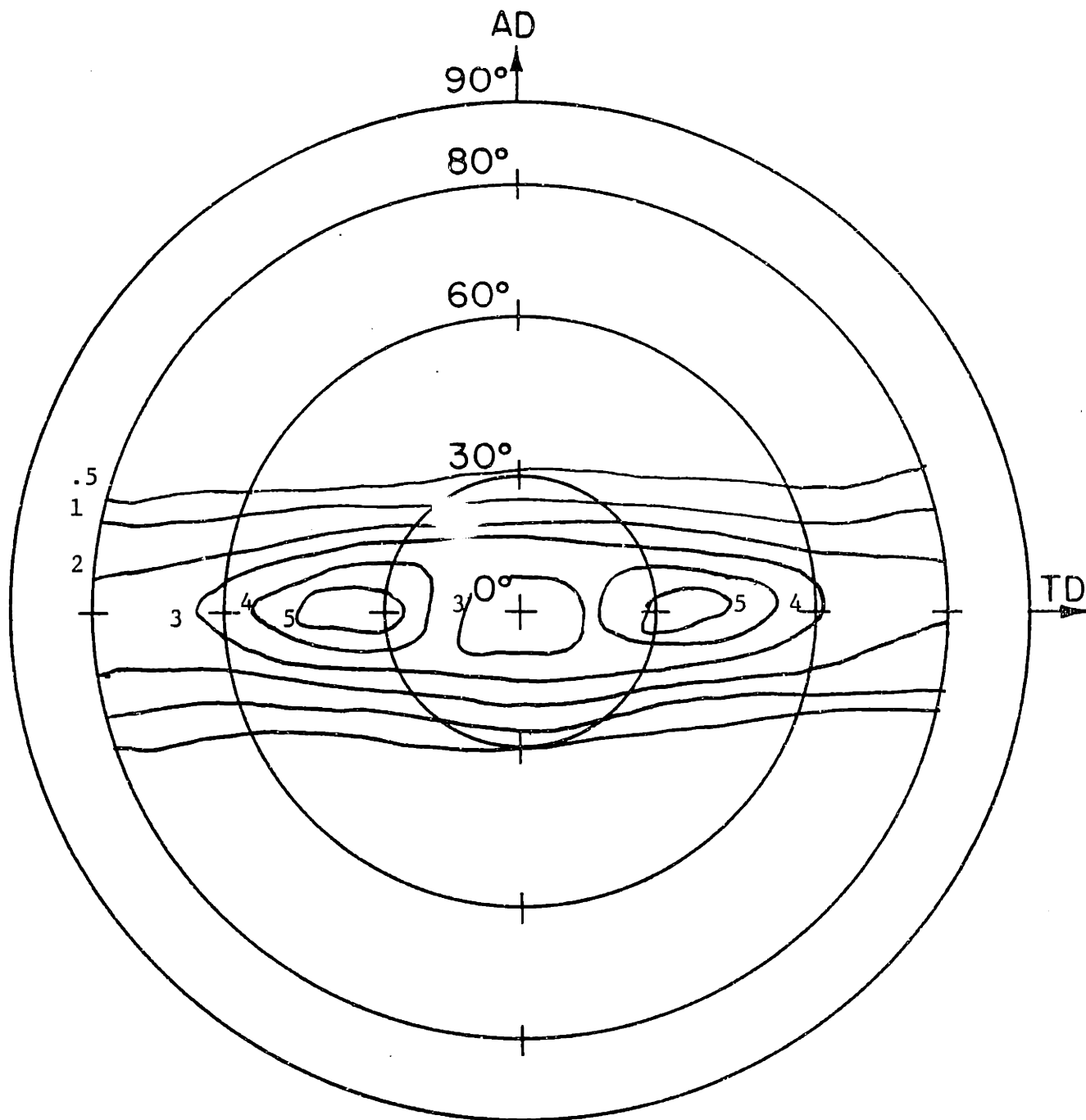
Figure B.24

Basal Pole Figure 0.10 mm from OD of Supplier A Tubing
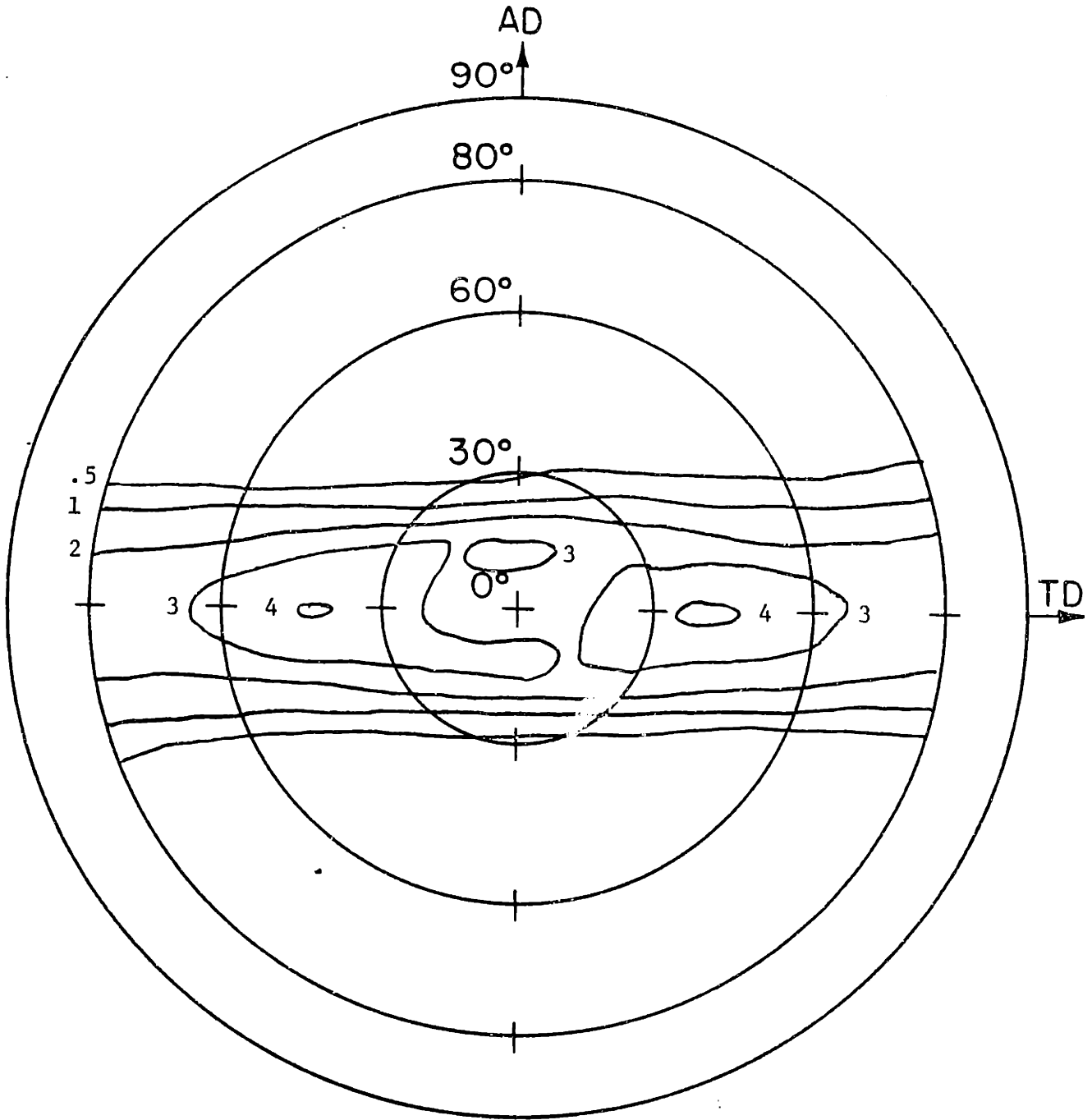
Figure B.25

Basal Pole Figure 0.47 mm from OD of Supplier B Tubing
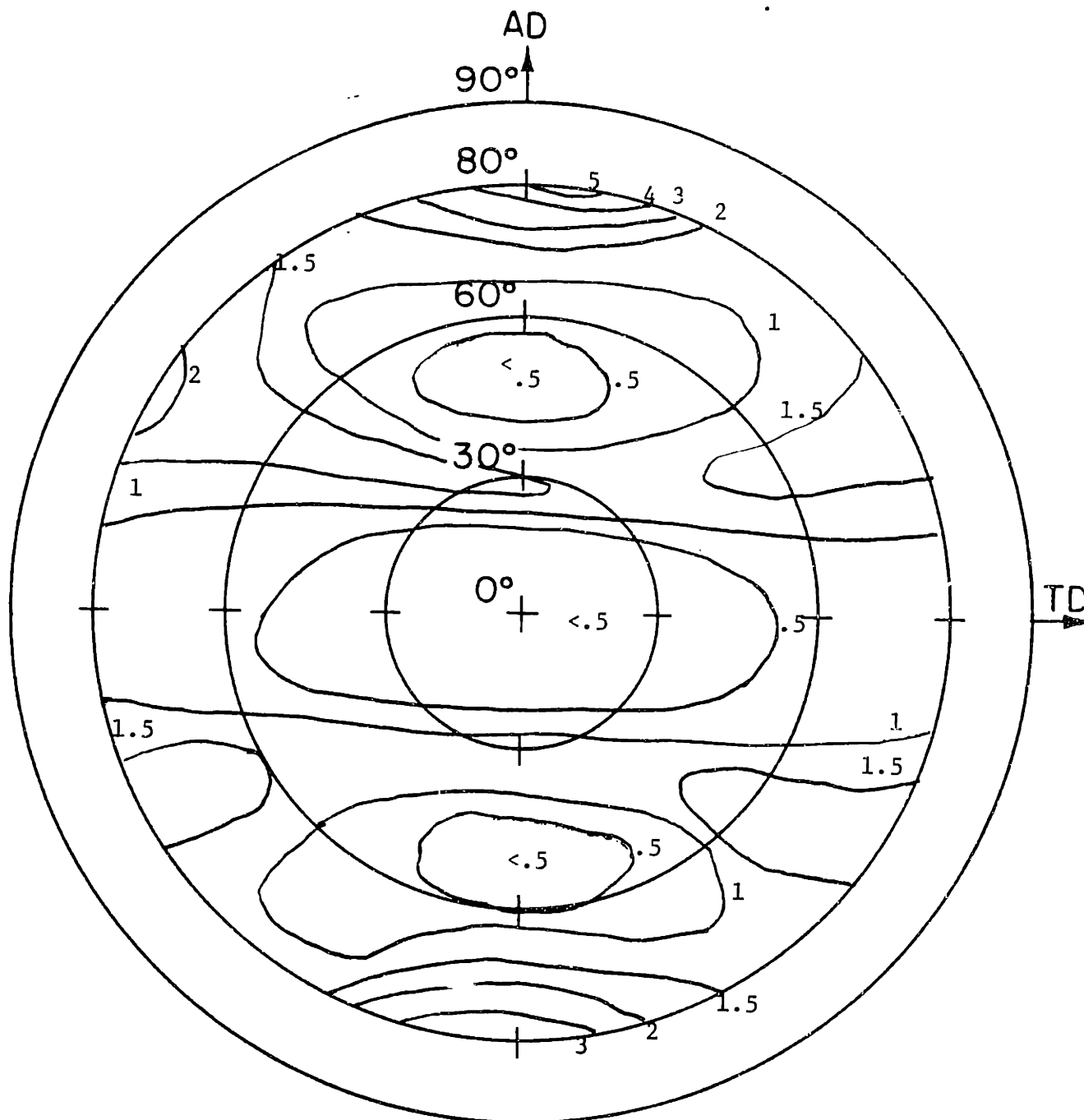
Figure B.26

{10$\bar{1}$0} Pole Figure 0.47 mm from OD of Supplier B Tubing

Figure B.27

Inverse Pole Figure 0.47 mm from OD of Supplier B Tubing
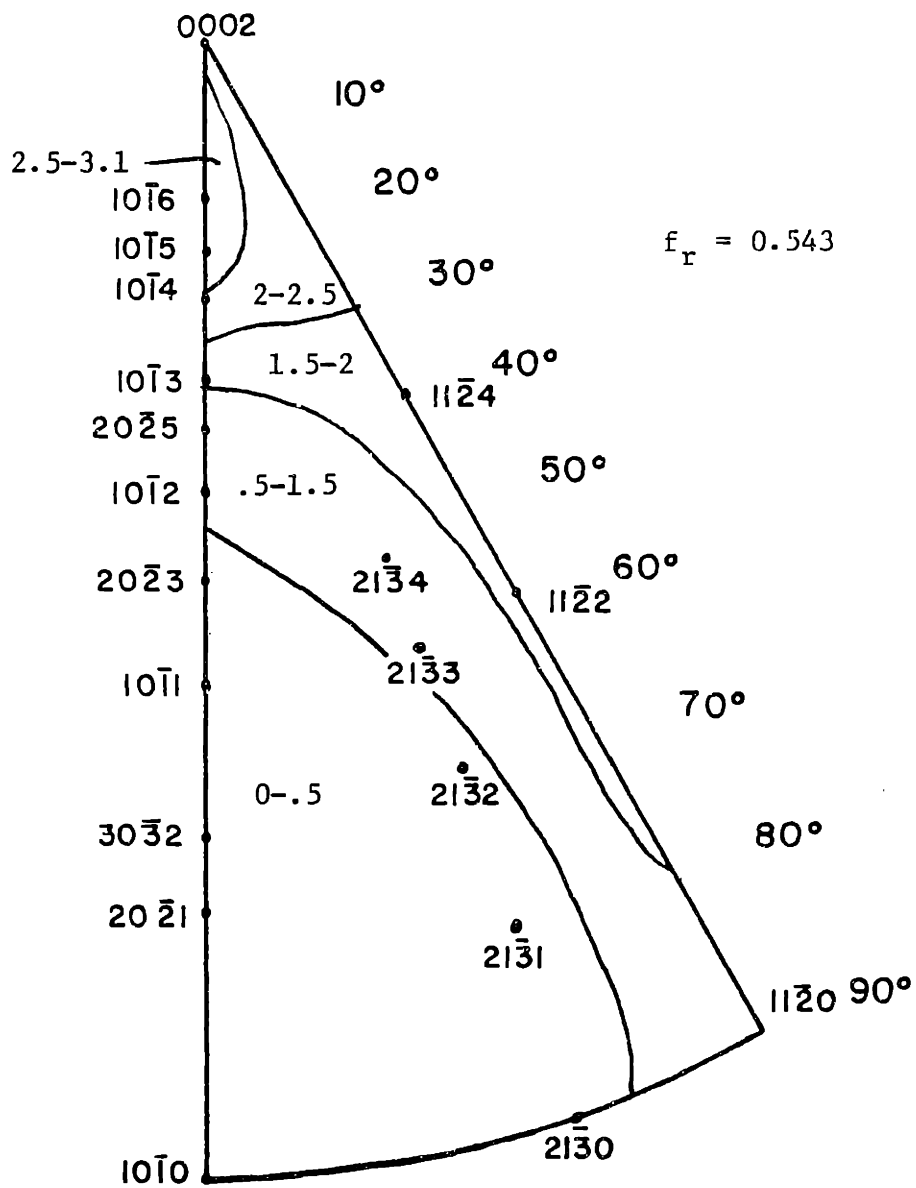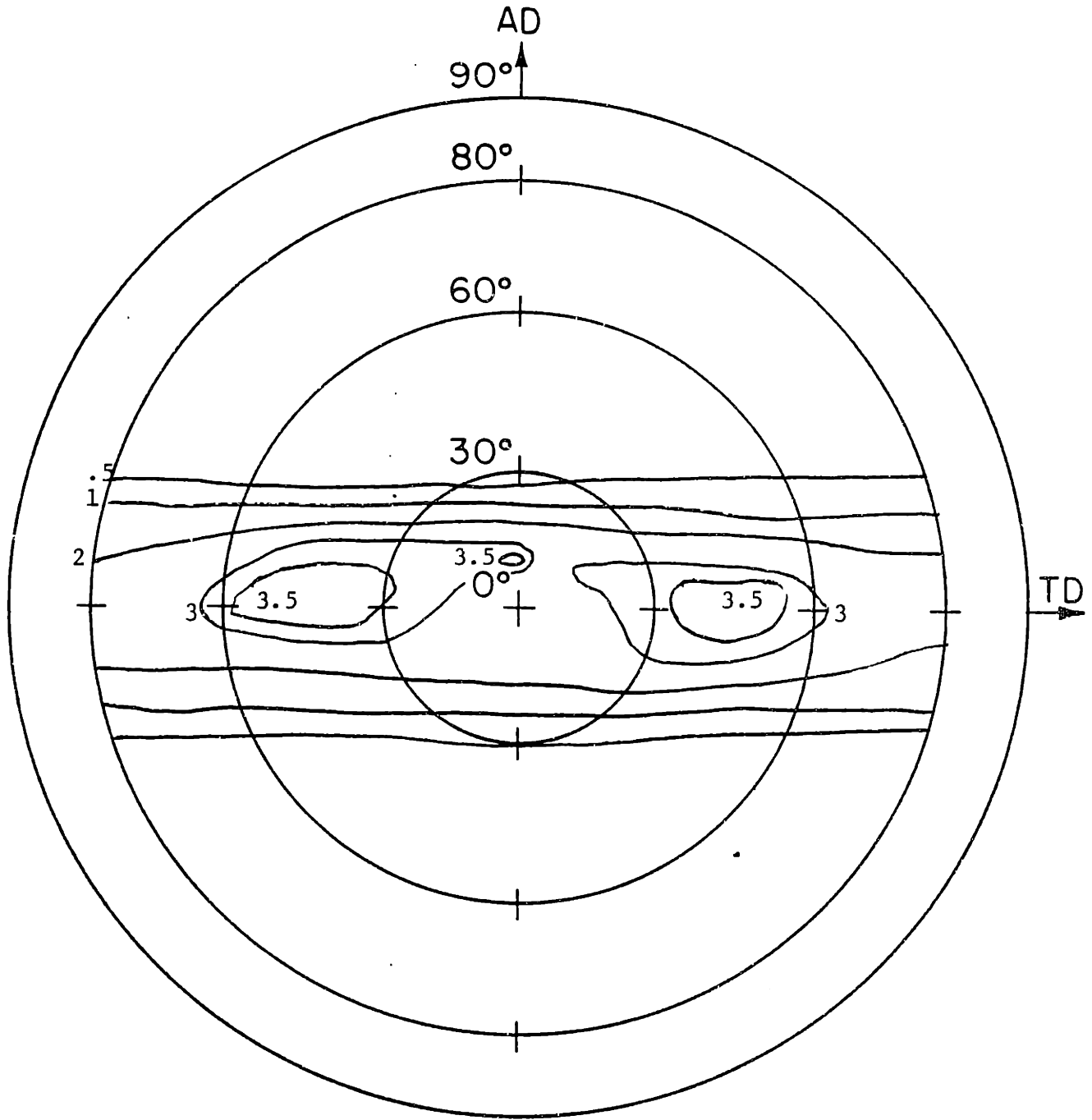
Figure B.28

Basal Pole Figure 0.10 mm from OD of Supplier B Tubing
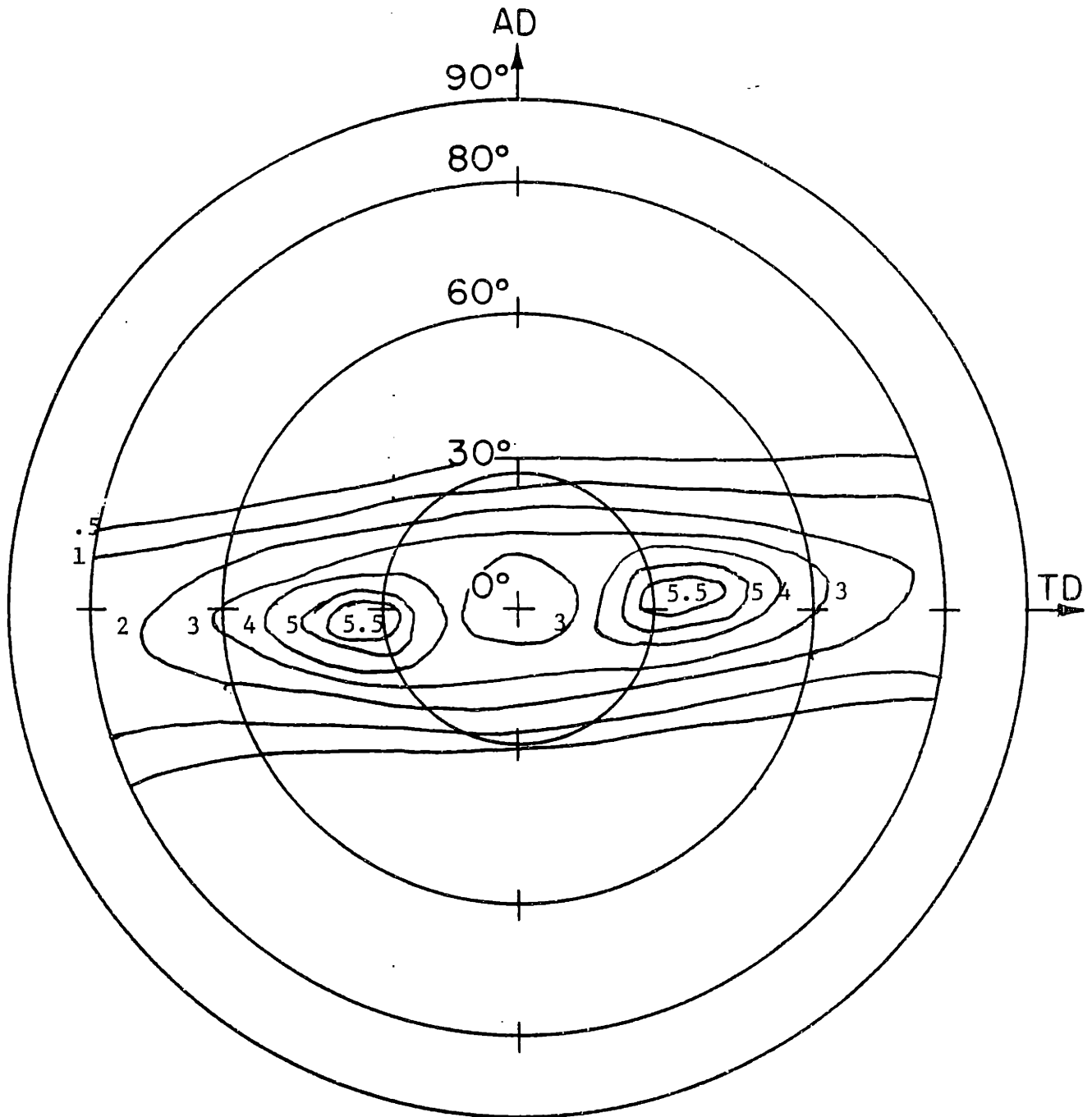
Figure B.29

Basal Pole Figure for ID Surface of Lot 1340 Tubing

Figure B.30
RADIAL-TANGENTIAL SCAN FOR
LOT 1340, ID SURFACE
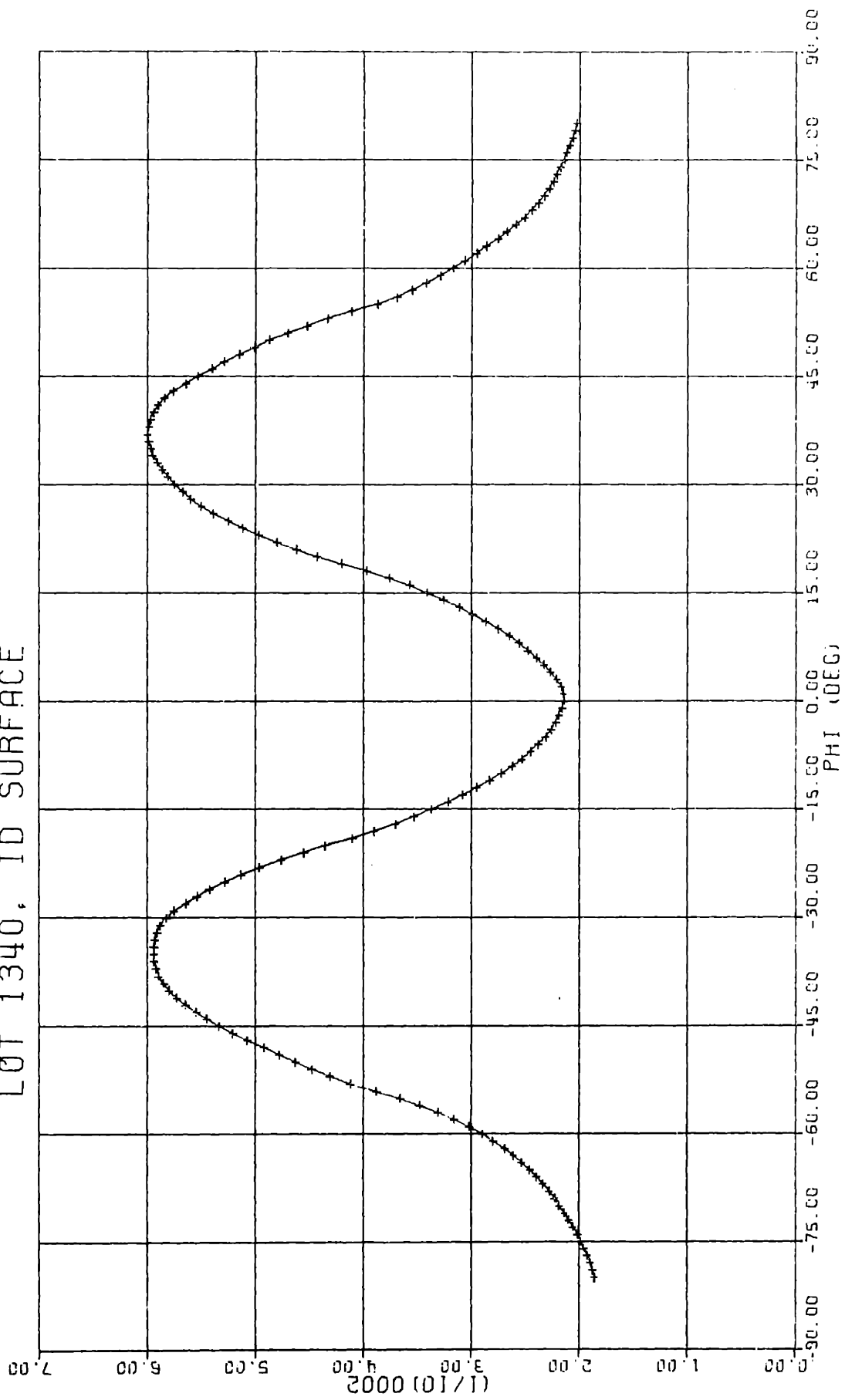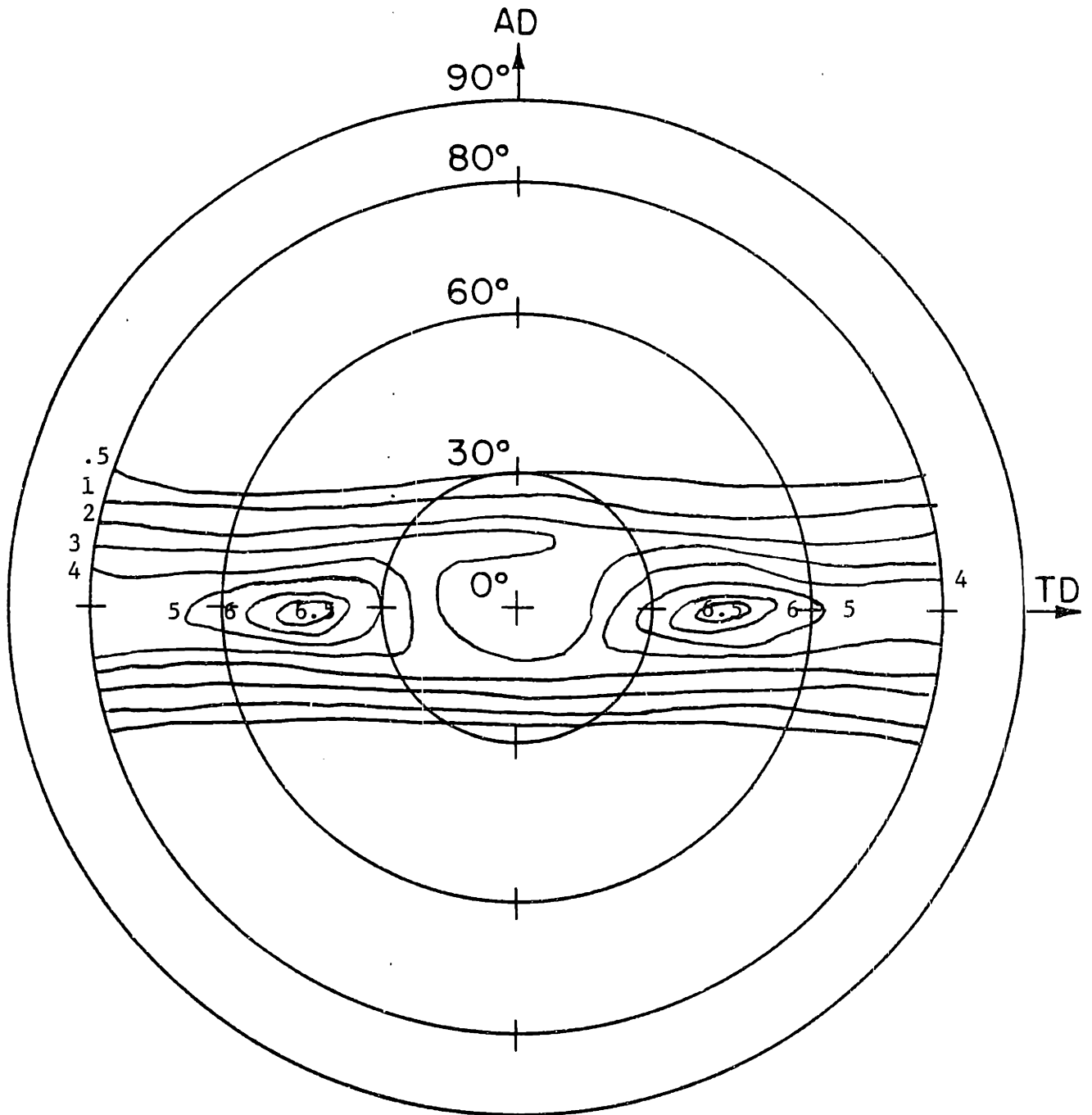
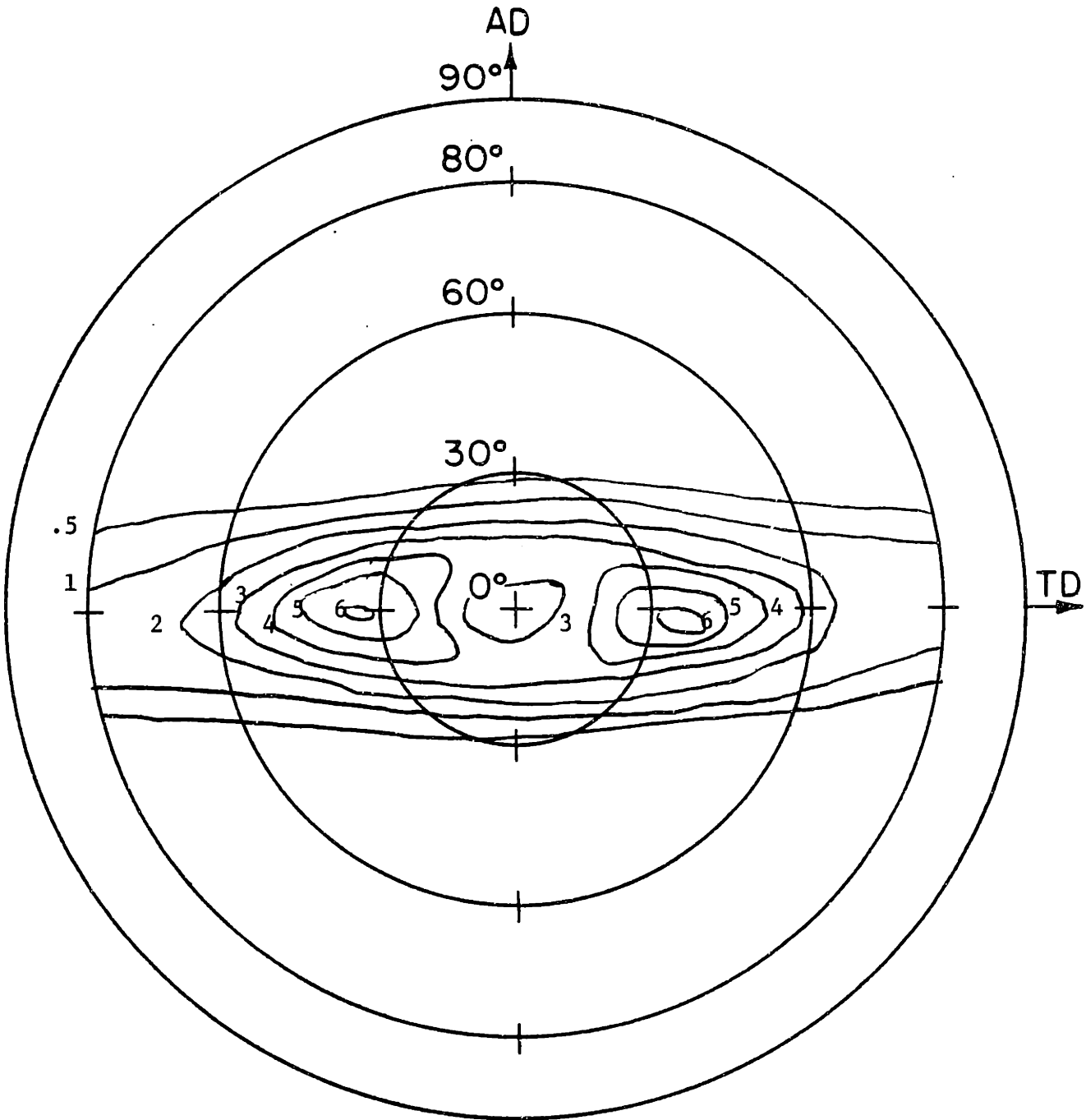Figure B.31
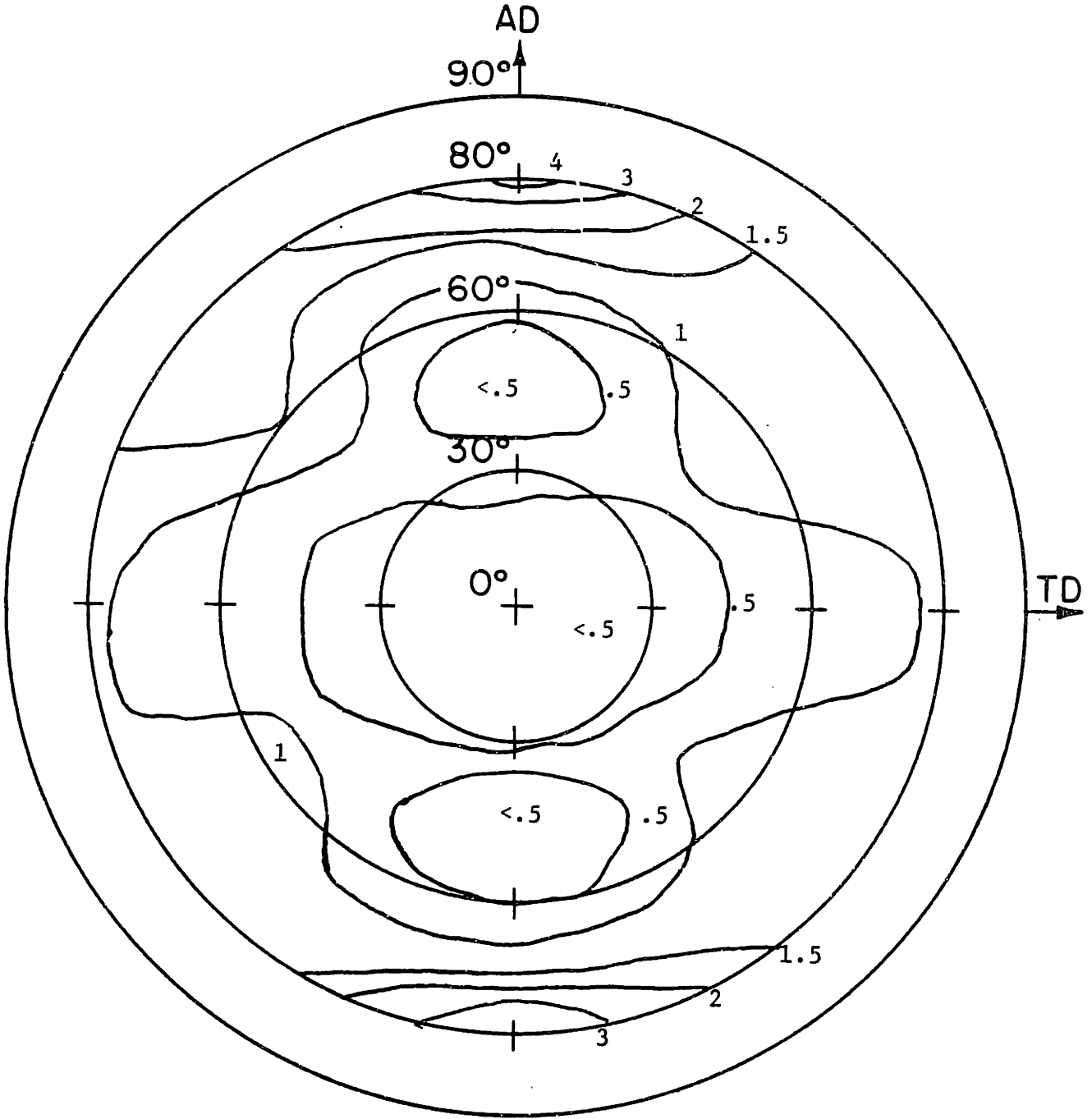
Basal Pole Figure 0.46 mm from OD of Lot 1340 Tubing
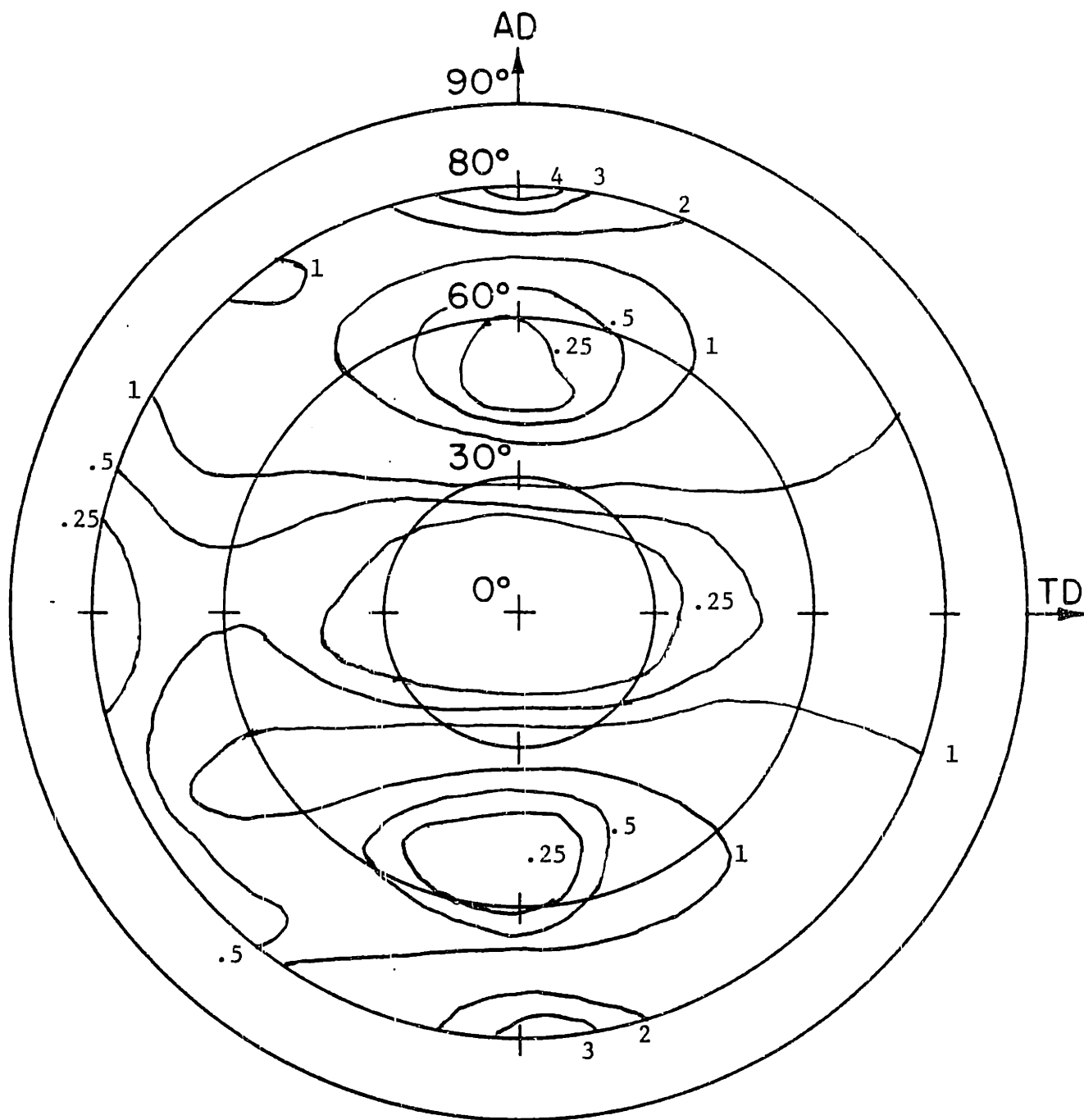
Figure B.32

{10$\bar{1}$0} Pole Figure 0.46 mm from OD of Lot 1340 Tubing

Figure B.33

Inverse Pole Figure 0.46 mm from OD of Lot 1340 Tubing
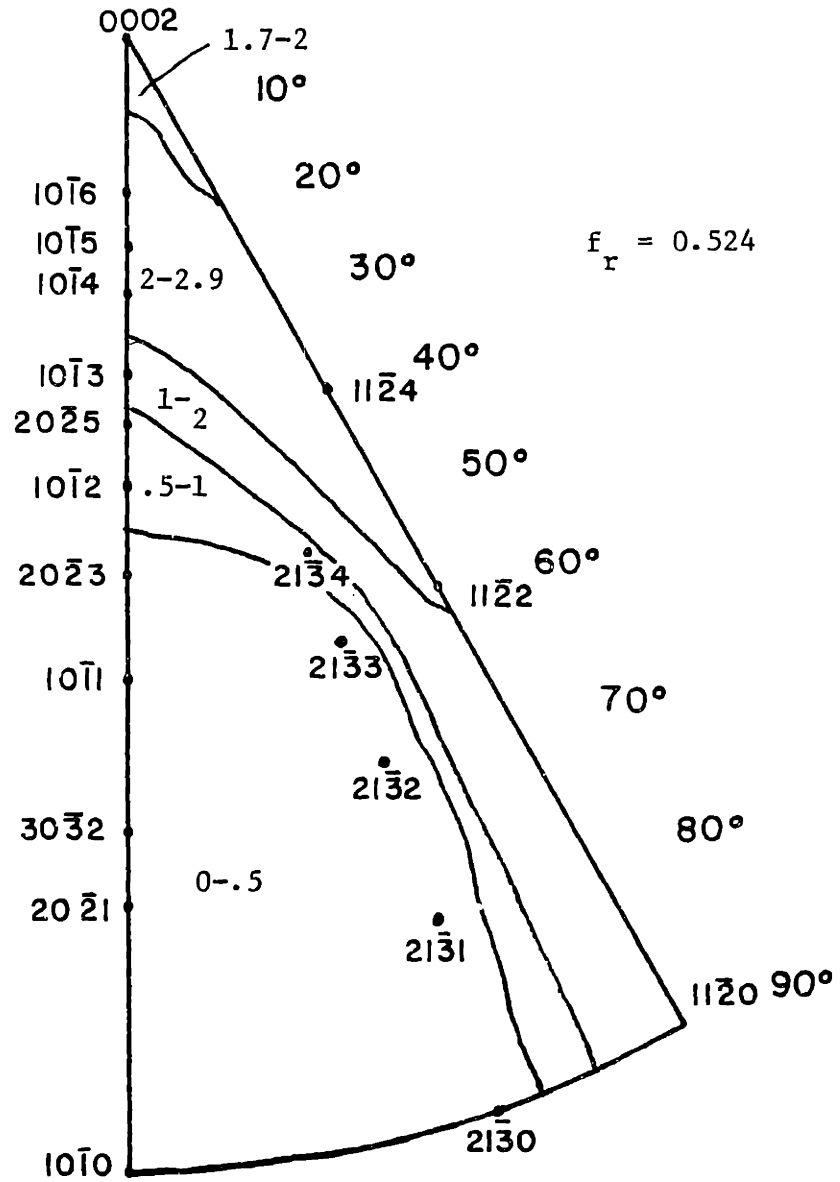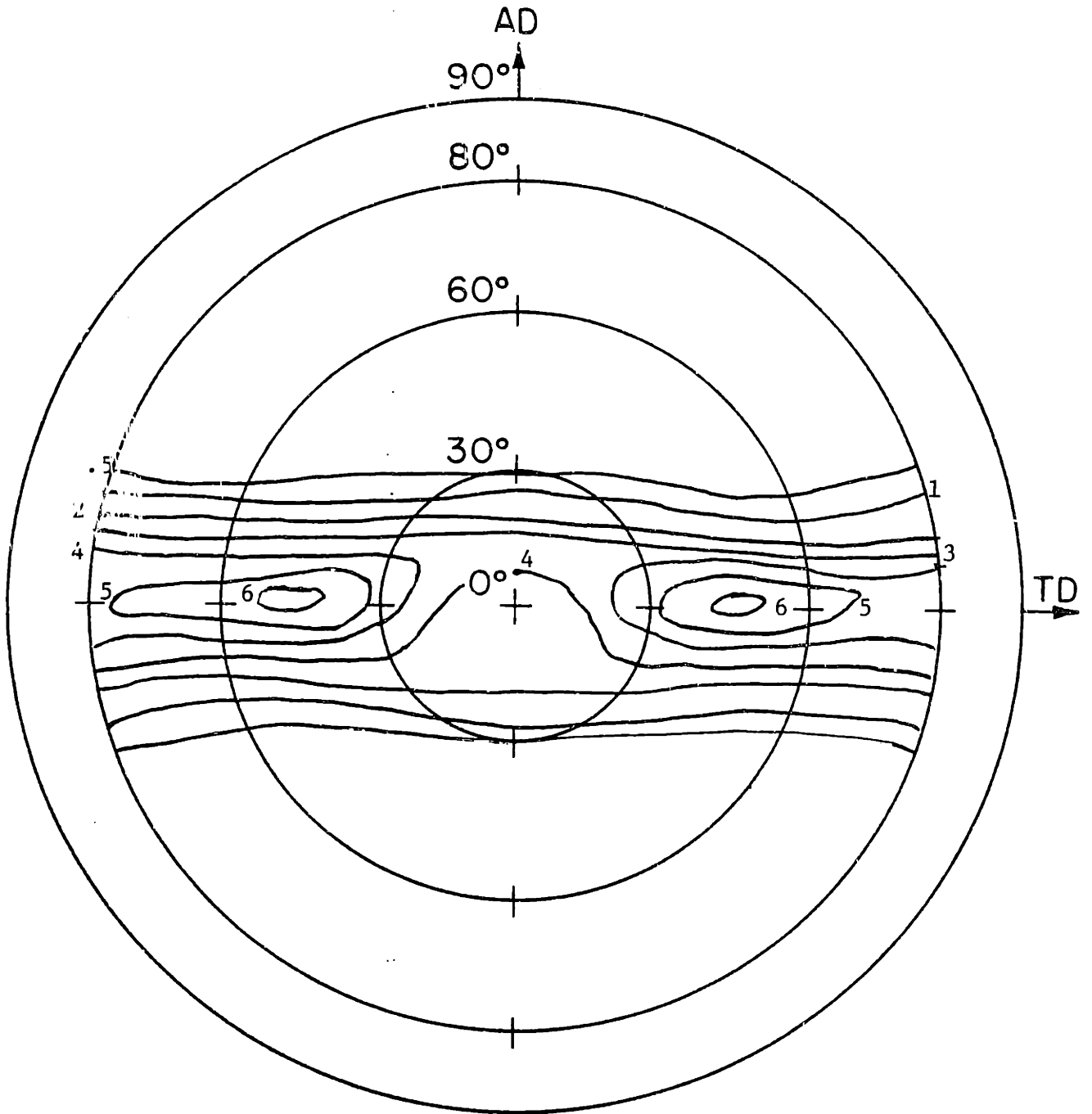
Figure B.34

Basal Pole Figure 0.10 mm from OD of Lot 1340 Tubing

Appendix C

Compositions and Fabrication Schedules for Experimental Materials

The chemical compositions for the plate and tubing are given in Table C.1. The plate fabrication schedules are shown in Table C.2. No fabrication histories are available for the tubing materials due to the proprietary nature of the production processes.

-

Table C.1

Chemical Composition for Tubing and Plate Materials

Element[a]	9908 Plate	9912 Plate	Supplier A Tubing	Supplier B Tubing	Lot 1340 Tubing
Sn(w/o)	1.51	1.52	1.47	1.51	1.60
Fe(w/o)	0.14	0.20	0.15	0.14	0.15
Cr(w/o)	0.10	0.11	0.11	0.07	0.12
Ni(w/o)	0.05	<0.0035	0.07	0.05	0.06
O	1280	1180	1170	1395	1310
H	7	10	12	7	12
N	37	40	32	30	47
C	130	120	176	200	180
Al	48	42	44	40	35
Si	71	<50	73	56	49
Zr	bal	bal	bal	bal	bal

(a) Quantities in ppm unless otherwise noted

Table C.2

Zircaloy Plate Fabrication Schedules

9908

Beta Quench 100 mm Slab

Heat at 897°C and Roll to 33 mm

Reheat to 797°C and Quench

Heat at 347°C and Cross Roll to 12.7 mm

3A — Stress-Relieve at 497°C for 4 hr

3B — Recrystallize at 567°C for 2 hr

9912

Beta Quench 100 mm Slab

Heat at 897°C and Roll to 33 mm

Reheat to 797°C and Quench

Heat at 347°C and Roll to 12.7 mm

SR — Stress-Relieve at 485°C for 4 hr

RX — Recrystallize at 625°C for 4 hr
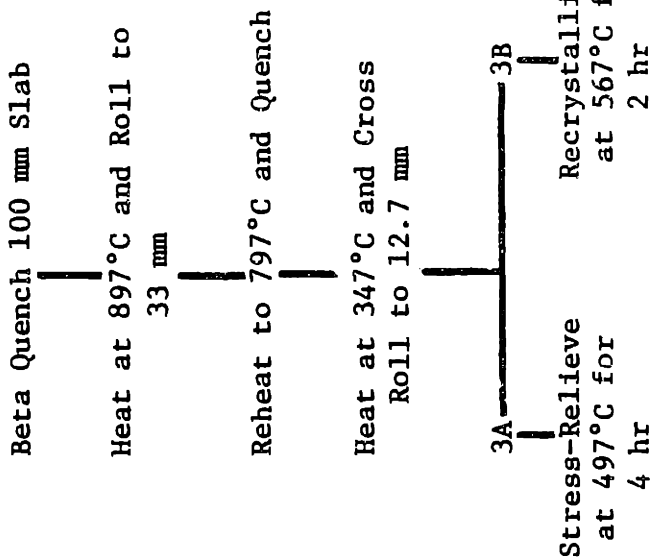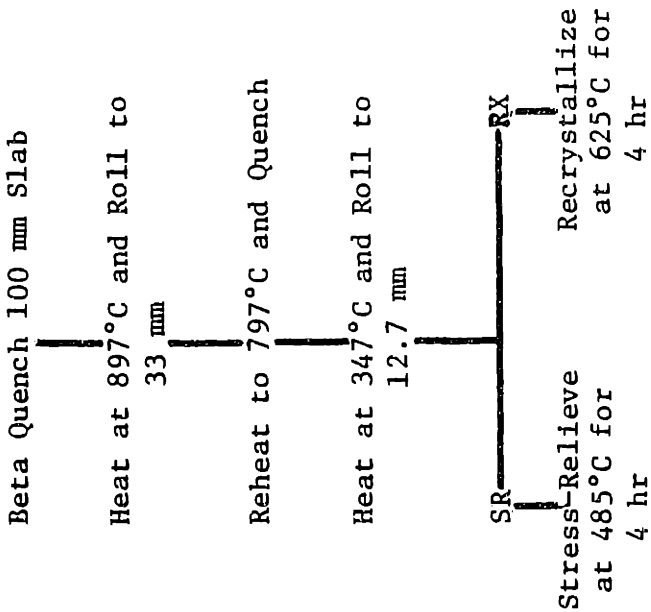
Appendix D

Verification of K_{ISCC} Values in Fracture Mechanics Specimens

D.1 Introduction

An important consideration regarding the validity of the K_{ISCC} values from fracture mechanics specimens is the accurate measurement of the final load line opening value, Δ_f. The true value must be known to accurately calculate K_f by Eqn. (4-1). The opening decreases during the test as observed in Table 6.1. Three phenomena might contribute to this behavior:

1. Plasticity in the specimen arms when initially loading the specimen;

2. Incomplete crack closure after unloading;   .

3. Creep in the arms of the specimen during the test.

Incomplete crack closure would introduce the most error since the specimen remains, in a sense, partially loaded. Low values of K_f are calculated if this is the case. Plasticity and creep of the specimen arms change only Δ and allow accurate K_f to be determined if the specimen is fully unloaded.

D.2 Procedures and Results

Several experiments are run on stress-relieved material to ascertain the relative contribution of these three factors to the decrease in Δ. A DCB-NL specimen is precracked in fatigue to give a crack length of 9.82 mm. It is loaded to an opening of 0.55 mm corresponding to K = 47.6 MPa$\sqrt{m}$ Complete unloading gives load line opening of 0.51 mm. Thus, the opening is primarily elastic where plasticity effects decrease the opening values by less than 10%. The plasticity effect is less for the lower initial K values reported in Table 6.1. The same specimen is

reloaded to an opening of 0.35 mm corresponding to K = 29.7 MPa$\sqrt{m}$

which is comparable to the K_i values in Table 6.1. The loaded specimen

is placed in a furnace at 300°C, left for a period of time, removed and

measured for load line opening, and finally reloaded to an opening equal

to that prior to unloading. This sequence is repeated in several steps

to develop a curve of time versus relaxation of opening. The final

opening is 0.26 mm. Following this series of measurements, the crack

length is increased by machining a slot 13.4 mm deep. The specimen is

loaded to an initial load line opening of 0.33 mm which corresponds to

K = 19.1 MPa$\sqrt{m}$ if the slot were a sharp crack. A series of measurements

are done as before to generate a relaxation curve. The final opening

is 0.30 mm. The two relaxation curves are plotted in Fig. D.1.

A second test uses a fatigue precracked DCB-NT specimen with a

crack length of 8.89 mm. The specimen is loaded to an initial displace-

ment corresponding to K = 25.2 MPa$\sqrt{m}$ in a test chamber attached to an

Instron machine. Load relaxation at 300°C is monitored. After several

hours, the steadily decreasing load is increased to slightly above the

initial value (i.e. to K = 25.8 MPa$\sqrt{m}$) and monitored for several hours

until an iodine SCC crack starts to grow. The plot of time versus load

relaxation is given in Fig. D.2.

D.3 Discussion

Plasticity accompanying loading is a small contribution to the

total relaxation of the specimen crack opening. Since no SCC crack grows

during either of the tests, the closure of a growing crack is not a

problem. 20 - 25% of the initial load line opening is relaxed within

several hours, and the rate of relaxation decreases with time. Since

closure and plasticity do not provide large contributions, the relaxation

must be due to creep of the specimen beam arms. The relaxation fractions in Figs. D.1 and D.2 are compared with the δ_i/δ_f values in Table 6.1. With a few exceptions, the δ_i/δ_f are comparable to the levels of relaxation observed in these control tests.

Another possible concern for the crack arrest tests is continued relaxation after crack arrest occurs. The fracture mechanics specimens are generally left in the test atmosphere at 300°C for up to several days after fast SCC propagation ceases. The test with the long slot length in Fig. D.1 indicates that the rate of relaxation is quite low at the lower K value ($\lesssim 20$ MPa m). The rate of relaxation would be even less at the lower K_f values reported in Table 6.1.

No relaxation tests are run on recrystallized material. However, specimen 9908-3B-DCB-TL-23 which is a fatigue precracked sample, had no SCC propagation, therefore, it is useful as a check on relaxation. The δ_i/δ_f for this specimen is comparable to that in other recrystallized samples. This indicates that incomplete crack closure is not a problem in tests on recrystallized material. The δ_i/δ_f values for recrystallized material are lower as a group than those for stress-relieved material. This is consistent with an expected larger creep contribution to relaxation and with a somewhat greater plasticity effect in the softer recrystallized material

The tests reveal that most relaxation occurs early in the period of the test, i.e. during the incubation period prior to crack growth. The K values during propagation are more accurately calculated with the final specimen opening.

A final issue deals with the difference in K_{ISCC} values comparing WOL and DCB specimens from stress-relieved 9912 plate in the TL orient-

ation. Two possible explanations are inaccuracies in the K expressions, Eqs. (4-1) and (4-2), or differences in crack closure chacteristics between WOL and DCB specimen designs. The K formulations are standard expressions verified by continued use over several years. It is unlikely that they would fail to apply to this case. The ASTM validity criterion to insure plane strain loading conditions is met by both specimen designs at K_f. The δ_i/δ_f is comparable for both specimen types as indicated in Table 6.1. If the final opening was greater in the WOL specimen due to less creep relaxation or less crack closure, higher K_f values might be calculated, however this is not the case. Thus, no explanation is available to account for the $\sim 50\%$ difference in K_{ISCC} as measured between the DCB specimens and the WOL specimens.

D.4 Summary

Three possible explanations for the decrease in the initial load line opening deflection in fracture mechanics specimens are explored. Plasticity is observed to make only a secondary (<10%) contribution to the decrease. Incomplete crack closure is not responsible since the decrease is observed in the slotted or fatigue precracked specimens where no crack propagation occurs. Creep relaxation is the best explanation since the levels of relaxation in the control tests are comparable to the levels observed in the iodine SCC tests. The greater relaxation in recrystallized specimens compared to stress-relieved specimens is consistent with this conclusion.
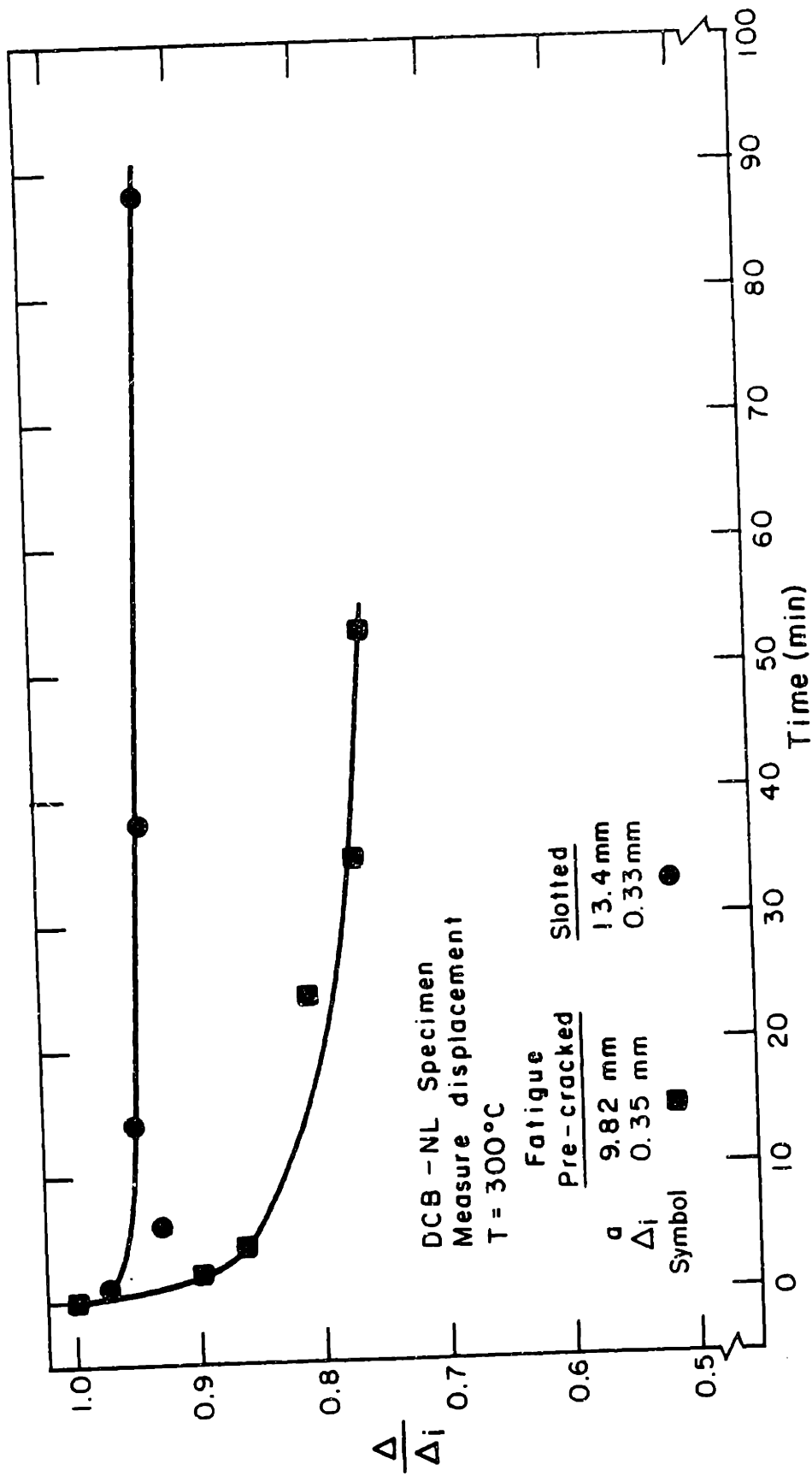
Figure D.1

Relaxation of Load Line Opening in a DCB-NL Specimen at 300°C
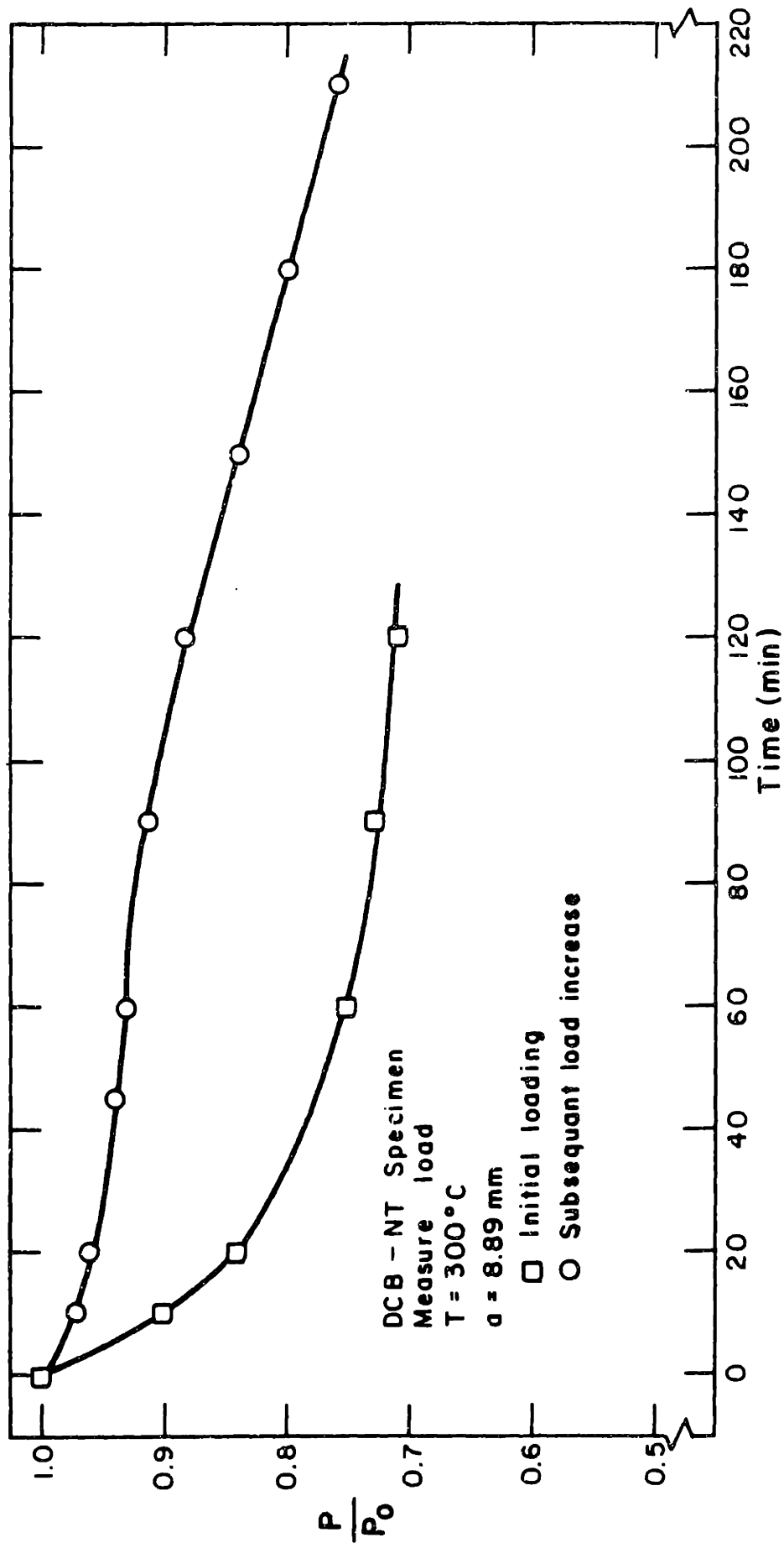
Figure D.2   Load Relaxation in a DCB-NT Specimen at 300°C

Appendix E

Description of Tube Pressurization Facility

E.1 Introduction

The tube pressurization facility is designed to provide a high pressure inert gas environment for internal pressurization tests on Zircaloy fuel cladding. The system is shown schematicly in Fig. 4.3. High purity argon gas (>99.999%) is pumped into a reservoir by an air driven gas booster pump. The gas is then bled through a micrometering valve into the specimen to attain the desired pressure. The specimen is held at pressure until failure occurs. Subsequent discussion describes the system operation in detail, then gives information on specimen assembly.

E.2 Operation

Two sequences of steps are required to perform a test: pressurization of the reservoir and specimen pressurization. The test system is shown in Fig. E.1. All high pressure lines and fittings are assembled under the table top. Only the inlet to the specimen through Valve 6 is located above the table.

Argon gas (Matheson, high purity) is supplied to the gas booster through a high pressure regulator. The line between the bottled argon and the pump is flushed several times prior to reservoir pressurization. The supply pressure to the booster pump is 8.3 MPa (1200 psi). The booster pump is operated by bottled compressed air supplied at 1.16 MPa (160 psi) through a high flow gas regulator. All fittings to the gas booster are Swagelok to copper tubing. All components beyond the gas booster are stainless steel. The reservoir is usually pressurized to 76 MPa (11,000 psi) which is sufficient for several SCC tests. Valve 1

(valves are numbered on both Fig. 4.3 and Fig. E.1) is opened to admit argon whose pressure is monitored on a large face gage. The gage is visible through the opening in the table on the left of Fig. E.1. Following reservoir pressurization, Valve 1 is closed and the inlet lines to the gas booster are bled of the remaining gas.

Specimen pressurization and venting is accomplished through manipulation of several valves. Gas is admitted to the specimen by opening Valves 4 and 6. The micrometering valve, Valve 3, is slowly opened to control the rate of pressure rise which is monitored by a pressure transducer indicator shown in Fig. E.1. The specimen is pressurized to ∿2.2 MPa (300 psi), Valve 4 is shut, and Valve 5 is slowly opened to vent the specimen. The specimen is purged in this manner 8-10 times prior to a SCC test to remove residual traces of air and water vapor.

To start a test a protective chamber of stainless steel pipe is placed around the specimen assembly, then enclosed in the furnace. An argon cover gas is flowed over the specimen to minimize OD oxidation. Heatup is controlled from a control panel shown at the lower right of Fig. E.1 and enlarged in Fig. E.2. The controller is set at a temperature 20-25°C below the test temperature since the thermal inertia causes the temperature to initially overshoot the setpoint. The setpoint is gradually raised until the test temperature is reached. An ammeter gives the current drawn by the furnace and the temperature is read by a thermocouple (TC) output shown in Fig. E.2. When the specimen temperature is stabilized, normally within 3 hours, Valve 4 is opened and argon gas is bled into the specimen through Valve 3 until the desired pressure is reached. Both valves are then closed and the timer is started. An indicator light shows

when the timer is "On". A limit indicator on the transducer indicator is set ∿2 MPa below the initial pressure. When the specimen fails, the limit switch opens a circuit which stops the timer and shuts off the furnace. Finally, Valve 6 is closed manually and the specimen is disassembled after the furnace cools.

E.3 Specimen Assembly

The assembled specimen prior to a test is shown in Fig. E.3. Fig. E.4 gives an exploded view of all the components. A Zircaloy tube specimen is cleaned in methanol and rinsed in acetone. The rear end plug is inserted and the Swagelok end cap secured with a nut and ferrules. The rear volume displacing mandrel is inserted. 10±1 mg of iodine crystals are weighed on an analytical balance and dumped into the specimen. The front mandrel and front end plug are put inplace. The specimen is secured to the fitting which connects to the high pressure line by Swagelok components as shown in Fig. E.4. A third mandrel displaces some volume in this fitting.

Care must be exercised in specimen assembly to minimize leaks at the Swagelok fittings. The end plugs must not be pushed against the back of the fitting, rather they should be recessed ∿1 mm. When the nuts are attached to the fitting, the tightening must be done slowly to achieve an efficient "bite" of the inner ferrule into the tube. Experience indicates that a tight seal must be obtained upon initial assembly. Swagelok components can be reused several times before leaks develop. Threads are coated with "Neolube" graphite lubricant prior to assembly to facilitate the subsequent disassembly.

Following the test, the failure location on the specimen is

determined prior to removing the specimen assembly from the system.

For tight cracks this requires coating the specimen OD with liquid leak

detector while applying a low internal gas pressure. The Swagelok nuts

are removed. The specimen is cut open above the ferrules at one end.

The mandrels are removed and the end plugs are forcibly pounded out.

The specimen is washed in methanol and sectioned for examination as

indicated in Section 4.
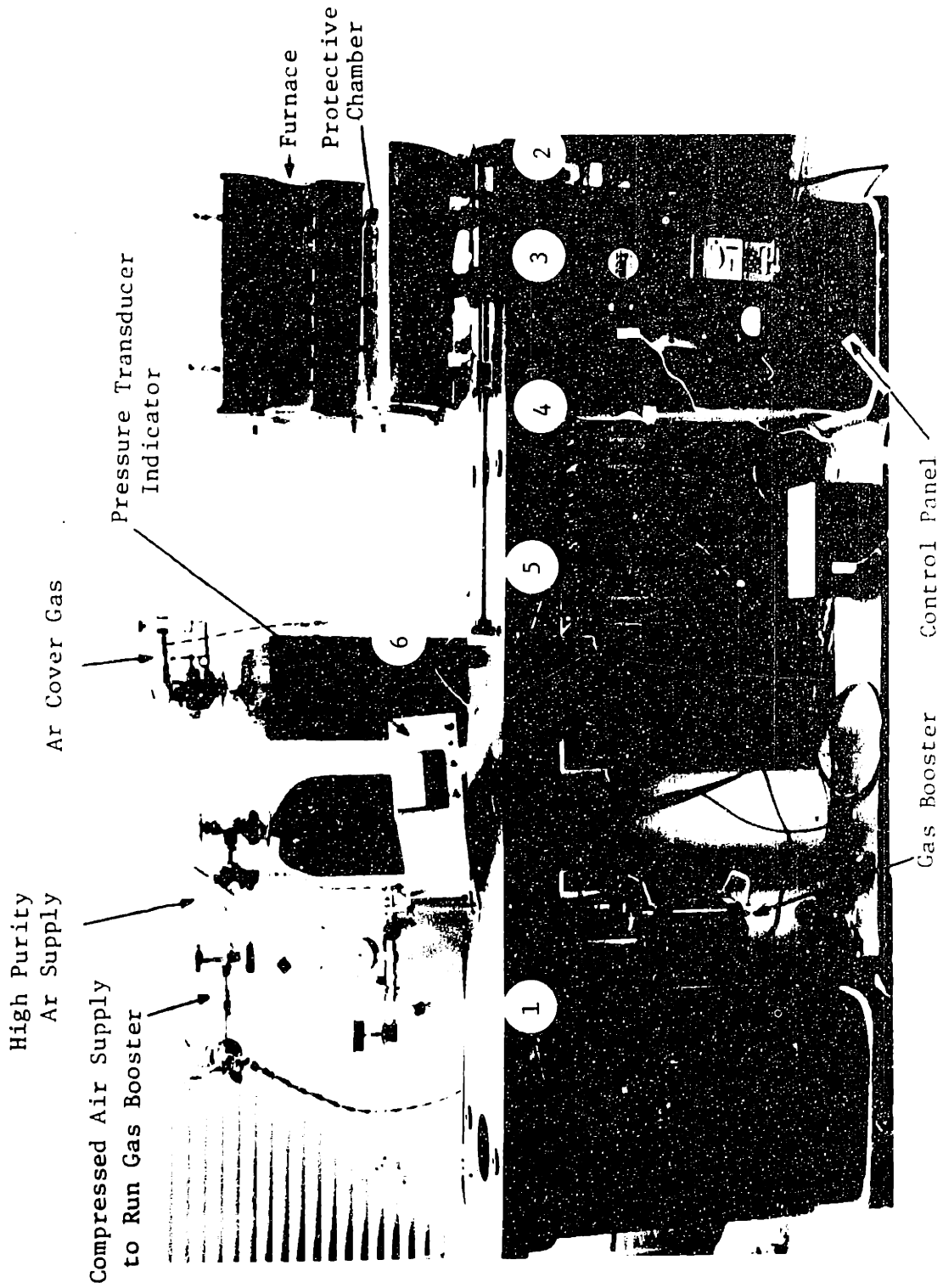
Figure E.1   Large Field View of the Internal Gas Pressurization System
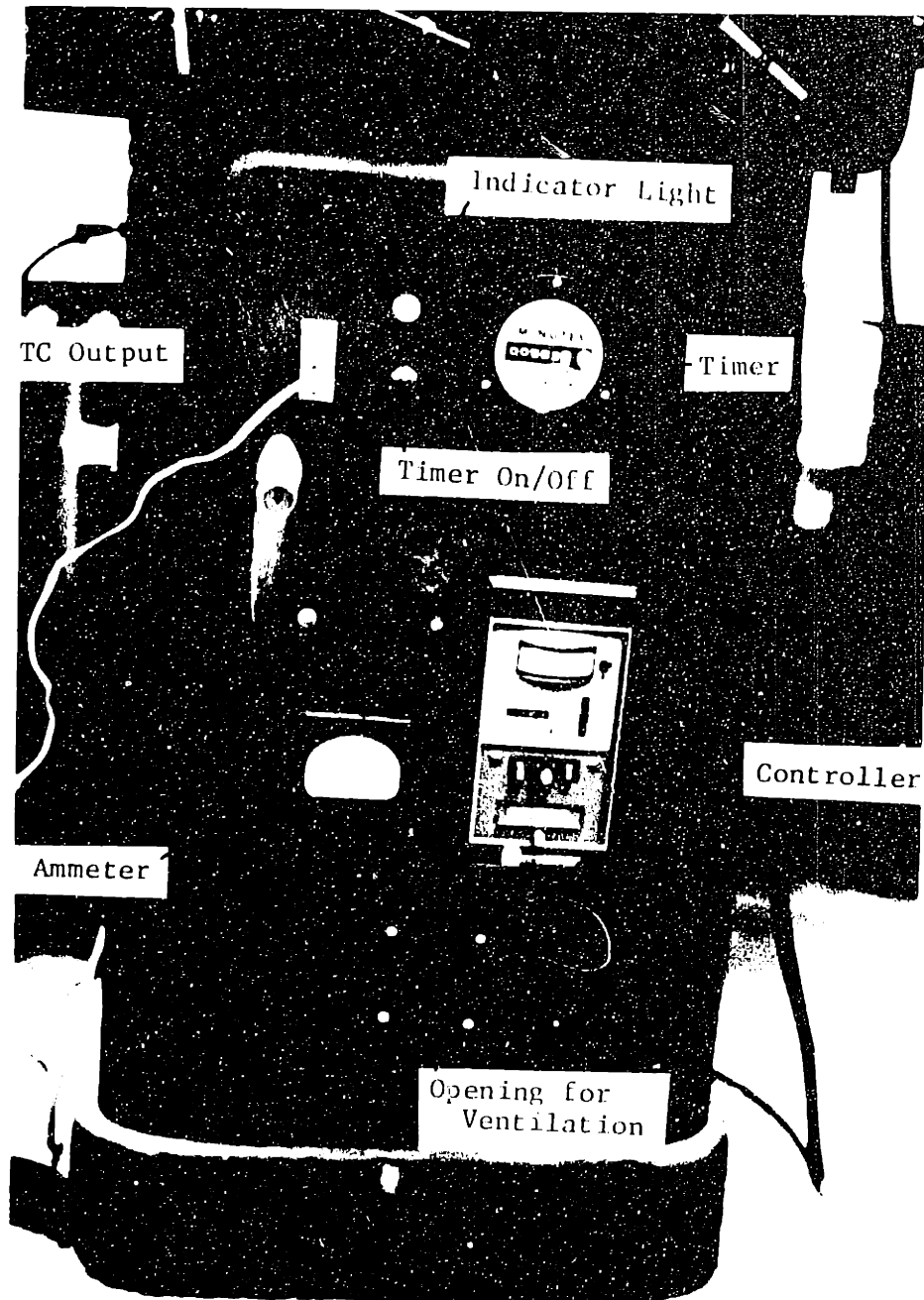
Figure E.2   Closeup of Control Console for the Gas Pressurization System

Specimen Isolation Valve

Cover Gas Inlet

Specimen

End Fittings

Thermocouple
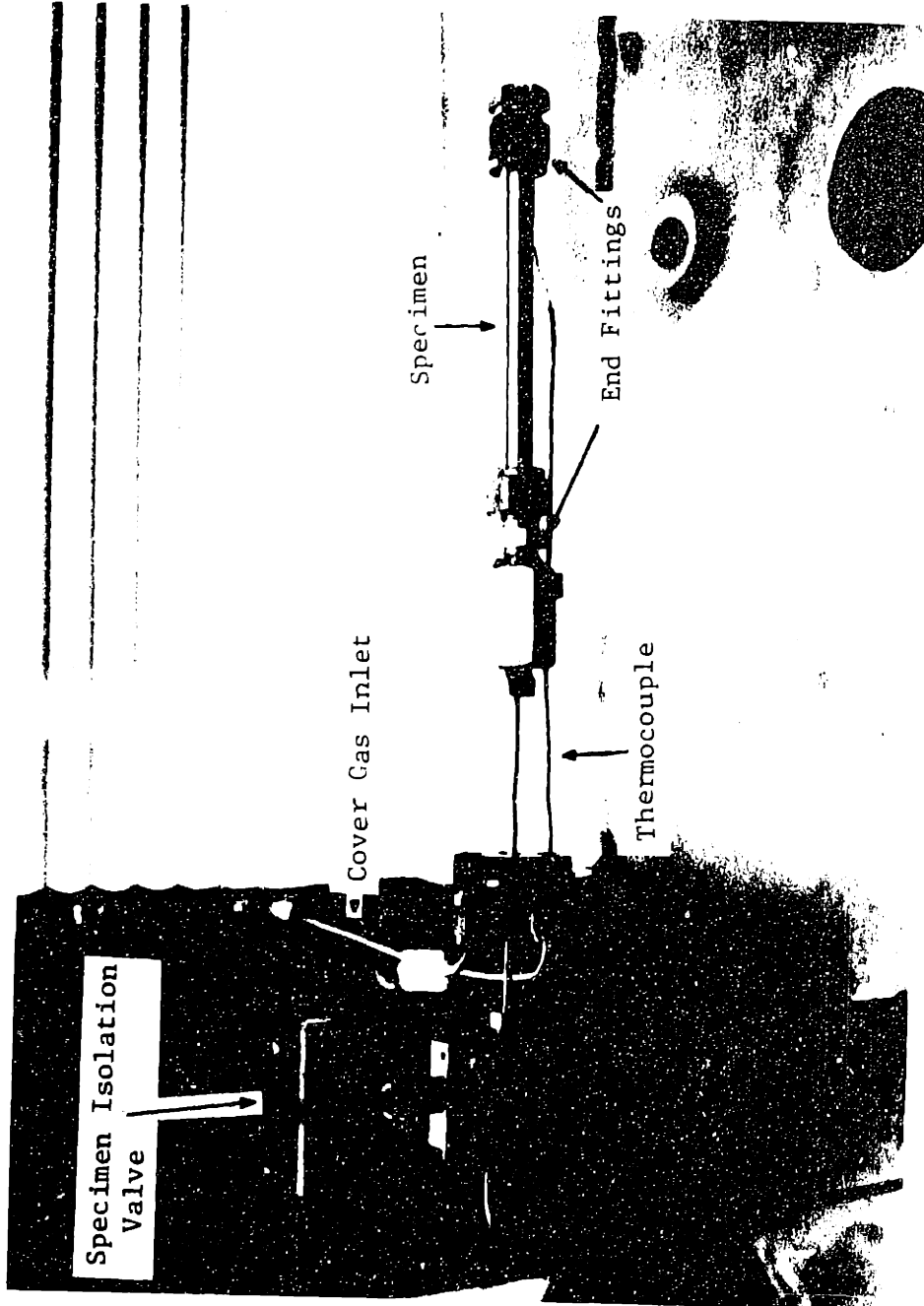
Figure E.3   View of Assembled Tube Specimen in Place Prior to Test

263

Figure E.4   Exploded View of Tube Pressurization Specimen Showing All Internal Components
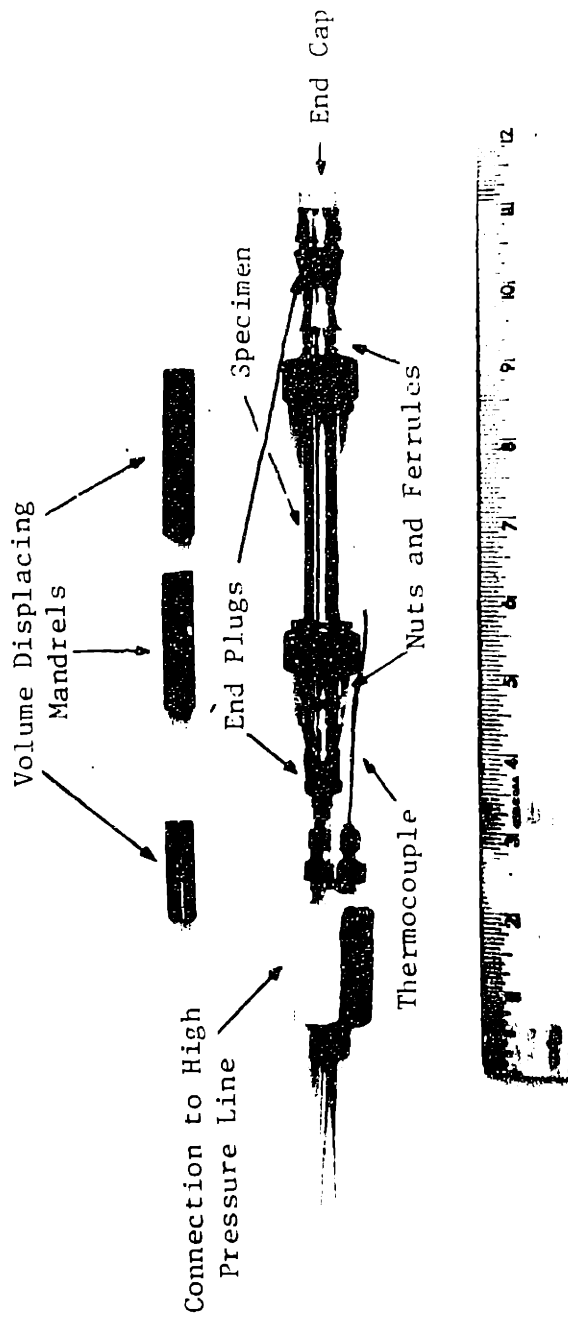
Appendix F

Split Ring Specimen Calibration

The goal of this analysis is to derive the stress versus deflection expressions for the two split ring configurations presented in Section 4.3. The loading geometry is given in Fig. F.1(a) and the free body diagram is shown in Fig. F.1(b).

The energy method attributed to Castigliano is used. It is described in any basic textbook on the mechanics of solids. The initial elastic strain energy, U, for a body in bending is given as:

$$U = \int_s \frac{M^2}{2EI} \, ds \qquad (F-1)$$

where E is Young's modulus and I is the moment of inertia. From the free body diagram, the following substitutions are apparent:

$$M = Px \quad \text{where } x = R(1 - \cos\Theta) \qquad (F-2a)$$

$$ds = R \, dx \qquad (F-2b)$$

Substituting into Eqn. (F-1) gives:

$$U = \frac{P^2}{2EI} \int_0^\Theta [R(1 - \cos\Theta)]^2 \, R \, d\Theta \qquad (F-3)$$

Factoring out R and integrating the resulting relationship yields:

$$U = \frac{P^2 R^3}{2EI} \left\{ \frac{3\Theta}{2} \Big]_0^\Theta - 2\sin\Theta \Big]_0^\Theta + \frac{1}{4} \sin 2\Theta \Big]_0^\Theta \right\} \qquad (F-4)$$

To find deflection Castigliano's theorem is applied:

$$\Delta = \partial U / \partial P \qquad (F-5)$$

The specimen opening, $\delta = 2\Delta$, gives the final result:

$$\delta = \frac{4.524 \, P \, R^3}{EI} \qquad (F-6)$$

The expression for the maximum stress due to bending is:

$$\sigma_{max} = \frac{PRt[1 - \cos(.791\pi)]}{2I} \qquad (F-7)$$

Substitution of Eqn. (F-6) into (F-7) produces the final result:

$$\sigma_{max} = \frac{0.79\delta Et}{D_m^2} \qquad (F-8)$$

which is the same expression as Eqn. (4-4).

A similar procedure is used for the narrow slit specimen design. Instead of $.791\pi$, π is used in the limits of integration of Eqn. (F-4) and the stress formula, Eqn. (F-7). The result is:

$$\sigma_{max} = \frac{4\delta Et}{3\pi D_m^2} \qquad (F-9)$$

which is very similar to Eqn. (4-5).

Strain gage measurements on a wide gap specimen are used to verify this analysis. Eqn. (F-8) is rearranged and the substitution $\epsilon_{max} = \sigma_{max}/E$ is made to give:

$$\delta = \frac{1.27 \, D_m^2}{t} \epsilon_{max} \qquad (F-10)$$

A strain gage (BLH type FAE - 03G - 12 - S6L) is attached at the location of maximum tensile stress and strain. The specimen is wedged a measured amount and the strain is read using a half bridge circuit. Three load/unload runs are made. The data are plotted in Fig. F.2 along with the prediction of Eqn. (F-10). The very good agreement is readily evident.
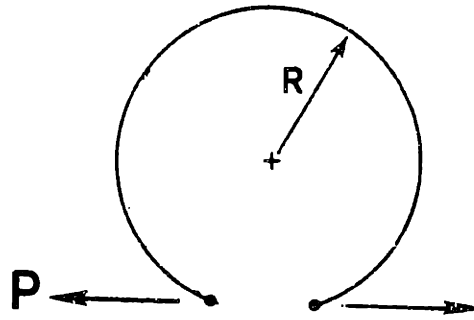
(a) Loading geometry
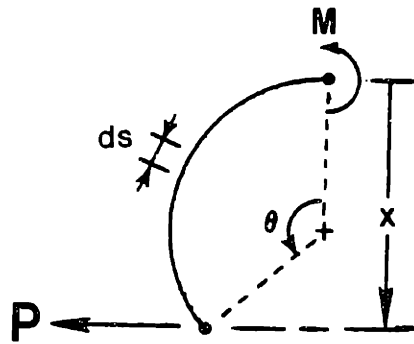
(b) Free body diagram

Figure F.1

Schematic diagram of split ring specimen

Figure F.2

Plot of Strain versus Displacement for Wide Gap Split Ring Specimen
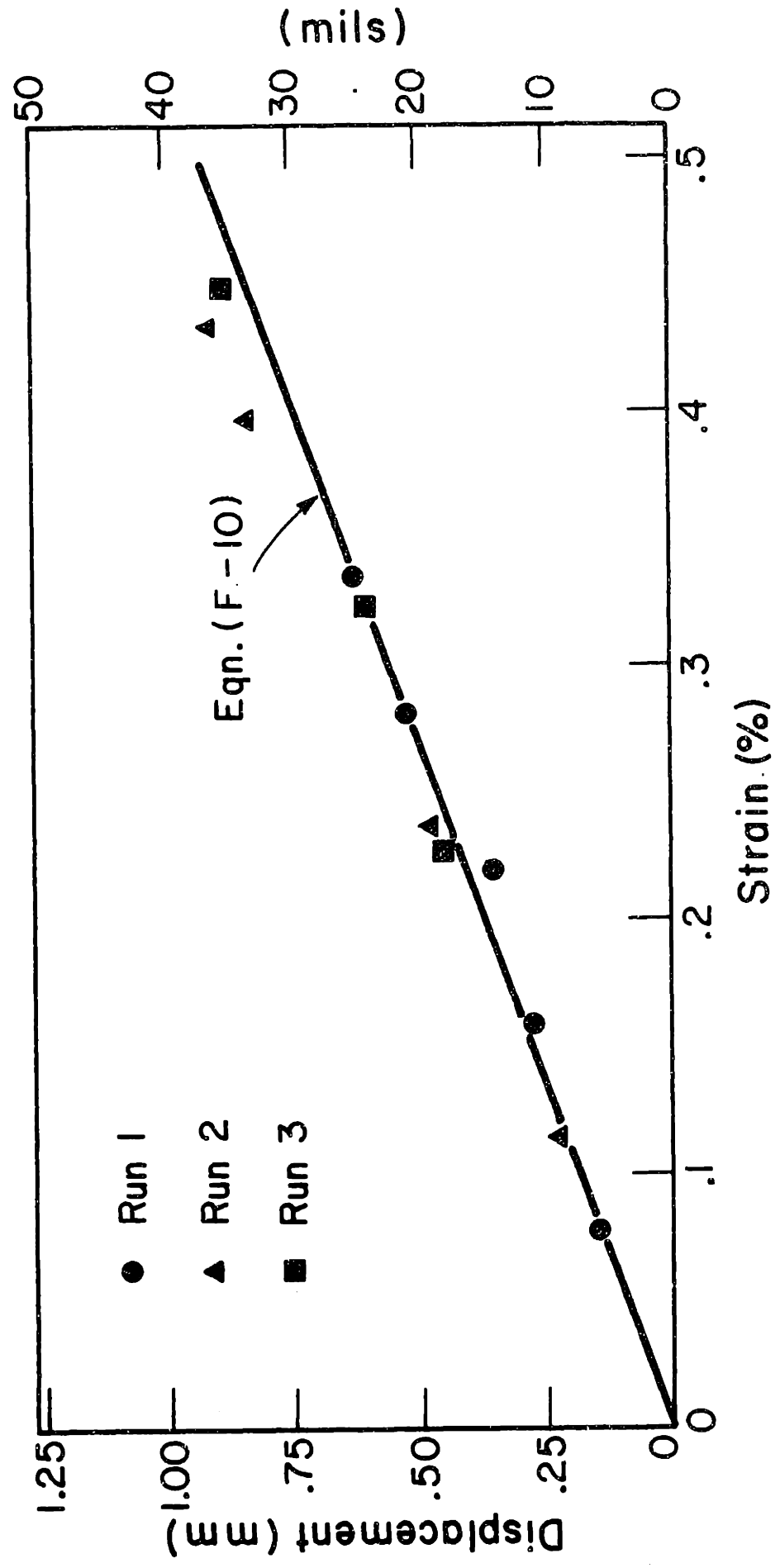
Appendix G

Role of Materials Variables in Crack Initiation

This appendix presents a detailed discussion of the role of
surface finish and heat treatment variables on crack initiation. It is
intended to supplement the discussion of crack initiation in Section
7.4.1. Heat treatment receives initial consideration. The surfaces are
usually pickled so a thin oxide, easily penetrated by iodine, is present.
The effect of surface finish on crack initiation is then discussed.
The role of oxide coatings, surface flaws, and mechanical damage is
evaluated by attempting to analyze how these treatments alter the prop-
erties of the surface compared to the bulk. Both studies by other
investigators and this work are considered.

G.1 Heat Treatment

Intergranular sites are most evident in recrystallized material,
but inconsistencies exist regarding the stress level for attack.
Cubicciotti et al. [75] found intergranular attack below the threshold
stress and initiation at intergranular particles above the threshold
stress while Videm and Lunde [117] report the opposite result, i.e.
attack at particles below the threshold stress and intergranular attack
with no particles present above the threshold stress. The G.E. group
[76, 78] reports intergranular initiation in both irradiated and unirrad-
iated recrystallized material. Intergranular initiation is not generic
to recrystallized material since transgranular initiation sites are also
observed [118].

Although intergranular initiation is preferred in recrystallized
material, any role of intergranular initiation in cold-worked material
is difficult to define because of the heavily deformed and twinned

microstructure. Areas of indeterminate features are observed which are
judged to be intergranular initiation sites [12]. Similar features are
sometimes observed at suspected initiation sites of through wall cracks
in this study. Although these features are clearly not transgranular
cleavage, they are not sufficiently distinct to be confirmed as inter-
granular features. The preferential attack at particles in unstressed
material is not observed to result in crack initiation in stressed
specimens based on examination of small incipient cracks and regions
associated with either the indistinct features (possibly intergranular)
or transgranular sites. Propagation from the crack initiation sites
become clearly transgranular at depths no more than a few grain diameters
from the tube ID as seen near the tube ID in Figs. 6.18 - 6.20.

G.2 Surface Finish

Several mechanisms are postulated [121] to explain the effects of
surface finish:

1. oxide film breakdown at surface flaws;

2. local stress concentrations at surface damage locations;

3. initiation through local chemistry changes;

4. change in the surface texture;

5. introduction of high ID surface residual stresses;

6. introduction of a "damaged", i.e. cold-worked, layer without a
   texture change.

It is important to note that the effect can be either to increase or to
decrease SCC susceptibility. Different mechanisms are potentially
relevant to different surface treatments.

When an impervious oxide film or oxidizing environment is present,
attack occurs at oxide cracks which are not necessarily associated with

particles or grain boundaries [12, 79, 117]. This demonstrates how the initiation site changes due to a change in surface condition.

Crack initiation occurs from pre-existing flaws [104], from the large pits of supplier B/AR condition, and from surfac, treatment defects reported from other work [111, 114, 121]. A comparison of supplier B materials in the AR and AR+P conditions show that the surface finish has some effect on SCC susceptibility. The most likely explanation is a slight decrease in initiation time by mechanism 2 above.

Many studies comparing mechanically treated surfaces with un-treated report increased SCC susceptibility [111, 113, 121] while others [111, 113] report decreased susceptibility under certain circumstances. Without a detailed evaluation of surface condition, it is not possible to determine which of the previous mechanism(s) is responsible for the behavior. The H+SR+P material condition offers several advantages for evaluating which mechanism is responsible for the somewhat greater iodine SCC susceptibility compared to the other material conditions, particularly the SR+P condition which is the same except for the initial honing treatment. The final pickling operation removes most of the damaged layer and thereby eliminates many of the six possible explanations listed above. Local chemistry differences introduced by honing (mech-anism 3) and anomolous surface texture (mechanism 4) become unlikely. Texture analysis reported in Table F.1 shows that the f_r values are un-changed at the H+SR+P surface. Both the SR+P and H+SR+P conditions have a thin, air formed oxide film easily penetrated by iodine [12] so mech-anism 1 is not relevant. The SR treatment makes mechanism 5, high tensile residual stress, unlikely. The pickling operation removes the deep honing gouges so the H+SR+P surface is less rough than supplier B/AR whose large

pits have only a marginal impact on SCC performance making mechanism 2

unlikely. The surface pickling might not remove enough metal to compl-

etely eliminate the cold-worked surface and/or possible small honing

cracks. Thus, mechanism 6 is the most feasible explanation for the in-

creased SCC susceptibility of the H+SR+P condition. The presence of a

layer with greater cold-work is verified by the line broadening measure-

ments,Table 7.1. How the layer affects the mechanics of crack initiation

is only a matter of conjecture.

Table G.1

f_r Values for Various Material Conditions

Material Condition	Specimen Group	Texture Number, f_r Supplier A	Supplier B
AR	1	0.647	0.550
H+SR+P	1	0.649	0.567
SR+P	2	0.618	0.551

REFERENCES

1. M. F. Lyons, D. H. Coplin, R. C. Nelson, and D. L. Zimmerman, General Electric Company Reports GEAP-3771-12, 13 (1964).

2. S. Aas, K. D. Olsausen, and K. Videm, Paper 55, British Nuclear Energy Society Conference (October 1973).

3. A. S. Bain, .T. C. Wood, and C. E. Colemen, Paper 56, British Nuclear Energy Society Conference (October 1973).

4. J. H. Davies et al., General Electric Company Report NEDO-21551 (February 1977); also ANS Topical Meeting, Water Reactor Fuel Performance, St. Charles, Illinois (1977), p. 230.

5. H. S. Rosenbaum, J. H. Davies, and J. W. Pon, General Electric Company Report GEAP-51005 (1966).

6. H. S. Rosenbaum, Electrochem. Tech., 4 (1966), 153.

7. R. D. MacDonald, D. G. Hardy, and C. E. L. Hunt, Trans. ANS, 17 (1973), 216.

8. A. Garlick and J. G. Gravenor, ANS Topical Meeting, Water Reactor Performance, St. Charles, Illinois (1977), p. 305.

9. N. Furman et al., Electric Power Research Institute Report EPRI-NP-218 (1976); also ANS Topical Meeting, Water Reactor Fuel Performance, St. Charles, Illinois (1977), p. 262.

10. J. T. A. Roberts and F. E. Gelhaus, Zirconium in the Nuclear Industry (Fourth Conference), ASTM STP ·681, American Society for Testing and Materials (1979), p. 19.

11. F. Garzarolli, R. van Jan, and H. Stehle, Atomic Energy Rev., 17 (1979), 31.

12. B. Cox and J. C. Wood, Corrosion Problems in Energy Conversion and Generation, Electrochemical Society (1974), p. 275.

13. G. Kjaerheim and E. Rolstad, Nucl. Appl. Tech., 7 (1969), 347.

14. S. Aas, Nucl. Engr. Des., 21 (1972), 237.

15. H. M. Ferrari, Nucl. Engr. Inter., (July/August 1970), 623.

16. R. Holzer, D. Knodler, and H. Stehle, ANS Topical Meeting, Water Reactor Fuel Performance, St. Charles, Illinois (1977), p. 207.

17. V. Pasupathi and J. S. Perrin, ANS Topical Meeting on Light Water Reactor Fuel Performance, Portland, Oregon (1979), p. 141.

18. R. P. Gangloff and L. F. Coffin, General Electric Company Report 79 CRD 016 (February 1979).

19. D. Cubicciotti and R. L. Jones, Electric Power Research Institute Report EPRI-NP-717 (March 1978).

20. D. Cubicciotti, Final Report, EPRI Project RP-355-11, Electric Power Research Institute (December 1978).

21. M. G. Adamson, E. A. Aitken, S. K. Evans, and J. H. Davies, Thermodynamics of Nuclear Materials, Vol. I, International Atomic Energy Agency (1975), p. 59.

22. M. H. Rand and L. E. J. Roberts, Thermodynamics, Vol. I, International Atomic Energy Agency (1965), p. 3.

23. M. H. Rand and T. L. Markin, Thermodynamics, Vol. I, International Atomic Energy Agency (1965), p. 637.

24. M. G. Adamson and R. F. A. Carney, J. Nucl. Mater., 54 (1974), 121.

25. E. H. P. Cordfunke, Thermodynamics of Nuclear Materials 1974, Vol. II, International Atomic Energy Agency (1975), p. 185.

26. H. Kleykamp, J. Nucl. Mater., 84 (1979), 109.

27. F. H. Megerth, C. P. Rulz, and U. E. Wolff, General Electric Company Report GEAP-10371 (June 1971).

28. J. Bazin, J. Jouan, and N. Vignesoult, Trans. ANS, 20 (1975), 235.

29. C. R. A. Catlow, J. Nucl. Mater., 79 (1979), 432.

30. T. L. Markin and E. C. Crouch, J. Inorg. Nucl. Chem., 32 (1970), 77.

31. M. Tenenbaum, Thermodynamics of Nuclear Materials 1974, Vol. II, International Atomic Energy Agency (1975), p. 305.

32. N. A. Javed, J. Nucl. Mater., 47 (1973), 336.

33. C. E. Johnson et al., ANL-7977, Argonne National Lab (January 1973).

34. R. E. Woodley, J. Nucl. Mater., 74 (1978), 290.

35. P. E. Blackburn, J. Nucl. Mater., 46 (1973), 244.

36. D. R. Olander, Fundamental Aspects of Nuclear Fuel Elements, Chap. 11 and 12, Energy Research and Development Administration (1976).

37. C. E. Johnson et al., ANL-8122, Argonne National Lab (January 1975).

38. F. Garzarolli, R. Manzel, M. Peehs, and H. Stehle, Kerntechnik, 20 (1978), 27.

39. M. Peehs, R. Manzel, W. Schweighofer, W. Haas, E. Haas, and R. Wurtz, J. Nucl. Mater., 97 (1981), 157.

40. D. Cubicciotti and J. E. Sanecki, J. Nucl. Mater., 78 (1978), 96; also ANS Topical Meeting, Water Reactor Fuel Performance, St. Charles, Illinois (1977), p. 282.

41. J. Bazin et al., Bull. Inform. Sci. Tech., CEA, France, 196 (1974), 55.

42. D. C. Fee and C. E. Johnson, J. Nucl. Mater., 78 (1978), 219.

43. W. T. Grubb and M. H. Morgan III, Zirconium in the Nuclear Industry (Fourth Conference), ASTM STP 681, American Society fot Testing and Materials (1979), p. 145.

44. J. C. Wood, B. A. Surette, I. M. London, and J. Baird, J. Nucl. Mater., 57 (1975), 155.

45. B. C. Syrett, D. Cubicciotti, and R. L. Jones, Zirconium in the Nuclear Industry, ASTM STP 633, American Society for Testing and Materials (1977), p. 281.

46. D. Cubicciotti and J. H. Davies, Nucl. Sci. Engr., 60 (1976), 314.

47. J. H. Davies, F. T. Frydenbo, and M. G. Adamson, J. Nucl. Mater., 80 (1979), 366.

48. J. D. Corbett, R. L. Daake, K. R. Poeppelmeier, and D. H. Guthrie, J. Amer. Chem. Soc., 100 (1978), 652.

49. J. D. Corbett, R. L. Daake, A. Cisar, and D. H. Guthrie, Proceedings of the Symposium on High Temperature Metal-Halide Chemistry, The Electrochemical Society (1977), p. 210.

50. R. L. Daake and J. D. Corbett, Inorg. Chem., 17 (1978), 1192.

51. R. L. Daake and J. D. Corbett, Inorg. Chem., 16 (1977), 2029.

52. M. A. Bhatti, D. B. Copley, and R. A. J. Shelton, J. Less-Common Metals, 55 (1977), 293.

53. D. Cubicciotti, K. H. Lau, and M. J. Ferrante, J. Electrochem. Soc., 125 (1978), 972.

54. D. Cubicciotti and K. H. Lau, J. Electrochem. Soc., 128 (1981), 196.

55. D. Cubicciotti and K. H. Lau, J. Electrochem. Soc., 126 (1979), 771.

56. R. H. Lamoreaux and D. Cubicciotti, J. Electrochem. Soc., 128 (1981), 457.

57. F. R. Sale and R. A. J. Shelton, J. Less-Common Metals, 9 (1965), 64.

58. D. Cubicciotti, D. L. Hildenbrand, K. H. Lau, and P. D. Kleinschmidt, Proceedings of the Symposium on High Temperature Metal-Halide Chemistry, The Electrochemical Society (1977), p. 217.

59. L. Brewer, Proceedings of the Symposium on High Temperature Metal-Halide Chemistry, The Electrochemical Society (1977), p. 177.

60. F. R. Sale and R. A. J. Shelton, J. Less-Common Metals, 9 (1965), 54.

61. E. M. Larson and J. J. Leddy, J. Amer. Chem. Soc., 78 (1956), 5983.

62. F. R. Sale and R. A. J. Shelton, J. Less-Common Metals, 9 (1965), 60.

63. L. F. Dahl, T. Chiang, P. W. Seabaugh, and E. M. Larson, Inorg. Chem., 9 (1964), 1236.

64. I. E. Newnham and J. A. Watts, J. Amer. Chem. Soc., 82 (1960), 2113.

65. T. M. Besmann and T. B. Lindemer, Nucl. Tech., 40 (1978), 297.

66. D. Cubicciotti, R. L. Jones, and B. C. Syrett, paper presented at the 5th International Conference on Zirconium in the Nuclear Industry, Boston, MA (August 1980).

67. L. N. Shelest, E. K. Safronov, and A. S. Mikhailova, Russ. J. Inorg. Chem., 18 (1973), 9.

68. R. M. Horton and R. L. Kinney, Metal-Slag-Gas Reactions and Processes, The Electrochemical Society (1975), p. 317.

69. H. Feuerstein, ORNL-4543, Oak Ridge National Laboratory (August 1970).

70. G. N. Krishnan, B. J. Wood, and D. Cubicciotti, J. Electrochem. Soc., 127 (1980), 2738.

71. F. R. Sale, J. Less-Common Metals, 19 (1969), 53.

72. D. Cubicciotti and A. C. Scott, J. Less-Common Metals, 77 (1981), 241.

73. P. L. Danial and R. A. Rapp, Advances in Corrosion Science and Technology, Vol. 5, Plenum Press (1976), 55.

74. L. F. Coffin and R. P. Gangloff, ANS Topical Meeting, Water Reactor Fuel Performance, St. Charles, Illinois (1977), p. 346.

75. D. Cubicciotti, S. M. Howard, and R. L. Jones, J. Nucl. Mater., 78 (1978), 2.

76. D. S. Tomalin, R. B. Adamson, and R. P. Gangloff, Zirconium in the Nuclear Industry (Fourth Conference), ASTM STP 681, American Society for Testing and Materials (1979), p. 122.

77. D. S. Tomalin, Zirconium in the Nuclear Industry, ASTM STP 633, American Society for Testing and Materials (1977), p. 557.

78. D. Lee and R. B. Adamson, Zirconium in the Nuclear Industry, ASTM STP 633, American Society for Testing and Materials (1977), p. 385.

79. R. P. Gangloff, D. E. Graham, and A. W. Funkenbusch, Corrosion, 35 (1979), 316.

80. A Garlick and P. D. Wolfenden, J. Nucl. Mater., 41 (1971), 274.

81. M. Peehs, H. Stehle, and E. Steinberg, Zirconium in the Nuclear Industry (Fourth Conference), ASTM STP 681, American Society for Testing and Materials (1979), p. 244.

82. J. C. Wood, J. Nucl. Mater., 45 (1972/73), 105.

83. J. C. Wood, Nucl. Tech., 23 (1975), 63.

84. B. Van der Schaaf, Zirconium in Nuclear Applications, ASTM STP 551, American Society for Testing and Materials (1974), p. 479.

85. A. Garlick, J. Nucl. Mater., 49 (1973/74),209.

86. K. Videm and L. Lunde, Ann. Nucl. Energy, 3 (1976), 305.

87. N. W. Polan and R. P. Tucker, WAPD-TM-1313, Westinghouse Electric Corp. (December 1977).

88. K. Une, J. Nucl. Sci. Tech., 14 (1977), 443.

89. J. G. Weinberg, WAPD-TM-1048, Westinghouse Electric Corp., (February 1974).

90. K. Une, J. Nucl. Sci. Tech., 14 (1977), 610.

91. K. Une, ANS Topical Meeting on Light Water Reactor Fuel Performance, Portland, Oregon (1979), p. 148.

92. H. Wachob and H. G. Nelson, Environment Sensitive Fracture of Engineering Materials, Proceedings TMS-AIME Symposium (1977), p. 314.

93. Z. M. Shapiro, The Metallurgy of Zirconium, McGraw-Hill (1955), p. 135.

94. O.Kubaschewski, E. L. Evans, and C. B. Alcock, Metallurgical Thermochemistry, 4th ed., Pergamon Press (1967).

95. I. Barin and O. Knacke, Thermochemical Properties of Inorganic Substances, Springer-Verlag (1973).

96. L. F. Coffin, Zirconium in the Nuclear Industry (Fourth Conference), ASTM STP 681, American Society for Testing and Materials (1979), p. 72.

97. W. T. Grubb, Nature, <u>265</u> (1977), 36.

98. W. T. Grubb and M. H. Morgan, <u>ANS Topical Meeting, Water Reactor Fuel Performance</u>, St. Charles, Illinois (1977), p. 295.

99. J. C. Wood, A. S. Bain, and D. G. Hardy, <u>ANS Topical Meeting on Light Water Reactor Fuel Performance</u>, Portland, Oregon (1979), p. 169.

100. B. Cox, Rev. Coat. Corr., <u>1</u> (1975), 366.

101. R. Sejnoha and J. C. Wood, <u>Zirconium in the Nuclear Industry (Fourth Conference)</u>, ASTM STP 681, American Society for Testing and Materials (1979), p. 261.

102. B. Cox, <u>Zirconium in the Nuclear Industry (Fourth Conference)</u>, ASTM STP 681, American Society for Testing and Materials (1979), p. 366.

103. R. B. Adamson, J. Nucl. Mater., <u>92</u> (1980), 363.

104. R. L. Jones, F. L. Yaggee, R. A. Stoer, and D. Cubicciotti, J. Nucl. Mater., <u>82</u> (1979), 26.

105. D. Cubicciotti, R. L. Jones, and B. C. Syrett, EPRI NP-1329, Electric Power Research Institute (March 1980).

106. F. L. Yaggee, R. F. Mattas, and L. A. Neimark, EPRI NP-1155, Electric Power Research Institute (Sept. 1979).

107. F. L. Yaggee, R. F. Mattas, and L. A. Neimark, EPRI NP-1557, Electric Power Research Institute (October 1980).

108. I. Aitchison and B. Cox, Corrosion, <u>28</u> (1972), 83.

109. R. L. Jones, D. Cubicciotti, and B. C. Syrett, J. Nucl. Mater., <u>91</u> (1980), 277.

110. R. F. Mattas, F. L. Yaggee, and L. A. Neimark, <u>ANS Topical Meeting on Light Water Reactor Fuel Performance</u>, Portland, Oregon (1979), p. 128.

111. B. C. Syrett, D. Cubicciotti, and R. L. Jones, J. Nucl. Mater., <u>92</u> (1980), 89; also <u>ANS Topical Meeting on Light Water Reactor Fuel Performance</u>, Portland, Oregon (1979), p. 113.

112. B. C. Syrett, R. L. Jones, and D. Cubicciotti, J. Nucl. Mater., <u>96</u> (1981), 160.

113. B. C. Syrett, D. Cubicciotti, and R. L. Jones, "The Effect of Texture and Surface Condition on the Iodine Stress Corrosion Cracking Susceptibility of Unirradiated Zircaloy", submitted to J. Nucl. Mater.

114. D. Cubicciotti, B. C. Syrett, and R. L. Jones, "Influence of Surface Condition on Crack Initiation in Iodine Stress Corrosion Cracking of Zircaloys", submitted to Nucl. Tech.

115. M. Peehs, W. Jung, H. Stehle, and E. Steinberg, Paper 11, IAEA Specialists Meeting on Pellet Clad Interaction in LWR's, Riso (September 1980).

116. C. C. Busby, R. P. Tucker, and J. E. McCauley, WAPD-TM-1149, Westinghouse Electric Corp. (July 1974).

117. K. Videm and L. Lunde, Zirconium in the Nuclear Industry (Fourth Conference), ASTM STP 681, American Society for Testing and Materials (1979), p. 229.

118. K. Videm and L. Lunde, ANS Topical Meeting, Water Reactor Fuel Performance, St. Charles, Illinois (1977), p. 274.

119. K. Videm, L.Lunde, T. Hollowell, K. Vilpponen, and C. Vitanza, J. Nucl. Mater., 87 (1979), 259.

120. L. Lunde and K. Videm, J. Nucl. Mater., 95 (1980), 210.

121. H. W. Wilson, K. K. Yoon, and D. L. Baty, ANS Topical Meeting on Light Water Reactor Fuel Performance, Portland, Oregon (1979), p. 246.

122. J. H. Payer, W. E. Berry, and W. K. Boyd, Stress Corrosion – New Approaches, ASTM STP 610, American Society for Testing and Materials (1976), p. 82.

123. W. G. Clark, Jr. and J. D. Landes, Stress Corrosion – New Approaches, ASTM STP 610, American Society for Testing and Materials (1976), p. 108.

124. S. T. Rolfe and J. M. Barsom, Fracture and Fatigue Control in Structures, Chap. 10, Prentice-Hall (1977).

125. G. V. Rajan, G. N. Brooks, M. Eisenberger, J. M. Thomas, and A. K. Miller, FAA-EPRI-73-3-3(D-2), Failure Analysis Associates Report for Electric Power Research Institute Project RP 971, (October 1979).

126. D. Lee, Trans. ASM, 61 (1968), 742.

127. H. Maki and M. Ooyama, J. Nucl. Sci. Tech., 12 (1975), 423.

128. T. Andersson and A. Wilson, Zirconium in the Nuclear Industry (Fourth Conference), ASTM STP 681, American Society for Testing and Materials (1979), p. 60.

129. R. G. Ballinger, S. M. Thesis, MIT (September 1977); also R. M. Pelloux, R. Ballinger, and G. Lucas, EPRI NP-982, Electric Power Research Institute (1979).

130. K. Kallstrom, Scand. J. Met., 4 (1975), 65.

131. K. Kallstrom, T. Andersson, and A. Hofvenstam, Zirconium in Nuclear Applications, ASTM STP 551, American Society for Testing and Materials (1974), p. 160.

132. J. J. Kearns, J. Nucl. Mater., 22 (1967), 292.

133. G. F. Rieger and D. Lee, Zirconium in Nuclear Applications, ASTM STP 551, American Society for Testing and Materials (1974), p. 355.

134. D. G. Hardy, Irradiation Effects on Structural Alloys for Nuclear Applications, ASTM STP 484, American Society for Testing and Materials (1970), p. 215.

135. A. L. Bement, J. C. Tobin, and R. G. Hoagland, Flow and Fracture of Metals and Alloys in Nuclear Environments, ASTM STP 380, American Society for Testing and Materials (1965), p. 364.

136. J. T. A. Roberts, R. L. Jones, D. Cubicciotti, A. K. Miller, H. F. Wachot, E. Smith, and F. L. Yaggee, Zirconium in the Nuclear Industry (Fourth Conference), ASTM STP 681, American Society for Testing and Materials (1979), p. 285.

137. E. Smith, J. Nucl. Mater., 95 (1980), 285.

138. H. Ocken, EPRI Journal, (March 1981), 18.

139. F. W. Buckman, C. E. Crouthamel, and M. D. Freshley, ANS Topical Meeting on Light Water Reactor Fuel Performance, St. Charles, Illinois (1977), p.

140. S. G. McDonald, R. D. Fardo, P. J. Sipush, and R. S. Kaiser, IAEA Specialists Meeting on Pellet Clad Interaction in LWR's, Riso (September 1980).

141. R. Ballinger, R. Christensen, R. Eibert, S. Oldberg, E. Rumble, and G. Was, paper presented at 5th International Conference on Zirconium in the Nuclear Industry, Boston, MA (August 1980).

142. C. L. Mohr, P. J. Pankaskie, P. G. Heasler, and J. C. Wood, NUREG/CR-1165 (PNL-2755), Battelle Pacific Northwest Laboratories (December 1979).

143. B. L. Adams, D. L. Baty, and K. L. Murty, Scripta Met., 12 (1978), 1151.

144. B. Tomkins and J. Gittus, Advances in Research on the Strength and Fracture of Materials, Vol. 4, ICF4, Waterloo, Canada (1977), p. 75.

145. P. H. Kreyns, G. L. Spahr, and J. E. McCauley, J. Nucl. Mater., 61 (1976), 203.

146. J. H. Gittus and D. A. Howl, ANS Topical Meeting, Water Reactor Fuel Performance, St. Charles, Illinois (1977), p. 169.

147. D. B. Knorr, S. M. Thesis, MIT (February 1977).

148. D. B. Knorr and R. M. Pelloux, J. Nucl. Mater., 71 (1977), 1.

149. L. G. Schulz, J. Appl. Phys., 20 (1949), 1030.

150. J. J. Kearns, WAPD-TM-472, Westinghouse Electric Corp. (1965).

151. W. M. Evans, R. F. Gesner, and J. G. Goodwin, Met. Trans., 3 (1972), 2879.

152. G. Sacks and G. Espey, Trans. AIME, 147 (1942), 348.

153. A. F. Reid and R. Mills, J. Inorg. Nucl. Chem., 26 (1964), 892.

154. E. T. Wessel, Eng. Fract. Mech., 1 (1968), 77.

155. S. R. Nowak and S. T. Rolfe, J. Mater., 4 (1967), 701.

156. M. O. Speidel and H. V. Hyatt, Advances in Corrosion Science and Technology, Vol. 2, Plenum Press (1972), 115.

157. M. V. Hyatt, Boeing Report D6-24466 (November 1969).

158. B. Stellwag and H. Kaesche, Int. J. Fract., 14 (1978), R303.

159. A Saxena and S. J. Hudak, Int. J. Fract., 14 (1978), 453.

160. S. Mostovoy, P. B. Crosley, and E. J. Ripling, J. Mater., 2 (1967), 661.

161. D. B. Dawson and R. M. Pelloux, to be published Met. Trans. A.

162. F. R. Larson and A. Zarkades, Advances in Deformation Processing, Plenum Press (1978), p. 321.

163. E. Tenckhoff, Zirconium in Nuclear Applications, ASTM STP 551, American Society for Testing and Materials (1974), p. 179.

164. W. Tyson, J. Nucl. Mater., 24 (1967), 101.

165. J. A. Jenson and W. A. Backofen, Can. Met. Quart., 11 (1972), 39.

166. J. Spurrier and J. C. Scully, Corrosion, 21 (1972), 453.

167. F. A. McClintok and A. S. Argon, Mechanical Behavior of Materials, Addison-Wesley (1966), p. 433.

168. B. D. Cullity, Elements of X-ray Diffraction, 2nd. ed., Addison-Wesley (1978), Chap. 9.

169. Exxon Nuclear Company Report XN-NF-77-21, EPRI Contract RP 895-1-4, (October 1977).

170. P. A. Ross-Ross, V. Fidleris, and D. E. Fraser, Can. Met. Quart., 11 (1972), 101.

171. P. Chemelle, S. M. Thesis, MIT (September 1980).

172. A. K. Miller, K. D. Challenger, A. Tasooji, G. V. Ranjan, G. N. Brooks, M. Eisenberger, and J. M. Thomas, EPRI NP-1798, Electric Power Research Institute (April 1981).

173. E. Smith and A. K. Miller, J. Nucl. Mater., 80 (1979), 291.

174. E. Smith, J. Nucl. Mater., 89 (1980), 87.

175. D. Broek, Elementary Engineering Fracture Mechanics, Sijthoff and Noordhoff (1978), Chap. 3.

176. T. G. F. Gray, Int. J. Fract., 13 (1977), 65.

177. J. C. Newman, Jr., Eng. Fract. Mech., 5 (1973), 667.

178. P. T. Heald, G. M. Spink, and P. J. Worthington, Mater. Sci. Engr., 10 (1972), 129.

179. B. A. Bilby, A. H. Cottrell, and K. H. Swinden, Proc. Roy. Soc. London, A272 (1963), 304.

180. M. Gell and E. Smith, Acta Met., 15 (1967), 253.

181. G. Senski, Paper C3/10, Transactions of the 4th International Conference on Structural Mechanics in Reactor Technology, San Francisco (1977).

Biographical Note

The author was born August 20, 1952 in Buffalo, New York and grew up in East Aurora, New York where he attended the East Aurora Public Schools. Undergraduate education was obtained at Lehigh University in Bethlehem, Pennsylvania majoring in Metallurgy and Materials Science. Following undergraduate school, the author accepted a position as an engineer at General Electric Company, Knolls Atomic Power Laboratory in Schenectady, New York from July 1974 until January 1976. The author enrolled at MIT starting in February 1976, earned an SM degree in February 1977, and spent the remaining time completing the requirements for the Doctor of Science in Metallurgy. The author enjoys performing music being a bassoon player in a variety of music groups since childhood and at MIT. He also likes sports and is an avid runner.